Full vector-field control of femtosecond laser pulses with an improved optical design

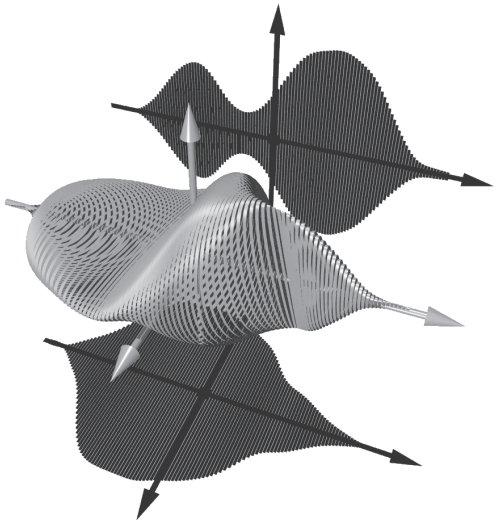

Dissertation zur Erlangung
des naturwissenschaftlichen Doktorgrades
der Bayerischen Julius-Maximilians-Universität Würzburg

vorgelegt von

Christoph Benjamin Schwarz

aus Coburg

Würzburg 2015

Eingereicht am: 18.05.2015
bei der Fakultät für Physik und Astronomie

1. Gutachter: Prof. Dr. Tobias Brixner
2. Gutachter: Prof. Dr. Sven Höfling
der Dissertation

1. Prüfer: Prof. Dr. Tobias Brixner
2. Prüfer: Prof. Dr. Sven Höfling
3. Prüfer: Prof. Dr. Björn Trauzettel
im Promotionskolloquium

Tag des Promotionskolloquiums: 20.12.2016

Doktorurkunde ausgehändigt am: _____

List of publications

[1] C. Schwarz, O. Hüter, and T. Brixner.
Full vector-field control of ultrashort laser pulses utilizing a single dual-layer spatial light modulator in a common-path setup.
Journal of the Optical Society of America B **32**, 933–945 (2015).

Additional publications not presented in this thesis:

[2] U. Selig, F. Langhojer, F. Dimler, T. Löhrig, C. Schwarz, B. Gieseking, and T. Brixner.
Inherently phase-stable coherent two-dimensional spectroscopy using only conventional optics.
Optics Letters **33**, 2851–2853 (2008).

Parts of this dissertation are published in Ref. [1] as listed in the following table. The text and figures presented in Ref. [1] were written and created by the first author and influenced by the co-authors. Figures reproduced or modified from Ref. [1] are identified in the respective captions.

Publication [1]	**Use**	**Dissertation**
Section 1 pp. 933–934	text reproduced, modified, and extended	pp. 121–123
Section 2 pp. 934–935	text reproduced, modified, and extended	pp. 51–55
Section 3 pp. 935–937	text reproduced, modified, and extended	pp. 56–60
Section 4 pp. 937–938	text reproduced, modified, and extended	pp. 68–70 pp. 97–98
Section 5 pp. 938–940	text reproduced, modified, and extended	pp. 98–99 pp. 103–106
Section 6A pp. 940–941	text reproduced, modified, and extended	pp. 99–100 p. 103 pp. 106–108
Section 6B pp. 941–943	text reproduced, modified, and extended	pp. 80–81 p. 101 pp. 109–118
Section 7 pp. 943–944	text reproduced, modified, and extended	p. 73 pp. 118–119 pp. 121–123

Following figures, created and published in Ref. [3] by Dr. Stefan Rützel, are used with permission in this thesis. Their source is additionally marked in the respective caption.

Publication [3]	**Use**	**Dissertation**
Figure 2.3, p. 12	figure adapted and modified	Figure 2.1, p. 8
Figure 2.8, p. 19	figure adapted and modified	Figure 2.2, p. 10
Figure 2.9, p. 21	figure adapted and modified	Figure 2.3, p. 12
Figure 2.10, p. 22	figure adapted and modified	Figure 2.4, p. 13
Figure 3.5, p. 46	figure adapted and modified	Figure 3.4, p. 30

Contents

1 Introduction

The goal of research is not only to gain insights into fundamental natural phenomena, but also to utilize the acquired knowledge for manipulating those phenomena and for creating new technologies which enables further scientific advances. The studies of light by Albert Einstein and other scientists laid the foundation for the development of the laser. The steady evolution of lasers nowadays makes it possible to generate pulsed light fields with a temporal duration of only a few femtoseconds (10^{-15} s) [4–10] which has turned out to be a key technology in numerous research fields and commercial applications. Even more fascinating is the fact that such ultrashort laser pulses can also be manipulated to generate tailored light fields.

The devices used to produce arbitrary optical waveforms are called pulse shapers. Pulse shaping in the femtosecond regime was first reported by Weiner et al. [11] using a static mask. However, due to the use of fixed masks, the applicability of such a device was very limited. From a technological point of view, the breakthrough for pulse shaping was the development of programmable spatial light modulators [12–14], which allow the flexible generation of arbitrary modulated pulses with a single device. Today, the control of ultrashort laser pulses in the frequency or the time domain is a well-established technique in many research areas such as spectroscopy and microscopy [15–22] or quantum control [23–33]. Apart from that, pulse shaping is also used for commercial applications such as telecommunication [34–36] or material processing [37].

In our group, the active control of femtosecond laser pulses is utilized to study and to control ultrafast photochemical reactions, energy transfer in molecular systems, and optical near-fields in nanostructures. In all these fields, light–matter interactions which have a strong vectorial character occur. Therefore, it is desired to control all parameters of the vector-field of ultrashort laser pulses: phase, amplitude, and polarization. However, while major advances on pulse shaping techniques have been achieved in the last three decades, most pulse shapers are only capable of generating linearly polarized pulses, shaped in phase and amplitude [38–41]. Polarization control is feasible with some of these conventional pulse shapers, but limited regarding the accessible polarization states and this method lacks simultaneous amplitude control [42]. Despite these restrictions, the benefits of polarization shaping have been demonstrated in numerous studies, especially in the field of quantum control [43–52]. However, only by unrestricted polarization control the complete potential of quantum control can be exploited. Moreover, this technique is required to compensate arbitrary polarization distortions which can occur in optical fibers used in many commercial applications such as telecommunication, material processing, and endoscopy. Besides unrestricted polarization control, also the simultaneous control of polarization and amplitude is desired as this enables the generation of polarization-shaped multipulse sequences which are of high interest for some state-of-the-art experimental methods used in femtochemistry, nano-optics, and

plasmonics.

One of these methods is two-dimensional spectroscopy [53–61]. This technique is basically an extension of pump–probe spectroscopy [62–65] and allows the examination of couplings and population transfer in atoms [66–70], molecular systems [71–81], as well as solid state samples [82–85]. Two-dimensional spectroscopy is particularly powerful in order to understand the process of energy transfer, for example, in light-harvesting complexes, which may have future applications in organic solar cells. For this spectroscopic approach, the generation of multiple identical phase-stable pulse copies and the precise control over the temporal delay between these subpulses is crucial. This is a critical issue when conventional optics are used [2, 86–89], whereas a pulse shaper delivers phase stable pulse copies inherently, thus making it an ideal tool for multidimensional methods [66, 90–92]. Nevertheless, when conventional pulse shapers are used, these subpulses are all linearly polarized with the same orientation angle and therefore do not account for the vectorial character of light–matter interactions. Hence, the independent control of the polarization states for each subpulse within the multipulse sequence is desired, but not feasible with a conventional pulse shaper. Polarization-sensitive two-dimensional spectroscopy can for example be used to enhance or suppress certain signal contributions in a two-dimensional spectrum [82, 93–97], remove scattering contributions [98], measure the angles between transition dipole moments [99–101], and to extract chiral-sensitive signals [102–105]. In general, the precise and unrestricted generation of polarization-shaped laser pulses is also of high interest for chiral femtochemistry and control as theoretically proposed [106–108].

More recently, the principles of pulse-shaper assisted two-dimensional spectroscopy have been combined with photoemission electron microscopy (PEEM) [109] to simultaneously achieve a high temporal and high spatial resolution below the diffraction limit. This technique, called two-dimensional nanoscopy [110], is suited to perform experiments in the field of nano-optics [111–113] and plasmonics [114–118]. Similar to conventional two-dimensional spectroscopy, the control over the individual polarization states within the multipulse sequence is desired since in general the response of nanostructures and the generation of optical near-fields strongly depend on the polarization state of the used laser pulses. Using polarization-shaped pulses, the realization of near-field spectroscopy [119–122] was proposed and coherent control of optical near-fields were theoretically [123–128] and experimentally demonstrated [47, 49–51, 129, 130]. By combining the concepts of two-dimensional nanoscopy and coherent control, energy transport, e.g., in molecular aggregates, could be directly mapped spatiotemporally [131].

Due to the numerous potential applications of polarization shaping and the increased interest in unrestricted polarization control, pulse shaping devices capable of overcoming the restrictions of conventional polarization shapers have been developed lately. The first approaches allowed unrestricted polarization control [132] or amplitude and limited polarization control [133], but also different approaches for complete vector-field control over the pulse's phase, amplitude, and polarization were reported [134–136]. Some of the first promising applications of these devices included the control over the ionization of NaK [137], vibrational excitation control [138], 2D mid-IR spectroscopy [139], the improvement of the structural contrast in nonlinear microscopy [140], and the generation of polarization-shaped pulses guided through a fiber [141, 142].

However, all reported setups have different advantages and disadvantages and the optimal design has not been found, yet. The goal of this work is the development of a vector-field shaper which is able to generate polarization-shaped multipulse sequences with high fidelity and phase stability in order to perform time-consuming multidimensional measurements.

The outline of this thesis is as follows. In Chapter 2, the mathematical description of ultrashort laser pulses in the frequency and time domain, the polarization state, the spatial beam profile, as well as the Jones matrix formalism is introduced. Furthermore, the required experimental techniques such as knife-edge scan, dual-channel Fourier-transform spectral interferometry, and frequency-resolved optical gating are summarized. The principle of frequency-based pulse shaping, the conventional pulse shaper, and setups published in the literature providing extended or full vector-field control are described and compared in Chapter 3. The analyses of Chapter 3 represent the foundation for the design of the vector-field shaper constructed in this work, which is presented in Chapter 4. The calculation of the optimal parameters for the $4f$ setup, the used optics, and results of ray-tracing simulations are discussed to examine the optical properties of the setup. Chapter 4 concludes with an overview over the complete layout of the presented vector-field shaper and possible improvements. The required software implementation is treated in Chapter 5. Various parameterizations for the complete vector-field control are discussed and two software programs are introduced to operate the vector-field shaper and to use these parameterizations in an experiment. In Chapter 6, the used laser system, the pulse characterization setups, and the first experimental results obtained with the developed pulse shaper are presented. These include the measured frequency distribution, the pulse compression, the phase stability of the setup, the verification of the implemented phase reduction and stabilization routine, and the characterization of various polarization-shaped multipulse sequences to prove the capabilities of the presented setup. This thesis concludes with a short summary and outlook in Chapter 7.

2 Theoretical and experimental background

In the first chapter of this thesis, a short overview over the theoretical and experimental concepts used in this work is given. Most of this chapter summarizes common knowledge and is therefore based on the descriptions found in textbooks [143–146], theses of (former) group members [3, 147, 148], and the literature given in the respective section.

To manipulate and characterize ultrashort laser pulses, a solid understanding of their mathematical definition is necessary. First, the time- and frequency-dependent linear (Section 2.1) and vectorial (Section 2.2) properties of ultrashort laser pulses are introduced. Their spatial properties are covered in Section 2.3. The influence of optical elements on the spectral and temporal properties of a laser pulse can be calculated using the Jones matrix formalism (Section 2.4). In the last section (Section 2.5) of this chapter, three experimental techniques are described to characterize some properties of ultrashort laser pulses. First, the knife-edge scan is introduced, a technique to measure the spatial profile of a laser pulse (Section 2.5.1). To characterize the spectral properties, dual-channel Fourier-transform spectral interferometry (Section 2.5.2) and frequency-resolved optical gating (Section 2.5.3) can be utilized. The combination of these two techniques is called POLLIWOG (polarized light interference versus wavelength of only a glint) [149] and employed in this work to characterize the polarization-shaped laser pulses created with the developed setup.

2.1 Ultrashort laser pulses in time and frequency domain

Ultrashort laser pulses are wave packets of light and generated by a superposition of monochromatic electromagnetic waves. For describing laser pulses, it is in most cases sufficient to consider only their electric field $\vec{E}(x,y,z,t)$ as a function of the spatial coordinates x, y, and z as well as the time t. It can be calculated by solving the inhomogeneous electromagnetic wave equation, which is derived from Maxwell's equations [143].

Following Ref. [143] and [146] the electric field of a laser pulse at a certain point in space can be described by

$$E(t) = 2A(t)\cos\left[\phi_0 + \omega_0 t + \varphi(t)\right] = 2A(t)\cos\left[\Phi(t)\right]. \tag{2.1}$$

Here, $2A(t)$ is the temporal amplitude, also called envelope function, and $\Phi(t)$ the temporal phase. It consists of the absolute phase ϕ_0, also known as carrier-envelope phase (CEP), the term $\omega_0 t$ giving rise to a harmonic oscillation with the carrier or center frequency ω_0, and a time-dependent phase $\varphi(t)$. The influence of the carrier-envelope

phase on the laser pulse can be neglected as long as the slowly varying envelope approximation (SVEA) can be applied [143]. The SVEA is the assumption that the envelope varies only slowly during one oscillation period of the electric field. This holds for all laser pulses discussed in this thesis and only breaks down for very short laser pulses.

In Eq. (2.1) and following equations, the vectorial character of the electric field is neglected, but will be introduced in Section 2.2. $E(t)$ describes the laser pulses in time-domain, even though an equivalent description in the frequency domain $E(\omega)$ is also possible. Both are linked via Fourier transform

$$E(\omega) = \mathcal{F}\{E(t)\} = \frac{1}{\sqrt{2\pi}} \int_{-\infty}^{+\infty} E(t) \mathrm{e}^{-\mathrm{i}\omega t} \, \mathrm{d}t, \tag{2.2}$$

$$E(t) = \mathcal{F}^{-1}\{E(\omega)\} = \frac{1}{\sqrt{2\pi}} \int_{-\infty}^{+\infty} E(\omega) \mathrm{e}^{\mathrm{i}\omega t} \, \mathrm{d}\omega. \tag{2.3}$$

The complex valued spectrum $E(\omega)$ contains positive and negative frequency components, however, since $E(t)$ is real valued $E(\omega) = E^*(-\omega)$ holds and it is sufficient and more intuitive to only use the positive frequency components $E^+(\omega)$ for the description of the laser pulse [143]

$$E^+(\omega) = \begin{cases} E(\omega) & \forall \quad \omega \geq 0 \\ 0 & \forall \quad \omega < 0. \end{cases} \tag{2.4}$$

By inverse Fourier transformation of $E^+(\omega)$ a complex valued electric field in time domain is derived

$$E^+(t) = \frac{1}{\sqrt{2\pi}} \int_{-\infty}^{+\infty} E^+(\omega) \mathrm{e}^{\mathrm{i}\omega t} \, \mathrm{d}x. \tag{2.5}$$

Both complex valued quantities, in time and frequency domain, can be composed of an amplitude A and a phase function ϕ as follows:

$$E^+(t) = A(t) \, \mathrm{e}^{\mathrm{i}\phi(t)} = A(t) \, \mathrm{e}^{\mathrm{i}[\varphi(t)+\omega_0 t]}, \tag{2.6}$$

$$E^+(\omega) = A(\omega) \, \mathrm{e}^{-\mathrm{i}\phi(\omega)}. \tag{2.7}$$

The time-dependent parameter $\varphi(t) = \phi(t) - \omega_0 t$ is here called temporal phase modulation[1].

The spectral (or temporal) amplitude cannot directly be measured. However, the spectral intensity can easily be obtained by using a spectrometer. Under the assumption of the SVEA, the relationship between the temporal/spectral intensity and the amplitude is given by

$$I(t) = 2\epsilon_0 c n \, A(t)^2 \; \propto A(t)^2, \tag{2.8}$$

[1] Commonly only this temporal phase modulation $\varphi(t)$ is plotted in the time domain representation of an ultrashort laser pulse. See for example Fig. 2.1.

$$I(\omega) = 2\epsilon_0 cn\, A(\omega)^2 \propto A(\omega)^2. \tag{2.9}$$

In most cases only the temporal/spectral profile of the envelope and not the absolute values are of interest, hence, the prefactors in Eq. (2.8) and Eq. (2.9) are often neglected. Based on the intensity, the pulse duration $\Delta\tau_p$ and the spectral bandwidth $\Delta\omega_p$ can commonly be defined by the full-width at half-maximum (FWHM):

$$\Delta\tau_p = \mathrm{FWHM}\{I(t)\}, \tag{2.10}$$

$$\Delta\omega_p = \mathrm{FWHM}\{I(\omega)\}. \tag{2.11}$$

These definitions are, however, only meaningful for pulses with simple envelope functions, e.g., a Gaussian shaped envelope. Both values depend on each other since the properties in time and frequency domain are linked via Fourier transform. The so-called time-bandwidth product is given by

$$\Delta\omega_p \Delta\tau_p \geq 2\pi c_b, \tag{2.12}$$

where the value c_b depends on the actual pulse profile, i.e., the shape of the envelope function, and is in the order of 1. The equality holds if the pulse has only a constant (or linear) spectral phase $\phi(\omega)$. In this case, the pulse is called bandwidth-limited.

The relation between time and frequency domain is exploited in most pulse shaping devices. By changing the spectral phase or amplitude of the pulse, the pulse will be changed in time domain, as well. This is illustrated in Fig. 2.1. For basic pulse shaping it is useful to express the temporal and spectral phase as a Taylor series

$$\phi(t) = \sum_{j=0}^{\infty} \frac{a_j}{j!}\, t^j, \tag{2.13}$$

$$\phi(\omega) = \sum_{j=0}^{\infty} \frac{b_j}{j!}\, (\omega - \omega_0)^j \tag{2.14}$$

with the Taylor coefficients

$$a_j = \left.\frac{\partial^j \phi(t)}{\partial t^j}\right|_{t=0} \tag{2.15}$$

and

$$b_j = \left.\frac{\partial^j \phi(\omega)}{\partial \omega^j}\right|_{\omega=\omega_0}. \tag{2.16}$$

Figure 2.1(a) shows a bandwidth-limited pulse with a flat spectral and temporal phase of zero. While the absolute phase can be neglected for a longer single pulse due to the SVEA, the relative zero-order phase between multiple pulses, frequencies, and polarization components (see Section 2.2) is of high relevance. In Fig. 2.1(b) a phase jump of π between the frequency below and above the center frequency is introduced. The temporal zero-order phase directly reflects this as $a_0 = -b_0$ holds. The phase jump of π at ω_0 causes a dip in $E(t)$. By applying a linear spectral phase ($b_1 = 400$ fs in this example) the pulse will be shifted in time [Fig. 2.1(c)] without affecting the pulse shape and thus the pulse duration. This is not the case for higher-order phases. A second-order spectral phase will cause a second-order temporal phase and a temporal broadening of

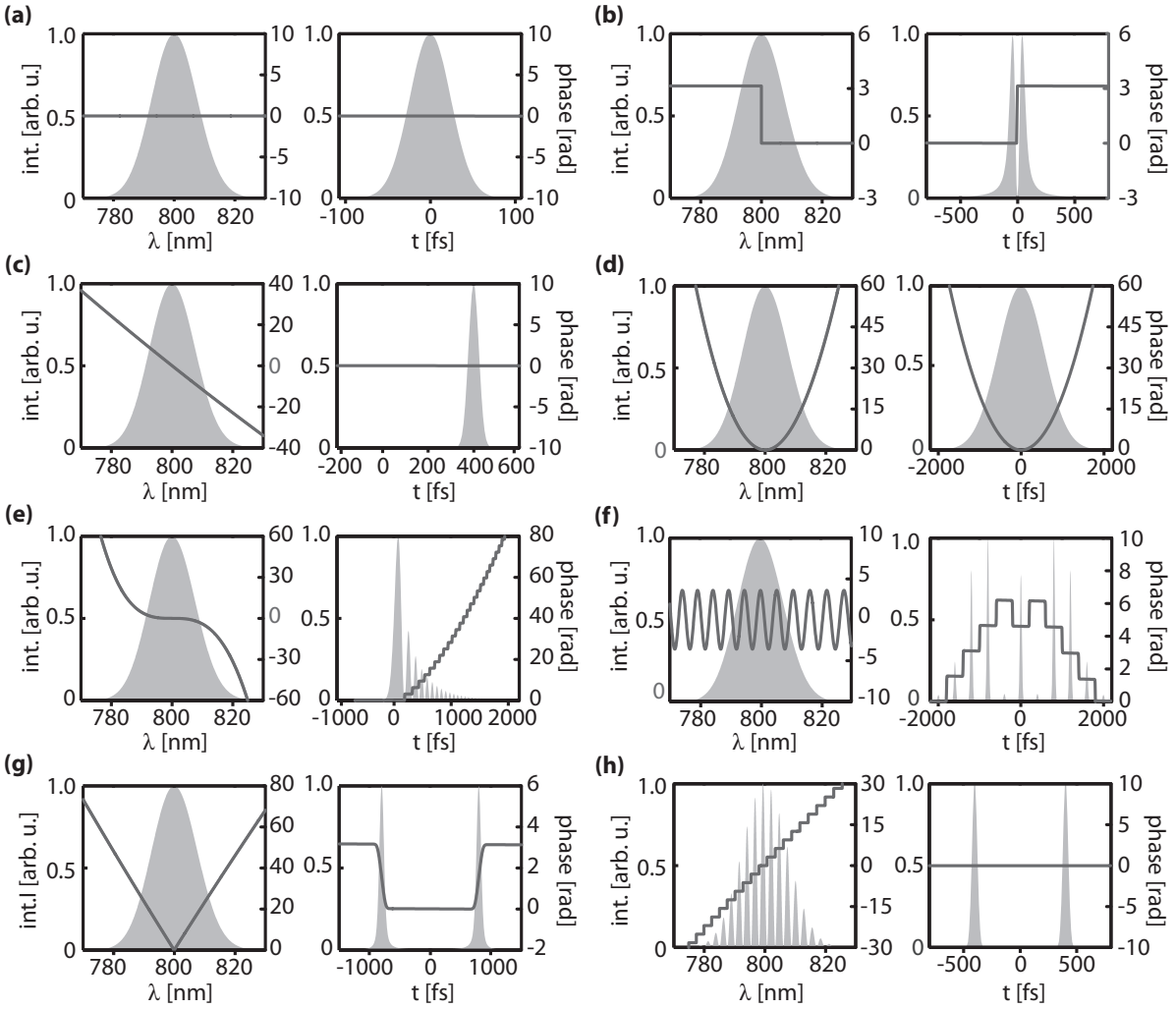

Figure 2.1 | Effect of the phase and amplitude modulation in the frequency domain on the pulse in the time domain. The intensity is plotted as light gray shaded area and the phase as dark gray line. (a) Bandwidth limited pulse with a flat spectral and temporal phase. (b) A phase jump of π at the center frequency causes a temporal dip at $t = 0$ fs. (c) A linear spectral phase ($b_1 = 400$ fs) delays the pulse in time domain. It is still bandwidth-limited. (d) Pulse broadening due to a second-order spectral phase ($b_2 = 2.5 \times 10^4$ fs^2), which causes a linear chirp. (e) A third-order spectral phase ($b_3 = 1 \times 10^6$ fs^3) induces temporal subpulses. (f) By applying a sinusoidal spectral phase a multipulse sequence is generated. (g) A triangular spectral phase creates a double pulse composed of pulses containing different frequency components. (h) To produce a double pulse sequence with exact pulse copies, amplitude and phase modulation is required. Modified from Ref. [3] © (2014) Dr. Stefan Rützel.

the laser pulse as the frequency components of the pulse will be delayed with respect to each other [Fig. 2.1(d)]. This effect is called chirp. In this context it is useful to define the instantaneous frequency

$$\omega(t) = \frac{\mathrm{d}\phi(t)}{\mathrm{d}t} = \omega_0 + \frac{\mathrm{d}\varphi(t)}{\mathrm{d}t} = \omega_0 + a_2 t + \cdots \ . \tag{2.17}$$

If $a_2 \neq 0$ and $a_j = 0$ for $j \geq 3$, the instantaneous frequency will change linearly with time and thus a second-order temporal phase causes linear chirp. The effect of a third-order spectral phase is depicted in Fig. 2.1(e). It results in temporal subpulses with a phase difference of π between consecutive pulses. To generate a more suitable multipulse sequence, a sinusoidal spectral phase can be employed [150] [Fig. 2.1(f)], nevertheless, the control of the pulse sequence is very limited. The time difference between the pulses is given by the frequency of the sinusoidal spectral phase and its amplitude affects the temporal intensity of all pulses. The phase difference between consecutive pulses is also fixed. A double pulse sequence without additional subpulses can be created by using a triangle spectral phase centered around ω_0 [150] [Fig. 2.1(g)]. This will shift the frequency below and above ω_0 to different times hence creating a "colored" double pulse since the two pulses contain different frequency components. In general, the generation of multipulse sequences by phase-only shaping is restricted. The creation of identical pulse copies is for example not possible. To generate such pulse copies, the spectral amplitude must be modulated [Fig. 2.1(h)]. The spectral modulation frequency determines the temporal delay between both pulses and the actual position in time is specified by the spectral phase. The spectral phase can additionally be manipulated to modify each pulse copy and more complex pulse sequences can be generated by combining phase and amplitude shaping.

2.2 Polarization description and representation

The electric field of a laser pulse is not a scalar but a vector and can be constructed by the superposition of two orthogonal polarization components [144] in time

$$\vec{E}^{+}(t) = \begin{pmatrix} E_1^{+}(t) \\ E_2^{+}(t) \end{pmatrix} = \begin{pmatrix} A_1(t)\, \mathrm{e}^{\mathrm{i}\phi_1(t)} \\ A_2(t)\, \mathrm{e}^{\mathrm{i}\phi_2(t)} \end{pmatrix} = \begin{pmatrix} A_1(t)\, \mathrm{e}^{\mathrm{i}[\varphi_1(t)+\omega_0 t]} \\ A_2(t)\, \mathrm{e}^{\mathrm{i}[\varphi_2(t)+\omega_0 t]} \end{pmatrix} \tag{2.18}$$

or analogously in frequency domain

$$\vec{E}^{+}(\omega) = \begin{pmatrix} E_1^{+}(\omega) \\ E_2^{+}(\omega) \end{pmatrix} = \begin{pmatrix} A_1(\omega)\, \mathrm{e}^{-\mathrm{i}\phi_1(\omega)} \\ A_2(\omega)\, \mathrm{e}^{-\mathrm{i}\phi_2(\omega)} \end{pmatrix}. \tag{2.19}$$

The actual polarization state in time domain depends on the amplitude ratio $A_1(t)/A_2(t)$ and the phase difference $\varphi_2(t) - \varphi_1(t)$, but for its visual description it is more intuitive to use the elliptical pulse parameters introduced in Ref. [151] and [152]. Equations (2.20)–(2.34) are described in the following in time domain, but the explicit dependency on the time t will be omitted for the sake of simplicity. An analogous definition of these parameters in frequency domain is also possible.

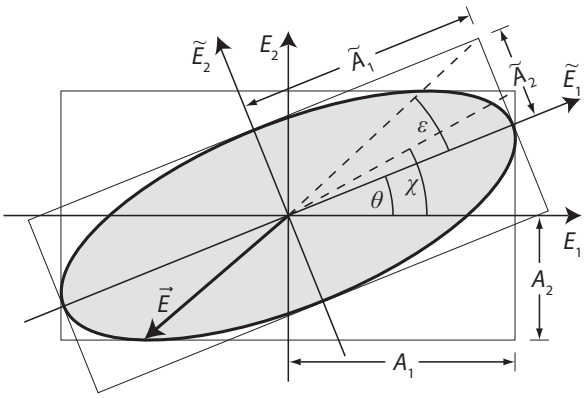

Figure 2.2 | Elliptical pulse parameters. The polarization state of a light $\vec{E}$ can be described as an ellipse. It is defined by its orientation θ and the ellipticity ϵ. The axes E_1 and E_2 describe the "laboratory" coordinate system and $\widetilde{E}_1$ and $\widetilde{E}_2$ the coordinate system of the ellipse. $A_{1/2}$ and $\widetilde{A}_{1/2}$ are the amplitudes in their respective coordinate system. The auxiliary angle χ is used for calculating θ and ϵ based on the parameters given in the "laboratory" coordinate system. Modified from Ref. [3] © (2014) Dr. Stefan Rützel.

In general, the electric field is elliptically polarized thus the tip of the electric field vector rotates and its absolute value changes with time forming an ellipse within one oscillation period, assuming that the SVEA holds [152, 153]. Such a polarization ellipse is shown in Fig. 2.2. The electric field in the "laboratory" frame is described in the coordinate system spanned by E_1 and E_2. The axes $\widetilde{E}_1$ and $\widetilde{E}_2$ represent the coordination system of the polarization ellipse. This ellipse is described by its orientation θ and its ellipticity ϵ. The orientation θ is defined by the angle of the semi-major axis $\widetilde{A}_1$ along the $\widetilde{E}_1$ direction with respect to the E_1 axis of the "laboratory" frame. The ellipticity ϵ characterizes the shape of the ellipse which is given by the ratio of the semi-minor axis $\widetilde{A}_2$ and the semi-major axis $\widetilde{A}_1$. It can be calculated by

$$\tan\epsilon = \frac{\widetilde{A}_2}{\widetilde{A}_1}. \tag{2.20}$$

However, $\widetilde{A}_{1/2}$ are not directly given. In order to calculate θ and ϵ based on the "laboratory" frame amplitudes A_1 and A_2, the auxiliary angle

$$\chi = \arctan\frac{A_2}{A_1} \qquad \in \left[0,\, \frac{\pi}{2}\right] \tag{2.21}$$

is introduced. In combination with the phase difference

$$\delta = \varphi_2 - \varphi_1 \qquad \in [-\pi,\, \pi] \tag{2.22}$$

between the two polarization components, the orientation can be calculated via

$$\theta = \begin{cases} \tilde{\theta} & \in [-\frac{\pi}{4},\, \frac{\pi}{4}] \quad \forall \quad \chi \leq \frac{\pi}{4} \\ \tilde{\theta} + \frac{\pi}{2} & \in [\frac{\pi}{4},\, \frac{\pi}{2}] \quad \forall \quad \chi > \frac{\pi}{4} \wedge \tilde{\theta} < 0 \\ \tilde{\theta} - \frac{\pi}{2} & \in [-\frac{\pi}{2},\, -\frac{\pi}{4}] \quad \forall \quad \chi > \frac{\pi}{4} \wedge \tilde{\theta} \geq 0 \end{cases} \tag{2.23}$$

with

$$\tilde{\theta} = \frac{1}{2}\arctan[\tan(2\chi)\cos\delta] \qquad \in \left[-\frac{\pi}{4},\, \frac{\pi}{4}\right] \tag{2.24}$$

and the ellipticity by

$$\epsilon = \frac{1}{2}\arcsin[\sin(2\chi)\sin\delta] \qquad \in \left[-\frac{\pi}{4},\, \frac{\pi}{4}\right]. \tag{2.25}$$

The orientation θ is defined in the range $[-\pi/2, \pi/2]$, thus in the first and fourth quadrant of the "laboratory" coordinate system, and the ellipticity in the range $[-\pi/4, \pi/4]$. The rotation direction of the electric field vector is encoded in the ellipticity. The field is left-handed polarized if $\epsilon > 0$ and right-handed polarized if $\epsilon < 0$. The handedness is defined for the view along the negative propagation direction. Since θ and ϵ depend only on the relative amplitudes and the relative phases, two additional parameters are necessary to completely describe the electric field, namely the total intensity I_{tot} and the "total phase" φ_{tot}. The total intensity of the electric field is given by

$$I_{\mathrm{tot}} = A_1^2 + A_2^2 = \tilde{A}_1^2 + \tilde{A}_2^2 \tag{2.26}$$

and describes the "size" of the polarization ellipse. The "total phase" can be defined as

$$\varphi_{\mathrm{tot}} = \varphi_1 + \mathrm{sign}\{\theta\,\epsilon\} \arccos\left[\sqrt{\frac{I_{\mathrm{tot}}}{A_1^2}}\cos\theta\cos\epsilon\right], \tag{2.27}$$

where the reference point for the phase is set at the perihelion of the ellipse. The elliptical pulse parameter "total phase" φ_{tot} should not be confused with the "cumulative phase" $\Phi(t)$ in Eq. (2.1). It does not contain the carrier-envelope phase or the rapid harmonic oscillation $\omega_0 t$. This definition was suggested in Ref. [42], but for a detailed explanation the reader is referred to Ref. [151].

These elliptical pulse parameters cannot only be used for the representation of a laser pulse, but also as parameterization for the generation of target polarization states with a pulse shaper. Since the pulse shaper modulates A_1, A_2, φ_1, and φ_2, it is required to calculate these parameters based on I_{tot}, φ_{tot}, θ, and ϵ. Following Ref. [154] the inversion of Eq. (2.23)–(2.27) is given by

$$A_1 = \sqrt{I_{\mathrm{tot}}}\cos\xi, \tag{2.28}$$

$$A_2 = \sqrt{I_{\mathrm{tot}}}\sin\xi, \tag{2.29}$$

$$\varphi_1 = \varphi_{\mathrm{tot}} - \mathrm{sign}\{\theta\,\epsilon\} \arccos\left[\sqrt{\frac{I_{\mathrm{tot}}}{A_1^2}}\cos\theta\cos\epsilon\right], \tag{2.30}$$

$$\varphi_2 = \varphi_1 + \Delta. \tag{2.31}$$

The auxiliary parameters ξ and Δ are

$$\xi = \frac{1}{2}\arccos\left[\cos(2\theta)\cos(2\epsilon)\right], \tag{2.32}$$

and

$$\Delta = \begin{cases} +\arccos\left(+\sqrt{1-c}\right) & \forall \quad \epsilon \geq 0 \wedge \theta \geq 0 \\ +\arccos\left(-\sqrt{1-c}\right) & \forall \quad \epsilon \geq 0 \wedge \theta < 0 \\ -\arccos\left(-\sqrt{1-c}\right) & \forall \quad \epsilon < 0 \wedge \theta < 0 \\ -\arccos\left(+\sqrt{1-c}\right) & \forall \quad \epsilon < 0 \wedge \theta \geq 0 \end{cases} \tag{2.33}$$

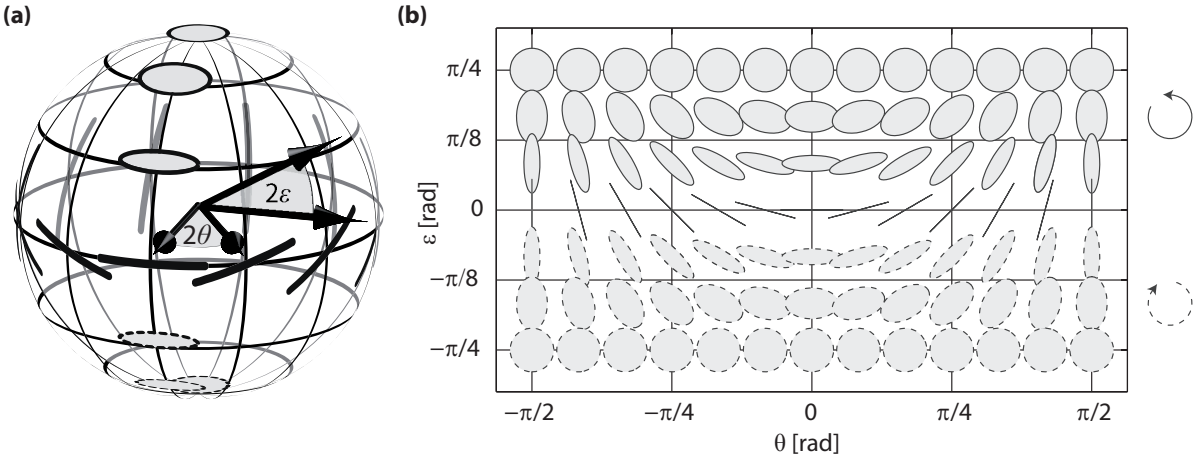

Figure 2.3 | Polarization representation using the Poincaré sphere and the Poincaré plane. (a) Linear polarization states are located at the equator of the Poincaré sphere. The upper hemisphere of the sphere represents left-handed and the lower hemisphere right-handed elliptical polarization states. The poles describe circularly polarized light. The coordinates of the sphere are given by 2θ and 2ϵ with θ being the orientation and ϵ the ellipticity of the polarization ellipse. (b) The Poincaré plane is obtained by projecting the Poincaré sphere onto a two-dimensional plane spanned by the orientation θ and the ellipticity ϵ. The solid ellipses represent left-handed and dashed ellipses right-handed polarization states. Modified from Ref. [3] © (2014) Dr. Stefan Rützel.

with

$$c = \frac{\sin^2(2\epsilon)}{1 - \cos^2(2\theta)\cos^2(2\epsilon)}. \tag{2.34}$$

The Poincaré sphere [Fig. 2.3(a)] is an established visualization of polarized light and can be used to intuitively describe the change in polarization by optical elements [155, 156]. However, more complex laser pulses can easier be represented in the so-called Poincaré plane [Fig. 2.3(b)]. It is given by the projection of the surface of the Poincaré sphere onto a plane spanned by the orientation θ and the ellipticity ϵ [152]. The upper half of the Poincaré plane represents left-handed polarization states (solid) and the lower half the right-handed states (dashed). Left- and right-handed circular polarized light are represented by exactly two points in the Poincaré sphere – the poles. However, in the Poincaré plane these two polarization states correspond to vertical lines at $\epsilon = \pm\pi/4$, since the orientation θ is irrelevant for circular polarized light, as both polarization components have the same amplitude. It should be noted that also the orientations $\theta = \pm\pi/2$ correspond to the same polarization states.

2.3 Gaussian beam profile

In the previous sections, the spatial properties of laser beams were neglected and time-dependent plane waves were used to describe the electric field of a laser pulse at a certain point in space. However, the intensity of the beam profile of laser pulses is neither constant nor infinitely broad. For the laser pulses treated in this thesis, the transverse

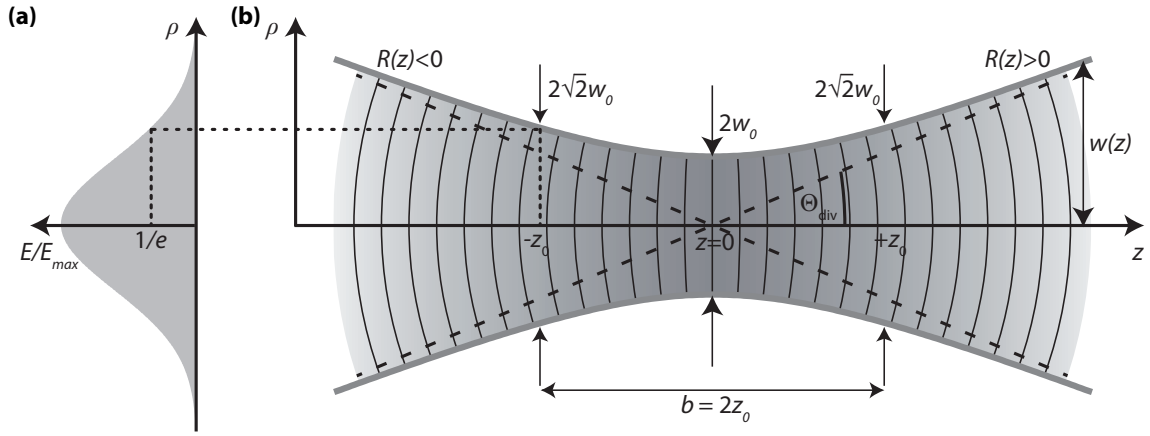

Figure 2.4 | Gaussian beam properties. (a) Gaussian distribution of the spatial intensity of a laser beam along the cylinder coordinate ρ. The beam radius $w(z)$ is defined by the point at which the amplitude of the electric field drops to $1/e$ (dotted line). (b) Dependence of beam radius (gray shaded area) on the z coordinate, which corresponds to the propagation direction. w_0 is the beam waist radius at $z = 0$, z_0 the Rayleigh length, and Θ_{div} the divergence angle. b is called confocal parameter and $R(z)$ describes the wavefront (black solid lines) radius. Modified from Ref. [3] © (2014) Dr. Stefan Rützel.

beam profile $u(x,y,z)$ and the time-dependent electric field $\vec{E}^+(t)$ propagating along the z direction [143] can be separated

$$\vec{E}(x,y,z,t) \propto\ u(x,y,z)\ \vec{E}^+(t). \tag{2.35}$$

Most laser resonators emit beams in the fundamental transverse electromagnetic mode (TEM_{00}) which possesses a Gaussian shape. The amplitude of this mode can mathematically be described in cylindrical coordinates (ρ,z), following Ref. [145], by

$$u(\rho,z) = u_0 \frac{w_0}{w(z)}\ \mathrm{e}^{-\left[\frac{\rho}{w(z)}\right]^2}\ \mathrm{e}^{\mathrm{i}\frac{k\rho^2}{2R(z)}}\ \mathrm{e}^{\mathrm{i}[kz-\eta(z)]}. \tag{2.36}$$

The real-valued first part of this equation describes the amplitude of the beam profile, i.e., the transverse field distribution. The second part (the first complex-valued exponential factor) determines the spherical curvature of the wavefront (surface of constant phase) and the third complex-valued part refers to the phase evolution in z direction. k is the wavenumber $k = 2\pi/\lambda$. The parameters of the Gaussian beam are depicted in Fig. 2.4. The beam is completely characterized by the values w_0 and z_0. w_0 is the smallest beam radius $w(z)$ – the beam waist radius – located at $z = 0$ and z_0 is the Rayleigh length. The beam radius $w(z)$ is defined as the distance ρ from the z axis where the field amplitude drops to $1/e$ of the maximum field amplitude u_0. The beam radius can be calculated by

$$w(z) = w_0 \sqrt{1 + \left(\frac{z}{z_0}\right)^2}. \tag{2.37}$$

The Rayleigh length z_0 is linked to the beam waist radius w_0 via

$$z_0 = \frac{w_0^2 \pi n}{\lambda}, \tag{2.38}$$

with n being the refractive index of the corresponding media. The Rayleigh length is the distance in z direction after which the beam radius has increased by the factor of $\sqrt{2}$ in regard to the beam waist radius w_0 (Fig. 2.4). It can be seen from Eq. (2.38) that a stronger focused beam (smaller w_0) has a shorter Rayleigh length than a weakly focused beam (larger w_0). The confocal parameter $b = 2z_0$, also called Rayleigh zone, is twice the Rayleigh length. For $z \ll z_0$ (near field) the laser pulse propagates almost as plane wave and the wavefront varies only slightly. Inside the Rayleigh zone, a laser beam is therefore often referred to as collimated beam. The radius of the wavefront can be calculated with

$$R(z) = z \left[1 + \left(\frac{z_0}{z} \right)^2 \right]. \tag{2.39}$$

In the near field ($z \ll z_0$) $R(z) \to \infty$ holds for $z \to 0$ and in the far field ($z \gg z_0$) $R(z) \approx z$ holds. The divergence angle Θ_{div} is defined by

$$\Theta_{\text{div}} = \frac{w_0}{z_0}, \tag{2.40}$$

which in the far field can be approximated by $\Theta_{\text{div}} = w(z)/z$ for $z \to \infty$. The last function $\eta(z)$ in Eq. (2.36) is the Gouy phase

$$\eta(z) = \arctan \frac{z}{z_0}. \tag{2.41}$$

It describes an additional phase shift acquired along the propagation through the focus. The total Gouy phase is π if the far fields before and after the focus are compared.

Two effects concerning the beam profile are of particular interest for the work presented in this thesis. The first is the focus size, i.e. the beam waist radius, behind a lens with the focal length f. According to Ref. [145] the beam waist radius after the lens w_0^{out} can be approximated by

$$w_0^{\text{out}} \approx \frac{\lambda f}{\pi w_0^{\text{in}}} \tag{2.42}$$

if the incident Gaussian beam (w_0^{in}) is collimated, i.e., $z_0^{\text{in}} \gg f$.

The second effect is the transmitted intensity through an aperture. The intensity of the Gaussian beam profile is proportional to the squared absolute value of the field amplitude [145]

$$I(\rho,z) \propto |E(\rho,z)|^2 = u_0 \left(\frac{w_0}{w(z)} \right)^2 \mathrm{e}^{-2\left(\frac{\rho^2}{w^2(z)} \right)} \tag{2.43}$$

in cylindrical coordinates or

$$I(x,y,z) \propto |E(x,y,z)|^2 = u_0 \left(\frac{w_0}{w(z)} \right)^2 \mathrm{e}^{-2\left(\frac{x^2+y^2}{w^2(z)} \right)} \tag{2.44}$$

Table 2.1 | Transmission of a Gaussian beam through a round aperture and a slit. The aperture size a for the round aperture is defined as its radius and for the slit as the half width of the slit. The slit is assumed to limit the two-dimensional Gaussian beam profile only in one dimension. Along the receptive other dimension the whole intensity is transmitted. Therefore, transmission values for the slit exceed the values for the round aperture.

Aperture size a	$I(a)/I(0)$	**Transmission** [%]	
		Circle	Slit
$\sqrt{0.5}\,w_0$	$1/e$	63.212	84.270
$\sqrt{1}\,w_0$	$1/e^2$	86.467	95.450
$\sqrt{2}\,w_0$	$1/e^4$	98.168	99.532
$\sqrt{3}\,w_0$	$1/e^6$	99.752	99.947
$\sqrt{4}\,w_0$	$1/e^8$	99.967	99.994
$\sqrt{5}\,w_0$	$1/e^{10}$	99.996	99.999

in Cartesian coordinates. In the following discussion a collimated beam is considered. The beam radius is assumed to be constant $w(z) = w_0$ and thus the intensity of the beam profile does not depend on the z coordinate. The peak amplitude u_0 is supposed to be $u_0 = 2/(\pi w_0^2)$, so that the total intensity of the two-dimensional Gaussian beam profile is normalized

$$\int_0^{2\pi}\int_0^{\infty} I(\rho)\, r\, \mathrm{d}\rho\, \mathrm{d}\varphi = \int_{-\infty}^{+\infty}\int_{-\infty}^{+\infty} I(x,y)\, \mathrm{d}x\, \mathrm{d}y = 1. \tag{2.45}$$

The transmission through a round or rectangular aperture can be calculated by integrating Eq. (2.43) or Eq. (2.44) in between the borders given by the dimensions of the aperture. The transmission values after a round aperture and a one-dimensional slit are listed in Tab. 2.1. If the entire intensity of the beam should be transmitted through the aperture (i.e. $T > 99.9$ %), the aperture size should be at least twice the beam radius. For a smaller aperture size the beam is clipped. This must also be considered when choosing the proper size of optical elements such as mirrors or lenses.

2.4 Jones matrix formalism

The Jones matrix formalism is a method to calculate the linear influence of optical elements on the laser pulse [157–160]. The electric field $E^{\mathrm{out}}(\omega)$ after an optical element can be calculated by multiplying the complex-valued two-by-two Jones matrix $\boldsymbol{J}(\omega)$

$$\boldsymbol{J}(\omega) = \begin{pmatrix} J_{11}(\omega) & J_{12}(\omega) \\ J_{21}(\omega) & J_{22}(\omega) \end{pmatrix} \tag{2.46}$$

with the incoming electric field $E^{\mathrm{in}}(\omega)$

$$\begin{pmatrix} E_1^{\mathrm{out}}(\omega) \\ E_2^{\mathrm{out}}(\omega) \end{pmatrix} = \begin{pmatrix} J_{11}(\omega) & J_{12}(\omega) \\ J_{21}(\omega) & J_{22}(\omega) \end{pmatrix} \begin{pmatrix} E_1^{\mathrm{in}}(\omega) \\ E_2^{\mathrm{in}}(\omega) \end{pmatrix}. \tag{2.47}$$

Table 2.2 | Examples for ideal Jones matrices.

Element	Jones matrix
Ideal Mirror	$\begin{pmatrix} 1 & 0 \\ 0 & -1 \end{pmatrix}$
Linear polarizer in direction 1	$\begin{pmatrix} 1 & 0 \\ 0 & 0 \end{pmatrix}$
Linear polarizer in direction 2	$\begin{pmatrix} 0 & 0 \\ 0 & 1 \end{pmatrix}$
$\lambda/2$ plate fast axis at angle α	$\begin{pmatrix} \cos(2\alpha) & \sin(2\alpha) \\ \sin(2\alpha) & -\cos(2\alpha) \end{pmatrix}$
Arbitrary phase retarder fast axis at 0° or 90°	$\begin{pmatrix} \mathrm{e}^{-\mathrm{i}\varphi_1} & 0 \\ 0 & \mathrm{e}^{-\mathrm{i}\varphi_2} \end{pmatrix}$

The complex-valued vectors of the incoming and outgoing light are also called Jones vectors and they are defined analogously to Eq. (2.19). The electric field in time domain can be calculated by the inverse Fourier transformation. The Jones matrix $\boldsymbol{J}(\omega)$ cannot only illustrate the influence of a single optical element, but also the influence of n consecutive elements. In general, the total Jones matrix $\boldsymbol{J}(\omega)$ is given by the multiplication of the Jones matrices of the individual elements

$$\boldsymbol{J}(\omega) = \boldsymbol{J}_n(\omega)\, \boldsymbol{J}_{n-1}(\omega) \cdots \boldsymbol{J}_2(\omega)\, \boldsymbol{J}_1(\omega). \tag{2.48}$$

This multiplication is not commutative, consequently the order of the elements has to be taken into account. The first element of the setup is located on the right-hand side, and the last element on the left-hand side of Eq. (2.48). Examples for Jones matrices of different (ideal) optical elements are given in Tab. 2.2. Most of these matrices are given for a certain orientation of the optical element with respect to the electric field. The Jones matrix for an arbitrary orientation α can be calculated by

$$\boldsymbol{J}^{\alpha}(\omega) = \boldsymbol{R}(\alpha)\, \boldsymbol{J}(\omega)\, \boldsymbol{R}^{-1}(\alpha) = \boldsymbol{R}(\alpha)\, \boldsymbol{J}(\omega)\, \boldsymbol{R}(-\alpha) \tag{2.49}$$

with

$$\boldsymbol{R}(\alpha) = \begin{pmatrix} \cos(\alpha) & -\sin(\alpha) \\ \sin(\alpha) & \cos(\alpha) \end{pmatrix} \tag{2.50}$$

being the two-dimensional rotation matrix. The Jones Matrix for a linear polarizer orientated under 45° with respect to direction 1 of the light field is for example

$$\begin{aligned}\boldsymbol{P}_{\text{lin.}}^{45^\circ} =& \boldsymbol{R}(45^\circ)\, \boldsymbol{P}_{\text{lin.}}^{0^\circ}\, \boldsymbol{R}(-45^\circ) \\ =& \begin{pmatrix} \sqrt{0.5} & -\sqrt{0.5} \\ \sqrt{0.5} & \sqrt{0.5} \end{pmatrix} \begin{pmatrix} 1 & 0 \\ 0 & 0 \end{pmatrix} \begin{pmatrix} \sqrt{0.5} & \sqrt{0.5} \\ -\sqrt{0.5} & \sqrt{0.5} \end{pmatrix} \\ =& \begin{pmatrix} 0.5 & 0.5 \\ 0.5 & 0.5 \end{pmatrix}. \end{aligned} \tag{2.51}$$

The electric output field after this polarizer depends on the polarization of the input field:

$$\begin{pmatrix} 0.5 \\ 0.5 \end{pmatrix} = \boldsymbol{P}_{\text{lin.}}^{45^\circ} \begin{pmatrix} 1 \\ 0 \end{pmatrix}, \tag{2.52}$$

$$\begin{pmatrix} \frac{1}{\sqrt{0.5}} \\ \frac{1}{\sqrt{0.5}} \end{pmatrix} = \boldsymbol{P}_{\text{lin.}}^{45^\circ} \begin{pmatrix} \frac{1}{\sqrt{0.5}} \\ \frac{1}{\sqrt{0.5}} \end{pmatrix}, \tag{2.53}$$

$$\begin{pmatrix} 0 \\ 0 \end{pmatrix} = \boldsymbol{P}_{\text{lin.}}^{45^\circ} \begin{pmatrix} \frac{1}{\sqrt{0.5}} \\ -\frac{1}{\sqrt{0.5}} \end{pmatrix}. \tag{2.54}$$

Normalized Jones vectors are used for these simple examples. All three input electric fields are linearly polarized but differ in their orientations. If the input orientation is $\theta = 0°$, half of the intensity is transmitted with an output polarization parallel to the polarizer [Eq. (2.52)]. If the input orientation is $\theta = 45°$ and therefore parallel to the polarizer, the entire intensity is transmitted [Eq. (2.53)] and for $\theta = -45°$ the intensity is completely blocked [Eq. (2.54)]. These basic examples demonstrate the benefits of the Jones formalism. In Chapter 3, it is used to calculate the electric output field for different pulse shapers.

2.5 Pulse characterization

The previous sections covered the mathematical description of different properties of ultrashort laser pulses. In this section, various experimental methods are discussed to measure some of these properties.

2.5.1 Knife-edge scan

In order to build the setup presented in this thesis it is crucial to characterize and adapt the beam profile of an ultrashort laser pulse. The knife-edge scan is a technique to measure the beam radius [161]. The principle of this method is that a sharp edge, e.g., a razor blade is moved stepwise, perpendicular to the propagation direction through the beam profile thus blocking it partly in one dimension (Fig. 2.5). The intensity of the

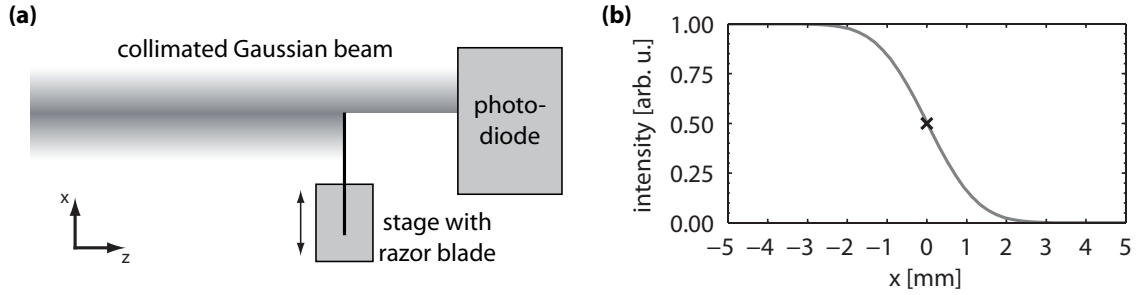

Figure 2.5 | Principle of the knife-edge scan. (a) To measure the beam radius a razor blade is gradually moved perpendicular (x direction) to the propagation direction (z direction) across the beam profile. The intensity of the remaining beam depends on the x position of the edge of the razor blade and is recorded with a photodiode. (b) Photodiode signal [Eq. (2.57)] for a Gaussian beam profile with a beam radius of 2 mm. The black cross marks the signal yield at the position of the razor blade shown in (a).

beam behind the razor blade is recorded with a photodiode for each step. The signal is given by

$$P(x') = \int_{-\infty}^{x'} \int_{-\infty}^{+\infty} I(x,y)\,\mathrm{d}x\,\mathrm{d}y, \tag{2.55}$$

where x' is the position of the razor blade and $I(x,y)$ the intensity of the beam at the z position of the razor blade [see Eq. (2.44)]. Following Ref. [162], for Gaussian beams in the TEM_{00} (see Section 2.3) Eq. (2.55) can also be written as

$$P(x) = \frac{1}{2}\,P_{\mathrm{tot}}\left[1 + \mathrm{erf}\left(\frac{\sqrt{2}x}{w_z}\right)\right] \tag{2.56}$$

with

$$P_{\mathrm{tot}} = \frac{\pi}{2}\,w_z^2\,u_0\left(\frac{w_0}{w_z}\right)^2 \tag{2.57}$$

being the total intensity of the unblocked beam and

$$\mathrm{erf}(h) = \frac{2}{\sqrt{\pi}} \int_0^h \mathrm{e}^{-g^2}\,\mathrm{d}g \tag{2.58}$$

the Error function. The beam radius w_z at the z position of the razor blade can be determined by fitting Eq. (2.56) to the measured data. Still, fitting of Eq. (2.56) is not trivial due to the Error function, thus also different alternative methods were developed to extract the beam radius w_z from the measured data. For more details the reader is referred to Refs. [163–166].

The evaluation of the knife-edge scan assumes an ideal Gaussian beam profile and is not suitable to reconstruct the shape of arbitrary beam profiles. However, for simple Gaussian-like beam profiles, it is sufficient to take a knife edge scan along the x and another along the y direction to approximate the two-dimensional beam profile. To

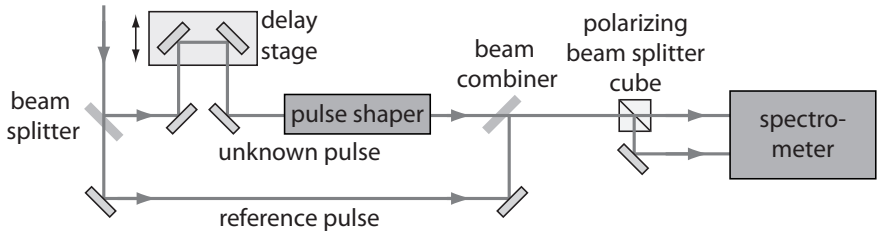

Figure 2.6 | Dual-channel FTSI setup. The reference and the unknown pulse propagate in the two arms of a Mach-Zehnder interferometer. The unknown pulse can be temporally delayed with respect to the reference pulse and manipulated, in this example, with a pulse shaper. To characterize the complete vector field of the shaped pulse, the spectral interference of the reference and the unknown pulse is recorded with a spectrometer for two orthogonal polarization components and for a fixed delay.

determine the divergence of the beam, knife-edge scans at different positions along the propagation direction of the beam can be taken into account.

2.5.2 Dual-channel Fourier-transform spectral interferometry

The spectral intensity and hence the amplitude [see Eq. (2.9)] of an ultrashort laser pulse can straightly be measured with a spectrometer. However, the spectral phase which is required to characterize the laser pulse completely and to calculate the pulse in time domain cannot be directly obtained. To determine the phase of polarization-shaped laser pulses, dual-channel Fourier-transform spectral interferometry (FTSI) [149, 151] is employed in this thesis.

FTSI is a cross-referencing technique where a well-characterized pulse – the reference pulse – is used to extract the phase information of an unknown laser pulse [167–169]. This method features a high sensitivity and reliability as only the measurement of a linear signal – the spectral interference (SI) of the two pulses – is required. The experimental setup for dual-channel FTSI is shown in Fig. 2.6. The incident pulse is split by a beam splitter of a Mach-Zehnder interferometer into two pulses. One pulse is used as reference pulse $\vec{E}_{\mathrm{r}}^{+}$ and the other $\vec{E}_{\mathrm{u}}^{+}$ is used to perform the experiment, in this case a modulation of the pulse with a pulse shaper. The phase and the amplitude of the pulse after the pulse shaper are unknown. Both pulses are recombined by a second beam splitter into a single beam line. The delay τ between the reference and the unknown pulse is fix and can be adjusted using a delay stage. To characterize the complete vector field of the shaped laser pulse, the interference of the reference and the unknown pulse is measured for two orthogonal polarization components using a polarizing beam splitter cube. This approach is called dual-channel FTSI.

The extraction of the phase of the unknown pulse using FTSI is discussed for a single polarization component in the following. The detected interference signal I_{SI} of the

reference pulse $E_\mathrm{r}^+(\omega)$ and the unknown pulse $E_\mathrm{u}^+(\omega)$ delayed by the time τ is given by

$$\begin{aligned} I_\mathrm{SI}(\omega) &= \left|E_\mathrm{r}^+(\omega) + E_\mathrm{u}^+(\omega)\,\mathrm{e}^{-\mathrm{i}\omega\tau}\right|^2 \\ &= \left|E_\mathrm{r}^+(\omega)\right|^2 + \left|E_\mathrm{u}^+(\omega)\right|^2 + S(\omega) \\ &= I_\mathrm{r}(\omega) + I_\mathrm{u}(\omega) + S(\omega) \end{aligned} \tag{2.59}$$

with $S(\omega)$ being the interference term

$$\begin{aligned} S(\omega) &= \left[E_\mathrm{r}^+(\omega)\right]^* E_\mathrm{u}^+(\omega)\,\mathrm{e}^{-\mathrm{i}\omega\tau} + E_\mathrm{r}^+(\omega)\left[E_\mathrm{u}^+(\omega)\right]^*\,\mathrm{e}^{\mathrm{i}\omega\tau} \\ &= 2\sqrt{I_\mathrm{r}(\omega)I_\mathrm{u}(\omega)}\,\cos\left[\phi_\mathrm{r}(\omega) - \phi_\mathrm{u}(\omega) - \omega\tau\right]. \end{aligned} \tag{2.60}$$

This interference term can be extracted from the measured signal $I_\mathrm{SI}(\omega)$ by measuring the spectra $I_\mathrm{r}(\omega)$ and $I_\mathrm{u}(\omega)$ separately and subtracting them from $I_\mathrm{SI}(\omega)$. To derive the unknown phase $\phi_\mathrm{u}(\omega)$ from Eq. (2.60), the arccosine function could be applied. However, this is prone to phase errors if the value of the cosine function approaches unity [167]. To avoid this, Fourier filtering can be utilized. The interference term $S(t)$ in time domain is given by

$$\begin{aligned} S(t) &= \frac{1}{\sqrt{2\pi}}\int_{-\infty}^{+\infty} S(\omega)\,\mathrm{e}^{\mathrm{i}\omega t}\,\mathrm{d}\omega \\ &= \widetilde{S}(t-\tau) + \widetilde{S}^*(-t-\tau) \end{aligned} \tag{2.61}$$

with

$$\widetilde{S}(t) = \frac{1}{\sqrt{2\pi}}\int_{-\infty}^{+\infty}\left[E_\mathrm{r}^+(\omega)\right]^* E_\mathrm{u}^+(\omega)\,\mathrm{e}^{\mathrm{i}\omega t}\,\mathrm{d}\omega. \tag{2.62}$$

$\widetilde{S}(\omega)$ is a real-valued quantity thus $\widetilde{S}(t) = \widetilde{S}^*(-t)$ holds and all information is contained in either $\widetilde{S}(t-\tau)$ or $\widetilde{S}^*(-t-\tau)$. By using an appropriated filter function, e.g., a rectangular function, the desired part of $S(t)$ can be extracted. It should be noted that τ must be large enough so that the signals $\widetilde{S}(t-\tau)$ and $\widetilde{S}^*(-t-\tau)$ are temporally separated, but do not exceed the resolution of the spectrometer. By Fourier transform of $\widetilde{S}(t-\tau)$, the cosine function in Eq. (2.60) can be transferred into a complex exponential function

$$\begin{aligned} S^+(\omega) &= \frac{1}{\sqrt{2\pi}}\int_{-\infty}^{+\infty}\widetilde{S}(t-\tau)\,\mathrm{e}^{-\mathrm{i}\omega t}\,\mathrm{d}t \\ &= \left[E_\mathrm{r}^+(\omega)\right]^* E_\mathrm{u}^+(\omega)\,\mathrm{e}^{-\mathrm{i}\omega\tau} \\ &= \sqrt{I_\mathrm{r}(\omega)I_\mathrm{u}(\omega)}\,\mathrm{e}^{\mathrm{i}[\phi_\mathrm{r}(\omega)-\phi_\mathrm{u}(\omega)-\omega\tau]}. \end{aligned} \tag{2.63}$$

The phase $\phi_\mathrm{u}(\omega)$ can then be calculated via

$$\phi_\mathrm{u}(\omega) = \phi_\mathrm{r}(\omega) - \arg\{S^+(\omega)\} - \omega\tau. \tag{2.64}$$

If the temporal delay τ is unknown, it can be determined by a linear fit of $\phi_{\mathrm{u}}(\omega)+\omega\tau$.

Employing dual-channel FTSI, the signal recording and evaluation is done for two orthogonal polarization components. The complete vector field is given by the superposition of both evaluations

$$\begin{aligned}\vec{E}^{+}(\omega) &= \begin{pmatrix} \sqrt{I_{\mathrm{u},1}(\omega)}\,\mathrm{e}^{-\mathrm{i}\phi_{\mathrm{u},1}(\omega)} \\ \sqrt{I_{\mathrm{u},2}(\omega)}\,\mathrm{e}^{-\mathrm{i}\phi_{\mathrm{u},2}(\omega)} \end{pmatrix} \\ &= \begin{pmatrix} \sqrt{I_{\mathrm{u},1}(\omega)}\,\mathrm{e}^{-\mathrm{i}\left[\phi_{\mathrm{r},1}(\omega)-\arg\{S_1^{+}(\omega)\}-\omega\tau_1\right]} \\ \sqrt{I_{\mathrm{u},2}(\omega)}\,\mathrm{e}^{-\mathrm{i}\left[\phi_{\mathrm{r},2}(\omega)-\arg\{S_2^{+}(\omega)\}-\omega\tau_2\right]} \end{pmatrix}. \end{aligned} \tag{2.65}$$

To determine the polarization state, the phase difference $\Delta\phi_{\mathrm{u}}(\omega)=\phi_{\mathrm{u},2}(\omega)-\phi_{\mathrm{u},1}(\omega)$ must be correctly characterized. Hence, the delay between the reference and the unknown pulse must be exactly the same for both measurements $\tau_2=\tau_1=\tau$ to determine the proper relative phase. To avoid errors in $\Delta\phi_{\mathrm{u}}(\omega)$ due to phase stability issues of the Mach-Zehnder interferometer, i.e. $\tau_2\neq\tau_1$, the measurements of the interference signal for both polarization components should be performed simultaneously.

It must be emphasized that the interference signal $S^{+}(\omega)$ only depends on the relative phase $\phi_{\mathrm{r}}(\omega)-\phi_{\mathrm{u}}(\omega)$ between the reference and the unknown pulse and is not sensitive to identical phase modifications applied to both pulses. The consequence of this is illustrated using the following gedanken experiment: After the recombination of the unknown pulse $[I_{\mathrm{u}}(\omega),\ \phi_{\mathrm{u}}(\omega)]$ and the reference pulse $[I_{\mathrm{r}}(\omega),\ \phi_{\mathrm{r}}(\omega)]$, both propagate through a glass block which does not alter the amplitude but only introduce an additional phase $\varphi_{\mathrm{o}}(\omega)$. The electric fields after the glass block for the reference $\widetilde{E}_{\mathrm{r}}^{+}(\omega)$ and the unknown pulse $\widetilde{E}_{\mathrm{u}}^{+}(\omega)$ are given by

$$\widetilde{E}_{\mathrm{r}}^{+}(\omega)=\sqrt{I_{\mathrm{r}}(\omega)}\,\mathrm{e}^{-\mathrm{i}\widetilde{\phi}_{\mathrm{r}}(\omega)}=\sqrt{I_{\mathrm{r}}(\omega)}\,\mathrm{e}^{-\mathrm{i}[\phi_{\mathrm{r}}(\omega)+\varphi_{\mathrm{o}}(\omega)]} \tag{2.66}$$

and

$$\widetilde{E}_{\mathrm{u}}^{+}(\omega)=\sqrt{I_{\mathrm{u}}(\omega)}\,\mathrm{e}^{-\mathrm{i}\widetilde{\phi}_{\mathrm{u}}(\omega)}=\sqrt{I_{\mathrm{u}}(\omega)}\,\mathrm{e}^{-\mathrm{i}[\phi_{\mathrm{u}}(\omega)+\varphi_{\mathrm{o}}(\omega)]}, \tag{2.67}$$

where $\widetilde{\phi}_{\mathrm{u}}(\omega)$ is unknown phase and $\widetilde{\phi}_{\mathrm{r}}(\omega)$ the reference phase after the glass block. The interference signal $S^{+}(\omega)$ of these electric fields is

$$\begin{aligned} S^{+}(\omega) &= \sqrt{I_{\mathrm{r}}(\omega)I_{\mathrm{u}}(\omega)}\,\mathrm{e}^{\mathrm{i}\left[\widetilde{\phi}_{\mathrm{r}}(\omega)-\widetilde{\phi}_{\mathrm{u}}(\omega)-\omega\tau\right]} \\ &= \sqrt{I_{\mathrm{r}}(\omega)I_{\mathrm{u}}(\omega)}\,\mathrm{e}^{\mathrm{i}\{[\phi_{\mathrm{r}}(\omega)+\varphi_{\mathrm{o}}(\omega)]-[\phi_{\mathrm{u}}(\omega)+\varphi_{\mathrm{o}}(\omega)]-\omega\tau\}} \\ &= \sqrt{I_{\mathrm{r}}(\omega)I_{\mathrm{u}}(\omega)}\,\mathrm{e}^{\mathrm{i}[\phi_{\mathrm{r}}(\omega)-\phi_{\mathrm{u}}(\omega)-\omega\tau]} \end{aligned} \tag{2.68}$$

and the phase term $\varphi_{\mathrm{o}}(\omega)$ is cancelled out, because it appears in the phase of the reference and the phase of the unknown pulse. This means that even if the spectral interference is measured behind additional optical elements placed in the recombined beam path the unknown pulse is characterized in front of these elements since only $\phi_{\mathrm{u}}(\omega)$ and not $\widetilde{\phi}_{\mathrm{u}}(\omega)$ can be retrieved if $\phi_{\mathrm{r}}(\omega)$ is known. To obtain $\widetilde{\phi}_{\mathrm{u}}(\omega)$, the reference phase $\widetilde{\phi}_{\mathrm{r}}(\omega)$ must be known [see first line of Eq. (2.68)]. It is therefore important to characterize the reference pulse at the same location at which the unknown pulse should be characterized, for example at the sample position.

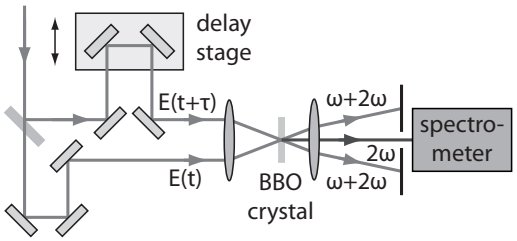

Figure 2.7 | FROG setup. Two pulse copies of an unknown pulse are created with a beam splitter. One copy is delayed (τ) with respect to the other copy. The two pulses are focused into a BBO crystal. When both pulses overlap temporally and spatially, an SHG signal is emitted along the optical axis which is filtered with an aperture and recorded with the spectrometer. By scanning τ, a FROG trace is recorded.

2.5.3 Frequency-resolved optical gating

To characterize a linearly polarized pulse, e.g., the reference pulse used for the FTSI characterization, frequency-resolved optical gating (FROG) [170–172] can be employed. There are different variants of FROG. The technique used in this work is called SHG FROG [173]. SHG is the abbreviation for second-harmonic generation [174]. FROG is a self-referencing technique, thus in contrast to FTSI no well-known reference pulse is needed, but requires the measurement of a non-linear signal. The unknown pulse is split into two pulse copies which propagate parallel to each other before they are focused non-collinearly with a lens in a non-linear crystal, e.g., a Beta Barium Borat (BBO) crystal (Fig. 2.7). The SHG FROG signal is measured by scanning the delay τ between the two pulses and recording the frequency resolved SHG signal. The generation of the frequency doubled signal requires phase matching

$$\vec{k}_{\mathrm{SHG}} = \vec{k}_1 + \vec{k}_2. \tag{2.69}$$

Due to this conservation of momentum, the SHG signal is emitted along the angle bisector of the two pulses, when the two pulses overlap temporally and spatially, and can straightforwardly be separated using an aperture. For more details about SHG the reader is referred to Ref. [175] and [176]. In general, also a collinear FROG geometry can be employed [177–180].

The signal of the SHG FROG measurement, also called FROG trace is given by

$$I_{\mathrm{FROG}}^{\mathrm{SHG}}(\omega,\tau) \propto \left| \int_{-\infty}^{+\infty} E^{+}(t)\, E^{+}(t-\tau)\, \mathrm{e}^{-\mathrm{i}\omega t} \right|^2 . \tag{2.70}$$

The electric field $E^{+}(t)$ can be obtained from the FROG trace without any significant ambiguity by using an iterative algorithm [181–183]. The remaining ambiguities are the absolute phase of the laser pulse, the arrival time of the pulse, and in the case of SHG FROG the direction of time as

$$I_{\mathrm{FROG}}^{\mathrm{SHG}}(\omega,\tau) = I_{\mathrm{FROG}}^{\mathrm{SHG}}(\omega,-\tau) \tag{2.71}$$

holds [170]. Therefore, the sign of the spectral phase cannot be determined with a single SHG FROG measurement. This ambiguity can be removed by applying the FROG phase to the pulse via a pulse shaper, record a second FROG trace, and verifying if the pulse duration is increased or decreased compared to the first measurement.

The FROG technique is particularly suitable to characterize linearly polarized laser pulses. In principle, an arbitrarily polarized pulse could be characterized by recording a FROG trace for the two orthogonal polarization components. However, due to the ambiguities concerning the absolute phase and the pulse arrival time, the actual polarization state cannot be reconstructed by these two SHG FROG measurements. Only by recording additional FROG traces for different linear projections of the two orthogonal polarization states the polarization state can be retrieved [184]. This method is termed TURTLE (tomographic ultrafast retrieval of transverse light E-fields), but not used in this work.

3 Vector-field control

Over the last decades many techniques were developed to manipulate the electric field of ultrashort laser pulses. Shaping an ultrashort signal on the femtosecond time scale directly in time domain is technically highly challenging. Therefore, most established techniques manipulate the pulse in frequency domain [12–14, 185] and utilize the fact that the electric field in time domain is linked to the electric field in frequency domain via Fourier transform [143]. Only recently developed devices, such as the acousto-optic programmable dispersive filter (AOPDF), also known as Dazzler[1], allow direct pulse shaping in the time domain [40, 186, 187].

The pulse shaper (PS) presented in this thesis is based on frequency-domain shaping. For this purpose, different programmable spatial light modulators (SLMs), such as deformable mirrors, micro-mirror arrays, acousto-optic modulators (AOM), and liquid-crystal spatial light modulators (LC SLMs) can be used [13, 14]. Due to their versatility, AOMs and LC SLMs are most often utilized. A comparison of these two can be found in Ref. [13] and [185].

In this thesis, an LC SLM is employed. Its functional principle is discussed in the first section of this chapter (Section 3.1). The well-established pulse shaper setup using a dual-layer LC SLM, its shaping capabilities, and applications are presented in Section 3.2. This setup is the basis for all attempts to expand the control over the electric field, as presented and analyzed in Section 3.3 and Section 3.4. These analyses do not simply describe what is stated in the corresponding publications, but discuss and compare them in a broader context of pulse shaping. The chapter concludes with a summary of the presented pulse shapers (Section 3.5).

3.1 Principles of LC SLM pulse shaping

3.1.1 Frequency-domain shaping

For frequency domain pulse shaping it is first necessary to transfer the pulse from the time into the frequency domain. For this purpose, a so called $4f$ setup is employed (Fig. 3.1). This setup consists of two gratings and two lenses. The spacing between the grating and the lens matches the focal length f for both grating–lens pairs. The two lenses are separated by $2f$. This arrangement is also known as zero-dispersion compressor [188, 189]. The incoming laser beam hits the first grating and is spectrally dispersed. The first lens after the grating collimates the single frequency components and focuses them in the Fourier plane. The second lens collimates each frequency component and directs them onto a second grating, where they will be recombined to a single pulse.

[1] Dazzler is the commercial name used by *FASTLITE* for their AOPDF.

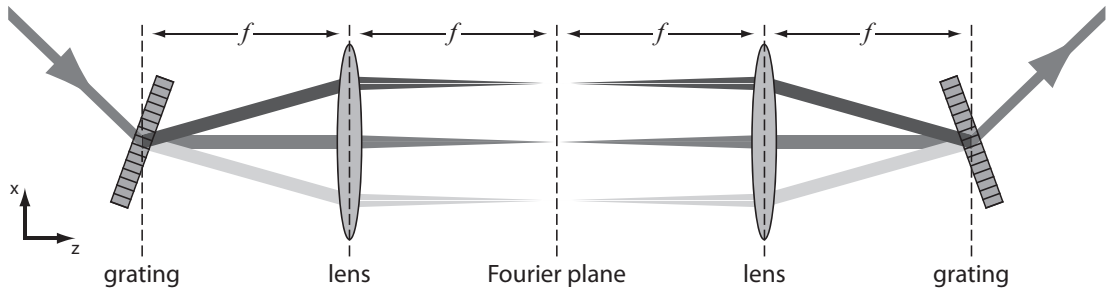

Figure 3.1 | Schematic of a $4f$ setup. The incident laser pulse is angular dispersed by a grating. The first lens collimates the single frequency components and focuses them into the Fourier plane. The second lens and the grating recombine the separated frequency components to a single pulse. In an ideal $4f$ setup, the optical path length is not frequency dependent, thus such a setup is also called zero-dispersion compressor.

By placing a spatial light modulator into the Fourier plane, an independent modulation of each frequency is possible. The frequency resolution and the shaping capabilities are restricted by the used SLM.

An LC SLM consists of a fixed number of liquid-crystal (LC) pixels, which can be independently controlled. In most cases, these pixels are arranged in a one-dimensional array, but also LC SLMs with a two-dimensional array are available. To distinguish between these, the latter will be labeled as 2D LC SLM. An LC pixel is formed by two indium tin oxide electrodes on two parallel glass substrates [Fig. 3.2(a)]. Between these substrates nematic LC molecules are located, which are aligned parallel to the glass substrate [Fig. 3.2(b)]. The pixels are separated by a certain gap (typically in the order of 3 % of the pixel width). In these gap areas the LC molecules cannot be manipulated. The functional principle of such a pixel is the same as in video displays: manipulating the properties of the passing light by an external voltage.

An LC pixel can be viewed as an adjustable uniaxial birefringent crystal. The optical axis of the pixel is given by the alignment of the LC molecules (Fig. 3.2). The polarization component of the incident light perpendicular to the optical axis is influenced by the ordinary refractive index n_o and the parallel polarization component by the extraordinary refractive index n_e. The optical axis of the LC pixels, or more precisely the projection of optical axis onto the plane of the electrodes, is also referred to as the modulation axis of the LC SLM. The optical anisotropy $\Delta n(\omega) = n_\mathrm{e}(\omega) - n_\mathrm{o}(\omega)$ for an LC pixel is indeed not fixed for a given frequency ω but can be influenced by an external voltage U

$$\Delta n(\omega,U) = \widetilde{n}_\mathrm{e}(\omega,U) - n_\mathrm{o}(\omega). \tag{3.1}$$

The voltage dependency of the extraordinary refractive index $\widetilde{n}_\mathrm{e}(\omega,U)$ is the result of the tilting of the molecules, thus of the optical axis, in an external electric field as shown in Fig. 3.2(c). The voltage dependency can be expressed by

$$\frac{1}{\widetilde{n}_\mathrm{e}(\omega,U)} = \frac{\cos^2\theta(U)}{n_\mathrm{o}^2(\omega)} + \frac{\sin^2\theta(U)}{n_\mathrm{e}^2(\omega)}, \tag{3.2}$$

but for practical use it is determined experimentally in the so called pulse shaper cali-

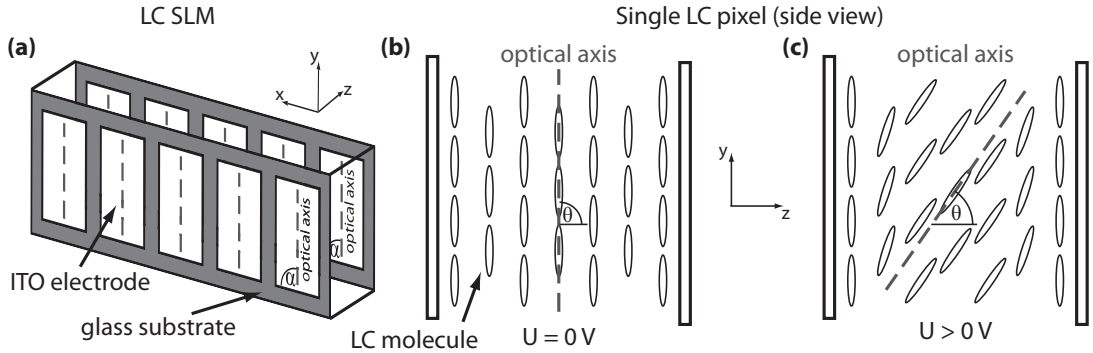

Figure 3.2 | Schematic of an LC SLM. (a) The sketched LC SLM consists of an array of 5 LC pixels. Each pixel is defined by the indium tin oxide (ITO) electrodes on two parallel glass substrates containing LC molecules. The projection of the optical axis of these LC molecules onto the plane of the electrodes is called modulation axis of the LC SLM. The orientation angle α of the modulation axis is defined in the x–y plane. (b,c) Side view of a single LC pixel. The LC molecules between the glass substrates are aligned parallel to the substrate, if no voltage is applied [(b)]. The optical axis (dashed line) is parallel to these molecules. For a voltage greater than zero, the LC molecules and thus the optical axis is tilted in the y–z plane and the angle θ gets smaller [(c)].

bration [13, 38] by measuring the phase retardation

$$\Delta\varphi(\omega,U) = \frac{\omega\, d_{\mathrm{LC}}}{c}\Delta n(\omega,U), \tag{3.3}$$

where d_{LC} is the thickness of the LC pixel and c the speed of light.

It is also worth noting that the optical anisotropy of an LC pixel is indeed not only voltage but also temperature dependent: $\Delta n(\omega,U,T)$. There are different mathematical models to describe this temperature dependency [190, 191]. In general, $\Delta n(\omega,U,T)$ decreases with rising temperature [190]. The technical documentation of the LC SLM used in this thesis states a 0.6 % decrease of the optical anisotropy for a temperature increment of 1°C [192]. This has to be kept in mind under a practical point of view, resulting in the importance to calibrate and operate the LC SLM under constant temperature.

The effect of an LC pixel onto the electric light field passing that pixel can be described using the Jones matrix formalism

$$\vec{E}_{\mathrm{out}}(\omega) = \boldsymbol{M}_{\mathrm{LC}}\, \vec{E}_{\mathrm{in}}(\omega), \tag{3.4}$$

where $\boldsymbol{M}_{\mathrm{LC}}$ is the Jones matrix of the LC pixel. The modulation axis of the LC pixel sketched in Fig. 3.2 is orientated under 90° with respect to the x axis, thus introducing a voltage-dependent phase retardation for the y component of the incident light. The orientation of the modulation axis is fixed for a given LC SLM, but can vary for different LC SLM models. The Jones matrix for an arbitrary LC pixel depends therefore not only on the applied phase retardation $\Delta\varphi$ but also on the orientation α of its modulation axis

$$\boldsymbol{M}^{\alpha}_{\mathrm{LC}}(\Delta\varphi) = \boldsymbol{R}(\alpha) \begin{pmatrix} \mathrm{e}^{-\mathrm{i}\Delta\varphi} & 0 \\ 0 & 1 \end{pmatrix} \boldsymbol{R}(-\alpha) \tag{3.5}$$

with $\boldsymbol{R}(\alpha)$ being the rotation matrix. The explicit dependency on ω and U of the applied phase $\Delta\varphi$ is omitted for the sake of simplicity. Common orientations of the modulation axis are 0°, ±45°, and 90°. The effect of the LC pixel on the light field depends on the angle between the polarization direction of the laser pulse and the orientation of the modulation axis. The incoming light field will be considered as linearly polarized parallel to the x axis in the following. This polarization component will henceforth referred to as p component or p polarization, while the component along the y axis will be called s component/polarization. For $\alpha = 0°$ the modulation axis is aligned parallel to the incoming p polarized light and only its phase can be manipulated. Its polarization state is not affected

$$\vec{E}_{\text{out}}(\omega) = \boldsymbol{M}_{\text{LC}}^{0°}(\Delta\varphi) \begin{pmatrix} E_{\text{in}}(\omega) \\ 0 \end{pmatrix} = E_{\text{in}}(\omega)\, \mathrm{e}^{-\mathrm{i}\Delta\varphi} \begin{pmatrix} 1 \\ 0 \end{pmatrix}. \tag{3.6}$$

However, for an orientation of $\alpha = \pm 45°$ the LC pixel can shift amplitude of the electric field from one into the other polarization (similar to a wave plate), but there will also be an additional phase introduced [193]. This can be easily seen by calculating the electric field after the LC pixel

$$\begin{aligned} \vec{E}_{\text{out}}(\omega) &= \boldsymbol{M}_{\text{LC}}^{45°}(\Delta\varphi) \begin{pmatrix} E_{\text{in}}(\omega) \\ 0 \end{pmatrix} = \frac{1}{2}\, E_{\text{in}}(\omega) \begin{pmatrix} 1 + \mathrm{e}^{-\mathrm{i}\Delta\varphi} \\ -1 + \mathrm{e}^{-\mathrm{i}\Delta\varphi} \end{pmatrix} \\ &= E_{\text{in}}(\omega)\, \mathrm{e}^{-\mathrm{i}\frac{\Delta\varphi}{2}} \begin{pmatrix} \cos(\frac{\Delta\varphi}{2}) \\ \mathrm{e}^{-\mathrm{i}\frac{\pi}{2}}\, \sin(\frac{\Delta\varphi}{2}) \end{pmatrix}. \end{aligned} \tag{3.7}$$

The sine and cosine depend on the same parameter $\Delta\varphi/2$, thus describe the amplitude shift between the two polarization components. However, this parameter is also present in the unwanted phase term $\mathrm{e}^{-\mathrm{i}\Delta\varphi/2}$. Moreover, an additional relative phase of $\pi/2$ between both polarization components is introduced.

The first reported LC SLM consisted of an array of 32 pixels in a single layer [194]. However, the undesired phases in Eq. (3.7) significantly limit the use of such a single-layer LC SLM with regard of polarization (or amplitude) shaping which is for this reason mainly used for phase-only shaping [38, 194].

3.1.2 Temporal shaping window

Equations (3.5) and (3.7) describe the effect of the LC SLM in frequency domain. However, the generated electric field in time domain depends on the phase function applied across all LC SLM pixels and is not only restricted by the spectral transfer function but also influenced by the frequency distribution and spot size of each frequency component in the Fourier plane. One effect of particular interest in this thesis is the so called "shaping window". It is a consequence of the finite spot size in the Fourier plane and the pixelated nature of the LC SLM so that only stepwise defined phase functions can be applied. The shaping window restricts the maximum time delay which can be introduced using the pulse shaper and causes a reduction of the amplitude of the electric field

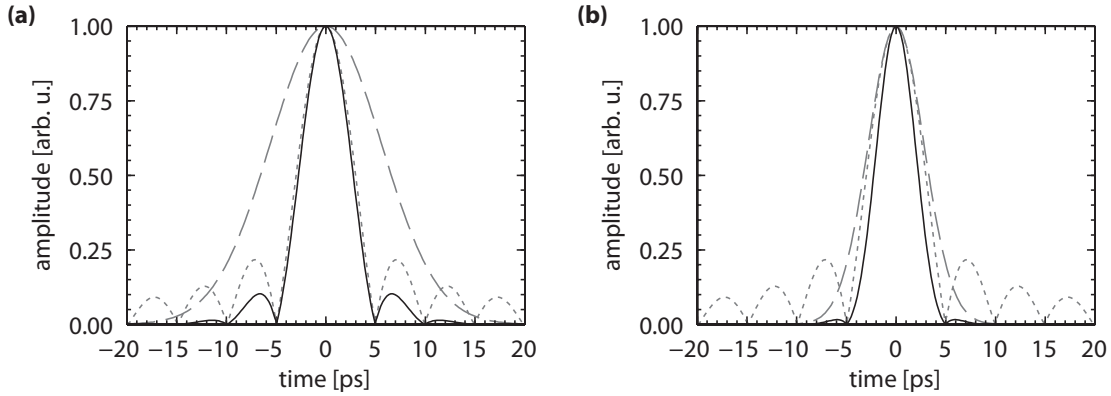

Figure 3.3 | Shaping window of a pixelated LC SLM pulse shaper. The shaping window depends on the spot size (Gaussian function, dashed line) and the frequency bandwidth passing each pixel (sinc function, dotted line). The multiplication (solid line) of these restricts the maximum amplitude in time domain. (a) For a spot size of 2/5 of the pixel width, the Gaussian function influences mainly the sidebands of sinc function. (b) If the spot size gets larger, in this case 4/5 of the pixel width, the exponential function gets narrower, thus limiting the shaping window.

with increasing time delay. Mathematically, the shaping window can be explained by Fourier transform of the spatial transfer function of the LC SLM. This spatial transfer function is given by the convolution of the beam profile with the pixelated spatial phase modulation. In general, the resulting electric field in time domain can only be calculated numerically, but with some simplifications Vaughan et al. [195] found

$$E_{\mathrm{out}}(t) \propto \mathrm{e}^{-(\frac{\delta\Omega}{4}t)^2}\ \mathrm{sinc}\left(\frac{\Delta\Omega}{2}t\right), \tag{3.8}$$

where $\delta\Omega = w_0\Delta\Omega/\Delta x$ is the frequency spot size of a single frequency component in the Fourier plane, with w_0 being the spatial spot size and $\Delta\Omega$ the frequency bandwidth at one single pixel - not of the whole laser spectrum. Δx is the spatial pixel size. The sinc function is a result from the pixelation of the LC SLM and its width is indirectly proportional to the frequency bandwidth $\Delta\Omega$. The Gaussian function arises from the finite Gaussian spot size $\delta\Omega$ of each spectral component. The product in Eq. (3.8) defines the shaping window and is plotted in Fig. 3.3.

There are various other effects related to the analysis of $E_{\mathrm{out}}(t)$, such as replica pulses and space–time coupling. Replica pulses arise also from the discrete sampling of the applied phase. This causes that the shaped pulse sequence is reproduced infinitely in time with a certain temporal distance given by $2\pi/\Delta\Omega$. However, the amplitude of these replica pulses is significantly reduced by the shaping window which can be considered as a temporal envelope function. The maximum feasible time delay generated by a pixelated pulse shaper is limited to $\pm\pi/\Delta\Omega$, due to the replica pulse in the first maximum of the shaping window centered around $t = 0$. The effect of space–time coupling describes the change in the transversal spatial coordinates of the shaped beams depending on the applied phase. If a pulse is for example shifted in time, its profile will also be slightly shifted in the transversal direction. For a more detailed description, the reader is referred

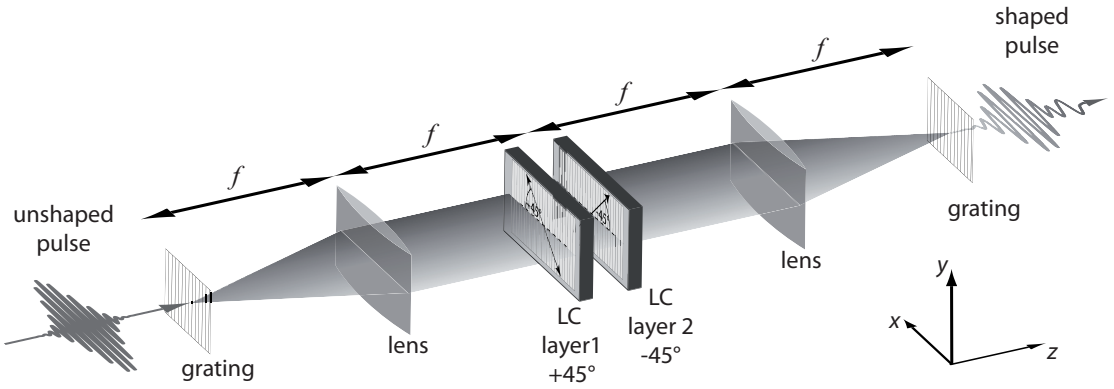

Figure 3.4 | Schematic of a conventional pulse shaper setup using a 2-layer SLM in a $4f$ setup. The SLM is placed in the Fourier plane of the $4f$ setup (see Fig. 3.1) to manipulate the dispersed frequency components. The modulation axes of the LC layers are orientated under $+45°$ and $-45°$ with respect to the x axis. The distance between the two layers is exaggerated for better visibility. The incident light field is in this case linearly p polarized (parallel to the x direction). Figure modified from Ref. [3] © (2014) Dr. Stefan Rützel.

to Refs. [193, 195–202].

3.2 Conventional dual-layer pulse shaper

The first attempt to gain more control over the electric field compared to a single-layer LC SLM was to employ two consecutive single-layer LC SLMs [203]. Shortly afterwards LC SLMs with two LC layers (2-layer SLM) in one device were commercially available [39]. By adding the second layer another degree of freedom is gained, as it allows, for example, the compensation and manipulating of the unwanted phase $\Delta\varphi/2$ introduced by a layer orientated under $\pm45°$ [see Eq. (3.7)]. For this purpose, the orientations of the two LC layers can differ by either $45°$ ($\alpha_1 = 0°/90°$, $\alpha_2 = \pm45°$) or $90°$ ($\alpha_1 = \pm45°$, $\alpha_2 = \mp45°$). The later arrangement is commonly used as it has less restrictions in the polarization and propagation direction of the incident light and eliminates multiple-diffraction effects [193]. Pulse shapers employing a 2-layer SLM are widely available nowadays and are taken as a benchmark for the more advanced setups presented in Section 3.3 and 3.4.

3.2.1 Shaping capabilities

Figure 3.4 shows the schematic of a dual-layer LC SLM as it is used in conventional pulse shaper setups, where the SLM is placed in the Fourier plane of a $4f$ setup. Following the Jones matrix formalism the transfer matrix of the 2-layer SLM can be calculated via

$$\boldsymbol{M}^{\mathrm{2l.}}_{\mathrm{PS}}(\Delta\varphi_1,\Delta\varphi_2) = \boldsymbol{M}^{-45°}_{LC}(\Delta\varphi_2)\,\boldsymbol{M}^{45°}_{LC}(\Delta\varphi_1). \tag{3.9}$$

For simplification, all optical elements are assumed to be ideal and their unwanted effects on the amplitude and phase are neglected in all following calculations. For a p polarized

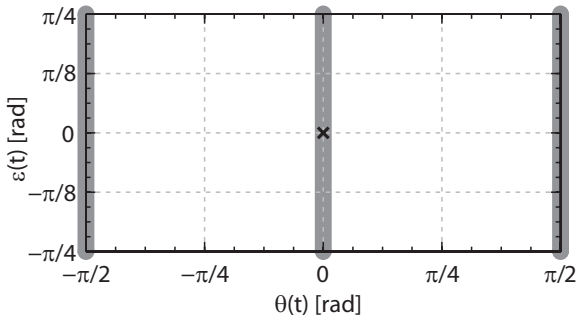

Figure 3.5 | All producible polarization states using a conventional 2-layer phase/polarization shaper. The conventional 2-layer pulse shaper is only able to generate polarization states with the orientation $\theta = 0, \pm\pi/2$ rad, the ellipticity ϵ can be controlled in the whole definition range (gray dots). The input pulse is linearly p polarized (black cross).

incoming electric field the resulting output field is given by

$$\begin{aligned}\vec{E}_{\mathrm{out}}(\omega) &= \boldsymbol{M}^{\mathrm{2l.}}_{\mathrm{PS}}(\Delta\varphi_1,\Delta\varphi_2)\begin{pmatrix}E_{\mathrm{in}}(\omega)\\0\end{pmatrix}\\ &= E_{\mathrm{in}}(\omega)\,\mathrm{e}^{-\mathrm{i}\frac{\Delta\varphi_1+\Delta\varphi_2}{2}}\begin{pmatrix}\cos\left(\frac{\Delta\varphi_1-\Delta\varphi_2}{2}\right)\\ \mathrm{e}^{-\mathrm{i}\frac{\pi}{2}}\,\sin\left(\frac{\Delta\varphi_1-\Delta\varphi_2}{2}\right)\end{pmatrix}.\end{aligned} \tag{3.10}$$

The phase and the amplitude ratio between the p and s component is modulated by the sum and the difference of the applied phase retardations. By choosing proper combinations of $\Delta\varphi_1$ and $\Delta\varphi_2$, both parameters can be shaped independently. However, the relative phase between the two components $\Delta\phi(\omega) = \phi_{\mathrm{s}}(\omega) - \phi_{\mathrm{p}}(\omega) = \pi/2$ is constant, thus restricting the possible polarization states. For example, the generation of light linearly polarized under 45° is not possible using this setup, since this polarization state requires a phase difference of zero between both polarization components. The possible polarization states for a certain frequency or a bandwidth-limited pulse are plotted in Fig. 3.5. The plot shows that the orientation is restricted to $\theta = 0, \pm\,\pi/2$ rad, but that the ellipticity ϵ can be varied in the full range of $[-\pi/4,\ \pi/4]$. It is worth mentioning that in a complex shaped pulse other polarization states can be reached using this setup [42, 151, 152, 204] by introducing a relative phase and/or time delay between different frequency components. However, this leads in return to limitations of the possible pulse shapes in time domain. Hence, for the further discussion of the polarization shaping capabilities of various setups, only the generation of bandwidth-limited pulses, which is equivalent to manipulating the polarization state of a single frequency component, is taken into account.

The total intensity $I_{\mathrm{tot}} = I_p + I_s$ of the light field cannot be modulated, if the 2-layer pulse shaper is used as phase/polarization shaper. However, by adding a linear polarizer after the setup (see Fig. 3.4), the change in polarization can be transferred into a change in amplitude and thus in the total intensity

$$\begin{aligned}\vec{E}_{\mathrm{out}}(\omega) &= \begin{pmatrix}1&0\\0&0\end{pmatrix}\boldsymbol{M}^{\mathrm{2l.}}_{\mathrm{PS}}(\Delta\varphi_1,\Delta\varphi_2)\begin{pmatrix}E_{\mathrm{in}}(\omega)\\0\end{pmatrix}\\ &= E_{\mathrm{in}}(\omega)\,\mathrm{e}^{-\mathrm{i}\frac{\Delta\varphi_1+\Delta\varphi_2}{2}}\,\cos\left(\frac{\Delta\varphi_1-\Delta\varphi_2}{2}\right)\begin{pmatrix}1\\0\end{pmatrix}.\end{aligned} \tag{3.11}$$

This phase/amplitude shaper was introduced first [39] and later the possibilities in (limited) polarization control of the phase/polarization shaper were utilized [42].

3.2.2 Applications of phase, amplitude, and polarization shaping

One of the main applications of phase-only shaping is dispersion compensation [38, 194, 205]. This technique is not only used to compensate the dispersion introduced by optical elements [206] but also to optimize the output of chirped-pulse amplifiers (CPA) [207] by compensating the inherent higher-order dispersion [208–210]. It is also widely adopted in fiber-optic communication [34–36]. Phase shaping could, in general, also be achieved with fixed phase masks [11, 13], but this requires a well characterized and fixed optical system. LC SLM based pulse shapers provide flexible phase control and allow the phase compensation of unknown pulses by employing iterative learning algorithms [211–214] and by measuring a suitable feedback signal [206, 215, 216]. The concept of using an iterative algorithm to achieve a certain optimization goal can also be used to adoptively generate specific target pulse shapes [217] and especially for coherent control [27, 33, 218] as suggested by Judson and Rabitz [219]. The flexibility of LC SLM based phase shaping makes these setups highly suitable for adaptive quantum control of unknown quantum systems as numerous experiments demonstrate [25, 28, 29, 220–227]. Phase shaping is not limited to phase compensation or quantum control. It is also employed in spectroscopy and microscopy [16, 17, 20–22], as well as for temporal delay generation [38], quantum optics [228], and pulse characterization [229–231].

Phase shaping can be realized with a single- or dual-layer LC SLM, but the additional control over the amplitude or polarization provided by the second layer enabled new and improved experimental methods. One advantage of amplitude shaping is the generation of sophisticated multipulse sequences. A sequence with several identical pulse copies can, for example, not be realized by phase-only shaping (see Section 2.1, Fig. 2.1). However, such sequences are required for many established spectroscopy methods [15] such as two-dimensional spectroscopy [53, 75]. 2-layer SLM assisted two-dimensional spectroscopy was, for example, demonstrated on atomic vapor [91], nanostructures [110], and merocyanine isomers [81]. Other nonlinear spectroscopy or microscopy methods [18, 232] and quantum control techniques [31, 233–237] benefit from the additional control over the spectral amplitude, as well. Further applications of the LC SLM based phase/amplitude shaping include band-pass filtering [238], pulse characterization [239], material processing [37] and molecular cooling [240].

The polarization shaping capabilities of 2-layer SLMs, instead of amplitude shaping, were also successfully employed in different experiments. The benefit of polarization shaping was demonstrated in quantum control of atoms [43], diatomic molecules [44, 45], free-electron wave packets [48, 52], and near-fields at nanostructures [47, 49–51]. Polarization shaping was also used in coherent anti-Stokes Raman spectroscopy [19] and it was theoretically shown that it can be utilized in near-field spectroscopy [119–122].

These given examples for phase/amplitude and phase/polarization shaping are only a small selection of published experiments. Both variants found numerous applications and the conventional 2-layer SLM pulse shaper is today a standard device in many femtosecond laser laboratories.

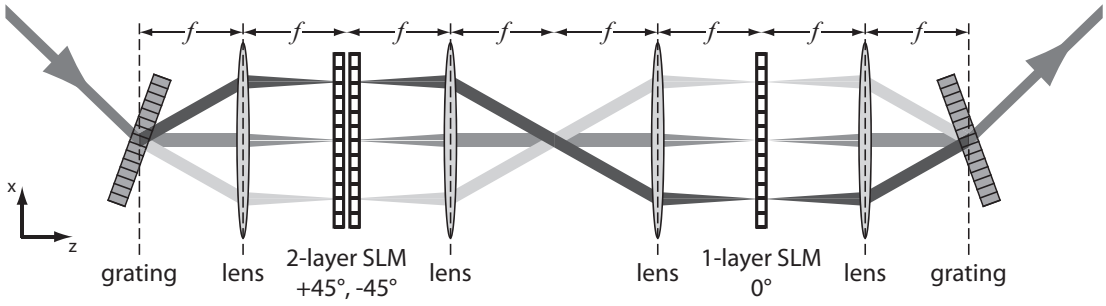

Figure 3.6 | Full polarization shaper using two LC SLMs. To substitute a 3-layer SLM, Polachek et al. [132] built an $8f$ arrangement and used a 2-layer and a 1-layer SLM in each telescope. The orientation of the modulation axes are $+45°$ and $-45°$ for the first and $0°$ for the second LC SLM. Figure following Ref. [132].

3.3 Improved vector-field control

The conventional 2-layer SLM pulse shaper enables control over two degrees of freedom: either phase and amplitude or phase and ellipticity[2]. However, for full vector field control, manipulating all four degrees of freedom – phase, amplitude, ellipticity, and orientation – is necessary. This section discusses two different approaches to extend the capabilities of the conventional 2-layer pulse shaper. Both are capable of shaping three of the four degrees of freedom and form the basis for the development of a full vector-field shaper (VFS).

3.3.1 Full polarization control

The first approach to control the ellipticity and the orientation was published by Polachek et al. [132] (Silberberg group). They added a third layer to manipulate the relative phase between the two polarization components. Since a 3-layer SLM was not available a 2-layer and a 1-layer SLM were used in an $8f$ arrangement (Fig. 3.6). The modulation axes of these three layers are orientated under $+45°$, $-45°$ and $0°$. The Jones matrix[3] of this 3-layer pulse shaper is

$$\boldsymbol{M}^{3\text{l.}}_{\text{PS}}(\Delta\varphi_1,\Delta\varphi_2,\Delta\varphi_3) = \boldsymbol{M}^{0°}_{\text{LC}}(\Delta\varphi_3)\,\boldsymbol{M}^{-45°}_{\text{LC}}(\Delta\varphi_2)\,\boldsymbol{M}^{45°}_{\text{LC}}(\Delta\varphi_1) \tag{3.12}$$

and the output electric field

$$\begin{aligned}\vec{E}_{\text{out}}(\omega) &= \boldsymbol{M}^{3\text{l.}}_{\text{PS}}(\Delta\varphi_1,\Delta\varphi_2,\Delta\varphi_3)\begin{pmatrix}E_{\text{in}}(\omega)\\0\end{pmatrix}\\ &= E_{\text{in}}(\omega)\,\mathrm{e}^{-\mathrm{i}\frac{\Delta\varphi_1+\Delta\varphi_2}{2}}\begin{pmatrix}\mathrm{e}^{-\mathrm{i}\Delta\varphi_3}\,\cos\left(\frac{\Delta\varphi_1-\Delta\varphi_2}{2}\right)\\ \mathrm{e}^{-\mathrm{i}\frac{\pi}{2}}\,\sin\left(\frac{\Delta\varphi_1-\Delta\varphi_2}{2}\right)\end{pmatrix}.\end{aligned} \tag{3.13}$$

The comparison of the electric field after the 2-layer polarization shaper [Eq. (3.10)]

[2]The orientation is limited to $\theta = 0, \pm\pi/2$ rad.

[3]In Ref. [132] the phase retardation is defined with opposite sign as in this thesis causing the minor differences between Eq. (3.12) and Eq.(1) in Ref. [132].

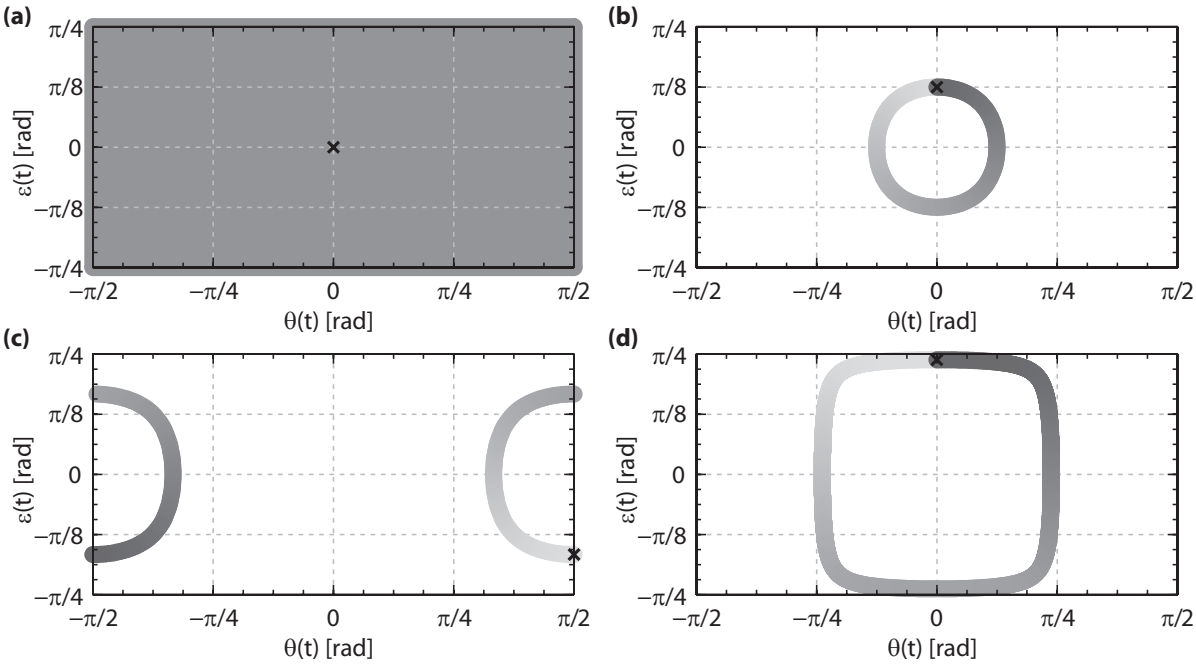

Figure 3.7 | Possible polarization states with a 3-layer pulse shaper as designed by Polachek et al. [132]. (a) With a 3-layer SLM all possible polarization states (gray dots) can be generated from a linearly p polarized input pulse (black cross) at a given frequency. (b–c) Influence of phase applied to the third layer on the polarization generated by the first two layers. The black crosses mark three different potential polarization states generated by the first two layers [$\theta_\mathrm{b} = 0$ rad & $\epsilon_\mathrm{b} = \pi/8$ rad (b), $\theta_\mathrm{c} = \pi/2$ rad & $\epsilon_\mathrm{c} = -\pi/3$ rad (c), $\theta_\mathrm{d} = 0$ rad & $\epsilon_\mathrm{d} = \pi/4.2$ rad (d)]. If the phase retardation of layer 3 $\Delta\varphi_3$ is increased from 0 to 2π (light to dark gray) polarization states can be generated, which are not accessible with a conventional 2-layer phase/polarization shaper (compare Fig. 3.5).

and this 3-layer setup [Eq. (3.13)] shows that the third layer allows controlling the phase difference $\Delta\phi(\omega) = \phi_\mathrm{s}(\omega) - \phi_\mathrm{p}(\omega)$ while the first two layers still control the phase and the amplitude ratio between the p and s component. With this setup, every point in the Poincaré plane can be reached for a single frequency component [Fig. 3.7(a)]. The influence of the third layer on three different polarization states generated by the first two layers is visualized in Fig. 3.7(b–d). In each subfigure, the black cross marks a potential polarization state generated by the first two layers. These polarization states are limited to $\theta = 0, \pm\,\pi/2$ rad (see Fig. 3.5). The final polarization state generated by the third layer depends on the applied phase. If the phase of the third layer is changed from 0 to 2π (light to dark gray) polarization states which are located on a circle or rounded rectangle within the Poincaré plane can be reached. By choosing a proper combination of all three applied phases every point in the Poincaré plane is accessible. This is a significant improvement over the conventional 2-layer phase/polarization shaper, since three degrees of freedom are controllable: phase, orientation and ellipticity. However, the total intensity of each frequency component still cannot be manipulated and the generation of multipulse sequences is significantly limited.

Instead of using two separated LC SLMs to build a full polarization shaper, a single

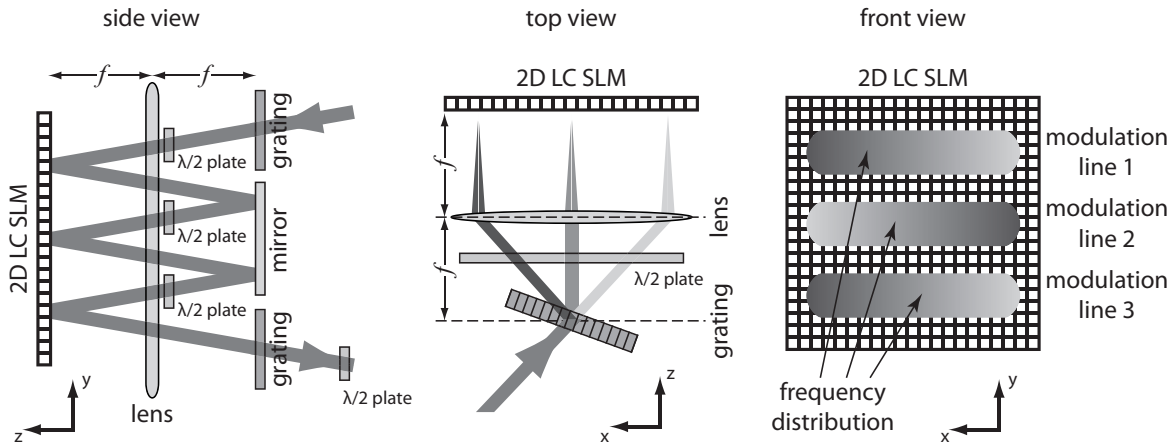

Figure 3.8 | Full polarization shaper using a 2D LC SLM by Esumi et al. [241]. The two gratings, the lens, the mirror and the reflective 2D LC SLM form a folded $12f$ setup. The pulse is manipulated within three vertically separated regions of the 2D LC SLM. The orientation of the light field is rotated using three $\lambda/2$ plates before each interaction to "simulate" different modulation axes for each region of the 2D LC SLM. The fourth $\lambda/2$ plate behind the second grating is optional and was not included in the setup of Esumi and coworkers [241]. It can be used to avoid a polarization rotation of the setup if no phases are applied. Including the fourth wave plate the "simulated" modulation axes correspond to 45°, 0°, and 90°. Figure following Ref. [241].

2D LC SLM can also be used, as demonstrated by Esumi and coworkers [241] (Kannari group). The schematic of such a setup is shown in Fig. 3.8. The electric field is manipulated by three consecutive interactions with different regions of the 2D LC SLM (768×768 pixels, 20×20 mm). Since the modulation axis of every LC pixel is orientated at 0° the incident light field is rotated using $\lambda/2$ plates before each interaction to "simulate" different modulation axes. The first wave plate turns the input polarization by 45° so that interaction 1 can shift field amplitude from one into the other polarization component. The second wave plate reverses the polarization change of the first wave plate and the third rotates the polarization by 90° so that in interaction 2 and 3 the phase of both polarizations can be individually manipulated. With the setup described in Ref. [241], the output electric field is rotated by 90° with respect to the incident field even if no phases are applied to the 2D LC SLM. This could be compensated with a fourth wave plate. This additional wave plate is included in the following calculations in order to provide a more intuitive result and for better comparability with the other setups in this thesis[4]. The Jones matrix of this (modified) setup can be either calculated[5] including

[4]This does not alter the author's principle findings [241] and both descriptions can be used equivalently to describe the shaping capabilities of the setup.

[5]The matrices for the reflections are neglected for simplification.

the wave plates or simply by using the substituted modulation axes

$$\begin{aligned}\boldsymbol{M}_{\mathrm{PS}}^{\mathrm{2D}}&(\Delta\varphi_1,\Delta\varphi_2,\Delta\varphi_3)\\ &= \boldsymbol{W}_{\lambda/2}^{45^\circ}\,\boldsymbol{M}_{\mathrm{LC}}^{0^\circ}(\Delta\varphi_3)\,\boldsymbol{W}_{\lambda/2}^{45^\circ}\,\boldsymbol{M}_{\mathrm{LC}}^{0^\circ}(\Delta\varphi_2)\,\boldsymbol{W}_{\lambda/2}^{22.5^\circ}\,\boldsymbol{M}_{\mathrm{LC}}^{0^\circ}(\Delta\varphi_1)\,\boldsymbol{W}_{\lambda/2}^{22.5^\circ}\\ &= \boldsymbol{M}_{\mathrm{LC}}^{90^\circ}(\Delta\varphi_3)\,\boldsymbol{M}_{\mathrm{LC}}^{0^\circ}(\Delta\varphi_2)\,\boldsymbol{M}_{\mathrm{LC}}^{45^\circ}(\Delta\varphi_1).\end{aligned} \tag{3.14}$$

The output field is given by

$$\begin{aligned}\vec{E}_{\mathrm{out}}(\omega) &= \boldsymbol{M}_{\mathrm{PS}}^{\mathrm{2D}}(\Delta\varphi_1,\Delta\varphi_2,\Delta\varphi_3)\begin{pmatrix}E_{\mathrm{in}}(\omega)\\0\end{pmatrix}\\ &= E_{\mathrm{in}}(\omega)\,\mathrm{e}^{-\mathrm{i}\frac{\Delta\varphi_1}{2}}\begin{pmatrix}\mathrm{e}^{-\mathrm{i}\Delta\varphi_2}\,\cos(\frac{\Delta\varphi_1}{2})\\ \mathrm{e}^{-\mathrm{i}\frac{\pi}{2}}\,\mathrm{e}^{-\mathrm{i}\Delta\varphi_3}\,\sin(\frac{\Delta\varphi_1}{2})\end{pmatrix}.\end{aligned} \tag{3.15}$$

This 2D LC SLM setup is, as the previously described 3-layer setup, capable to generate all possible polarization states for a given spectral component (see Fig. 3.7). This setup has the advantage that only one device is needed and the authors state that, in principle, amplitude shaping could be implemented by using a fourth modulation line. This was, however, not demonstrated. For amplitude shaping, a polarizer after the first interaction or dependent on the resolution of the 2D LC SLM a vertical phase modulation [41, 242] could be used. One disadvantage of this setup compared with the setup of Polachek et al. [132] is that a true zero dispersion compressor cannot be realized due to the differences in the incidence angles between each interaction and thus the phase introduced by the setup has to be compensated using the pulse shaper [241].

The benefit of a full polarization shaper compared with the conventional 2-layer polarization shaper is that not only every possible polarization state can be generated, but also that any phase and polarization distortions introduced by optical elements can be corrected. Therefore, such a setup is of great interest for pulse compression as suggested in Ref. [132], but its application is not limited to this field. The group of Brasselet, for example, built a setup similar to the one of Polachek and coworkers [132] and demonstrated the enhancement of the structural contrast in nonlinear microscopy by unrestricted polarization shaping [140].

3.3.2 Amplitude and limited polarization control

Both previous presented setups permit unrestricted polarization control, but cannot manipulate the spectral amplitude, thus do not allow the unrestricted generation of multipulse sequences with different target polarization states. Therefore, Plewicki et al. [133] (Lindinger group) presented another approach to expand the capabilities of the conventional phase/polarization shaper. They used a single 2-layer SLM inside a normal $4f$ setup and passed this arrangement twice [Fig. 3.9(a)]. On the first pass, one half of the LC pixels is used to generate a phase and amplitude modulation by using a linear polarizer before the SLM is passed a second time. On the second pass, the other half of the LC pixels operates in the phase/polarization shaper mode. The setup

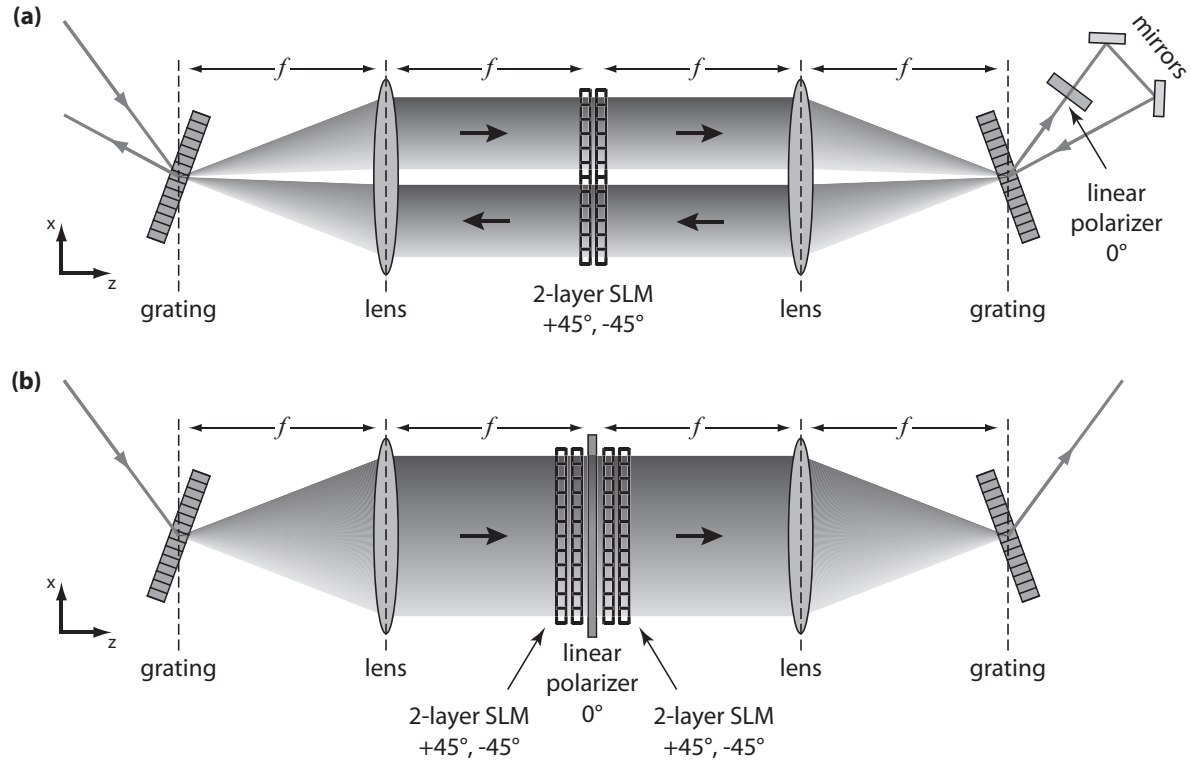

Figure 3.9 | Serial 2-layer pulse shapers. (a) Original double-pass design Ref. [133] (Lindinger group). The setup provides phase, amplitude, and limited polarization control by passing a normal $4f$ setup with a 2-layer SLM twice. On the first pass, the phase and polarization state is modulated using the upper half of the LC pixels. By using a polarizer after the first pass the polarization change is transferred into an amplitude modulation. The polarization state of this phase/amplitude modulated pulse can be changed using the lower half of the modulator in a second pass. By this, the ellipticity can manipulated, however, the control over the orientation is still limited to $\theta = 0, \pm\pi/2$ rad. (b) Simplified design using two consecutive LC SLMs [141] (Lindinger group). The shaping principle is analogous to the original design [(a)]. Instead of passing the same LC SLM twice, two LC SLMs are used. Figure following Ref. [133] [(a)] and [141] [(b)].

is therefore only capable of producing the same polarization states as the conventional phase/polarization shaper, if a single frequency is considered (see Fig. 3.5), but allows controlling the total intensity in addition. This can easily be seen by the transfer function of this serial 2-layer setup and the resulting electric field[6] for a p-polarized input pulse

$$\begin{aligned}\boldsymbol{M}_{\mathrm{PS}}^{\text{serial 2l.}}(\Delta\varphi_1^1,\Delta\varphi_2^1,\Delta\varphi_2^2,\Delta\varphi_1^2) &= \\ &= \boldsymbol{M}_{\mathrm{LC}}^{-45^\circ}(\Delta\varphi_1^2)\,\boldsymbol{M}_{\mathrm{LC}}^{45^\circ}(\Delta\varphi_2^2)\begin{pmatrix}1 & 0\\ 0 & 0\end{pmatrix}\boldsymbol{M}_{\mathrm{LC}}^{-45^\circ}(\Delta\varphi_2^1)\,\boldsymbol{M}_{\mathrm{LC}}^{45^\circ}(\Delta\varphi_1^1), \qquad (3.16)\end{aligned}$$

[6]The difference between Eq. (3.17) and Eq. (2) in Ref. [133] is due to the phase definition used in this thesis.

$$\vec{E}_{\mathrm{out}}(\omega) = \boldsymbol{M}_{\mathrm{PS}}^{\mathrm{serial\,2l.}}(\Delta\varphi_1^1,\Delta\varphi_2^1,\Delta\varphi_2^2,\Delta\varphi_1^2)\begin{pmatrix} E_{\mathrm{in}}(\omega) \\ 0 \end{pmatrix}$$

$$= E_{\mathrm{in}}(\omega)\,\mathrm{e}^{-\mathrm{i}\frac{\Delta\varphi_1^1+\Delta\varphi_2^1+\Delta\varphi_1^2+\Delta\varphi_2^2}{2}}\cos\left(\frac{\Delta\varphi_1^1-\Delta\varphi_2^1}{2}\right)\begin{pmatrix} \cos(\frac{\Delta\varphi_2^2-\Delta\varphi_1^2}{2}) \\ \mathrm{e}^{-\mathrm{i}\frac{\pi}{2}}\,\sin(\frac{\Delta\varphi_2^2-\Delta\varphi_1^2}{2}) \end{pmatrix}. \quad (3.17)$$

The subscript index i of the applied phase retardation $\Delta\varphi_i^j$ is the number of the LC SLM layer and the superscript index j is used to distinguish between the first and the second pass. For calculating $\boldsymbol{M}_{\mathrm{PS}}^{\mathrm{serial\,2l.}}$, one has to consider that even if the absolute orientation of the first and second layer is fixed in real space, their relative orientation with respect to the propagating light field changes from $+45°$ to $-45°$ for the first layer and from $-45°$ to $+45°$ for the second layer on the second pass due to the reversal of the propagation direction. The phase jumps at the ideal mirrors do not have to be considered since the pulse is p polarized at these positions. Instead of passing the same LC SLM twice, a serial setup can also be realized by placing two consecutive 2-layer SLMs, with a polarizer in between, inside a normal $4f$ setup [141] (Lindinger group). This basically adopts the idea of adding additional layers. The simplified serial setup is depicted in Fig. 3.17(b). The resulting electric field is equal to Eq. (3.17). Compared with the double pass setup, the simplified setup has the advantage that the LC SLM resolution is not halved, but the second LC SLM increases the costs of the setup significantly. It is also not possible to place both LC SLMs and the polarizer simultaneously in the Fourier plane which may have a negative effect on the shaped electric field [193].

The double pass setup was used by the Lindinger group to control the ionization of NaK [137, 243]. In contrast to only phase/amplitude shaping, the additional polarization control provided a 50 % higher ionization efficiency [137]. They also demonstrated the generation of target pulse sequences after transmission through different optical fibers using the simplified serial setup [141, 244–246].

3.4 Full vector-field control

Even if these setups – the 3-layer polarization shaper and the serial 2-layer shaper – are not capable of shaping all degrees of freedom of the vector field, they demonstrate successfully different approaches to gain more control over the electromagnetic output field and help to understand the principle of vector-field shaping. Based on these previous attempts to gain more control over the vector field, two different kinds of setups were developed to shape all four degrees of freedom. Both designs were first published by the group of Lindinger. Their first demonstrated setup is a modification of their serial 2-layer pulse shaper. Instead of passing the LC SLM twice, they included a 2-layer SLM in both arms of an interferometer and used the two halves of the LC SLM to shape two orthogonal linearly polarized beams in phase and amplitude and to recombine them to a single shaped pulse. There are different improved setups based on this principle. These interferometric setups are covered in the Section 3.4.1. The second design is based on the principle employed in the group of Silberberg to gain unlimited polarization control – adding another LC layer. In this case, not only a third, but also a fourth layer is needed

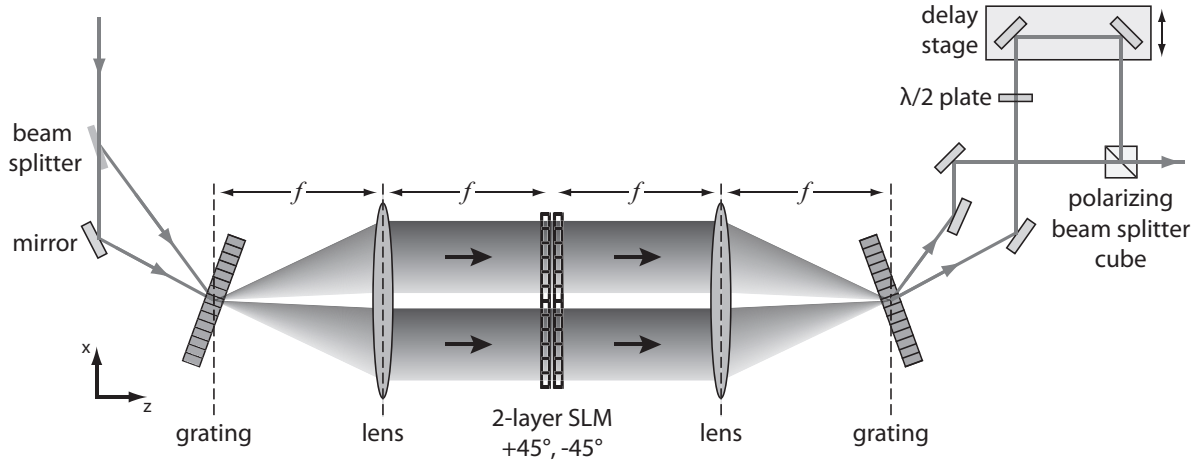

Figure 3.10 | Interferometric VFS (Lindinger group [134]). The incident pulse is splitted by a 50:50 beam splitter in two separated beams. These beams hit the grating of a $4f$ setup with two different angles of incidence and will therefore be spatially separated in the $4f$ setup. One beam can be manipulated with the left and the other with the right half of the LC SLM. Both spectral distributions will be recombined by the second grating and emitted under different exit angles. The polarization of one of these beams will be rotated by 90°. The delay between the two pulses can be adjusted by a delay stage. Both beams will be recombined to a single beam with a polarizing beam splitter cube. Figure following Ref. [134].

and, as in their simplified serial setup, there has to be a polarizer between these four layers to realize amplitude control (Section 3.4.2). Both variants, the interferometric as well as the 4-layer approach, allow complete unrestricted vector-field control.

3.4.1 Interferometric vector-field shaping

The general idea of all interferometric vector-field shapers is to shape two orthogonal polarizations in phase and amplitude and to combine these electric fields to a single pulse. All realized setups can be divided into two classes: the non-common path and the common-path setups.

Non-common-path setups

In a non-common path setup, different optics for both arms of the interferometer are used. However, some realizations employ the same modulator in both arms.

The first interferometric VFS was built by Plewicki et al. [134, 247] (Lindinger group, Fig. 3.10). A normal 50:50 beam splitter is used to generate two pulses with equal intensities. Both are directed onto the same grating of a normal $4f$ setup under two different angles of incidence. The two spectral dispersed beams are therefore spatially separated in the $4f$ setup and can be modulated with different pixel groups of the same 2-layer SLM. The polarization of one of the shaped pulses is rotated by 90° using a $\lambda/2$ plate and both beams are recombined using a polarizing beam splitter cube, to allow amplitude modulation of each beam. The optical path length between the two beams is adjusted with a delay stage. The transfer function for each beam is equivalent

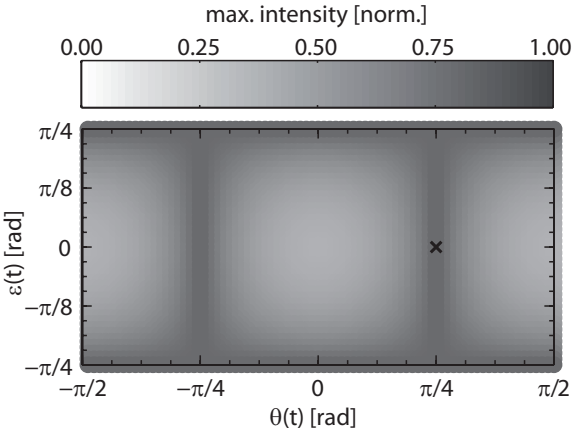

Figure 3.11 | Maximum possible intensity for all polarization states generated by an interferometric VFS. In an interferometric setup both polarizations are independently shaped in amplitude and phase. An intensity shift from one into the other polarization component is not possible, thus a manipulation of the intensity ratio is associated with a reduction of the total intensity. The maximum available intensity for each polarization state is in the range of 50–100 %.

to Eq. (3.9). The electric output field is given by the superposition of both pulses

$$\begin{aligned}\vec{E}_{\mathrm{out}}(\omega) &= \vec{E}^{1}_{\mathrm{out}}(\omega) + \vec{E}^{2}_{\mathrm{out}}(\omega) \\ &= \begin{pmatrix} 1 & 0 \\ 0 & 0 \end{pmatrix} \boldsymbol{M}^{\mathrm{2l.}}_{\mathrm{PS}}(\Delta\varphi^{1}_{1},\Delta\varphi^{1}_{2}) \begin{pmatrix} E^{1}_{\mathrm{in}}(\omega) \\ 0 \end{pmatrix} \\ &+ \begin{pmatrix} 0 & 0 \\ 0 & 1 \end{pmatrix} \boldsymbol{W}^{45^\circ}_{\lambda/2}\, \boldsymbol{M}^{\mathrm{2l.}}_{\mathrm{PS}}(\Delta\varphi^{2}_{1},\Delta\varphi^{2}_{2}) \begin{pmatrix} E^{2}_{\mathrm{in}}(\omega) \\ 0 \end{pmatrix} \\ &= \begin{pmatrix} E^{1}_{\mathrm{in}}(\omega)\, \mathrm{e}^{-\mathrm{i}\frac{\Delta\varphi^{1}_{1}+\Delta\varphi^{1}_{2}}{2}}\, \cos(\frac{\Delta\varphi^{1}_{1}-\Delta\varphi^{1}_{2}}{2}) \\ E^{2}_{\mathrm{in}}(\omega)\, \mathrm{e}^{-\mathrm{i}\frac{\Delta\varphi^{2}_{1}+\Delta\varphi^{2}_{2}}{2}}\, \cos(\frac{\Delta\varphi^{2}_{1}-\Delta\varphi^{2}_{2}}{2}) \end{pmatrix}. \end{aligned} \tag{3.18}$$

The superscript index is used for the interferometric setups to distinguish between the two shaped beams. From this equation it can be seen that the phase and amplitude of each polarization component can be independently controlled. Therefore, any intensity ratio and any relative phase between the p and s component can be generated, thus every point in the Poincaré plane can be reached [see Eq. (2.23) and Eq. (2.25) in Section 2.2]. However, there is a fundamental difference in this method of polarization shaping compared with the previous discussed 3-layer approach (Section 3.3.1). In the 3-layer approach, the amplitude is shifted from one into the other polarization component, maintaining the total intensity and changing only the amplitude ratio between the two components. This is not the case in this interferometric approach. The default amplitude ratio of both arms is 1:1. To adjust this ratio, the amplitude for one arm has to be reduced and cannot be shifted to the other polarization component. Therefore, the total intensity will also be reduced. For a circularly or linearly polarized pulse with an orientation of $\theta = \pm 45^\circ$, the amplitude does not have to be shaped and only the relative phase has to be adjusted. However, for a p or s linearly polarized pulse the whole amplitude of one arm has to be "blocked", thus lowering the total intensity to 50 %. The maximum possible intensity for all polarization states is plotted in Fig. 3.11. Beside this drawback there is another significant problem: the phase stability between the two arms of the interferometer. This is illustrated in the following example. A change of the

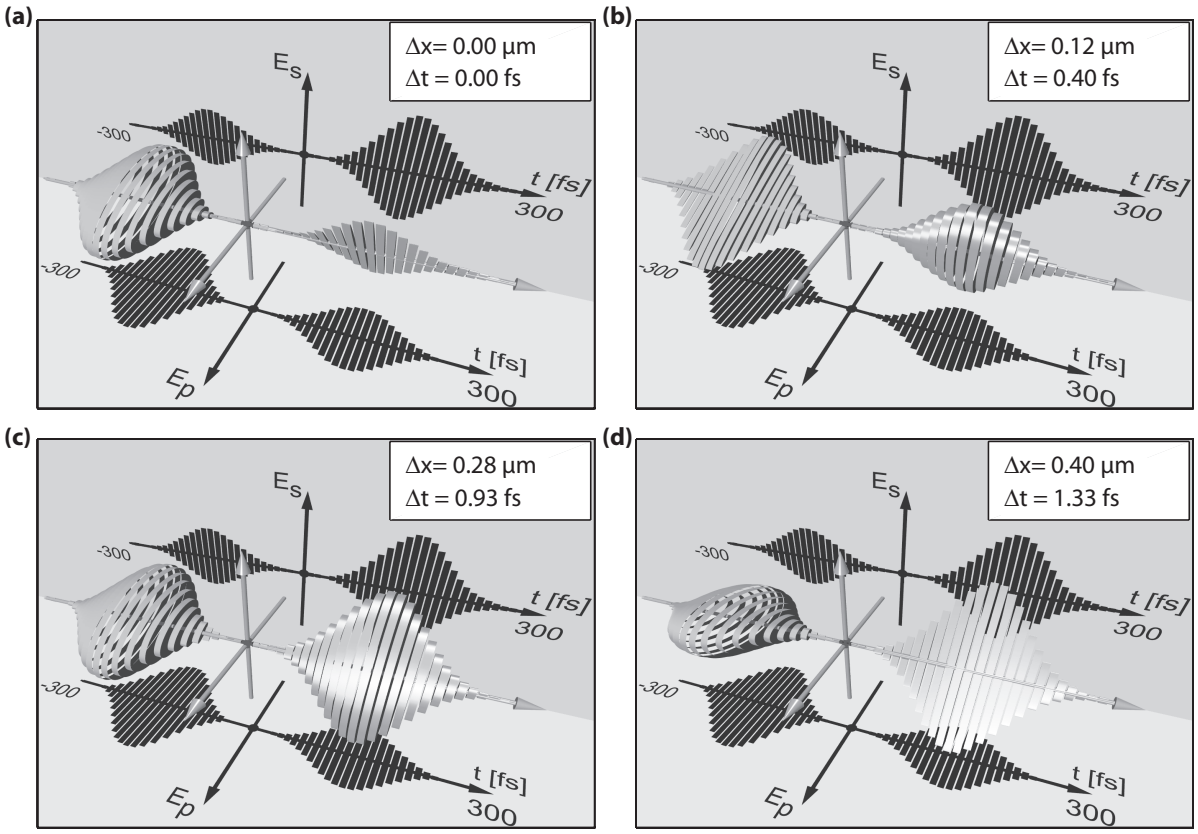

Figure 3.12 | Simulated polarization change for a temporal drift of 1.33 fs between the two orthogonal polarization components. In this pseudo 3D representation, the temporal polarization state is illustrated by cylinders with respective orientations and ellipticities. The amplitudes of the two polarization components are indicated by the shadows of the pulse. (a) A double pulse sequence without temporal drift is considered. The first pulse is elliptically and the second almost linearly polarized. (b–d) Pulse shape after a temporal drift of the s component of the pulse with respect to the p component. In all three cases the movement of the temporal envelope is barely noticeable, but the relative phase drift cause a clear change in the polarization state.

optical path difference between the two arms of 40 µm causes a temporal drift between the two polarizations of only 1.33 fs. The change in the envelope and thus the change in the temporal amplitude of a 100 fs pulse could be neglected, but not the resulting phase shift between the p and s component. The change of the polarization state due to this drift is depicted in Fig. 3.12. A difference of $\lambda/2$ in the path length already introduces a phase shift of π between the two polarization components and thus an inversion of the sign of ϵ and θ [see Eq. (2.23)–(2.25)]. This demonstrates, how crucial the phase stability between the two arms for polarization shaping is. The authors of Ref. [134] measured the intensity of the sum-frequency signal generated by the projection of both polarizations onto the optical axis of the nonlinear crystal to test the phase stability of the setup. They reported a fluctuation of the intensity of up to ±17 % over 14 minutes and suggested an active stabilization for longer measurements.

A similar setup using an acousto-optical modulator instead of an LC SLM was built

by Middleton et al. [139] (Zanni group) to generate polarization shaped pulses in the mid-IR. To stabilize their setup, they measured the relative phase drift between the two arms of the interferometer by observing the interference between the polarization components with a single channel detector. By applying the inverted relative phase to the AOM a long term stability of $\lambda/10$ over 3 hours was achieved. With this method, only the phase drift and not the actual temporal drift of the envelope was measured, hence requiring that the temporal fluctuations are small compared to the pulse duration. They demonstrated the application of vector-field shaping for 2D IR spectroscopy [139] and for the control of the vibrational excitation of $Mn(CO)_5Br$ [138]. An enhancement by polarization shaping of 150–230 % compared with phase-only shaping was reported [138].

Compensating the actual temporal drift of the envelope and not only the phase drift was demonstrated by Sato and coworkers [248] (Misawa group). Their setup is equivalent to the setup of Plewicki et al. (see Fig. 3.18) and also employs a 2-layer SLM. It is stabilized using a piezoelectric actuator to adjust the path length of one of the interferometer arms in a control feedback loop. Two monochromatic beams, generated from a single laser diode, propagate parallel to the laser beam in both arms of the interferometer. The interference of these two monochromatic waves was used as feedback signal. Measurements of the relative phase drift showed a change of about 5.2 rad after one hour for the unstabilized setup. With active stabilization, a standard deviation of the relative phase of 40 mrad over an hour and 70 mrad over 90 seconds was achieved. This corresponds to a stability of $\lambda/157$ (1 hour) and $\lambda/90$ (90 seconds) at 800 nm. This highlights the importance of active stabilization for non-common path setups.

The highest stability of an active stabilized interferometric VFS was recently published by Tyagi et al. [249] (Kambhampati group). Instead of an LC SLM, two acousto-optic programmable dispersive filters (AOPDFs) were used in the arms of an interferometer. AOPDFs shape the pulse not in the frequency domain, but directly in the time domain, making the conventional $4f$ setups obsolete and allowing compact and simple setups. The reduction of optical elements also diminishes stability issues. Employing an active stabilization, a very high phase stability of $\lambda/314$ over one hour at 630 nm was achieved. The stabilization was realized by measuring the interference between the two arms and applying the inverted relative phase drift to the AOPDFs. The setup was used for two-color 2D spectroscopy.

The concept of using different devices in the two arms of the interferometer was before employed by Seidel et al. [250, 251] (Tan group). They used two separated LC SLMs in the arms of the interferometer and an optical parametric amplifier (OPA) [252] in one arm to shape an 800 nm and an NIR/VIS pulse in phase and amplitude. By mixing these pulses in two non-linear crystals, the generation of phase, amplitude, and polarization shaped laser pulses in the mid-IR/UV was demonstrated.

Common-path setups

Actively stabilized non-common path setups are applicable for long-term measurements. However, this requires additional optics or mechanical elements and an active monitoring of the phase drift. By employing a common path setup, these stability issues can in principle be avoided and active stabilization should not be required. The first

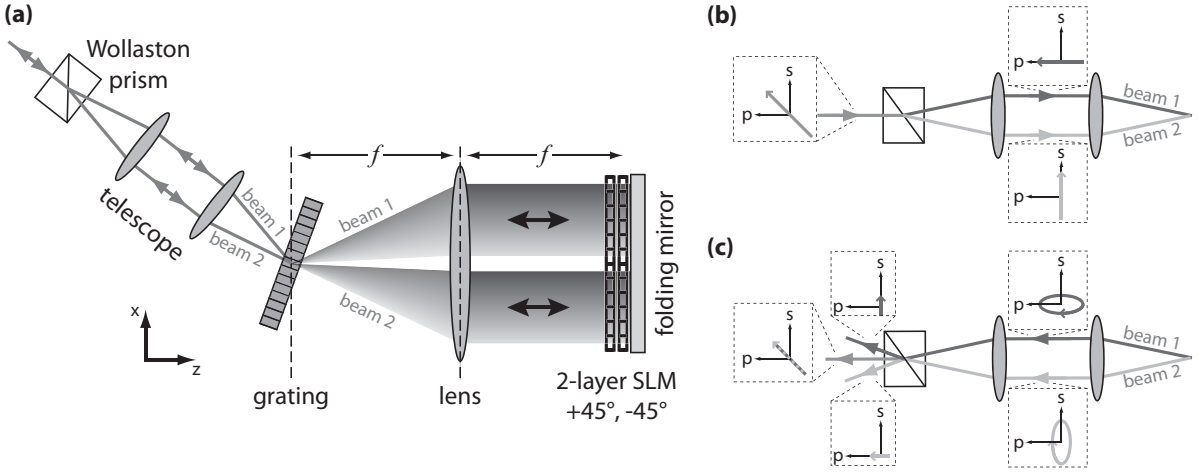

Figure 3.13 | Interferometric common-path VFS (Feurer group [135]). (a) The Wollaston prism emits the two polarization components of the incident laser pulse under two different exit angles. A telescope maps these angles onto the grating of a folded $4f$ setup. Both beams are spatially separated and can be shaped with different pixel groups of the 2-layer SLM. The folding mirror reverses the beam paths. The back-going beam can be separated from the incident beam by changing the beam height with the folding mirror. Both beams propagate over the same optics. Therefore, a common path setup is formed. (b) Wollaston prism as polarizing beam splitter. The incoming laser pulse is linearly polarized orientated under 45° (see inset). The Wollaston prism splits the incoming laser beam into two beams with orthogonal polarizations. (c) Wollaston prism as polarizing beam recombiner. The polarization state of the back-going beam can be altered by the SLM, in this case to slightly elliptical. The undesired polarization components are emitted in different directions at the Wollaston prism and only the p component of beam 1 and the s component of beam 2 form the outgoing pulse, which is in this case also linearly polarized orientated under 45°, but with a smaller amplitude compared to the incident pulse. Figure following Ref. [135].

interferometric common-path VFS was built by Ninck et al. [135] (Feurer group). Their setup is shown in Fig. 3.13(a). The incident laser pulse is separated in two orthogonal linearly polarized pulses by a Wollaston prism[7] [Fig. 3.13(b)]. Both are directed with two different angles of incident onto a grating using a telescope and shaped in a folded $4f$ setup with different pixel groups of a 2-layer SLM. The beams are back reflected from the folding mirror behind the SLM and pass all elements of the setup a second time. The Wollaston prism serves as a polarizing beam combiner for the back-going beam, as depicted in Fig. 3.13(c). The Wollaston prism directs the undesired polarization component of the back-going beams in different directions, thus transferring the polarization modulation introduced by the SLM into an amplitude modulation similar to the linear polarizer used in a conventional phase/amplitude shaper. Only the desired components of both beams are recombined in the direction of the incident beam. By introducing a slight tilt in the beam height using the folding mirror, the outgoing and the incoming beam can be separated. Since both beams propagate over the same optics, but at different positions, a (near) common-path setup is formed. The transfer matrix of the

[7]The Wollaston prism is described in Section 4.2.1.

folded $4f$ setup is slightly different from the one of the non-folded setup [see Eq. (3.9)]. One has to consider the phase jump of π at the mirror and the change of the relative orientation of the LC molecules with respect to the light field because of the change in propagation direction. The transfer matrix for one beam is given by

$$\begin{aligned}\boldsymbol{M}_{\mathrm{PS}}^{\text{folded 2l.}}(\Delta\varphi_1,\Delta\varphi_2) = \\ = \boldsymbol{M}_{\mathrm{LC}}^{-45^\circ}(\Delta\varphi_1)\,\boldsymbol{M}_{\mathrm{LC}}^{45^\circ}(\Delta\varphi_2)\begin{pmatrix}1 & 0\\ 0 & -1\end{pmatrix}\boldsymbol{M}_{\mathrm{LC}}^{-45^\circ}(\Delta\varphi_2)\,\boldsymbol{M}_{\mathrm{LC}}^{45^\circ}(\Delta\varphi_1).\end{aligned} \tag{3.19}$$

Comparing Eq. (3.9) and Eq. (3.19) shows that passing the LC SLM twice, doubles the introduced phase, but does not alter its function. Therefore, the resulting electric field is equivalent to Eq. (3.18)

$$\begin{aligned}\vec{E}_{\mathrm{out}}(\omega) &= \vec{E}^1_{\mathrm{out}}(\omega) + \vec{E}^2_{\mathrm{out}}(\omega)\\ &= \begin{pmatrix}1 & 0\\ 0 & 0\end{pmatrix}\boldsymbol{M}_{\mathrm{PS}}^{\text{folded 2l.}}(\Delta\varphi^1_1,\Delta\varphi^1_2)\begin{pmatrix}E^1_{\mathrm{in}}(\omega)\\ 0\end{pmatrix}\\ &+ \begin{pmatrix}0 & 0\\ 0 & 1\end{pmatrix}\boldsymbol{M}_{\mathrm{PS}}^{\text{folded 2l.}}(\Delta\varphi^2_1,\Delta\varphi^2_2)\begin{pmatrix}0\\ E^2_{\mathrm{in}}(\omega)\end{pmatrix}\\ &= \begin{pmatrix}E^1_{\mathrm{in}}(\omega)\,\mathrm{e}^{-\mathrm{i}\left(\Delta\varphi^1_1+\Delta\varphi^1_2\right)}\,\cos(\Delta\varphi^1_1-\Delta\varphi^1_2)\\ \mathrm{e}^{-\mathrm{i}\pi}\,E^2_{\mathrm{in}}(\omega)\,\mathrm{e}^{-\mathrm{i}\left(\Delta\varphi^2_1+\Delta\varphi^2_2\right)}\,\cos(\Delta\varphi^2_1-\Delta\varphi^2_2)\end{pmatrix}.\end{aligned} \tag{3.20}$$

The difference of π in the phase of the s component is due to the change in propagation direction compared to the setup in Fig. 3.10. The advantage of this folded geometry is not only that the introduceable phase is doubled, but also that less optics are needed and a more compact setup can be built. This interferometric common-path VFS was copied by Chen and coworkers to realize polarization line-by-line shaping [253].

Masihzadeh et al. [254] developed a similar setup for the short-wavelength IR regime. They also use a Wollaston prism for beam splitting and recombining and a telescope to employ a common-path geometry. However, their $4f$ setup contains a prism instead of a grating and a high-resolution single-layer LC SLM with 12288 pixels is employed. Amplitude shaping is realized by applying a rapid phase oscillation [255]. Besides the use of these different optical elements, there is no significant difference in the functional principle of this setup compared to the design of Ninck et al. [135].

A different design for a common-path VFS was suggested by Kupka et al. [256] (Bartels group). Their setup was a proof of concept and only phase shaping of two orthogonal polarizations using a 1-layer SLM with 640 pixels was demonstrated. However, this is not a general limitation of the setup and by employing a 2-layer SLM or a high-resolution single-layer LC SLM all four degrees of freedom could be shaped. Furthermore, it is based on the original design by Ninck and thus discussed in this section. To simplify the setup of Ninck, the Wollaston prism, the telescope, and the grating are replaced by a single birefringent prism (Fig. 3.14). The birefringent prism spatially

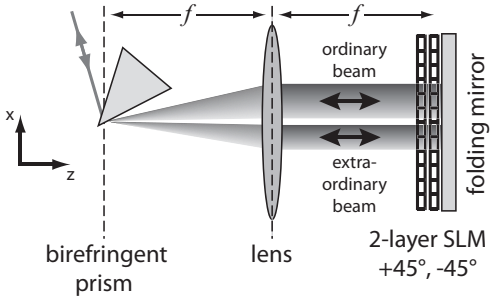

Figure 3.14 | Interferometric common-path VFS using a polarizing prism (Bartels group [256]). The incoming laser pulse gets spatially dispersed by a birefringent prism. Due to the difference in the ordinary and extraordinary refractive index of the birefringent prism, the incident laser pulse will be spatially separated in two perpendicular polarized frequency distributions, which can be independently shaped with different pixel groups of the LC SLM. The birefringent prism also acts as a linear polarizer for the back-going beams, transferring the polarization modulation introduced by the SLM into an amplitude modulation. Figure following Ref. [256].

separates the two polarization components of the incident pulse due to the different refractive indices for the ordinary and extraordinary polarization components. It acts also as a beam recombiner and polarizer, similar to the Wollaston prism, by directing the undesired polarization components of the two beams in other directions. Employing a 2-layer SLM, the outgoing electric field would be equal to Eq. (3.20). The authors state that the properties of the prism (e.g., the material, the prism geometry, the angle of the optical axis, and the angle of incidence) have to be carefully chosen [256], in order to support the wanted bandwidth without spatial overlap of the two polarizations. The used prism supports a spectral bandwidth of 100 nm. However, both polarizations cover only 110 and 130 pixels of the 640-pixel LC SLM [256], thus exhibiting a different spectral bandwidth passing a single pixel and a low sampling of the applied phases. The differing spectral bandwidths have a critical consequence for the setup considering the shaping window. Given that the shaping windows are different for the two polarizations, the delay-dependent amplitude reduction will also be different. This results in a delay-dependent change of the amplitude ratio between the p and s component and thus in a delay-dependent change of the polarization state. This effect must be compensated by introducing a delay-dependent amplitude modulation when, e.g., multipulse sequences are generated.

The stability of a common-path VFS should in general be superior to the stability of non-common-path setups, but was not reported for the presented setups. One drawback is that common-path setups suffer from a lack of flexibility and the implementation is not as straightforward as for non-common-path setups.

3.4.2 4-layer vector-field shaping

In contrast to the interferometric design, the multilayer approach shapes a single beam directly in all four degrees of freedom. Extending the principle employed by Polachek et al. [132] to gain control of any polarization state by adding a third layer, Plewicki and coworkers (Lindinger group) suggested to add a fourth layer and to sandwich a polarizer inside the LC SLM to shape a single laser beam directly in phase, amplitude

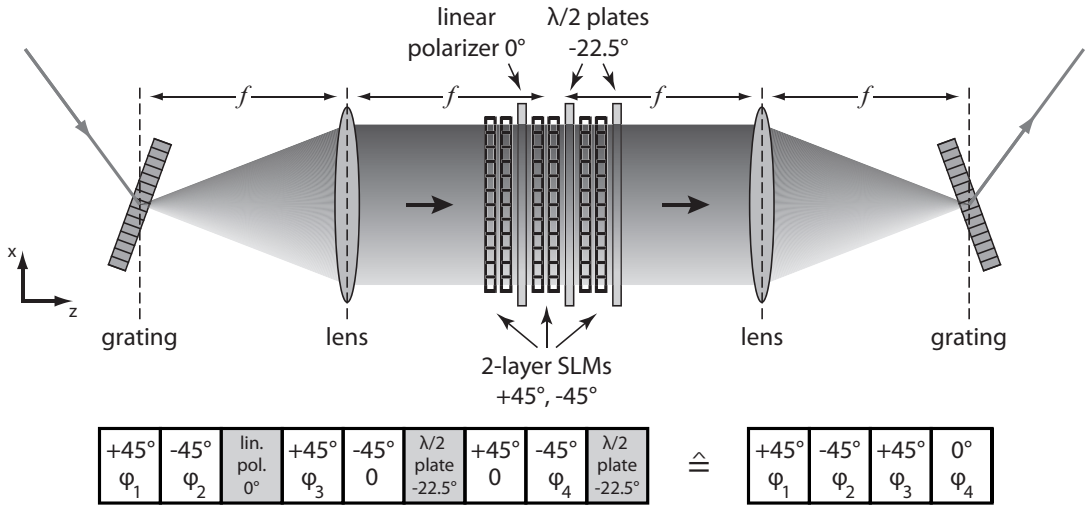

Figure 3.15 | "4-layer VFS" using three LC SLMs. To substitute a real 4-layer SLM, three consecutive LC SLMs are used. The first LC SLM in conjunction with polarizer allows control of the phase and amplitude. From the second and third LC SLM only one layer is used. The relative intensity between the p and s component can be controlled with the second LC SLM and the relative phase with the third LC SLM. The $\lambda/2$ plates are employed to "change" the orientation of the modulation axes of the third LC SLM. The orientations of the used modulation axes for the whole arrangement are $+45°$, $-45°$, $+45°$, and $0°$. Figure following Ref. [136].

and polarization [133]. Weise and Lindinger demonstrated this idea by using three consecutive 2-layer SLMs in a single $4f$ setup [136, 257] as depicted in Fig. 3.15. The first 2-layer SLM (layer 1 & 2) and the polarizer function as a normal phase/amplitude shaper. From the second LC SLM (layer 3 & 4) only one layer is used to shift amplitude from the p polarization component into the s component and to generate a certain amplitude ratio without changing the total intensity [see Eq. (3.7)]. The phase introduced by the third layer can be compensated by adjusting the phase of the first and second layer. The third LC SLM (layer 5 & 6) and both $\lambda/2$ plates "simulate" an orientation of $0°$ and $90°$ of the modulation axes of layer 5 and 6. By adjusting the phase of layer 5 or 6 (the respective other is unused), the relative phase between the p and s polarization of the laser pulse can be adjusted to reach every point in the Poincaré plane (see Fig. 3.7). This can also be seen from the Jones matrix and the resulting electric field for a p polarized input field

$$\begin{aligned}\boldsymbol{M}^{4\mathrm{l.}}_{\mathrm{VFS}}(\Delta\varphi_1,\Delta\varphi_2,\Delta\varphi_3,\Delta\varphi_4) &= \boldsymbol{W}_{\lambda/2}(-22.5°)\,\boldsymbol{M}^{-45°}_{\mathrm{LC}}(\Delta\varphi_4)\,\boldsymbol{M}^{45°}_{\mathrm{LC}}(0)\,\boldsymbol{W}_{\lambda/2}(-22.5°)\\ &\quad \boldsymbol{M}^{-45°}_{\mathrm{LC}}(0)\,\boldsymbol{M}^{45°}_{\mathrm{LC}}(\Delta\varphi_3)\begin{pmatrix}1 & 0\\ 0 & 0\end{pmatrix}\boldsymbol{M}^{-45°}_{\mathrm{LC}}(\Delta\varphi_2)\,\boldsymbol{M}^{45°}_{\mathrm{LC}}(\Delta\varphi_1)\\ &= \boldsymbol{M}^{0°}_{\mathrm{LC}}(\Delta\varphi_4)\,\boldsymbol{M}^{45°}_{\mathrm{LC}}(\Delta\varphi_3)\begin{pmatrix}1 & 0\\ 0 & 0\end{pmatrix}\boldsymbol{M}^{-45°}_{\mathrm{LC}}(\Delta\varphi_2)\,\boldsymbol{M}^{45°}_{\mathrm{LC}}(\Delta\varphi_1),\end{aligned} \tag{3.21}$$

$$\vec{E}_{\mathrm{out}}(\omega) = \boldsymbol{M}^{4\mathrm{l.}}_{\mathrm{VFS}}(\Delta\varphi_1,\Delta\varphi_2,\Delta\varphi_3,\Delta\varphi_4) \begin{pmatrix} E_{\mathrm{in}}(\omega) \\ 0 \end{pmatrix}$$

$$= E_{\mathrm{in}}(\omega)\, \mathrm{e}^{-\mathrm{i}\frac{\Delta\varphi_1+\Delta\varphi_2+\Delta\varphi_3}{2}} \cos\left(\frac{\Delta\varphi_1-\Delta\varphi_2}{2}\right) \begin{pmatrix} \mathrm{e}^{-\mathrm{i}\Delta\varphi_4}\, \cos(\frac{\Delta\varphi_3}{2}) \\ \mathrm{e}^{-\mathrm{i}\frac{\pi}{2}}\, \sin(\frac{\Delta\varphi_3}{2}) \end{pmatrix}. \qquad (3.22)$$

Compared with the interferometric common-path setups, a 4-layer VFS cannot be designed using a folded $4f$ geometry since the layer arrangement implies a certain propagation direction. Therefore, 4-layer VFS setups cannot be built as compact as folded interferometric setups, but they have the advantage that the total intensity is not influenced by the generated polarization state and that it is inherently phase stable. The realization of such a setup using a single 4-layer SLM is of high interest. A conventional non-folded 2-layer pulse shaper could be simply transformed into a VFS by replacing the SLM, but the required 4-layer SLM is commercially not available. Miao and coworker [258] reported the use of a custom-made four-layer LC SLM with the modulation axes oriented under 0°, 45°, 0°, and 90° without a sandwiched polarizer. Therefore, this LC SLM is not suited to be used in a VFS, but shows that fabrication of such a device is in principle possible. However, it must be considered that the optical anisotropy $\Delta n(\omega,U,T)$ of the LC molecules is temperature dependent. Absorption of light by the polarizer could cause a temperature change of the LC molecules and this would result in phase distortions dependent on the applied amplitude modulation, thus it is questionable if a 4-layer SLM with a sandwiched polarizer can be used without undesired side effects. Besides the high costs, a 4-layer SLM substituted with multiple separated SLMs has the disadvantage that the whole arrangement cannot be fitted in the Fourier plane of the $4f$ setup. This reduces the spectral resolution since the spot size of the single frequency components vary during the propagating through the three LC SLMs. However, the authors state that their modulator arrangement is 51 mm thick and that their shaping resolution is not significantly reduced. However, they do not discuss in detail how the spatial–temporal profile of the pulse is affected by the displacement from the Fourier plane. Wefers and Nelson discuss in Ref. [193] the effect on the space–time profile if a single-layer LC SLM is displaced from the Fourier plane. In this case, not only a transversal shift of the beam profile, but also a shift in the propagation direction occurs if the pulse is delayed in time. They describe also the effect for a dual-layer setup if the two LC layers are separated in space so that diffraction effects between both layers can arise. They state that it is in general not true that the modulation function of all layers can be simply calculated by the product of the transfer functions of each individual layer. Whether the modulation function is given or can at least be approximated by the product of the individual transfer functions depends on the orientation of the modulation axes and the actual alignment of the individual layers. Simulations showed that this is the case for two closely placed, perfectly aligned layers with orthogonal modulation axes. However, if these two layers are separated by 30 mm pronounced "temporal noise" (time-dependent amplitude smaller than 5 % along the temporal axis) is generated. The actual magnitude of these effects for the presented or similar setups cannot be easily deduced, but should kept in mind, if building of such a vector-field shaper is considered.

Table 3.1 | Overview over the conventional and the extended pulse shaper setups.

Setup	Degrees of freedom	$\boldsymbol{E}_{\mathbf{out}}$	Notes
Conventional PS			
[39] 2-layer SLM	Phase, amplitude	Eq. (3.11)	With polarizer
[42] 2-layer SLM	Phase, ellipticity, limited orientation	Eq. (3.10)	Without polarizer
Extended PS			
[132] 3-layer SLM	Phase, ellipticity, orientation	Eq. (3.13)	$8f$-setup with two separated LC SLMs
[241] 2D LC SLM	Phase, ellipticity, orientation	Eq. (3.15)	Three interactions with single 2D LC SLM
[133] Serial 2-layer SLM	Phase, amplitude, ellipticity, limited orientation	Eq. (3.17)	Passing same 2-layer PS twice; Polarizer after first pass
[141] Simplified serial 2-layer SLM	Phase, amplitude, ellipticity, limited orientation	Eq. (3.17)	Two consecutive LC SLMs in same $4f$ setup; Polarizer between SLMs

The Lindinger Group demonstrated the application of their substituted 4-layer VFS by generating arbitrary polarized laser pulses after transmission through a fiber [142]. This extended their previous experiments using the simplified serial 2-layer pulse shaper.

3.5 Summary

The design of our vector-field shaper, presented in the following chapter, is based on the considerations discussed in this chapter. First, the principles of frequency domain pulse shaping using a liquid-crystal spatial light modulator (LC SLM) were explained. In addition, the effects of the pixelation of the LC SLM and the finite beam size of each spectral component on the shaped pulse in time domain were discussed. Subsequent, the shaping capabilities of the common conventional dual-layer pulse shaper were derived and its applications were reviewed. With this setup, either the phase and amplitude or the phase and polarization can be controlled. Accessible orientations are, however, limited to $\theta = 0, \pm\pi/2$ rad. Given these limitations, the shaping capabilities, advantages, and disadvantages of various advanced pulse shaper designs were discussed.

Two approaches were introduced being capable of controlling three out of the four possible degrees of freedom: phase, amplitude, orientation, and ellipticity. The first approach uses three LC layers for phase modulation and unrestricted polarization control. The second approach demonstrated phase, amplitude, and the same limited polarization control as the conventional polarization shaper. The conventional dual-layer and these extended pulse shapers are listed in Tab. 3.1. Based on these extended pulse shapers,

so-called vector-field shapers were developed. The existing setups, which are able to manipulate all four degrees of freedom independently were reviewed and compared in the last section of this chapter and are summarized in Tab. 3.2. Unrestricted vector-field shaping can be achieved by using four LC layers with a sandwiched polarizer to manipulate a single pulse directly or by shaping two orthogonal polarized pulses individually in amplitude and phase in the two arms of an interferometer and by recombining them interferometrically to a single shaped pulse.

The demonstrated applications of the extended and the full vector-field shapers are very promising in the field of ultrafast spectroscopy, coherent control, microscopy, and endoscopy and inspired the development of the setup presented in this thesis with the goal to create multipulse sequences with high fidelity for multidimensional spectroscopy.

Table 3.2 | Overview over different realizations of vector-field shaping. All the listed setups are capable of manipulating all four degrees of freedom: phase, amplitude, orientation and ellipticity. Ordered by publication date.

Setup		Workgroup	E_{out}	Stability	Notes
Vector-field shaper					
[134]	Interferometric 1x 2-layer SLM	Lindinger (2006)	Eq. (3.18)	n/a	Non-common path; Not stabilized
[135]	Interferometric 1x 2-layer SLM	Feurer (2007)	Eq. (3.20)	n/a	Common path; Wollaston prism for polarization splitting and recombination; Grating based $4f$ setup
[254]	Interferometric 1x 1-layer SLM	Bartels (2007)	Eq. (3.20)	n/a	Common path; Wollaston prism; Prism instead of grating; High-resolution LC SLM
[136]	4-layer SLM	Lindinger (2009)	Eq. (3.22)	∞	Inherently phase stable; Max. intensity not polarization dependent; Three 2-layer SLMs used to substitute a single 4-layer SLM
[256]	Interferometric 1x 1-layer SLM	Bartels (2009)	Eq. (3.20)	n/a	Common path; Wollaston prism, telescope and grating replayed by birefringent prism; Proof of concept: vector-field shaping requires a 2-layer SLM or a high-resolution 1-layer SLM
[139]	Interferometric 1x AOM	Zanni (2009)	Eq. (3.18)	$\lambda/10$ (3 h)	Non-common path; Stabilized using the pulse shaper[8]
[248]	Interferometric 1x 2-layer SLM	Misawa (2009)	Eq. (3.18)	$\lambda/157$ (1 h) $\lambda/90$ (90 s)	Non-common path; Stabilized by piezoelectric actuator[9]
[249]	Interferometric 2x AOPDFs	Kambhampati (2013)	Eq. (3.18)	$\lambda/314$ (1 h)	Non-common path; Separated devices in both arms; Time-domain shaping; Stabilized by AOPDF[8]

[8]Feedback for stabilization: intensity of the interference between the p and s component of the generated pulse.
[9]Feedback for stabilization: intensity of the interference between the p and s component of an additional laser diode.

4 Design of the vector-field shaper

In the previous chapter, various setups which provide an unrestricted control over the vector field of an ultrashort laser pulse were discussed. All these setups have different advantages and disadvantages and no design is clearly superior compared to the others. The approach of shaping a single beam directly in phase, amplitude and polarization is very promising mainly due to its inherent phase stability. However, the required 4-layer SLM is not commercially available and the substitution of a 4-layer SLM by three 2-layer SLMs is expensive and may have a negative impact on the space-time profile of the shaped laser pulse (see Section 3.4.2). Therefore, we decided to use the concept of shaping two perpendicularly polarized pulses in an interferometer and to recombine them to a single polarization-shaped beam (see Section 3.4.1). To avoid stability issues and to utilize a single 2-layer SLM, a common-path geometry was chosen. This has also the advantage that a folded geometry can be employed to achieve a compact and robust setup, which can be used in different laboratories.

The two major designs for an interferometric common-path vector-field shaper (VFS) were developed by Ninck et al. [135] and Kupka et al. [256]. The difference between these two setups is that in the former a Wollaston prism and a telescope are used to direct two beams with orthogonal polarizations under different angles of incidence onto the grating of a $4f$ setup and in the latter all these elements (including the grating of the $4f$ setup) are replaced by a single birefringent prism. However, to improve the shaping capabilities of the setup, the optimization of the frequency distribution across the SLM pixels is crucial. The sampling points in frequency domain, the shaping window, and the temporal separation of the replica pulses are given by this distribution (see Section 3.1.2). Prism-based designs do not offer enough degrees of freedom to achieve an optimal frequency distribution for the two orthogonally polarized beams simultaneously. For this reason, a grating-based setup was preferred.

Numerical calculations were employed to find the necessary parameters of the optical elements used in the $4f$ setup in order to optimize the frequency distribution for both polarization components on the SLM (Section 4.1). The generation and recombination of these polarization components is essential for the performance of the setup. Two options are presented: a Wollaston prism (Section 4.2.1) and a thin film polarizer (TFP) (Section 4.2.2). A telescope combines the $4f$ setup and the polarizing beam splitter/combiner to a common-path setup. To determine the required parameters of the lenses and to investigate its influence on the beam profile, ray tracing was utilized (Section 4.3). The chapter concludes with an overview of the complete setup (Section 4.4) and a brief summary of possible improvements (Section 4.5).

The work presented in this chapter was partly done in collaboration with Ole Hüter and Fabian Ebert. Some preliminary results are given in their respective diploma theses [259, 260]. The final results as presented in this thesis are partly published in Ref. [1].

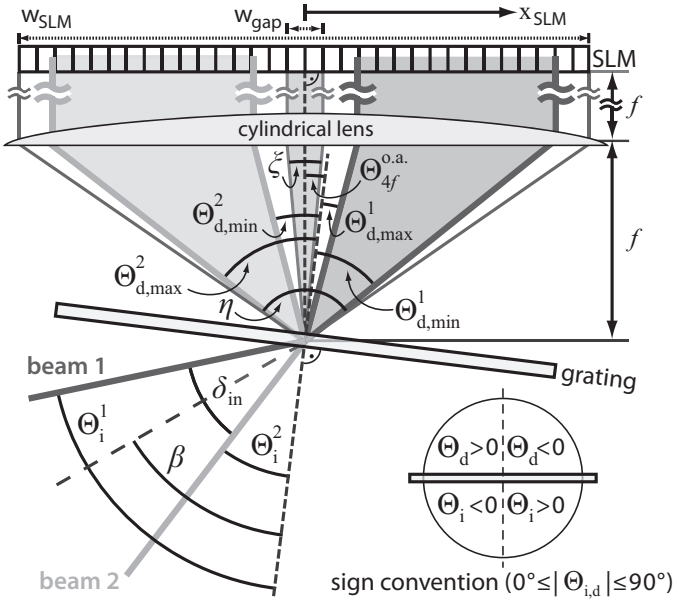

Figure 4.1 | Design parameters of the setup. Definitions of all relevant quantities for calculating the optimal set of parameters of the setup (see text for detailed explanation). Two beams [beam 1 (dark gray), beam 2 (light gray)] hit the grating of a $4f$ setup under two different angles of incidence Θ_i^1 and Θ_i^2. Their diffracted spectral components are collimated by a cylindrical lens and mapped onto the pixels of the spatial light modulator. Figure modified from Ref. [1] © (2015) Optical Society of America.

4.1 Numerical calculations of the $4f$ setup

In the presented interferometric common-path setup, two orthogonally polarized beams are modulated by different pixel segments of the same 2-layer SLM, as sketched in Fig. 4.1. The spatial separation of the two beams is obtained by using two different angles of incidence onto the grating of the $4f$ setup. The grating disperses both beams into their spectral components, which are parallelized and focused at the SLM by a cylindrical lens. To avoid a delay-dependent change of the polarization state due to the amplitude reduction caused by the shaping window, the spectral bandwidth passing a single pixel should be the same for the two beams (see Section 3.1.2 and 3.4.1). This is approximately achieved if both frequency distributions span the same amount of pixels (goal 1). In addition, the two frequency distributions should span as many pixels as possible (goal 2) without any spatial overlap (goal 3), to achieve a high number of sampling points in the frequency domain. The parameters of the $4f$ setup have to be carefully chosen to meet these three criteria.

The first parameter of the pulse shaper which has to be determined is the focal length f of the cylindrical lens within the $4f$ setup. A cylindrical lens focuses the frequency components only in the direction of the pixel array and not along the pixel height. A cylindrical optic rather than a spherical one is used to avoid damaging the SLM due to high intensities in the focus. Instead of a cylindrical mirror in combination with a folding mirror, a single cylindrical lens was chosen to reduce the number of optical elements where the two beams are spatially separated, for improved interferometric stability. The

focal length f is independent of all other setup parameters and only depends on the used beam radius within the $4f$ setup. The maximum beam radius w is limited by the pixel height of the LC pixels (in our case 10 mm) to avoid clipping at the SLM. Considering a Gaussian beam profile, the beam radius should be smaller than $w = 2.57$ mm (defined by $1/e^2$ of the intensity) so that 99.99 % of the intensity passes the SLM (see Section 2.3). The temporal shaping window of the pulse shaper is not only given by the frequency distribution, but also influenced by the spot size of the spectral components at the SLM pixels [195]. As a rule of thumb, the spot size should be smaller than one third of the pixel width (in our case 97 µm) to avoid narrowing of the shaping window due to the focus size (see Section 3.1.2, Fig. 3.3). To reach this value, a cylindrical lens with a focal length of $f = 250$ mm is used, which results in a spot size $w_0 < 27$ µm along the SLM pixels for an input radius of $w = 2.57$ mm.

All other parameters of the $4f$ setup depend on each other given that the spectral distribution is a function of the grating frequency g and of the angles of incidence onto the grating of both beams $\Theta_\mathrm{i}^1, \Theta_\mathrm{i}^2$. The optimal set of parameters can be found by numeric calculations. Figure 4.1 shows the relevant parameters for these calculations. The two different angles of incidence Θ_i^1 and Θ_i^2 can be substituted by the parameters β and δ_in,

$$\Theta_\mathrm{i}^1 = \beta - \delta_\mathrm{in}/2, \tag{4.1}$$

$$\Theta_\mathrm{i}^2 = \beta + \delta_\mathrm{in}/2, \tag{4.2}$$

$$\delta_\mathrm{in} = \Theta_\mathrm{i}^2 - \Theta_\mathrm{i}^1, \tag{4.3}$$

where β is the angle between the grating normal and the angle bisector of Θ_i^1 and Θ_i^2. δ_in is the difference angle between Θ_i^2 and Θ_i^1, called separation angle. The angles are positive if they are directed counterclockwise with respect to the grating surface normal, otherwise negative (see inset of Fig. 4.1).

The two beams are dispersed by the grating. The angles of diffraction $\Theta_\mathrm{d}^{1,2}$ are given by

$$\Theta_\mathrm{d}^{1,2}(\lambda) = \arcsin\left(gm\lambda + \sin\Theta_\mathrm{i}^{1,2}\right). \tag{4.4}$$

These angles depend on the wavelength λ, the grating frequency g, the order of diffraction m, and the angle of incidence $\Theta_\mathrm{i}^{1,2}$. The edges of the frequency distribution ($\Theta_{\mathrm{d,\,min}}^{1,2}$ and $\Theta_{\mathrm{d,\,max}}^{1,2}$) are given by the minimal and maximal used wavelength:

$$\Theta_{\mathrm{d,\,min}}^1 = \Theta_\mathrm{d}^1(\lambda_\mathrm{min}), \qquad \Theta_{\mathrm{d,\,max}}^1 = \Theta_\mathrm{d}^1(\lambda_\mathrm{max}), \tag{4.5}$$

$$\Theta_{\mathrm{d,\,min}}^2 = \Theta_\mathrm{d}^2(\lambda_\mathrm{min}), \qquad \Theta_{\mathrm{d,\,max}}^2 = \Theta_\mathrm{d}^2(\lambda_\mathrm{max}). \tag{4.6}$$

The angle of aperture η of the complete SLM pixel array is given by the width w_SLM of the pixel array and the focal length of the cylindrical lens f:

$$\eta = 2\arctan\left(\frac{w_\mathrm{SLM}}{2f}\right). \tag{4.7}$$

To avoid a spatial overlap of the spectral components of both beams there should be a distinct gap w_{gap} between both spectral distributions. The angle of aperture ξ of this gap is given by

$$\xi = 2 \arctan\left(\frac{w_{\mathrm{gap}}}{2f}\right). \tag{4.8}$$

The cylindrical lens and the center of the SLM should be placed in such a way that the angle of the optical axis of the $4f$ setup $\Theta_{4f}^{\mathrm{o.a.}}$ with respect to the grating normal matches the angle bisector of the inner angles of diffraction $\Theta_{\mathrm{d,\,max}}^{1}$ and $\Theta_{\mathrm{d,\,min}}^{2}$:

$$\Theta_{4f}^{\mathrm{o.a.}} = \frac{\Theta_{\mathrm{d,\,max}}^{1} + \Theta_{\mathrm{d,\,min}}^{2}}{2}. \tag{4.9}$$

The cylindrical lens collimates the dispersed beams and focuses the spectral components. Thus, the position for each spectral component at the SLM can be approximated by the position on the cylindrical lens and can be calculated based on the wavelength-dependent diffraction angle $\Theta_{\mathrm{d}}^{1,\,2}(\lambda)$ via

$$x_{\mathrm{SLM}}(\Theta_{\mathrm{d}}^{1,\,2}) = -f \tan\left(\Theta_{\mathrm{d}}^{1,\,2} - \Theta_{4f}^{\mathrm{o.a.}}\right). \tag{4.10}$$

The SLM is centered on the optical axis of the $4f$ setup by default and $x = 0$ mm defines the middle of the SLM.

The goals of using the LC pixel array in its full width [Eq. (4.11a)] without spatial overlap [Eq. (4.11b)] and with a similar frequency distribution [Eq. (4.11c)] are described by the following system of equations:

$$\Theta_{\mathrm{d,\,max}}^{2} - \Theta_{\mathrm{d,\,min}}^{1} = \eta, \tag{4.11a}$$

$$\Theta_{\mathrm{d,\,min}}^{2} - \Theta_{\mathrm{d,\,max}}^{1} = \xi, \tag{4.11b}$$

$$x_{\mathrm{SLM}}(\Theta_{\mathrm{d,\,min}}^{1}) = -x_{\mathrm{SLM}}(\Theta_{\mathrm{d,\,max}}^{2}). \tag{4.11c}$$

It should be noted that Eq. (4.11c) has to be based on the frequency components at the edges of the SLM since the frequency components in the middle of the SLM are by definition symmetrical with respect to $x = 0$ mm, as they are already used to define the optical axes of the $4f$ setup [Eq. (4.9)] and thus the center of the SLM.

The setup is designed for a spectral range of 740–880 nm. The value $w_{\mathrm{SLM}} = 64$ mm is given by our LC SLM (*Jenoptik SLM-S640d*) and a gap of $w_{\mathrm{gap}} = 1$ mm is desired. A focal length of $f = 250$ mm is chosen. The graphical solutions of Eq. (4.11a–c) for $\delta_{\mathrm{in}} = 10.76°$ are shown in Fig. 4.2(a). The three lines (black, dark gray, light gray) represent Eq. (4.11a–c) and intersect exactly in one point, thus fulfilling all three goals. This results in the optimal set of parameters

$$\delta_{\mathrm{in}} = 10.76°, \qquad \beta = -46.57°, \qquad g = 892.60\ \mathrm{mm}^{-1}. \tag{4.12}$$

Since in practice these parameters cannot be achieved exactly with available optics, one has to make trade-offs. Experimentally, $\delta_{\mathrm{in}} = 10.26°$ was realized (see Section 4.3) and

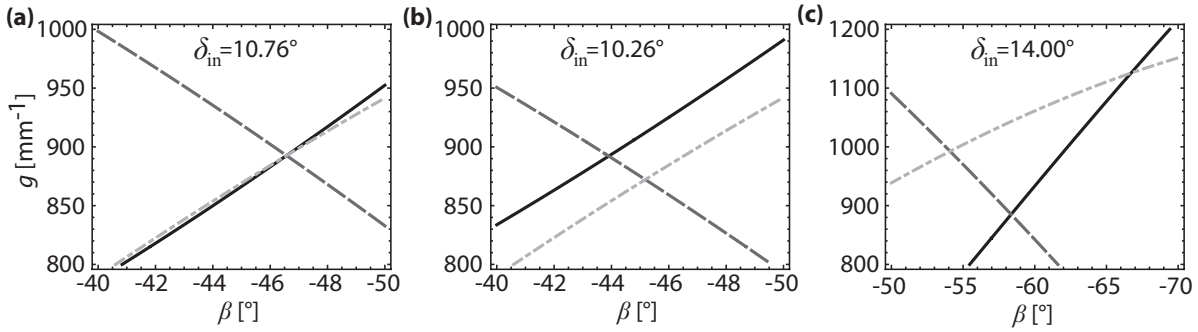

Figure 4.2 | Graphical solutions to Eq. (4.11a) (black solid line), Eq. (4.11b) (dark gray dashed line) and Eq. (4.11c) (light gray dash-dotted line) for different angles δ_{in}. (a) In the case of $\delta_{in} = 10.76°$, all three lines intersect at one point and all three equations are fulfilled for $\beta = -46.57°$ and $g = 892.60$ mm^{-1}. (b) For a slightly different value of $\delta_{in} = 10.26°$, only two of the three equations can be fulfilled simultaneously. The light gray and the black curves have no point of intersection in this special case. (c) For a larger value of $\delta_{in} = 14.00°$, the difference in β and g increase for the three different points of intersection. Figure modified from Ref. [1] © (2015) Optical Society of America.

β and g were recalculated according to this. In this case, only two of the three equations [Eq. (4.11a–c)] can be fulfilled simultaneously. Figure 4.2(b) shows that for a separation angle of $\delta_{in} = 10.26°$ two points of intersection exist where two of the three curves intersect. At the intersection of the dark gray [Eq. (4.11b)] and the black [Eq. (4.11a)] curve, Eq. (4.11c) is not fulfilled and the two frequency distributions span a different amount of pixels (Tab. 4.1). This is not the case at the second point where the dark gray and the light gray curves intersect. However, for this combination of β and g, the width of the SLM is not fully utilized (Tab. 4.1) and the shaping resolution is slightly reduced. It should be noted that for $\delta_{in} = 10.26°$ the deviation of the frequency distributions compared with the optimal distributions is small since the feasible separation angle nearly matches the optimal one. For a larger separation angle, e.g., of $\delta_{in} = 14.00°$ this would not be the case [Tab. 4.1 and Fig. 4.2(c)]. So, in general, either the gap size will differ from the target size and/or some pixels at the SLM edges will not be illuminated, if both frequency distributions should cover the same amount of pixels. The order of priority should be: i) similar frequency distribution, ii) sufficient gap size, iii) illumination of the pixel array in its full width.

Therefore, for $\delta_{in} = 10.26°$, the solution was chosen where Eq. (4.11b) and Eq. (4.11c) hold. The nearest commercially available grating frequency was $g = 850$ mm^{-1} and β was chosen in such a way that Eq. (4.11c) holds. The resulting parameters for the presented setup are:

$$\delta_{in} = 10.26°, \qquad \beta = -43.73°, \qquad g = 850 \text{ mm}^{-1}. \tag{4.13}$$

The resulting frequency distributions have the same width of 30 mm. The spatial gap between them is 2.6 mm and only 0.7 mm at each SLM edge cannot be illuminated. This is only a small deviation from the optimal frequency distribution.

Table 4.1 | Solutions to the equation system of Eq. (4.11) for different separation angles δ_{in}. For $\delta_{\text{in}} = 10.76°$, all three equation can be fulfilled [Fig. 4.2(a)]. This is not the case for $\delta_{\text{in}} = 10.26°$ [Fig. 4.2(b)] and $\delta_{\text{in}} = 14.00°$ [Fig. 4.2(c)]. For these values only two of three equations hold.

Separation angle δ_{in}	**10.76°**	**10.26°**	
Fulfilled equations	(4.11a,b,c)	(4.11a,b)	(4.11b,c)
Angle β [°]	−46.6	−43.9	−45.2
Grating frequency g [mm^{-1}]	892.6	892.1	872.2
Range of x^1_{SLM} [mm]	0.5 to 32	0.5 to 31.9	0.5 to 31.3
Range of x^2_{SLM} [mm]	-32 to -0.5	-32.1 to -0.5	-31.3 to -0.5
Separation angle δ_{in}	**14.00°**		
Fulfilled equations	(4.11a,b)	(4.11a,c)	(4.11b,c)
Angle β [°]	−58.4	−66.7	−54.1
Grating frequency g [mm^{-1}]	885.1	1125.6	992.5
Range of x^1_{SLM} [mm]	0.5 to 32.3	7.7 to 32	0.5 to 35.6
Range of x^2_{SLM} [mm]	-31.7 to -0.5	-32 to -7.7	-35.6 to -0.5

4.2 Polarization splitting and recombination

To achieve a beam separation angle of $\delta_{\text{in}} \approx 10°$, one option would be to use a Wollaston prism [261] as in previous designs [135, 254]. However, a detailed look at the Wollaston prism revealed some undesired side effects for the use in the presented setup. Hence, a thin film polarizer (TFP) instead of a Wollaston prism is utilized for the generation and recombination of the two orthogonally polarized beams. Both optical elements are discussed in the following.

4.2.1 Wollaston prism

Figure 4.3(a) shows a schematic of the polarization separation by a Wollaston prism. The Wollaston prism consists of two orthogonal prisms with perpendicular optical axes. The polarization of a laser beam which is perpendicular to the optical axis is influenced by the ordinary refractive index n_{o} and the parallel polarization component by the extraordinary refractive index n_{e}. Due to the change in the optical axis at the intersection of the two prisms, the beam will be split up into its parallel (p) and perpendicular (s) polarization component: The p component is influenced by n_{o} in the first half of the Wollaston prism and by n_{e} in the second half and vice versa for the s component. Wollaston prims feature a high extinction ratio of $> 10^6 : 1$ and it is a practical advantage that the separation angle $\delta_{\text{sep}}(\lambda)$ depends only on the angle α between both prisms for a given material with birefringence $\Delta n(\lambda) = n_{\text{e}}(\lambda) - n_{\text{o}}(\lambda)$

$$\delta_{\text{sep}}(\lambda) \approx 2\,\Delta n(\lambda) \cot \alpha. \tag{4.14}$$

To achieve a beam separation of $\delta_{\text{sep}} \approx 10°$, the use of a calcite Wollaston prism was considered. However, the high birefringence of $\Delta n \approx 0.166$ and dispersion of calcite has some disadvantages when used in the presented setup as described in the following.

The first disadvantage of Wollaston prisms is that the separation is not symmetric for both beams. The exit angle for the s polarization is about 3 % larger than the angle for the p polarization. This can be compensated by the alignment of the subsequent optics. However, the wavelength dependency of the refraction at the intersection of both calcite prisms and at the exit plane will lead to an angular dispersion of the exit beams and thus to a pulse front tilt [262]. The difference in the exit angle for the lowest and the highest wavelength is about 1.5 % for 740–880 nm and slightly different for both beams. This effect would have to be taken into account for the numerical calculations of the $4f$ setup (Section 4.1) by using wavelength-dependent angles of incidence in Eq. (4.1)–(4.4). However, since the beams emitted from the Wollaston prism will be mapped with a telescope onto the grating lateral chromatism will occur as well.

Another undesired effect is that the distance the beam travels as ordinary or extraordinary beam depends on the beam position in the Wollaston prism. Therefore, there will be an additional inherent varying dispersion along one dimension of the beam profile. The mean value of this dispersion can be compensated with the pulse shaper but not the spatial variation of the dispersion. For instance, the remaining group-delay dispersion across a beam radius of $w = 2.57$ mm[1] is on the order of ± 110 fs^2 and the remaining third-order dispersion about ± 100 fs^3 if the dispersion for the beam center is compensated with the pulse shaper. The mean value of the introduced dispersion depends on the length of the Wollaston prism, but the difference across the beam profile is actually independent of the Wollaston prism size and depends only on the beam radius, the angle α between the two halves of the Wollaston prism, and its material.

These effects are only discussed for a single pass of the Wollaston prism to create two perpendicularly polarized beams. However, the back-going beams of the vector-field shaper will pass the Wollaston prism a second time to be recombined to a single beam. To what extent these effects are compensated or aggravated for the outgoing shaped beam cannot easily be deduced as this would require a complex ray-tracing simulation of all (non-ideal) optical elements for Gaussian beams. Due to the divergence of the Gaussian beams, the optical aberration of the lenses in the setup, and the fact that the separation of the incoming and outgoing beam requires a tilting of the outgoing beam in the beam height, a complete compensation of these negative side effects of the Wollaston prism is not expected. To reduce these undesired effects of the Wollaston prism, a quasi-achromatic material is desired. MgF_2 is, for example, such a quasi-achromatic material but its small birefringence ($\Delta n \approx 0.011$) [263] results in a much lower separation angle and is therefore not suited for the presented setup. Another approach to diminish these chromatic effects is to combine two Wollaston prisms with positive and negative birefringence [264]. The suitability of such a Wollaston prism pair for a pulse shaper was, however, not further investigated as ray-tracing simulations showed a significant deformation of the outgoing beam profile due to the required tilting of the back-going beams if a Wollaston prism is used (see Section 4.3).

[1] In order to consider 99.99 % of the intensity of the Gaussian beam profile its width on the Wollaston prism is assumed to be $\sqrt{5} \times 2w$ (see Section 2.3).

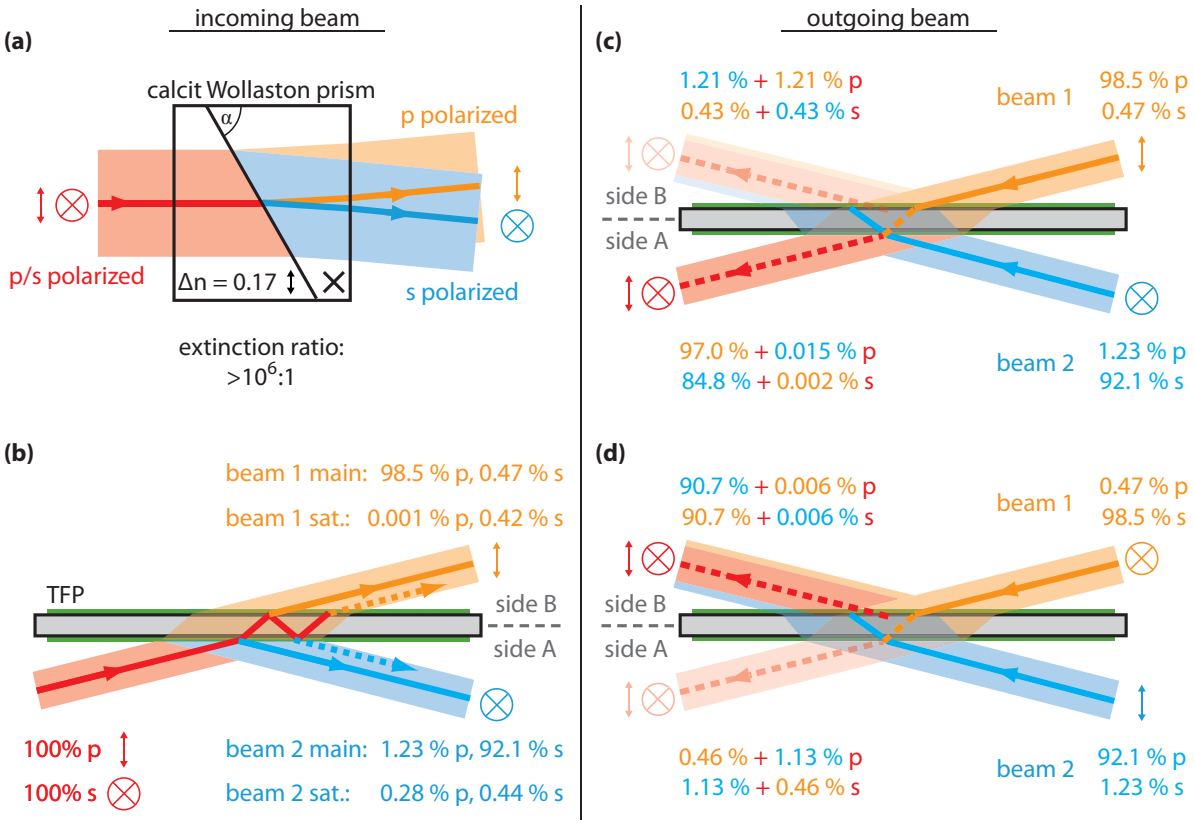

Figure 4.3 | Principle of the Wollaston prism and the thin-film polarizer (TFP) for polarization separation and recombination. (a) The Wollaston prism consists of two birefringent prisms with perpendicular optical axes. The separation of the incoming pulse (red) into a p- and s-polarized pulse (orange/blue) is based on refraction and offers a very high extinction ratio. (b) A TFP is a thin glass substrate (gray) with special coating (green) on both sides. The p-polarized component of the incoming beam (red) is transmitted (orange) and the s polarization is reflected (blue) with the given efficiencies. Multiple reflections inside the TFP lead to minor satellite pulses which are delayed by about 3.6 ps. (c,d) The back-going beams are recombined (red dotted beams) by passing the TFP a second time. The polarization states of the back-going beams determine the intensity which is emitted on both sides of the TFP. If the polarization of both beams is not changed by the SLM in the pulse shaper, the maximum intensity will be emitted on the side of the incident beam (side A) and the minimal intensity on the other side (side B) [(c)]. If the polarizations are rotated by 90°, this behavior is switched [(d)]. Due to this effect, amplitude shaping is realized for each beam. Either the beam emitted at side A or B can be used as shaped beam. The double-pass extinction ratio at side A is 43521:1 for beam 1 and 5605:1 for beam 2 [(c)] and 15619:1 for both beams at side B [(d)]. Figure modified from Ref. [1] © (2015) Optical Society of America.

4.2.2 Thin-film polarizer

Due to disadvantages of a Wollaston prism for the presented setup, a thin-film polarizer (TFP) is used for beam separation and recombination in this work. The separation angle of a TFP depends only on the angle of incidence α_{in}. Standard small-band TFPs can be used with $\alpha_{\text{in}} > 40°$ and offer an extinction ratio of about 200:1. For broadband

applications higher angles of incidence are needed, resulting in lower extinction ratios. The performance of such a TFP strongly depends on the used coating. The tailor-made TFP (*Laseroptik GmbH*) employed here is specified for an angle of incidence of 77° which results in a beam separation angle of $\delta = 26°$ [Fig. 4.3(b)], which will be demagnified to $\delta_{\text{in}} = 10.26°$ by a telescope (see Section 4.3). The glass substrate (wedge angle < 0.2") is coated on both sides to provide an extinction ratio of 210/75:1 (p/s) for a single pass. As shown in Fig. 4.3(b), the transmitted beam (beam 1, orange) behind the TFP is mainly p, the reflected one (beam 2, blue) primarily s polarized. One drawback of a TFP is that internal reflections inside the TFP results in the appearance of multiple transmitted and reflected beams behind the TFP. The intensity of the second transmitted beam is about 0.00/0.42 % of the incoming p/s component and for the second reflected pulse about 0.28/0.42 %. The consecutive post pulses are mainly s polarized with decreasing intensity. These multiple pulses overlap partially in space due to the finite beam size, but they are separated in time. The delay between consecutive pulses depends on the TFP thickness (in our case 0.5 mm) and is calculated to be about 3.6 ps. The small amplitude and the relative large temporal separation of these satellite pulses, therefore, do not hinder an application of the TFP in the pulse shaper setup. The values for the pulse intensities are gained by numerical calculations. For these calculations, polarization-dependent measurements by the manufacturer of the total transmission with coating at one and both sides were taken into account. Under the assumption that up to six consecutive pulses contribute to the total measured intensity, the transmission coefficients for the transition air–coating–substrate and substrate–coating–air for both polarizations were calculated for the center wavelength of 810 nm. Since the beam separation is not based on refraction, no angular dispersion occurs when using a TFP. The only chromatic effect is a slight parallel displacement of different wavelengths. However, this chromatic displacement is in the order of 0.3 µm for 740–880 nm and is therefore negligible.

Following the pulse-shaping procedure via the SLM in the $4f$ setup, the same TFP generates two outgoing beams which can be used as shaped beam. Either the beam is used which is emitted on the same side as the incident one [side A, Fig. 4.3(c,d)] or the emitted beam on the opposite side is used [side B, Fig. 4.3(c,d)]. The first option (using the outgoing beam from side A) has the advantage that the beam path inside the TFP is inverted, which therefore generates a perfect spatial overlap of both beams if the influence of the optics between the incoming and outgoing beams is neglected. By passing the TFP twice, the transmitted beam is slightly more dispersed compared to the reflected beam. This must be compensated with the pulse shaper. The maximum intensity at side A is emitted if the polarization of both beams is not changed [Fig. 4.3(c)]. The differing efficiencies [Fig. 4.3(c)] for both beams can also be compensated by the pulse shaper or by adjusting the intensity of the polarization components of the incoming beam. Due to the imperfect extinction, it must be considered that the p/s component of the exit beam is not only given by the transmitted/reflected beam but is additionally partly influenced by the respective other beam. This cross talk is, however, only 0.016 % (p) and 0.0026 % (s) and can thus be neglected. The double-pass extinction ratio is 43521:1 for the transmitted beam (orange) and 5605:1 for the reflected beam (blue). Shaping the amplitude of each spectral component is done by changing their polarization state with the SLM. The minimum exit intensity at side A is reached when each polarization

is rotated by 90°, respectively [Fig. 4.3(d)]. The expected minimal outgoing intensity for perfect shaping is about 1.59 % for both beams as shown in Fig. 4.3(d). However, this polarization rotation is not possible in the pixel gaps of the SLM. These gaps cover 3 % of the SLM array width and therefore the expected minimum intensity for zero transmission would be in practice at least 4.5 %. It should be noted that in this configuration the shaped pulse has to be tilted in height to separate it from the incoming pulse.

In the second variant, the beam is used which exits the TFP at the opposite side as the incoming beam [side B, Fig. 4.3(c,d)]. In this case, the polarization of each arm has to be rotated by 90° to get the maximum output intensity [Fig. 4.3(d)]. The benefit of this configuration is that not only the efficiencies for beam 1 and beam 2 are automatically equalized but also their extinction ratio. In addition, the dispersion introduced by the TFP is the same for both beams. The transmission for both beams is 90.7 % with a negligible cross talk of 0.0064 % and an extinction ratio of 15619:1. The minimum output intensity is $\approx$ 2.42 % (p) and $\approx$ 0.86 % (s) [Fig. 4.3(c)] and is not increased by the intensity passing the pixel gaps. Another advantage is that no tilt in the beam height is necessary to separate the outgoing from the incoming beam. This has positive effects on the beam profile of the outgoing beam (see Section 4.3). The downside of this option is that the beam paths are not inverted: the initially transmitted/reflected beam is reflected/transmitted on the second pass. This results in a minor lateral offset between both exit polarizations. This displacement depends on the angle of incidence and the thickness of the TFP and is in our case 0.20 mm. For the presented design, this last configuration is used, which is equivalent to the use of perpendicular entrance and exit polarizers in a non-folded amplitude pulse shaper and thus called crossed-polarizer arrangement.

4.3 Telescope ray tracing

The telescope connects the TFP and the $4f$ setup to a common-path setup as it directs the two orthogonally polarized beams under two different angles of incidence onto the grating using the same optics. Its second function is the demagnification of the separation angle between the two beams. As a side effect, the beam radius is magnified by the telescope. Due to the non-normal incidence of the beams onto the lenses and due to the lens thickness, ray tracing has to be utilized to determine the optimal lens combination to achieve a separation angle in the order of $\delta_{\text{in}} = 10.76°$ behind the telescope. As a constraint, the maximum usable focal lengths are limited by the space available on the breadboard.

The results of the ray-tracing simulation of the final telescope are shown in Fig. 4.4(a). The simulation was done with Optica 3 for Mathematica [265]. The best suited, commercially available focal lengths are $f_1 = 51.6$ mm and $f_2 = 125$ mm. Due to the large separation of the two beams in the x direction inside the telescope and due to the size of their beam profiles, lenses with a diameter of 1.5" and 2.0" are used. Some simplifications were made for the simulations. First, only a monochromatic light source and second, geometrical rays instead of Gaussian beams were used. Additionally, the thickness of the TFP was neglected. For the alignment of the telescope in the simulation a

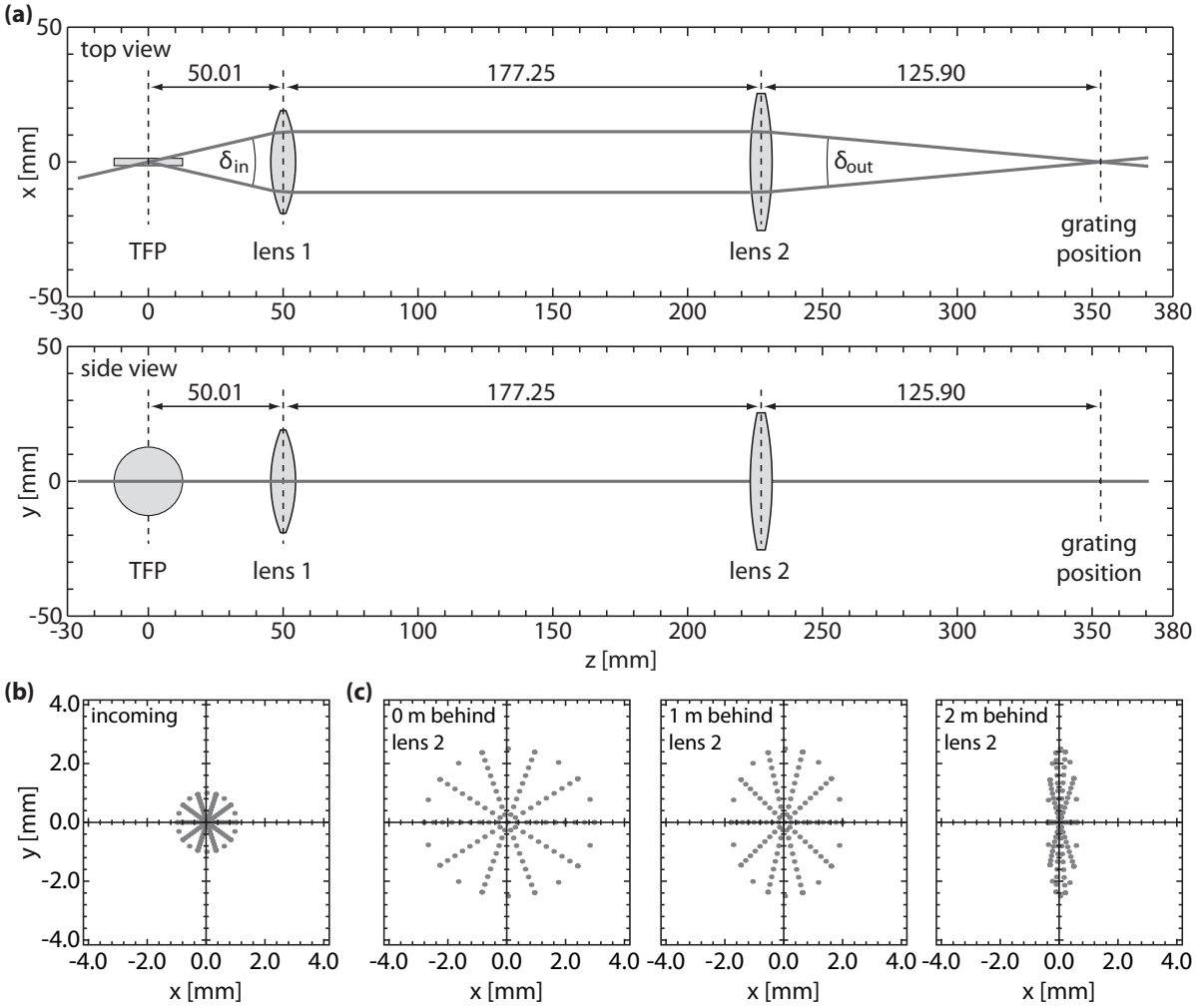

Figure 4.4 | Ray tracing of the telescope between the TFP and the grating. (a) Optical system shown from the top (upper panel) and from the side (lower panel). The distances and sizes are true to scale. The thickness of the TFP is magnified by a factor of four for better visibility. The simulation is based on ray optics and not on Gaussian optics. The wavelength of the ray matches the center wavelength of the used laser (800 nm). (b) Ray profile in front of the TFP. To examine the effect of the telescope on the beam profile, multiple parallel rays were used to simulated the beam profile. The ray profile radius is 1 mm. (c) Ray profile behind lens 2 for different propagation lengths. The profile is collimated in the y direction, but asymmetrically focused in the x direction due to comatic aberration of the telescope. The ray profiles are visualized in a plane perpendicular to the propagation direction.

ray with 800 nm was considered. The distance between the first lens ($f_1 = 51.6$ mm) and the TFP was chosen so that the two beams propagate parallel to each other between lens 1 and lens 2. The second lens ($f_2 = 125$ mm) was positioned in such a way that the beam profile behind the telescope is collimated in the y direction. A simultaneous collimation in the x and in the y direction is not possible (see discussion below). The collimation in the y direction is favored because the divergence in x will be influenced by the cylindrical lens of the $4f$ setup. The grating position is given by the point of

intersection of both beams behind the second lens. The distances differ slightly from the expected lengths, given by the focal lengths, due to the non-normal incidence and the thickness of the lenses. The simulations show that a very precise positioning of the lenses is required to achieve a collimation in the y (or x) direction. The separation angle behind the telescope is $\delta_{\text{out}} = 10.26°$, based on the ray-tracing simulations. The demagnification factor for the separation angle is 0.395. It can also be estimated by the ratio of the focal lengths. The estimated factor is 0.413, resulting in an expected separation angle of $\delta_{\text{out}} = 10.73°$, which is close to the optimal value [see Eq. (4.12)]. This is only a small discrepancy in the order of 4 % between the estimated and the ray-traced result, but the numerical calculations in Section 4.1 show that this difference already affects the expected frequency distribution at the SLM and influences which parameters for the setup should be chosen.

The ray-tracing simulations were also used to investigate the influence of the telescope on the beam profile [Fig. 4.4(b,c)]. Multiple parallel rays were used to approximate a collimated Gaussian beam profile. This simulated beam profile will, thus, be called "ray profile" in the following. A ray profile with a radius of 1.0 mm was defined as light source [Fig. 4.4(b)], matching the Gaussian beam radius used in the experiment. The simulated ray profile 0 m, 1 m, and 2 m behind the second lens is shown in Fig. 4.4(c). The magnification of the ray profile is clearly visible. The beam radius is 2.50 mm in the y direction behind the telescope. This matches nearly the magnification factor of 2.53 which can be calculated based on the demagnification factor for the separation angle. Since the beam waist radius inside the $4f$ setup should be smaller than $w_{\text{out}} = 2.57$ mm (see Section 4.1), the beam waist radius in front of the telescope must be smaller than $w_{\text{in}} = 1.03$ mm. The beam size in y is, as supposed by the alignment used in the simulation, constant over the simulated propagation length and therefore collimated. However, due to the non-normal incidence on the first lens, causing comatic aberration, the ray profile is focused in the x direction. Furthermore, a slight asymmetry of the ray profile in x direction is visible arising from the spherical aberration of the lenses. The "focus spot" occurs ≈ 3 m behind the second lens. The beam is stronger focused in the x direction if short focal lengths are used. It was further investigated whether combinations of bi-convex and/or plano-convex lenses reduce the optical aberrations due to the non-normal incidence. This was, however, not the case and the telescope's performance is best using two bi-convex lenses. Best form lenses could be utilized to reduce the effect of comatic aberration, but such lenses were not available with the required focal lengths and diameters.

To approximate the effects on the beam profile behind the entire vector-field shaper, a simplified setup was ray traced. This simplified setup, composed of the TFP, the telescope, and a $4f$ setup without grating is shown in Fig. 4.5(a). The grating was neglected as only monochromatic rays were considered and in order to simplify the alignment of the cylindrical lens and the folding mirror in the simulation as in this case the optical axis of the simplified $4f$ setup matches the optical axis of the telescope. The cylindrical lens was placed in such a way that the two rays propagate parallel to each other behind the cylindrical lens and the folding mirror was placed in the focus spot of the ray profile. If the incoming and back-going beams propagate in the same plane parallel to the table [Fig. 4.5(c)], the ray profiles of the exit beams nearly match the defined

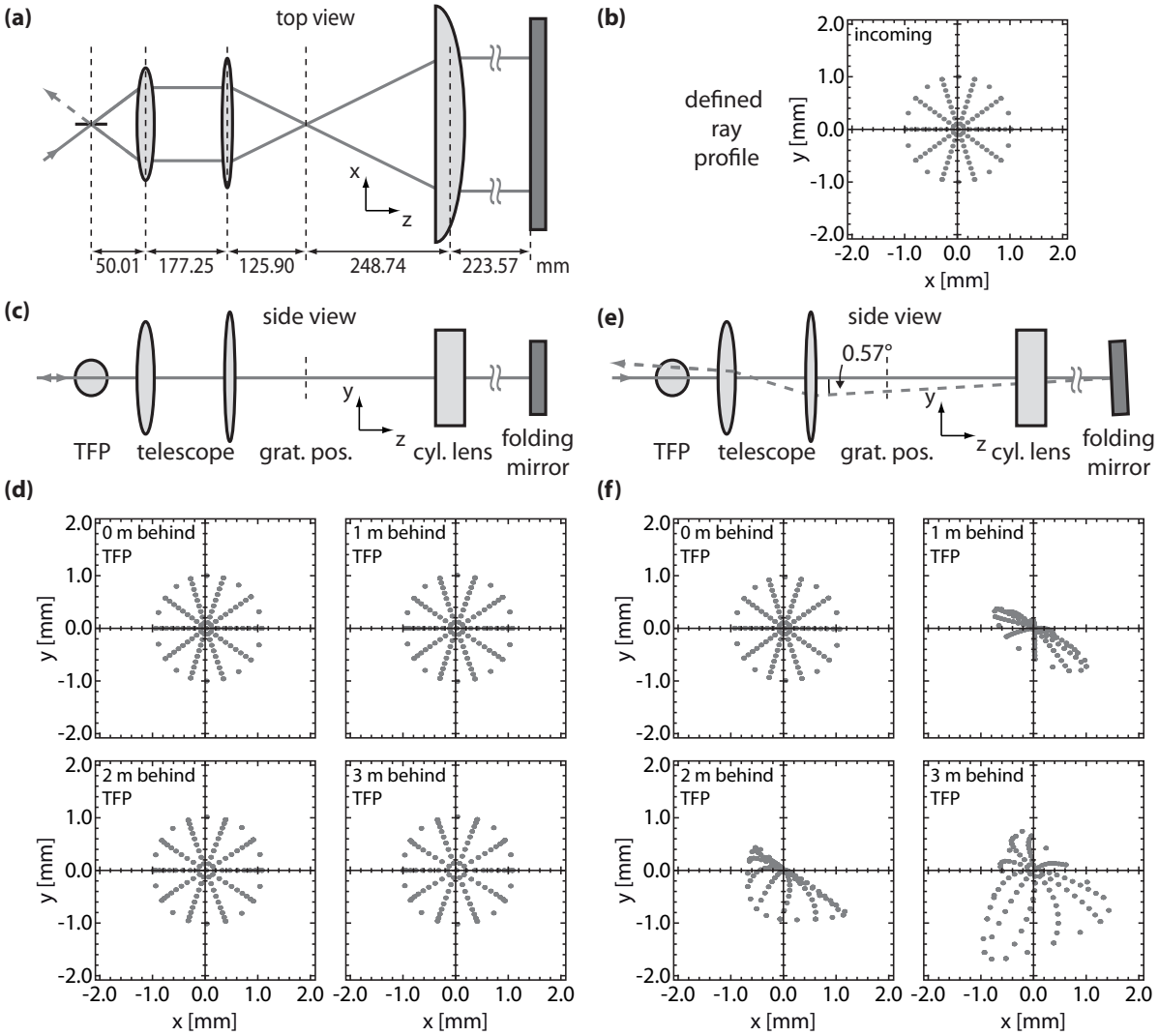

Figure 4.5 | Ray tracing of the simplified pulse shaper. (a) Schematic of the optical system (top view). Behind the TFP and the telescope, a simplified $4f$ setup is placed. The grating is neglected since only a single wavelength is simulated. Both back-going beams (dashed) are emitted on the opposite side from the incoming beam and overlap spatially. (b) Defined incoming ray profile composed of parallel rays. (c) Side view of the optical system and (d) corresponding ray profiles of the exit beams 0, 1, 2, and 3 m behind the TFP. (e) Same as (c) but with a tilted folding mirror and (f) the corresponding ray profiles. The ray profiles are visualized in a plane perpendicular to the propagation direction. When the incoming and back-going beams propagate parallel to the table, the ray profile is nearly collimated in the x and y direction [(c–d)]. Tilting the folding mirror along its x axis allows a separation of the incoming and outgoing beam in height, but causes deformation of the ray profile, which is no longer collimated [(e–f)].

incoming ray profile depicted in Fig. 4.5(b). The size of the ray profile observed 0 m, 1 m, 2 m, and 3 m behind the TFP is nearly constant over the propagation length [Fig. 4.5(d)]. Only a slight focusing in the x direction is visible. This may be a result of the manual alignment of the optics in the simulation as an automatic optimization of their position

was not possible. Apart from that, a minor radial deformation at the edges of the ray profile is observed for longer propagation lengths as the distance between the single points in the x–y plane is reduced. Both back-going beams (dashed in Fig. 4.5) are emitted on the same side of the TFP. Since the thickness of the TFP is neglected, both beams overlap perfectly and no displacement between the two outgoing ray profiles is shown in Fig. 4.5(d). The high quality of the outgoing ray profile compared with ray profile behind the telescope [Fig. 4.4(c)] is a result of the inversion of the ray paths by placing the folding mirror exactly in the focus spot. In this case, optical aberrations of the telescope are compensated.

In Fig. 4.5(e,f), the effect of tilting the folding mirror on the ray profile is presented. Such an alignment would be required if a Wollaston prism is used instead of a TFP or if the TFP should not be used in the crossed-polarizer arrangement so that the incoming and back-going beams must be spatially separated in height. The simulated ray profile behind the TFP shows a distinct asymmetric deformation. It is neither collimated in the x nor in the y direction. This emphasizes the advantage of the TFP in the crossed-polarizer configuration as no separation of the beam in height is required. Instead of tilting the folding mirror the incoming beam could be tilted to achieve a beam separation of the incoming and outgoing beam as well. This option requires an adjustment of the distances of the optical elements and was simulated for a telescope with shorter focal lengths, not presented in this thesis. The resulting ray profiles are more symmetrically deformed compared to the ray profiles in Fig. 4.5(d), but also not collimated in the x and y direction. Hence, this variant should also be avoided by employing a TFP in the crossed-polarizer arrangement, but is preferred if a beam separation in height is required. Rotating the cylindrical lens by 180° has for all variants a negative impact on the resulting ray profiles, even if its position is again optimized. Therefore, it must be used in the orientation depicted in Fig. 4.5(a).

To investigate the chromatic aberrations of the simplified system, the ray profile was also simulated for different wavelengths without realigning the setup. The ray-traced system is equivalent to the schematics shown in Fig. 4.5(a,c). The incoming and outgoing beams propagate both in the same plane parallel to the table. The ray profiles for six different wavelengths in the range of 760–860 nm and for four different propagation lengths (0 m, 1 m, 2 m, 3 m) behind the TFP are shown in Fig. 4.6. The spherical aberration of the cylindrical lens is not taken into account, since, without the grating, the wavelength dependency of the angle of incidence and the variation in the point of impact onto the cylindrical lens are not considered. The first result from this simulation is that the ray profile is collimated only for 800 nm [Fig. 4.6(c)], as this wavelength was used to align the setup. For wavelengths below 800 nm [Fig. 4.6(a,b)], the ray profile is focused with increasing propagation distance because of chromatic aberration of the system. The divergence is larger in the x than in the y direction due to comatic aberration of the telescope. This is also the case for wavelengths above 800 nm [Fig. 4.6(e,f)] but the ray profile is defocused instead of focused. The second effect which can be observed is a small angular chirp in the x direction as the center of the ray profiles moves away from $x = 0$ mm for increasing propagation length. This effect is, however, much smaller than the defocusing/focusing of the ray profile. Both effects increase for a larger difference between the simulated wavelength and the alignment wavelength of 800 nm.

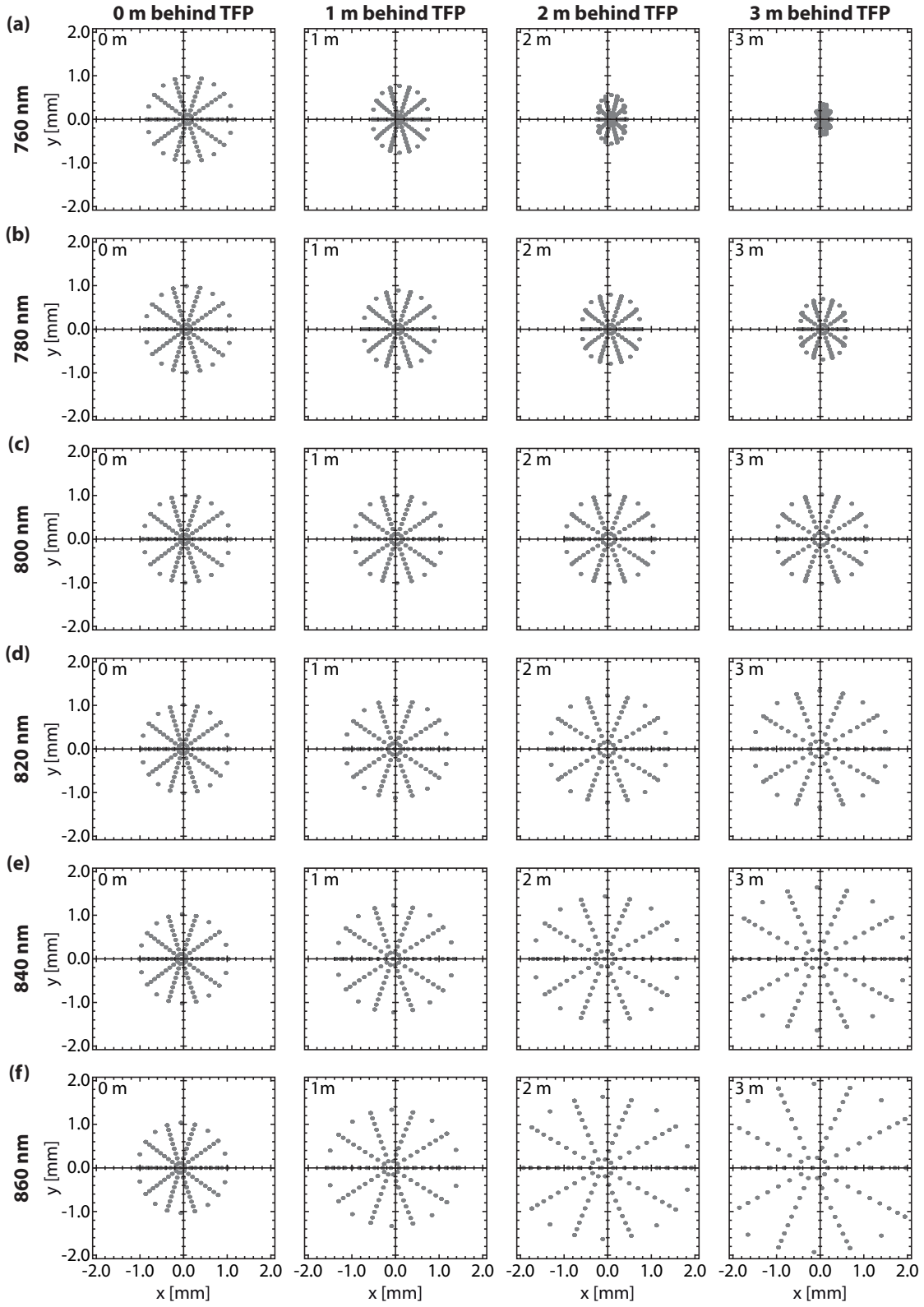

Figure 4.6 | Ray profiles behind the simplified setup for various wavelengths and propagation lengths. The ray profile is collimated for 800 nm [(c)]. It is focused for $\lambda < 800$ nm [(a,b)] and defocused for $\lambda > 800$ nm [(d–f)]. A slight wavelength-dependent difference between $x = 0$ mm and the center of the ray profiles is observed due to angular chirp.

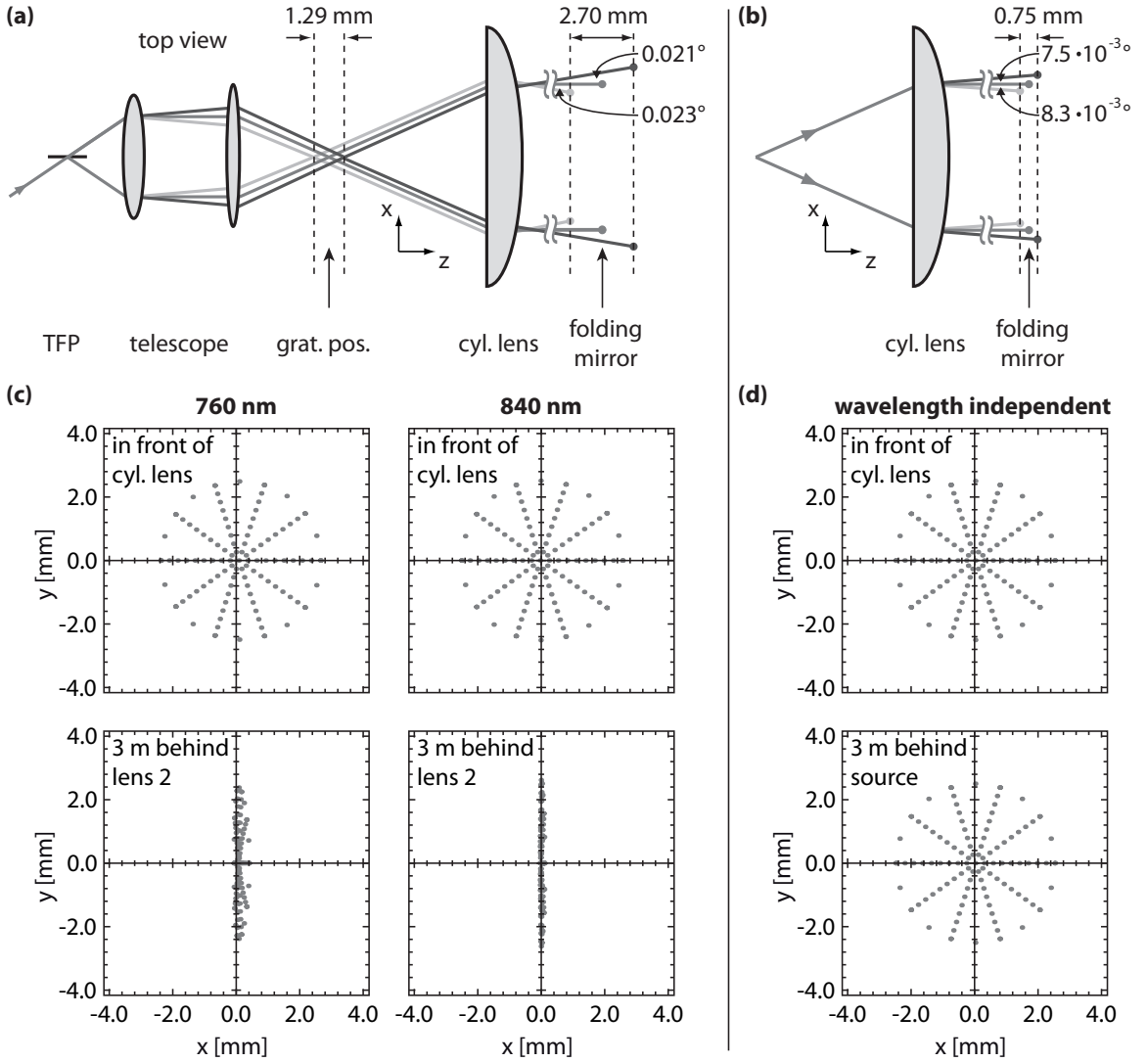

Figure 4.7 | Wavelength-dependent ray-tracing simulations of the simplified setup and the single cylindrical lens. (a,b) Schematic of the wavelength-dependent pathways inside the simplified setup and behind the single cylindrical lens [(a)/(b)] for 760 nm (light gray), 800 nm (medium gray), and 840 nm (dark gray). The position of the focus spot is marked for each beam by a dot at the end of the ray. (c) Incident ray profiles on the cylindrical lens for 760 nm (left) and 840 nm (right) behind the second lens of the telescope for two different propagation lengths. Due to the comatic and chromatic aberration of the telescope, the ray profile has a wavelength-dependent divergence in the x and y direction. The divergence in the x direction is much larger than in the y direction. (d) Ray profile of the light source used for ray-tracing simulations of the single cylindrical lens independent of all other optics. The ray profile consists of parallel rays and is therefore independent of the wavelength and the propagation distance. The ray profiles are observed perpendicular to the propagation direction [(c,d)].

A schematic of the ray pathways for 760 nm (light gray), 800 nm (medium gray), and 840 nm (dark gray) inside the simplified setup is depicted in Fig. 4.7(a). Due to chromatic aberration, rays with different wavelengths do not propagate parallel to each other inside the telescope and the z position of the point of intersection behind the telescope is wavelength dependent. The difference between the point of intersection for 840 nm and 760 nm is 1.29 mm. The separation angle is indeed nearly wavelength independent. The simulation shows only a difference smaller than 6.5×10^{-3} % compared to the separation angle for 800 nm. The point of impact in the x direction on the cylindrical lens is also slightly wavelength dependent, but the displacement for 760 and 840 nm is only in the order of ± 0.06 mm compared to the point of impact of the 800 nm ray. Due to the wavelength dependence of the point of intersection behind the telescope and the optical aberrations of the cylindrical lens, the rays for 760 nm and 840 nm do not propagate parallel to the z axis. The angle between the propagation direction of these rays and the z axis is $|0.023|^\circ/|0.021|^\circ$ for 760/840 nm. These angles cause the angular chirp observed for the simulated outgoing ray profiles in Fig. 4.6. The wavelength-dependent focusing/defocusing of the ray profiles is caused by the fact that the z position of the focus spot behind the cylindrical lens, indicated by the dots at the end of the rays in Fig. 4.7(a,b), is also wavelength dependent. The distance of the focus spots for 840 and 760 nm in the z direction is 2.70 mm. For this reason, the folding mirror is located at the focus position solely for one single wavelength component for which therefore the ray paths are exactly inverted for the back-going beams, canceling out the comatic aberration of the telescope [Fig. 4.6(c)]. The z position of the cylindrical lens has only a minor influence of the difference in the focus spot position. This effect is therefore not caused by the wavelength dependency of the point of intersection. To determine to what extent the difference in the focus spot position arises from the chromatic aberration of the cylindrical lens, the single cylindrical lens was ray traced independently from all other optics [Fig. 4.7(b)]. The angle of incidence onto the cylindrical lens matches the one from the simulation of the simplified setup for the alignment wavelength of 800 nm. The incoming ray profile was, analogously to the previous simulations, defined by parallel rays, but with a radius of 2.50 mm to account for the magnification of the telescope. The simulation shows in principle the same chromatic effects, but with a much lower magnitude. The difference in the z position of the focus spot is only 0.75 mm, and the angle between the rays and the z axis is only $|8.3 \times 10^{-3}|^\circ/|7.5 \times 10^{-3}|^\circ$ for 760 and 840 nm.

This confirms that the angular chirp is mainly a result of chromatic aberration of the telescope resulting in different points of intersection. The reason for the large distance between the focus spots in the z direction, observed in the simplified setup, is the divergence, or more precisely, the difference in divergence of the ray profiles in the x direction behind the telescope. Figure 4.7(c) shows the ray profiles for 760 and 840 nm behind the telescope – not the outgoing beams behind the simplified setup as Fig. 4.6 – which will incide on the cylindrical lens. The wavelength-dependent divergence is barely visible at the position of the cylindrical lens, but more pronounced 3 m behind the second lens of the telescope. By contrast, the incoming ray profile used for the simulation of the single cylindrical lens does not show any divergence and therefore has a constant shape independent of the propagation length or wavelength [Fig. 4.7(d)].

These analyses provide only qualitative and no quantitative results for the actual beam used in the laboratory, since no Gaussian beams were simulated. The two-dimensional profile of the beam in the laboratory could not be fully characterized. However, the principle findings match the observations in the experiment, especially the negative influence on the beam profile when the folding mirror is tilted. The laser used for building the setup and for the experiments presented in this thesis had only a spectral width of 780–816 nm for $I(\omega)/I_{\max}(\omega) > 1.0$ % (see Section 6.1). For this wavelength range only a minor deformation of the beam profile is observed – not substantially impeding the application of the presented VFS in an experiment.

4.4 Complete vector-field shaper setup

The complete setup of the vector-field pulse shaper is depicted in Fig. 4.8. The incoming beam (solid gray line) is collimated in a 1:1 telescope. A reference (transparent line) is separated with a pair of glass wedges (GW1). In comparison to a standard beam splitter, this has the advantage that multiple reflections are emitted under different angles and can thus be separated. To transfer the incoming p-polarized pulse to a pulse with equal intensity of the p and s component, a combination of a $\lambda/2$ plate and a 45° periscope is used. The $\lambda/2$ plate can also be used to compensate for different efficiencies between the two arms of the setup. The rotated beam is split up by the TFP (see Section 4.2.2), at which the p polarization is transmitted (beam 1, dark gray) and the s polarization is reflected (beam 2, light gray). Both beams pass the magnifying telescope (see Section 4.3) and are directed onto a volume phase holographic grating (*Wasatch Photonics*) optimized for the two different angles of incidence. The $4f$ setup is composed of the volume phase holographic grating, a cylindrical lens, a 2-layer SLM with 640 pixels (*Jenoptik SLM-S640d*) and the folding mirror. The specifications and calculated parameters for the setup are listed in Tab. 4.2.

The shaped pulse (gray dotted line) is extracted in the crossed-polarizer arrangement at the TFP, so that for maximum transmission the polarization of each arm has to be rotated at the SLM. The transfer function of the VFS is given by the superposition of the output field of beam 1 [$\vec{E}^1_{\text{out}}(\omega)$] and beam 2 [$\vec{E}^2_{\text{out}}(\omega)$]

$$\begin{aligned}
\vec{E}_{\text{out}}(\omega) &= \vec{E}^1_{\text{out}}(\omega) + \vec{E}^2_{\text{out}}(\omega) \\
&= \begin{pmatrix} 0 & 0 \\ 0 & 1 \end{pmatrix} \boldsymbol{M}^{\text{folded 2l.}}_{\text{PS}}(\Delta\varphi^1_1,\Delta\varphi^1_2) \begin{pmatrix} 1 & 0 \\ 0 & 0 \end{pmatrix} \begin{pmatrix} E^{\text{in}}_1(\omega) \\ E^{\text{in}}_2(\omega) \end{pmatrix} \\
&+ \begin{pmatrix} 1 & 0 \\ 0 & 0 \end{pmatrix} \boldsymbol{M}^{\text{folded 2l.}}_{\text{PS}}(\Delta\varphi^2_1,\Delta\varphi^2_2) \begin{pmatrix} 0 & 0 \\ 0 & 1 \end{pmatrix} \begin{pmatrix} E^{\text{in}}_1(\omega) \\ E^{\text{in}}_2(\omega) \end{pmatrix} \\
&= \mathrm{e}^{\mathrm{i}\frac{\pi}{2}} \begin{pmatrix} -E^{\text{in}}_2(\omega)\, \mathrm{e}^{-\mathrm{i}\left(\Delta\varphi^2_1+\Delta\varphi^2_2\right)}\, \sin(\Delta\varphi^2_1 - \Delta\varphi^2_2) \\ E^{\text{in}}_1(\omega)\, \mathrm{e}^{-\mathrm{i}\left(\Delta\varphi^1_1+\Delta\varphi^1_2\right)}\, \sin(\Delta\varphi^1_1 - \Delta\varphi^1_2) \end{pmatrix},
\end{aligned} \tag{4.15}$$

where $\boldsymbol{M}^{\text{folded 2l.}}_{\text{PS}}$ is given by Eq. (3.19). Due to the high extinction ratio of the TFP, the TFP is assumed to be ideal in Eq. (4.15) for the sake of simplicity. $\Delta\varphi^1_{1/2}$ are the

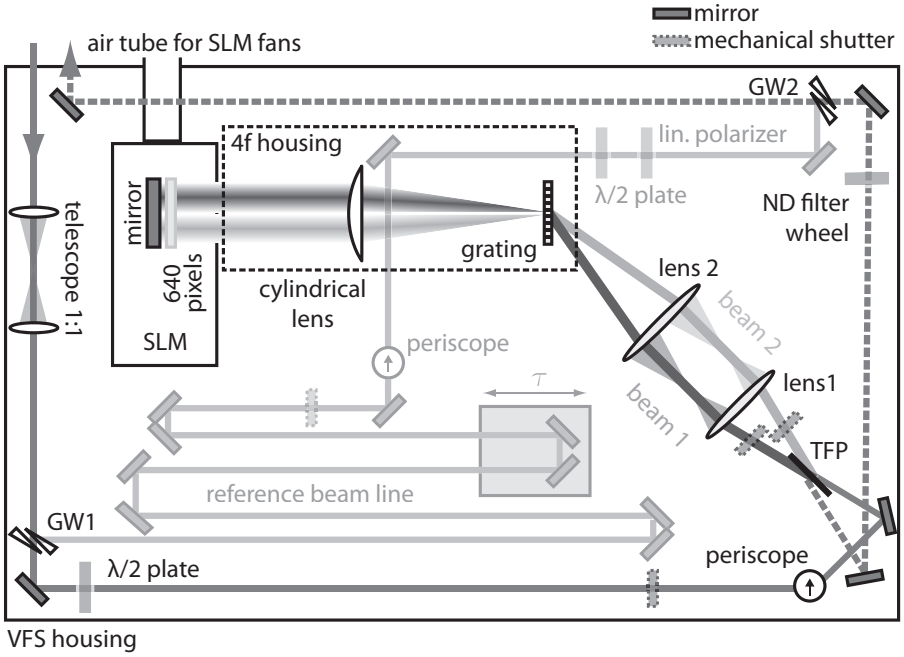

Figure 4.8 | Schematic vector-field shaper setup. The key elements to achieve vector-field control of the incoming pulse (solid gray line) are a thin-film polarizer (TFP) to generate two perpendicularly polarized pulses and the subsequent telescope to direct them onto the grating of a $4f$ setup in a common-path configuration. The transmitted (beam 1, dark gray) and reflected (beam 2, light gray) beams are shaped individually in amplitude and phase and recombined by the TFP to a single beam (gray dotted line). The reference beam line (transparent) is used for pulse characterization via dual-channel Fourier-transform spectral interferometry (FTSI). The reference is created by a pair of glass wedges (GW1) and recombined with the shaped pulse by a second pair (GW2). The time delay τ between the reference and the shaped pulse can be adjusted with a mechanical delay stage. See text for a detailed description. Figure modified from Ref. [1] © (2015) Optical Society of America.

phase retardations at layer 1 and 2 applied to beam 1 and $\Delta\varphi^2_{1/2}$ the phase retardations applied to beam 2. It can be seen from Eq. (4.15) that the p component of the shaped pulse is given by beam 2 and the s component by beam 1. In the following chapters, beam 1 will be referred as "transmitted beam" and beam 2 as "reflected beam" for easier identification. The nomenclature results from the beam splitting at the TFP for the incoming beam.

The crossed-polarizer arrangement improves the performance of the TFP and has the additional advantage that also the polarization-dependent efficiencies of the grating and cylindrical lens are automatically compensated. The incoming and outgoing beam can also propagate at the same height parallel to the table. This leads to a considerable improvement on the beam profile compared to a tilting of the outgoing beam. By exactly inverting the beam paths, optical aberrations introduced by the telescope due to the small focal lengths and the non-normal incidence can be almost fully compensated.

The shaped pulse and the reference are recombined using a second pair of glass wedges (GW2). The reference is used to characterize the shaped pulse via dual-channel

Table 4.2 | Specified and calculated parameters of the setup.

Parameter	Value	Parameter	Value
Wavelength range	740–880 nm	Tele. beam sep. δ_{out}	10.26°
Breadboard base area	1200 × 600 mm	Grating frequency g	850 mm^{-1}
Breadboard height	59 mm	Optical axis telescope β	−43.73°
Beam height	50 mm	Angle of incidence Θ_{i}^{1}	−48.86°
Height behind periscope	88 mm	Angle of incidence Θ_{i}^{2}	−38.60°
TFP diameter	1.0"	Optical axis $4f$ $\Theta_{4f}^{\text{o.a.}}$	0°
TFP thickness	0.5 mm	$4f$ max. beam radius	2.57 mm
TFP angle of incidence	77°	Cylindrical lens f_{cyl}	250 mm
TFP max. beam radius	1.03 mm	LC pixel beam radius	< 27 µm
TFP beam sep. δ_{in}	26°	Number of LC pixels	2 × 640
Tele. L1 focal length f_1	51.6 mm	LC pixel size	97 µm × 10 mm
Tele. L1 diameter	1.5"	LC pixel gap	3 µm
Tele. L2 focal length f_2	125 mm	Pos. beam 1 at SLM	1.3 to 31.3 mm
Tele. L2 diameter	2.0"	Pos. beam 2 at SLM	-31.3 to -1.3 mm
Tele. demag. factor	0.395	Max. temporal delay	$\approx \pm 2.5$ ps

Fourier-transform spectral interferometry (FTSI) (see Section 2.5.2). The reference is temporally delayed by a time delay τ with respect to the shaped beam using a mechanical stage and its polarization is rotated to 45° and cleaned with a combination of a $\lambda/2$ plate and a linear polarizer. The neutral density (ND) filter wheel allows the tuning of the intensity ratio between the shaped pulse and the reference. All beams can be individually blocked by mechanical shutters driven by servo motors.

The whole setup is placed in a sealed housing to improve the interferometric stability between the two shaped beams and the shaped beams and the reference. The housing has two small holes for the incoming and outgoing beam. The fans of the SLM are connected to the outside via an air tube for heat management. The ND filter wheel is connected to a motor so that the enclosure does not have to be opened to adjust the intensity of the shaped beam for the pulse characterization, as both pulses should have the same intensity for the FTSI characterization. The spatially dispersed beams within the $4f$ setup are particularly vulnerable to fluctuations due to airflow, for example caused by the mechanical shutters, thus, the $4f$ setup is surrounded by an additional enclosure.

4.5 Possible improvements

The measured throughput efficiency for the shaped pulse behind all optics shown in Fig. 4.8 is 10 %. It could be improved by coating both pairs of glass wedges and by using a nonstandard anti-reflective coating for lens 1 and lens 2 customized to the used angles of incidence. Employing a special coating for the second pair of glass wedges

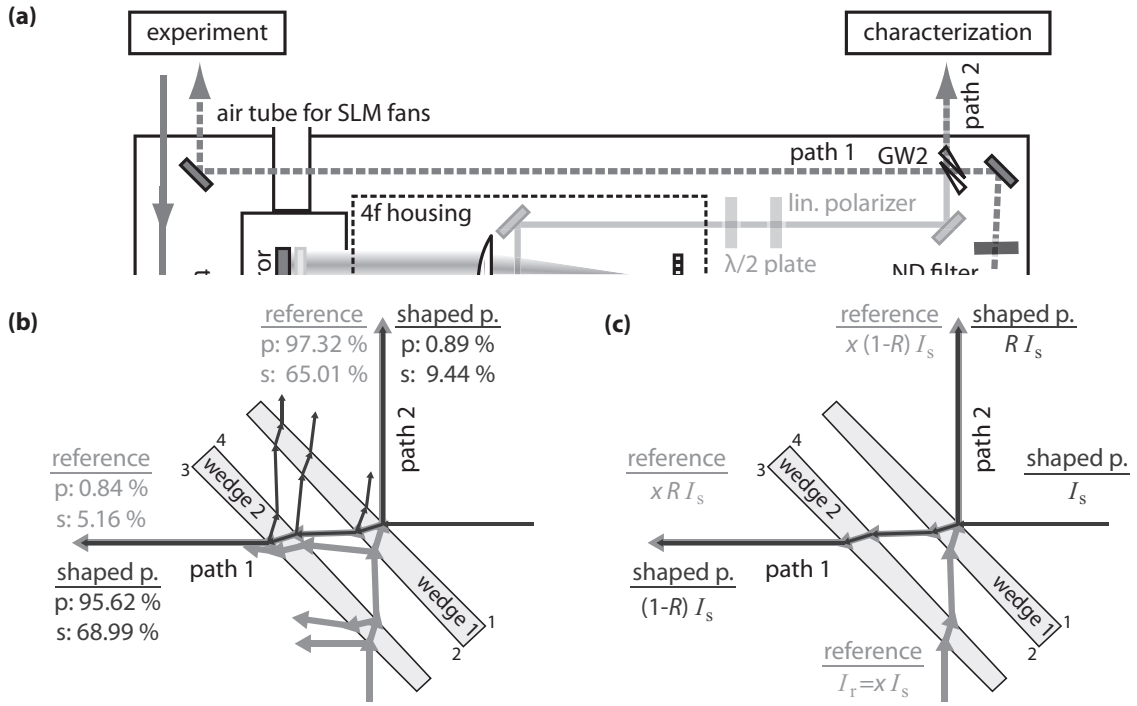

Figure 4.9 | Suggested VFS dual output by coating of the second glass-wedge pair (wedge angle 2°). (a) VFS dual output. By coating the second glass-wedge pair, the reflected part (path 2) of the shaped pulse could be used for the characterization and the transmitted part (path 1) for an experiment. (b) Uncoated glass wedges. Polarization-dependent transmission and reflection efficiencies for the shaped pulse (dark gray) and the reference (light gray) are based on the Fresnel coefficients. (c) Coated glass wedges. Side 2,3,4 have an ideal anti-reflective coating and side 1 employs a coating with polarization independent reflection coefficient R. The beam paths are ray traced for 810 nm. [(b,c)].

would have an additional significant advantage, since in principle the transmitted and the reflected part of the shaped beam emitted at the second glass wedge pair could be used for an experiment [Fig. 4.9(a)]. The reflected part (low intensity) of the shaped beam could be used for the FTSI characterization without the requirement to reduce its intensity with the ND filter wheel by coating the glass wedges such that the intensity of the reference and shaped pulse are inherently matched. The transmitted part (high intensity) could be used to perform an experiment, simultaneously. Figure 4.9(b) shows the efficiency, based on Fresnel reflections, of the shaped pulse (dark gray) and the reference (light gray) for the uncoated wedges. The reference and the shaped pulse are aligned such that they spatially overlap in both pathways behind the glass-wedge pair. The efficiencies for the p and s polarization are quite different and the intensity of the reference and the shaped pulse are matched neither along path 1 nor path 2. These polarization-dependent efficiencies are currently compensated using the $\lambda/2$ plates in the beam lines of the shaped pulse and the reference (see Fig. 4.8). By applying an (ideal) anti-reflective coating on side 2, 3, and 4 and a polarization independent reflective coating with the reflection coefficient R on side 1, the intensities in path 2 could be equalized

for

$$R = \frac{1}{1+x}, \tag{4.16}$$

where x is the ratio between the intensity of the shaped pulse and the reference in front of the second glass wedge pair [Fig. 4.9(c)]. A more exact equation could be derived by considering the remaining reflectivity of the anti-reflective coating. In order to characterize the pulse at the experiment (path 1) by characterizing the pulse emitted along path 2, the phase difference between the two paths has to be determined once. This could be done by comparing the FTSI characterization of the shaped pulses along the two pathways. This suggested dual output of the VFS would be especially valuable as the FTSI characterization can be used as feedback to compensate the remaining long-term stability issues of the presented setup (see Section 6.4) while performing an experiment.

Another possible improvement is the reduction of the optical aberrations of the setup. The ray-tracing simulation in Section 4.3 showed that the beam profile behind the VFS exhibits noticeable differences in the collimation for different frequency components and a slight horizontal angular chirp if the setup is used in combination with a broadband laser. The simulation showed that these deformations of the beam profile are primarily caused by the telescope and only to a minor extent by the cylindrical lens. The replacement of the cylindrical lens by a focusing mirror and folding mirror is therefore not recommended as this could also introduce an additional vertical angular chirp of the beam profile. Hence, the performance of the telescope should be improved if required. In general, a telescope with larger focal lengths should be preferred, reducing the optical aberrations. This can, however, not be realized due to limited space on the breadboard of the vector-field shaper. It must also be considered that a larger telescope could negatively affect the stability of the setup. To improve the performance of the telescope, the use of best form lenses or focusing mirrors for the telescope is suggested. Best form lenses minimize the comatic aberration. However, based on the simulations, it seems that the main problem is not the divergence in the x direction but the wavelength-dependent difference in the divergence. Therefore, ray-tracing simulation should be first employed to investigate the chromatic aberration of these lenses and to determine to what extent the outgoing beam profile can be actually improved by their application. Focusing mirrors are achromatic, but their application and the additionally required folding mirrors will reduce the interferometric stability of the setup. By using focusing mirrors in a folded geometry, larger focal lengths can, and properly must be used on the current breadboard as depicted in Fig. 4.10. This figure illustrates only the principle idea and not the results of ray-tracing simulations. The beam profile quality could be significantly reduced due to the non-normal angle of incidence in the horizontal and vertical direction on the focusing mirrors – even if off-axis parabolic mirrors are used. The possible optical aberrations of such an optical layout must, therefore, be examined in ray-tracing simulations in advance. For future improvements, more detailed ray-tracing simulations of the entire optical setup should also account for the TFP thickness, the grating, and the spherical aberration of the cylindrical lens.

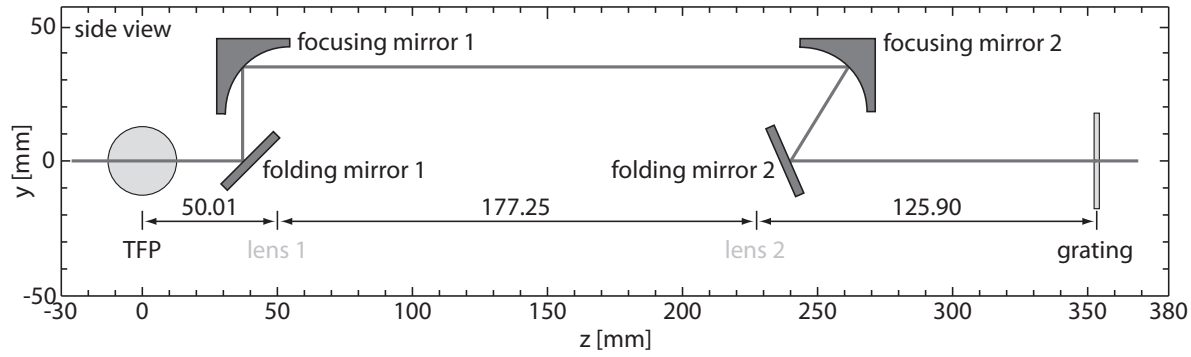

Figure 4.10 | Schematic of the telescope in front of the grating using focusing mirrors. Instead of using lenses, a combination of folding and focusing mirrors, with larger focal lengths, could be used to avoid chromatic aberrations.

4.6 Summary

Considering the current technology, an interferometric common-path vector-field shaper seems to be the best option for frequency-domain based manipulation of all four degrees of freedom (phase, amplitude, ellipticity, and orientation) of an ultrashort laser pulse. In this chapter, an insight into the design process of the presented setup was given. The optimal parameters for the $4f$ setup were found by numerical calculations. The goal of these calculations was to ensure that the two beams have similar frequency distributions at the liquid-crystal spatial light modulator and span as many pixels as possible without spatial overlap. The suitability of a Wollaston prism and of a thin-film polarizer (TFP) for separating the incoming laser beam into two orthogonally polarized beams and for recombining them to a single pulse were examined in depth. The benefits of the TFP outbalanced the advantages of a Wollaston prism for the presented setup. In the used crossed-polarizer arrangement, the TFP provides an extinction ratio in the order of 15000:1 and the polarization-dependent efficiencies of the TFP and the $4f$ setup are compensated. A telescope is used to demagnify the separation angle of the two beams behind the TFP and to realize a common-path setup. The separation angle behind the telescope was determined via ray tracing with high precision, which is required for the numerical calculations of the $4f$ setup. Further the effect of the telescope and the $4f$ setup on the beam profile of the shaped pulse was investigated. It was found that a significant beam profile deformation is present if the incoming and the back-going beams do not propagate in the same plane parallel to the table. A propagation of the incoming beams parallel to the back-going beams is only possible using a TFP in the cross-polarizer arrangement, emphasizing its benefit for the presented setup. It was also found that the cylindrical lens has only a minor influence on the chromatic aberrations of the system and that these are mainly caused by the telescope. At the end of this chapter the optical layout of the entire setup was discussed and possible improvements were suggested.

5 Software implementation

To operate the presented vector-field shaper, an implementation into the software environment used in our group was necessary. Furthermore, different parameterizations for manipulating the electric vector field for various experiments had to be programmed. This chapter covers the main software written for this project. It is not intended to be a manual for the selected applications, but rather gives an overview on their functional principles and their features.

Five different parameterizations are discussed, which were developed to exploit the extended shaping capabilities of the presented vector-field shaper (Section 5.1). These were integrated in two executables called *VFS Control Center* (Section 5.2) and *Parameter Scan* (Section 5.3). The *VFS Control Center* was newly created to operate the VFS and to manually manipulate the complete vector field of an ultrashort laser pulse. The *Parameter Scan* is an advanced measurement suite developed by former group members, which is used to perform nearly all the experiments in our group. Two new modules were integrated for the experiments presented in this thesis. The first module (Section 5.3.1) is used to generate and apply phase patterns based on the introduced parameterizations. The second module (Section 5.3.2) features an automated on-the-fly dual-channel FTSI evaluation and the generation of a phase pattern to compensate the remaining instabilities of the presented interferometric vector-field shaper.

5.1 Parameterizations for pulse manipulation

In general, the phase value for every pixel (or a group of pixels) and layer of the SLM can be used as parameters to manipulate the incident electric field. This pixel parameterization together with an optimization algorithm was, for example, used for pulse compression [206, 215], the generation of target pulse shapes [217] and quantum control [18, 25, 222]. However, the large number of parameters can negatively influence the performance and speed of convergence of the optimization algorithm. Hence, often a smaller set of variables, which describe certain characteristics of the pulse, is desired. This facilitates also the interpretation of the optimal pulse shape in the field of quantum control [225, 266].

Especially for quantum control, many different parameterizations were utilized. For example, the transition probability of a multiphoton process was manipulated by applying a phase step and scanning the position of this step [221]. Chirped laser pulses are also of high interest for quantum control [267–271]. Such chirped pulses can be generated using a pulse shaper and applying a polynomial phase function parameterized by the Taylor coefficients and the center wavelength [see Eq. (2.14) and Eq. (2.16)].

Other parameterizations were developed to generate pulse trains for spectroscopy

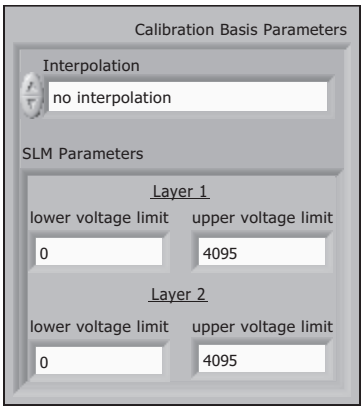

Figure 5.1 | GUI of the *Calibration Basis*. The parameters of the *Calibration Basis* are the lower and upper voltage limit for layer 1 and layer 2. The numbers of sampling points across the pixel array are determined by the size of the gene array (see text) and the applied voltage depends on the values of the elements of this gene array.

and quantum control. This can be realized by varying the position and height of a phase step [150] by applying a sinusoidal phase with parameters phase, amplitude, and frequency [17, 18, 20, 21, 150, 220, 225, 227, 233] or by applying a triangular phase with specified slopes and breakpoint [150, 226, 271] if phase-only shaping is employed.

More sophisticated pulse trains consisting of identical pulse copies can be generated by combining phase and amplitude shaping [66, 81, 91, 92, 110, 239]. For this purpose, e.g., the delay and relative phase between four consecutive pulses can be used as parameters [110].

In order to manipulate a pulse, the used parameters have to be converted to the corresponding phase retardation functions applied to layer 1 and layer 2. The software to perform this operation is in the following called "basis". Five different bases were realized for the extended shaping capabilities of the presented vector-field shaper. The bases are written in LabVIEW [272]. They are no standalone applications, but called as functions (in LabVIEW called SubVIs) which can be used in other LabVIEW VIs[1] and will be described in the following. They are based on parameterizations used in our group for conventional 2-layer pulse shapers and on approaches reported in the literature (see references in the corresponding section), but were extended to take full vector-field control into account.

5.1.1 Calibration Basis

The *Calibration Basis* is the simplest implemented basis as it does not automatically distinguish between the different pixel areas covered by the two beams. The parameters of this basis are the voltages applied to the pixels of the SLM. As it can be seen in its graphical user interface (GUI) (Fig. 5.1), only the lower and upper voltage limit for layer 1 and 2 will be specified in the controls of the basis. For the calculation of the voltage pattern for layer 1 and 2 a so-called gene array is required. The gene array is a one-dimensional array with an arbitrary number of elements, called genes. Each gene is a double-precision floating-point number in the range [0, 1]. The applied voltages are calculated by

$$\text{applied voltage} = \text{gene value} \times (\text{upper limit} - \text{lower limit}) + \text{lower limit}. \tag{5.1}$$

[1] Software applications created with LabVIEW are called virtual instruments (VIs).

The first half of the gene array controls the voltages applied to layer 1 and the second half the voltages applied to layer 2. The size of each half determines the number of sampling points used across the whole pixel array. These sampling points are linear distributed. If the gene array consists of only two genes, the first gene will control layer 1 and the second layer 2. As only one sampling point is present all pixels of the respective layer will be set to the same voltage. If each half contains 640 genes, every pixel will be addressed individually. For a gene number in between, the voltage values of each pixel will be determined either by interpolating between the sampling points or by setting the voltage of every pixel to the value of the nearest sampling point. Implemented interpolations methods are linear, spline, and cubic Hermite spline interpolation. The advantage of this basis is that no knowledge of the phase or wavelength calibration[2] is needed. It can for example be used in conjunction with an optimization algorithm, but was primarily created to provide an end-user friendly parameterization to calibrate the VFS.

5.1.2 Pixel Basis and Spectral Basis

The *Pixel Basis* and the *Spectral Basis* are extensions of the *Calibration Basis*. The main difference between those and the *Calibration Basis* is that they account for the fact that two separated beams are manipulated by different pixel groups. This provides a more advanced control over the created pulse shapes. The *Pixel Basis* samples both beams in the "pixel domain" and the *Spectral Basis* in the frequency domain. Besides this difference their functional principle is identical. Their controls are shown in Fig. 5.2.

Similar to the *Calibration Basis*, both bases mentioned above require a gene array as the parameters are not directly specified and only a range for these parameters is given. Using the *Pixel* or *Spectral Basis*, these genes values can be interpreted as voltages at layer 1 and 2, phase retardation at layer 1 and 2, or as phase and amplitude modulation applied to the two beams[3]. If the phase is used as parameterization, either the absolute phase of each sampling point or the relative phase between consecutive sampling points can be varied. The distribution of the gene array across the parameters depends on whether amplitude and/or polarization shaping is selected (Fig. 5.3). If amplitude shaping is disabled, layer 2 will be set to the same voltage/phase values as layer 1 and if polarization shaping is disabled, the voltage/phase values for the transmitted beam will be sampled to the reflected beam. The number of genes determines, analogously to the *Calibration Basis*, the number of sampling points in the pixel or frequency domain. The range in which the sampling points are distributed can be limited if only a part of the spectrum should be modulated. In the *Spectral Basis*, the sampling points can either be linearly distributed in frequency or wavelength. Other distributions could be easily implemented, for example, a Gaussian distribution in order to have more sample points in regions with high spectral intensity.

[2]The phase calibration is the assignment of the phase retardation to the voltage and the wavelength calibration is the assignment of the wavelength to the corresponding pixel number.

[3]It should be noted that it must be distinguished between the applied phase (retardation) at layer 1 and layer 2, and the applied phase (modulation) to the pulse, as the applied phase as well as the transmission are a function of the phase (retardation) applied at layer 1 and layer 2, see Eq. (4.15).

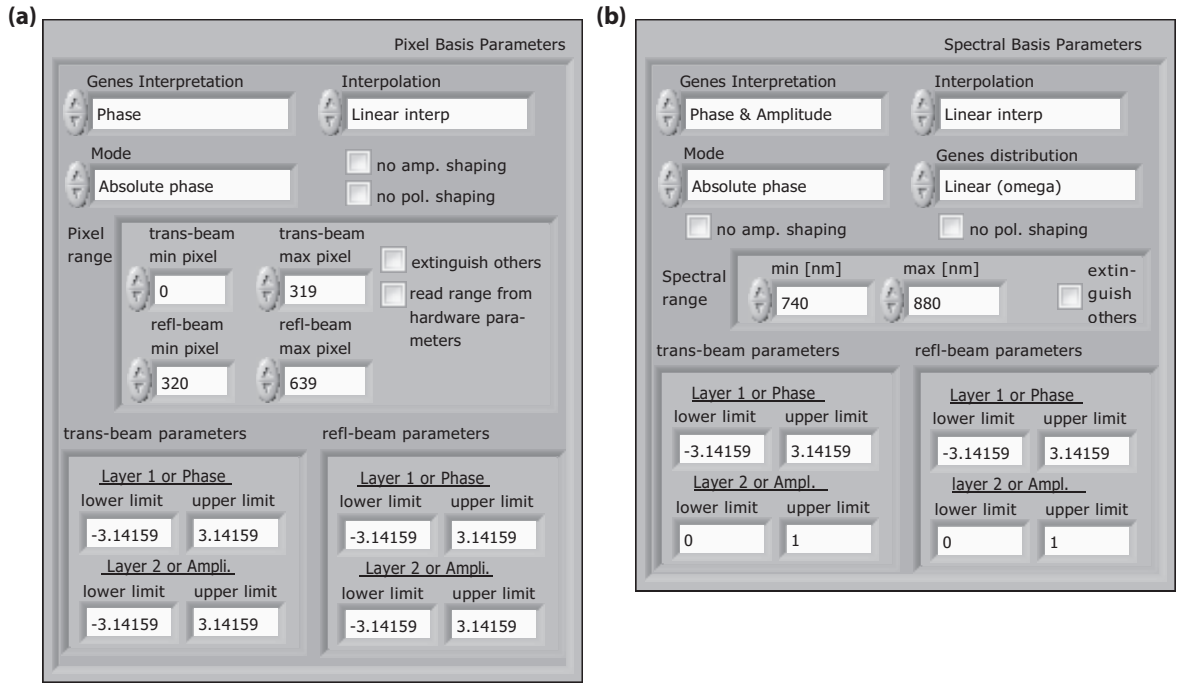

Figure 5.2 | GUIs of the *Pixel Basis* [(a)] and *Spectral Basis* [(b)]. The GUIs are used to select different options and independently specify the range of the "modulation parameters" for both beams. For a detailed description, see text.

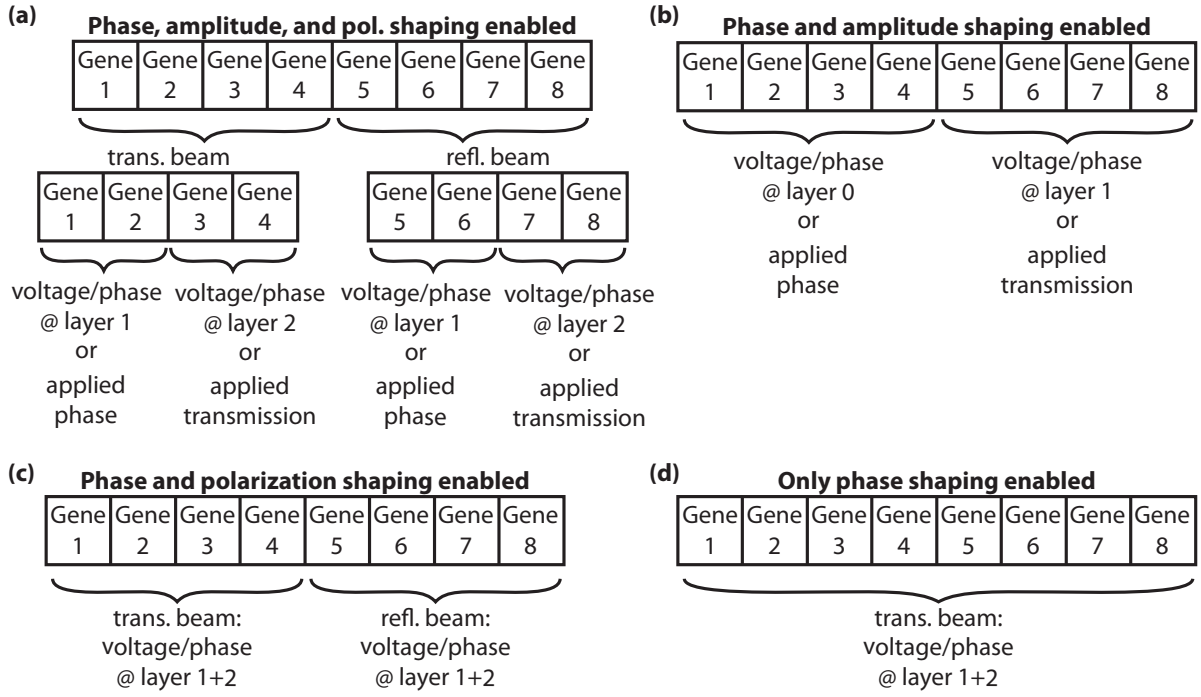

Figure 5.3 | Gene distribution in the *Pixel Basis* and *Spectral Basis*. The gene array will determine the applied parameters based on the specified upper and lower limits in the GUI of the basis. The distribution of the gene array across the available parameters depends on the allowed shaping modes [(a–d)]. The size of the gene array (here eight genes) for each parameter determines the sampling size [2 (a), 4 (b), 4 (c), 8 (d)] in pixel or frequency domain.

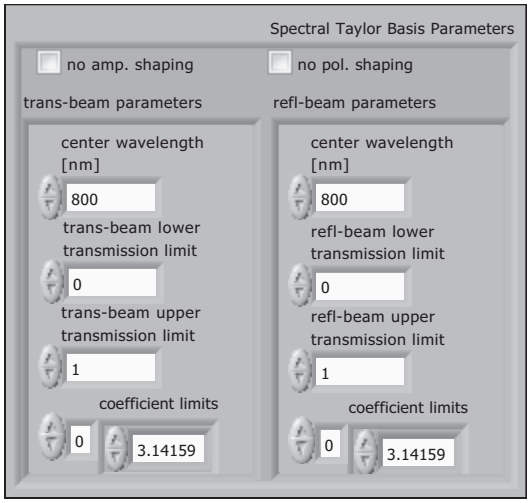

Figure 5.4 | GUI of the *Spectral Taylor Basis*. Chirped polarization shaped laser pulses can be generated by varying the transmission for each polarization component and by applying a polynomial phase. The limits of these coefficients are stored in a one-dimensional array with arbitrary length. The applied transmission and spectral phase will be determined by the gene array, see text.

The advantage of the *Pixel Basis*, compared to the *Spectral Basis*, is the ability to directly address certain pixel ranges. It can therefore be used to perform an experiment without the need to calibrate the VFS, if voltages are used as parameterization. However, this approach has some drawbacks due to the fact that, in general, the frequency distributions of the two beams can differ in the specified pixel ranges. As the sample points will be distributed linear across each pixel range, these sampling points will likely correspond to different frequencies of the two beams. This can lead to undesired shaping artifacts depending on the number of sampling points and the chosen interpolation method. Especially the resulting polarization state of the shaped pulse can be affected.

Both implemented bases are suitable to perform experiments employing an optimization algorithm or scanning simple phase patterns, for example frequency-independent amplitude and phase modulations. If a VFS calibration is present, the use of the *Spectral Basis* is recommended. Both bases were created mainly for future control experiments and were so far only used for simple experiments not presented in this thesis.

5.1.3 Spectral Taylor Basis

The *Spectral Taylor Basis* (Fig. 5.4) was created to generate chirped polarization shaped pulses. The spectral phase of both beams can independently be manipulated by using Taylor coefficients. The Taylor series is centered at the specified center wavelength [see Eq. (2.14) and Eq. (2.16)]. In addition, the transmission of both beams can be varied to generate arbitrary polarization states. For these parameters, a range has to be specified in the GUI of the *Spectral Taylor Basis* (Fig. 5.4), similar to the previously introduced bases. The lower and upper transmission value can independently be specified. For each Taylor coefficient $\widehat{b}_j$ only one value is defined. The lower limit is given by $-\widehat{b}_j$ and the upper limit by $+\widehat{b}_j$. The actual used Taylor coefficient $b_j^{\mathrm{p/s}}$ and transmission $m_{\mathrm{p/s}}$ is determined by the gene array. The modulation function generated by the *Spectral*

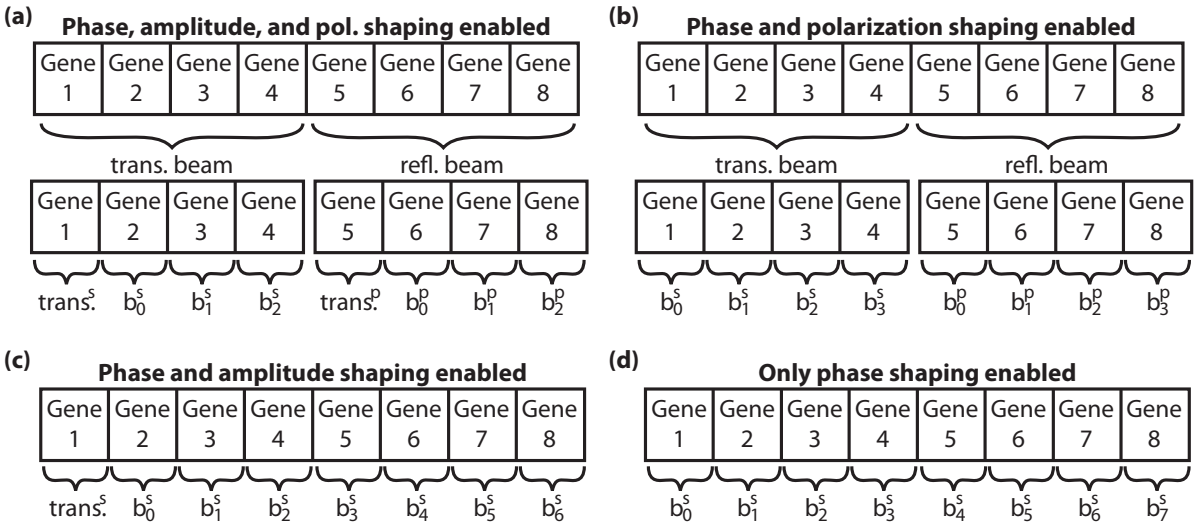

Figure 5.5 | Gene distribution in the *Spectral Taylor Basis*. The *Spectral Taylor Basis* requires a gene array to calculate the applied modulation function in Eq. (5.2). The number of genes determines the order of the applied polynomial phase given by the Taylor coefficients b_j, depending on the allowed shaping modes [(a–d)]. For the applied transmission only one gene value is required.

Taylor Basis is

$$\vec{M}(\omega) = \begin{pmatrix} m_\mathrm{p}\, \mathrm{e}^{-\mathrm{i}\left[\sum_{j=0}^{N} \frac{b_j^\mathrm{p}}{j!}\,(\omega-\omega_0)^j\right]} \\ m_\mathrm{s}\, \mathrm{e}^{-\mathrm{i}\left[\sum_{j=0}^{N} \frac{b_j^\mathrm{s}}{j!}\,(\omega-\omega_0)^j\right]} \end{pmatrix}, \tag{5.2}$$

where the order N of the polynomial phase is determined by the number of genes. The gene distribution for the parameters of the *Spectral Taylor Basis* depends also on the allowed shaping modes, as illustrated in Fig. 5.5. If amplitude shaping is disabled, no gene value will be used to determine the applied transmission. In this case, $m_\mathrm{p/s}$ is set to the value of the upper transmission limit. If polarization shaping is disabled, the same transmission and spectral phase is applied to both beams, i.e., $m_\mathrm{p} = m_\mathrm{s}$ and $b_j^\mathrm{p} = b_j^\mathrm{s}$.

The implemented *Spectral Taylor Basis* can be used for quantum control, either by deterministic variation of certain parameters or in combination with an optimization algorithm. In this thesis, it was used to generate a simple double pulse sequence by chirping both polarization components and delaying them with respect to each other (see Section 6.6.2).

5.1.4 Polarized Four-Pulse Basis

To generate more sophisticated multipulse sequences with different polarized subpulses, the *Polarized Four-Pulse Basis* was developed. The parameterization of this basis is similar to the quadruple-pulse basis described in [110, 147] and extended for polarization control by using elliptical pulse parameters (see Section 2.2). Figure 5.6 shows a schematic of such a four-pulse sequence and the parameters used to define the sequence. Four-pulse sequences are particularly relevant for coherent two-dimensional spectroscopy

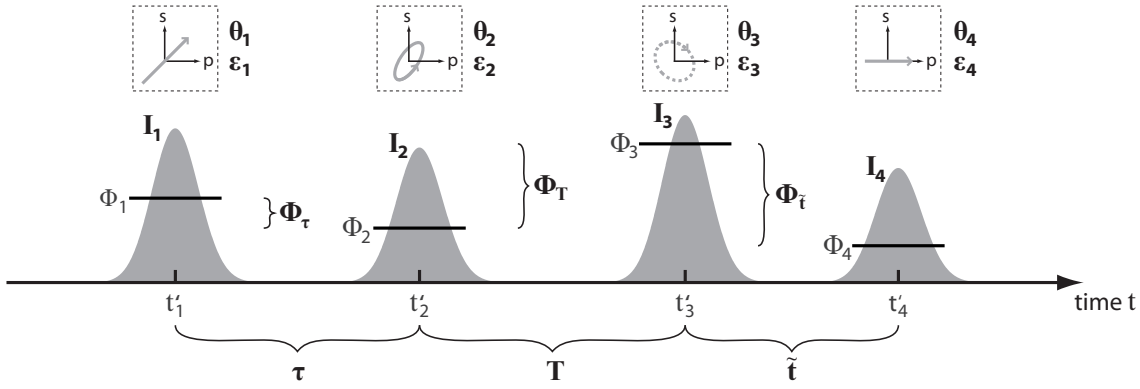

Figure 5.6 | Schematic pulse sequence generate by the *Polarized Four-Pulse Basis*. The pulse sequence is defined by several temporal parameters (bold). These parameters are equivalent to the elliptical pulse parameters described in Section 2.2. The position of each subpulse in time domain will be determined by the relative values coherence time τ, the population time T, and the signal time $\widetilde{t}$, instead of their arrival times t'_1, t'_2, t'_3, and t'_4. Instead of the total phases Φ^1_{tot}, Φ^2_{tot}, Φ^3_{tot}, and Φ^4_{tot}, only the relative phases Φ_τ, Φ_T, and $\Phi_{\widetilde{t}}$ are used. The total intensity of each subpulse can be varied by the parameters I_1, I_2, I_3, and I_4. Their polarization states (dotted insets) are defined by the respective orientations (θ_1, θ_2, θ_3, θ_4) and ellipticities (ϵ_1, ϵ_2, ϵ_3, ϵ_4). In this example, the first subpulse is linearly polarized with an orientation of 45°, the second is left-handed elliptically polarized, the third almost right-handed circularly polarized, and the fourth subpulse linearly polarized at 0°.

and other four-wave mixing experiments, thus the terms for the temporal delays are adapted from this spectroscopy method. Using the *Polarized Four-Pulse Basis*, the relative temporal delay and the relative temporal phase between four subpulses can be defined. In addition, for each subpulse the relative intensity, ellipticity, and orientation in the time domain can be specified.

The transfer function to generate such polarization-shaped pulse sequences will be derived in the following. A single pulse in the time domain with the center frequency ω_0 and an arbitrary arrival time t'_j is defined by

$$\vec{E}^+_j(t) = \begin{pmatrix} E^+_{\mathrm{p},j}(t) \\ E^+_{\mathrm{s},j}(t) \end{pmatrix} = \begin{pmatrix} A^j_{\mathrm{p}}(t-t'_j)\, \mathrm{e}^{\mathrm{i}\left[\omega_0(t-t'_j)+\widehat{\varphi}^j_{\mathrm{p}}(t-t'_j)\right]} \\ A^j_{\mathrm{s}}(t-t'_j)\, \mathrm{e}^{\mathrm{i}\left[\omega_0(t-t'_j)+\widehat{\varphi}^j_{\mathrm{s}}(t-t'_j)\right]} \end{pmatrix}. \tag{5.3}$$

The index j represents the pulse number and the index p and s refer to the respective polarization component. A multipulse sequence of N pulses is given by the superposition of the individual electric fields

$$\vec{E}^+(t) = \frac{1}{N} \sum_{j=1}^{N} \vec{E}^+_j(t). \tag{5.4}$$

The factor $1/N$ is used for normalization as the pulse sequence is generated with a pulse shaper by manipulating the unshaped pulse $\vec{E}^+_0(t)$ with the arrival time $t_0 = 0$. Hence, the total field intensity of the sequence is limited by the intensity of $\vec{E}^+_0(t)$. By using a constant prefactor, the energy of the unshaped pulse is equally distributed among the

N subpulses. The delayed pulses can either be generated by shifting only their envelope function and keep the rapid oscillation of the electric field fixed in time domain or by shifting both. The latter is realized by applying a zero-order phase depending on the arrival time t'_j. Following Ref. [239], therefore the parameter γ is introduced and the electric field of pulse j can be written as

$$\vec{E}_j^+(t) = \begin{pmatrix} E_{\mathrm{p},j}^+(t) \\ E_{\mathrm{s},j}^+(t) \end{pmatrix} = \begin{pmatrix} A_\mathrm{p}^j(t-t'_j)\, \mathrm{e}^{\mathrm{i}\left[\omega_0(t-\gamma t'_j)+\widehat{\varphi}_\mathrm{p}^j(t-t'_j)\right]} \\ A_\mathrm{s}^j(t-t'_j)\, \mathrm{e}^{\mathrm{i}\left[\omega_0(t-\gamma t'_j)+\widehat{\varphi}_\mathrm{s}^j(t-t'_j)\right]} \end{pmatrix}. \tag{5.5}$$

For $\gamma = 0$, no delay-dependent zero-order phase is introduced and only the envelope of the pulse is shifted by t'_j. For $\gamma > 0$, the phase is changed and the rapid oscillation is also shifted temporally. The envelope and the rapid field oscillation are equally shifted by t'_j if $\gamma = 1$, as would be the case in an interferometer. The polarization state will not be affected as the relative phase between the two polarization components is independent from γ.

For the sake of simplicity, the unshaped pulse $\vec{E}_0^+(t)$ is assumed to be bandwidth limited with equal amplitudes of both polarization components so that $\widehat{\varphi}_\mathrm{p}^j(t-t'_j) = \widehat{\varphi}_\mathrm{s}^j(t-t'_j) = 0$ and $A_\mathrm{p}^j(t-t'_j) = A_\mathrm{s}^j(t-t'_j) = A^j(t-t'_j)$ holds. If the unshaped pulse $\vec{E}_0^+(t)$ is initially not bandwidth limited, it can be compressed by applying an offset phase to the pulse shaper.

To manipulate the total intensity, or more precisely, the relative intensity $I_j \in [0, 1]$, the orientation θ_j, the ellipticity ϵ_j, and the total phase Φ_tot^j with the vector-field shaper, the parameters m_p^j, m_s^j, φ_p^j, and φ_s^j are introduced[4]. The amplitude modulations of the two orthogonal polarization components of pulse j are described by $m_\mathrm{p/s}^j$ and the phase modulations by $\varphi_\mathrm{p/s}^j$. These parameters are time independent as the generation of pulse sequences consisting of bandwidth-limited pulses with a time-independent polarization state is desired. Considering these parameters, the electric field of a subpulse is given by

$$\vec{E}_j^+(t) = \begin{pmatrix} E_{\mathrm{p},j}^+(t) \\ E_{\mathrm{s},j}^+(t) \end{pmatrix} = A_j(t-t'_j) \begin{pmatrix} m_\mathrm{p}^j\, \mathrm{e}^{\mathrm{i}\left[\varphi_\mathrm{p}^j+\omega_0(t-\gamma t'_j)\right]} \\ m_\mathrm{s}^j\, \mathrm{e}^{\mathrm{i}\left[\varphi_\mathrm{s}^j+\omega_0(t-\gamma t'_j)\right]} \end{pmatrix}. \tag{5.6}$$

The modulation of the relative intensity I_j depends on the absolute values of m_p^j and m_s^j, the total phase on the absolute values of φ_p^j and φ_s^j, and the polarization state is affected by the ratio $m_\mathrm{p}^j/m_\mathrm{s}^j$ and the phase difference $\varphi_\mathrm{s}^j - \varphi_\mathrm{p}^j$. To calculate m_p^j, m_s^j, φ_p^j and φ_s^j, based on given elliptical pulse parameters Eq. (2.28)–(2.34) can be used.

To derive the modulation function in frequency domain, $\vec{E}^+(t)$ is Fourier transformed. This results in

$$\vec{E}^+(\omega) = \frac{1}{N} \sum_{j=1}^{N} \vec{E}_j^+(\omega) \tag{5.7}$$

with

$$\vec{E}_j^+(\omega) = \begin{pmatrix} E_{\mathrm{p},j}^+(\omega) \\ E_{\mathrm{s},j}^+(\omega) \end{pmatrix} = A^j(\omega-\omega_0) \begin{pmatrix} m_\mathrm{p}^j\, \mathrm{e}^{-\mathrm{i}\{-\varphi_\mathrm{p}^j+[\omega-\omega_0(1-\gamma)]t_j\}} \\ m_\mathrm{s}^j\, \mathrm{e}^{-\mathrm{i}\{-\varphi_\mathrm{s}^j+[\omega-\omega_0(1-\gamma)]t_j\}} \end{pmatrix}. \tag{5.8}$$

[4] $m_\mathrm{p}^j,\, m_\mathrm{s}^j \in [0, 1]$.

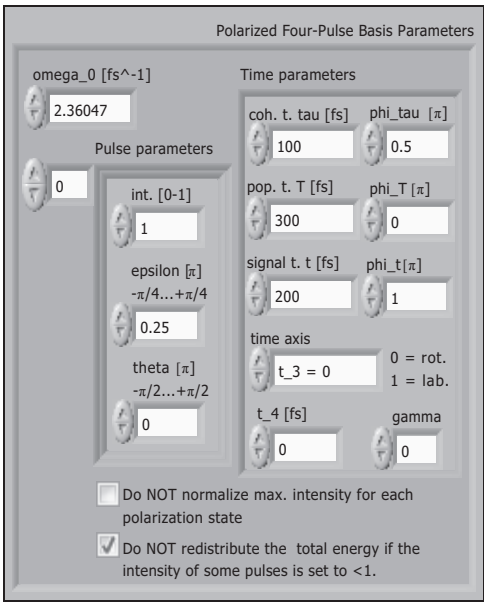

Figure 5.7 | GUI of the *Polarized Four-Pulse Basis*. The time delays between the four pulses and their relative phases can be specified. The other elliptical pulse parameters (I_j, θ_j, ϵ_j) can be specified for each such pulse individually in the array "pulse parameters". The center frequency in combination with parameter γ will determine whether the envelope and the rapid oscillation of the electric field is shifted in time or only the envelope, see text.

$A^j(\omega-\omega_0)$ corresponds to the spectral amplitudes centered on frequency zero. The term $[\omega-\omega_0(1-\gamma)]\,t_j$ corresponds to a linear phase in the spectral domain and causes the temporal delay of the pulse. The constant spectral phases $-\varphi^j_{\mathrm{p/s}}$ determine the zero-order phase in the time domain directly. The spectral amplitude is manipulated by m^j_{p} and m^j_{s}.

The modulation function required for four-pulse sequences, based on Eq. (5.7) and Eq. (5.8), is given by

$$M(\omega)=\begin{pmatrix}M_{\mathrm{p}}(\omega)\\ M_{\mathrm{s}}(\omega)\end{pmatrix}=\frac{1}{4}\sum_{j=1}^{4}\begin{pmatrix}m^j_{\mathrm{p}}\,\mathrm{e}^{-\mathrm{i}\{-\varphi^j_{\mathrm{p}}+[\omega-\omega_0(1-\gamma)]t_j\}}\\ m^j_{\mathrm{s}}\,\mathrm{e}^{-\mathrm{i}\{-\varphi^j_{\mathrm{s}}+[\omega-\omega_0(1-\gamma)]t_j\}}\end{pmatrix}. \tag{5.9}$$

The restriction of the output electric field to four subpulses is only due to the fact that this basis was created specifically for two-dimensional spectroscopy and not due to limitations of the shaping capabilities of the presented setup. The respective amplitude modulation applied to the p/s polarization is given by $\left|M_{\mathrm{p/s}}(\omega)\right|$ and the phase modulation by $\arg\{M_{\mathrm{p/s}}(\omega)\}$.

The GUI of the *Polarized Four-Pulse Basis* is depicted in Fig. 5.7. The relative intensity I_j, the orientation θ_j, and the ellipticity ϵ_j can be specified for each individual subpulse. The arrival times t'_j and the total phases Φ^j_{tot} cannot be specified directly, but are rather described by the coherence time τ, the population time T, the signal time $\widetilde{t}$, and the relative phases Φ_τ, Φ_T, and $\Phi_{\widetilde{t}}$, using the following relations:

$$\tau=t'_2-t'_1, \qquad \Phi_\tau=\Phi^2_{\mathrm{tot}}-\Phi^1_{\mathrm{tot}}, \tag{5.10}$$

$$T=t'_3-t'_2, \qquad \Phi_T=\Phi^3_{\mathrm{tot}}-\Phi^2_{\mathrm{tot}}, \tag{5.11}$$

$$\widetilde{t}=t'_4-t'_3, \qquad \Phi_{\widetilde{t}}=\Phi^4_{\mathrm{tot}}-\Phi^3_{\mathrm{tot}}. \tag{5.12}$$

To calculate t_j and Φ^j_{tot} from these differences, a reference time and reference phase must

be defined. Implemented reference points are

$$t_2 = 0 \quad \wedge \quad \Phi^2_{\mathrm{tot}} = 0, \tag{5.13}$$

$$t_3 = 0 \quad \wedge \quad \Phi^3_{\mathrm{tot}} = 0, \tag{5.14}$$

$$t_4 = x \quad \wedge \quad \Phi^4_{\mathrm{tot}} = 0, \tag{5.15}$$

$$-t_2 = t_3 = T/2 \quad \wedge \quad -\Phi^2_{\mathrm{tot}} = \Phi^3_{\mathrm{tot}} = \Phi_T/2, \tag{5.16}$$

where x is an arbitrary arrival time. It should be noted that specified total phases Φ^j_{tot} will match the realized ones only for $\gamma = 0$ and if the correct center frequency is specified. If ω_0 is incorrect or $\gamma > 0$, a delay-dependent zero-order phase will be introduced affecting the relative phase between consecutive pulses. This is especially important when phase-cycling is employed [66, 273] to extract a certain signal in pulse shaper assisted collinear two-dimensional spectroscopy.

The *Polarized Four-Pulse Basis* can also be used to generate a single polarization shaped pulse or a sequence of two or three pulses by setting certain delays $\left(\tau, T, \widetilde{t}\right)$ to zero and by adjusting the relative intensities (I_1, I_2, I_3, I_4). It should be noted that as soon as a single relative intensity is set to $I_j < 1$, energy of the unshaped pulse is "lost", due to the constant prefactor of 0.25 in Eq. (5.9). This "lost" energy can optionally be redistributed among the remaining subpulses by normalizing the applied amplitude modulation using $\max\{M^{\mathrm{VFS}}_{\mathrm{p/s}}(\omega)\}$. The relative intensity between the subpulses or their polarization state will not be affected by this normalization.

The maximum (sub-)pulse intensity depends in general on the created polarization state if an interferometric VFS is used (see Fig. 3.11). This effect is automatically compensated by using the described modulation function [Eq. (5.9)] and parameter transformation [Eq. (2.28)–(2.34)]. This normalization can be "disabled" by dividing m^j_{p} and m^j_{s} by $\max\{m^j_{\mathrm{p/s}}\}$. In this case, every subpulse will have the maximum possible pulse energy, but the intensity ratio between consecutive pulses will depend on their polarization states and is no longer given by the specified relative intensities I_j.

The versatility of the presented *Polarized Four-Pulse Basis* makes it highly suitable for different (multipulse) spectroscopy methods, but can also be utilized for quantum control. The *Polarized Four-Pulse Basis* was used in this thesis to generate most of the multipulse sequences presented in Section 6.6.

5.1.5 Possible extensions and future parameterizations

In this section, possible extension of the presented *Spectral Basis*, *Spectral Taylor Basis*, and *Polarized Four-Pulse Basis* are briefly suggested. In addition, a new basis – the *von Neumann Basis* – is discussed.

Spectral Basis and Spectral Taylor Basis

Currently, independent parameters are used for the two shaped polarization components in the *Spectral Basis* and the *Spectral Taylor Basis*. For a more intuitive parameterization of polarization-shaped laser pulses it is suggested that also elliptical pulse parameters (see Section 2.2) will be supported. This would be convenient if it is desired to

keep some parameters, for example, the total intensity, or the ellipticity constant in the experiment. It would also allow a normalization of the maximum available intensity of single frequency components, which depends on the generated polarization state using an interferometric VFS (see Fig. 3.11).

This could be realized in the *Spectral Basis* by specifying limits of the relative intensity, the total phase, the orientation, and the ellipticity and by calculating the applied values at each sampling point based on the gene array. For the *Spectral Taylor Basis*, the following modified modulation function is suggested:

$$\vec{M}(\omega) = \begin{pmatrix} m_\mathrm{p}\, \mathrm{e}^{-\mathrm{i}\left[-\varphi_\mathrm{p} - b_0 + \sum_{j=1}^{N} \frac{b_j^\mathrm{p}}{j!}\,(\omega-\omega_0)^j\right]} \\ m_\mathrm{s}\, \mathrm{e}^{-\mathrm{i}\left[-\varphi_\mathrm{s} - b_0 + \sum_{j=1}^{N} \frac{b_j^\mathrm{s}}{j!}\,(\omega-\omega_0)^j\right]} \end{pmatrix}. \tag{5.17}$$

The desired polarization state will be determined by specifying limits for the orientation θ and ellipticity ϵ. By assigning the relative intensity I, the pulse energy can be adjusted. These three parameters (I, θ, ϵ) can be used to calculate m_p, m_s, φ_p, and φ_s using Eqs. (2.28)–(2.34). The total phase of the resulting pulse is manipulated by the parameters b_0, b_j^p and b_j^s. It should be noted that the resulting polarization state in time domain will not be constant if different polynomial phases $b_j^\mathrm{p} \neq b_j^\mathrm{s}$ are applied, since the relative phase between the two polarization components will be frequency dependent in this case. For $b_j^\mathrm{p} = b_j^\mathrm{s}$, the polarization state in time domain will be given by θ and ϵ, as the absolute spectral phase is equal to the negative absolute temporal phase (see Section 2.1). For the transmission, currently only one gene is used in the *Spectral Taylor Basis*. This limits the possible pulse shapes in the time domain as the whole spectrum will be affected by the given transmission value. In general, it could be implemented that a variable number of genes can be used to sample the amplitude modulation in frequency domain, similar to the *Spectral Basis*.

Polarized Four-Pulse Basis

In contrast to the previous bases, the applied parameters of the *Polarized Four-Pulse Basis* are not determined by a gene array, but directly by the values specified in the GUI. Therefore, this basis can currently not be used in combination with an optimization algorithm. However, this could be implemented rather straight forward. For quantum control experiments, also the generation of chirped pulse copies would be of high interest. This could be realized by adding, analogous to the revised *Spectral Taylor Basis*, an additional polynomial phase in the modulation functions $M_{p/s}(\omega)$ [see Eq. (5.9)] of the current *Polarized Four-Pulse Basis*. An extension of this basis to generate N subpulses could, based on the derived equations Eq. (5.7) and Eq. (5.8), also be integrated.

von Neumann Basis

A possible parameterization to achieve a very intuitive control over the electric vector field could be realized by using the von Neumann formalism. It was initially developed as a joint time–frequency description for linearly polarized ultrashort laser pulses [274–277] and recently extended for the description of polarization-shaped pulses [3, 154],

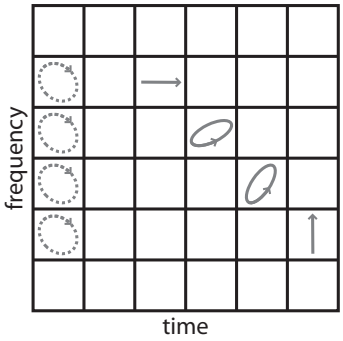

Figure 5.8 | Schematic von Neumann representation of a polarization shaped double-pulse sequence. This representation uses so-called von Neumann coefficients to represent laser pulses in a joint time–frequency picture. Every grid point corresponds to a Gaussian shaped von Neumann basis function. In this simplified example, a double pulse sequence is shown. The polarization state of each time–frequency point is illustrated by a polarization ellipse.

using von Neumann elliptical pulse coefficients. These are analogously defined to Section 2.2 but within this formalism as function of time and frequency on a two-dimensional time–frequency grid. A simplified von Neumann representation of a polarization shaped double pulse sequence is depicted in Fig. 5.8. It can be seen that the first pulse of the sequence is bandwidth-limited, as all frequency components arise at the same time, and it has a time-independent polarization state which is in this case almost right-handed circular. In contrast, the second pulse is down chirped (the frequency components arise at different times) and has a time-varying polarization state. It is first linearly p polarized, then elliptically polarized with increasing orientation and linearly s polarized at later times. The parameter set – the von Neumann coefficients – used for this representation can in principle also be used for the generation of arbitrary electric fields. Due to the limited shaping capabilities of the conventional 2-layer pulse shaper, this basis was not experimentally used for the generation of polarization-shaped pulses, yet. It has the advantage that complex polarization-shaped laser pulses or pulse sequences can intuitively be specified and that the parameters, e.g., the time/frequency position or polarization state, of each von Neumann basis function can easily be scanned. This is of high interest for quantum control and spectroscopy. For more details the reader is referred to Refs. [3] and [154].

5.2 VFS Control Center

To utilize the different bases, they have to be implemented into higher-order VIs. For this purpose, the standalone application *VFS Control Center* was created in LabVIEW [272]. Its main function is opening/closing the connection to the SLM, examining the SLM status, and providing a manual control over the voltages or phases applied at the two LC layers. Its GUI is shown in Fig. 5.9. The GUI and the functions of the VI are basically divided in three groups, corresponding to the three "rows" of the GUI, which will be briefly introduced in the following.

The first group contains the essential functions to operate the SLM. These are the opening and closing of the Firewire connection between the SLM and a computer and the ability to reset it. Other functions in this group are the switching of the driving voltage mode and a status report of the SLM. The driving voltage mode determines the maximal applied voltage. The *Jenoptik* SLM supports two modes: 0–5 V and 0–8 V. Independent of the selected mode, the voltage range is sampled and addressed by 4096 voltage steps.

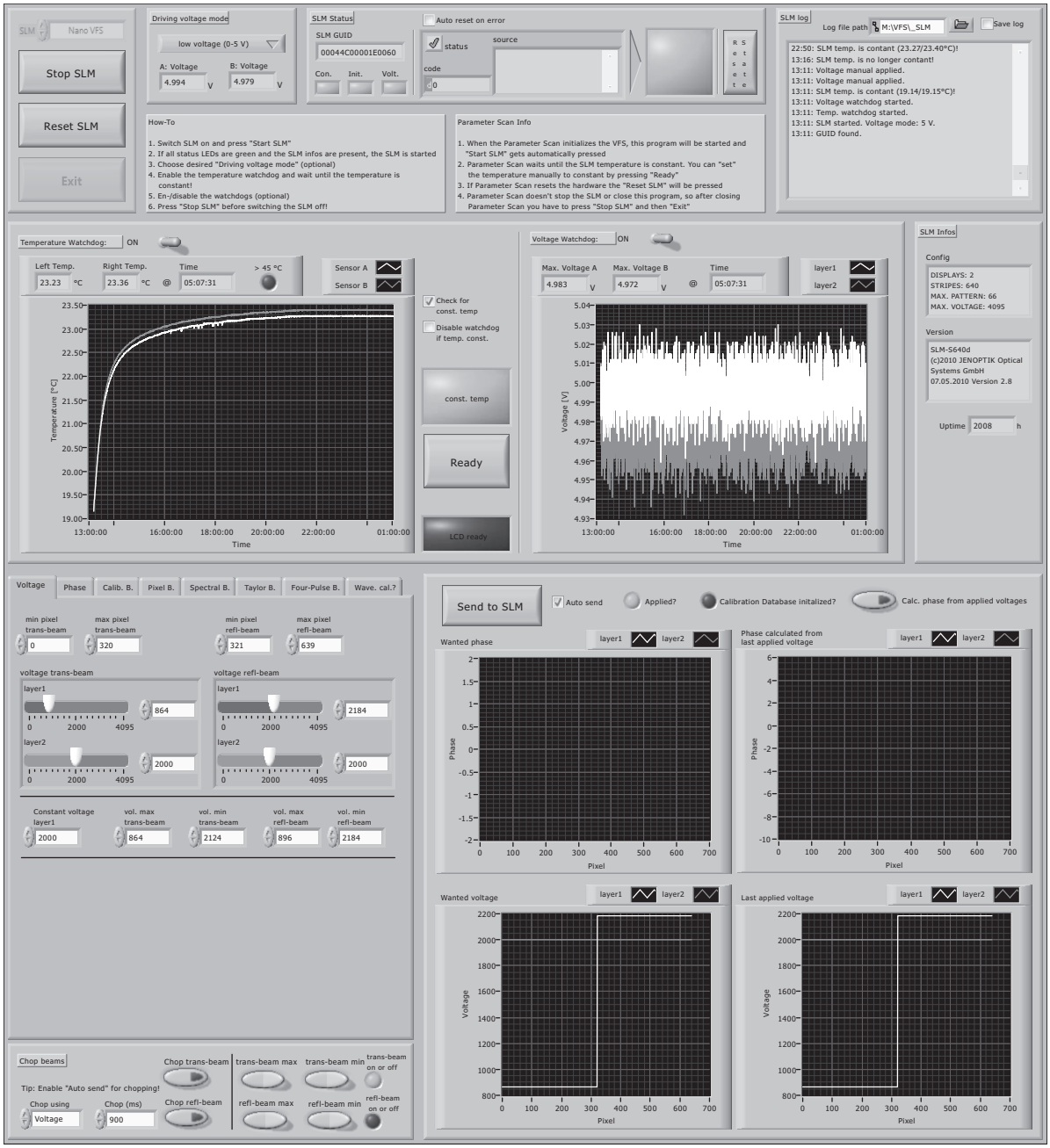

Figure 5.9 | GUI of the *VFS Control Center*. This software program was written in LabVIEW [272] and serves as a standalone toolbox to communicate with the SLM and manipulate the vector field of an ultrashort laser pulses with the presented VFS. For a more detailed discussion of its features, see text.

If an SLM error is reported, the *VFS Control Center* automatically resets the SLM if desired.

The second group contains monitoring of the temperature and the driving voltage. Both functions are realized via "watchdogs". These are background tasks which run independent from all other operations or VIs. Especially watching the temperature is crucial as the phase retardation is not only a function of the applied voltage but also of the SLM temperature (see Section 3.1.1). Therefore, operation and calibration of the SLM under constant temperature is required. For example, in Fig. 5.9 it can be seen that the SLM temperature reaches a constant level about 8 hours after it was switched on.

The third group provides a manual control of the applied voltages or phases. Applying voltages is already required during the building of the setup as the polarization of the two beams has to be rotated by 90° to have an outgoing beam if the crossed-polarizer arrangement is used (see Section 4.2.2). Also useful during the alignment is the option to maximize and minimize the transmission for each beam by a simple button press and to have an automated "chopping" of these beams. This can be used to check the overlap of the incoming and the outgoing beam or the overlap of both beams after the pulse shaper. Instead of (constant) voltages, also phase patterns can be applied if a pulse shaper calibration is present. One option to apply a (complex) phase pattern is to apply a so-called offset phase. This is a two-dimensional array containing a phase value for every pixel and layer. This offset phase is often used to compress the pulse (see Section 6.3) and generated in another software program. For simple experiments and testing it is preferable to generate phase patterns on-the-fly by using certain parameterizations instead of specifying every phase value for each pixel by hand. All bases discussed in Section 5.1 can be manually used to manipulate the incoming pulse with the *VFS Control Center*. Another useful feature is the possibility to verify the wavelength calibration by setting the transmission of a single pixel (specified by the wavelength calibration) to 100 % and all other pixels to 0 %, or vice versa, and checking the resulting spectrum with a spectrometer.

5.3 Parameter Scan

Since the *VFS Control Center* allows only a manual but no automatic variation of the basis parameters and no combination with other hardware, the VFS hardware control was also integrated in the software program *Parameter Scan* to perform more advanced experiments. The *Parameter Scan* is a non-commercial universal measurement suite developed in our group and written in LabVIEW [272]. It was initially created by the former group members Dr. Florian Langhojer and Frank Dimler and is continuously developed by current group members. The idea of this VI is that any implemented hardware or software component can be sequentially arranged in an arbitrary measurement procedure. An element of the measurement sequence is called data acquisition (DA), whether it is a hardware (e.g. a spectrometer) or software (e.g. normalization of the measured spectra) module. The parameters of each data acquisition can be automatically varied in a two-dimensional scan and the output of each data acquisition will be

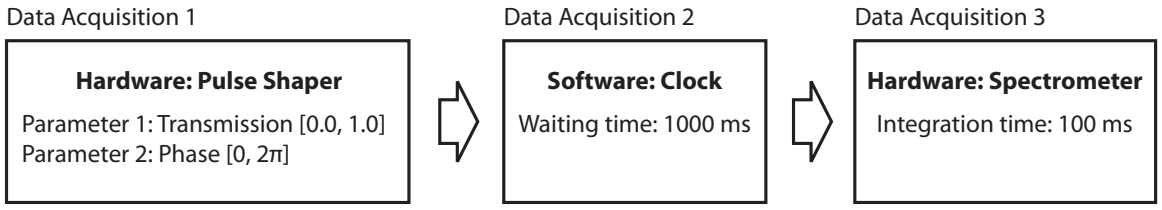

Figure 5.10 | Example for a measurement sequence executed with *Parameter Scan*. The sequence consists of three data acquisitions. The first is a pulse shaper. Two parameters (transmission and phase) will be varied in a two-dimensional scan. In data acquisition 2, a software clock is executed. The parameter "waiting time" is fixed and therefore equal for all steps of the scan. The spectrum is afterwards recorded in data acquisition 3 and saved for each step of the measurement sequence. The parameter "integration time" is also constant.

saved for each step of the scan.

An example for a simple measurement sequence is illustrated in Fig. 5.10. This sequence consists of two hardware modules and one software module. The first hardware is a pulse shaper. In this example, two parameters of this module can be scanned: the transmission and the phase applied to the incoming pulse. This could be done by using the *Spectral Taylor Basis* (Section 5.1.3). After sending the current parameters to the SLM of the pulse shaper, a software clock is executed. After 1000 ms the spectrum is recorded. The applied transmission is scanned in the range [0.0, 1.0] along the first dimension and the applied phase in the range [0, 2π] along the second dimension. The waiting time of the software clock and the integration time of the spectrometer will not be varied during the scan, but this would be also possible. Dimension 2 will be scanned for every step of dimension 1. The variation of the parameters can either be done directly by manipulating the basis controls or by varying the gene array. A more detailed description of the *Parameter Scan* can be found in Ref. [278].

In the following, two data acquisition modules are presented which were added to the *Parameter Scan* in order to perform the experiments presented in this thesis.

5.3.1 Data Acquisition: Vector-Field Shaper

The first hardware module is the data acquisition *Vector-Field Shaper*. Its simplified flowchart and output data are depicted in Fig. 5.11. The settings and parameters for the *Vector-Field Shaper* data acquisition, the gene array and the "binary data" array[5] containing the offset phase are specified within the GUI of the *Parameter Scan*. The *Vector-Field Shaper* module first converts the input parameters (together with the gene array) into phase patterns for layer 1 and layer 2 using the selected basis (see Section 5.1). In the next step, an optional offset phase is added. This offset phase contains for example the phase pattern required to compress the input pulse. In order to apply the resulting phase pattern at the LC SLM layers, the corresponding voltage values have to be calculated based on the pulse shaper calibration and sent to the SLM. If the SLM is not initialized, the *VFS Control Center* will be opened to initialize it and check if

[5]This array contains no binary data but "human readable data". The term is only used because this array is stored in a binary file at the end of the measurement.

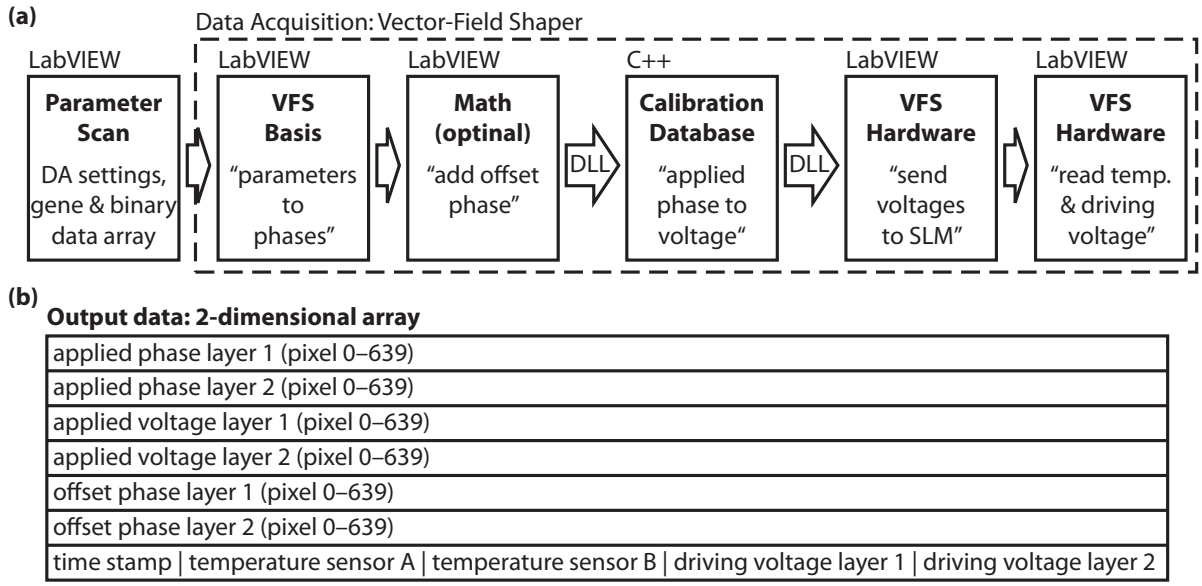

Figure 5.11 | *Parameter Scan* module *Vector-Field Shaper*. (a) Simplified flowchart. First, the basis parameters combined with the gene array specified in the *Parameter Scan* are transferred into phases for layer 1 and 2 of the LC SLM. Optionally, an offset phase is added to these phases and the required voltage values are calculated based on the pulse-shaper calibration. The offset phase is stored in the "binary data" array within the *Parameter Scan*. After the voltage patterns are sent to the SLM, the SLM temperature and driving voltage is read out. This phase-to-voltage operation is programmed in C++, whereas all others are realized in LabVIEW. (b) After the *Vector-Field Shaper* DA is executed, the output data is passed to the *Parameter Scan*. The output data contains the applied phase (including the offset phase), the corresponding voltage values, the used offset phase, a time stamp, the SLM temperature, and the driving voltage of the SLM.

the SLM temperature is already constant. In the last step of the *Vector-Field Shaper* module, the SLM temperature and driving voltage are acquired.

Except of the phase-to-voltage calculation, all steps are executed using LabVIEW. Initially, the phase-to-voltage operation was also realized using LabVIEW and the calibration data was stored for each pulse shaper of our group as global variables. However, due to the large size of the calibration data (2 layer $\times$ 640 pixels $\times$ 4096 voltage steps = 5,242,800 values), this had some negative side effects – especially a high memory consume. To reduce the memory use and to increase the calculation speed, the phase-to-voltage operation was rewritten in C++[6]. The communication between LabVIEW and C++ is realized by using a dynamic-link library (DLL). This reduced the memory use of LabVIEW from $\approx$ 200 MB to $\approx$ 100 MB and the phase-to-voltage calculation time from $\approx$ 30 ms to $\approx$ 20 ms. It has also the advantage that the calibration data is no longer stored as global LabVIEW variable, but loaded from a binary file on the initialization of C++ based *Calibration Database*. By implementing this for all pulse shaper used in our group, the overall memory consumption of the *Parameter Scan* was reduced by $\approx$ 400 MB.

[6]The actual coding in C++ was done in cooperation with Dr. Johannes Buback.

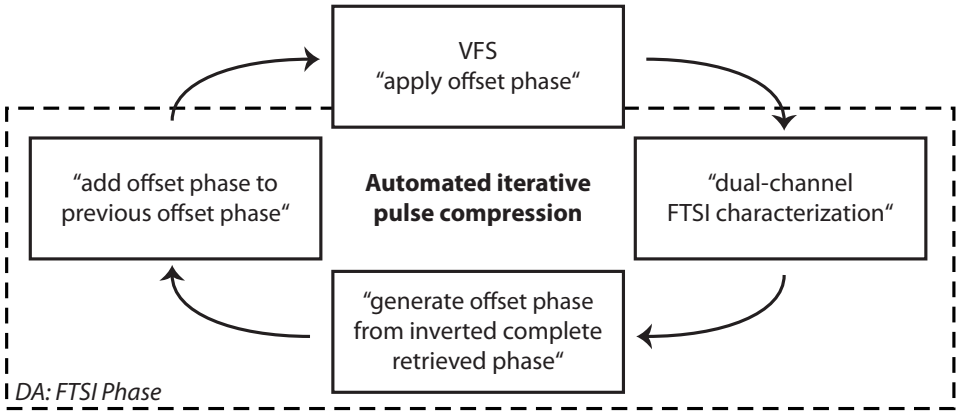

Figure 5.12 | Iterative pulse compression using the *Parameter Scan* in conjunction with the *FTSI phase* module. Pulse compression can be realized by characterizing the unknown pulse via dual-channel FTSI and by applying the complete inverted phase at the VFS. By automating the process of FTSI characterization and offset generation within the newly created *FTSI Phase* module, e.g., an automatized iterative pulse compression can be realized using the *Parameter Scan*. In each step of the iteration, the remaining phase of the pulse is inverted and added to the previous offset phase. This new offset phase will then be used for the next measurement step to improve the pulse compression.

The described *Vector-Field Shaper* data acquisition is the basis to operate the presented setup in conjunction with the *Parameter Scan* in complex measurement sequences and for different kinds of experiments. This module was used to perform the "pulse generation" experiments presented in Chapter 6.

5.3.2 Data Acquisition: FTSI Phase

Polarization-shaped pulses can be characterized using dual-channel FTSI (see Section 2.5.2). This method has the advantage that only the measurement of the linear spectra of the reference pulse, of the unknown pulse and of their interference are required, and that the phase retrieval takes only a few milliseconds using modern computers. Hence, this technique is suitable for a quasi on-the-fly characterization of the shaped pulse generated in each step of the *Parameter Scan*. The retrieved phase information of the pulse cannot be used only to characterize it, but also to directly generate an offset phase for the next measurement step to achieve a certain goal – for example the iterative compression of an unknown pulse. This principle is illustrated in Fig. 5.12. The "apply offset phase" operation can be realized within the *Parameter Scan* by using the presented data acquisition *Vector-Field Shaper*. For the other operations (FTSI evaluation and offset generation), the data acquisition *FTSI Phase* was written. The spectra needed for the dual-channel FTSI characterization are directly recorded with the *Parameter Scan* before the *FTSI Phase* DA is executed as shown in Fig. 5.13(a).

The *Vector-Field Shaper* DA is used to manipulate the shaped pulse. By using computer controlled shutters (DA 3,5,7), the spectra of the reference (DA 4), the unknown pulse (DA 6) and the spectral interference of both pulses (DA 8) can be measured and analyzed in the *FTSI Phase* module (DA 9). The simplified flowchart of the

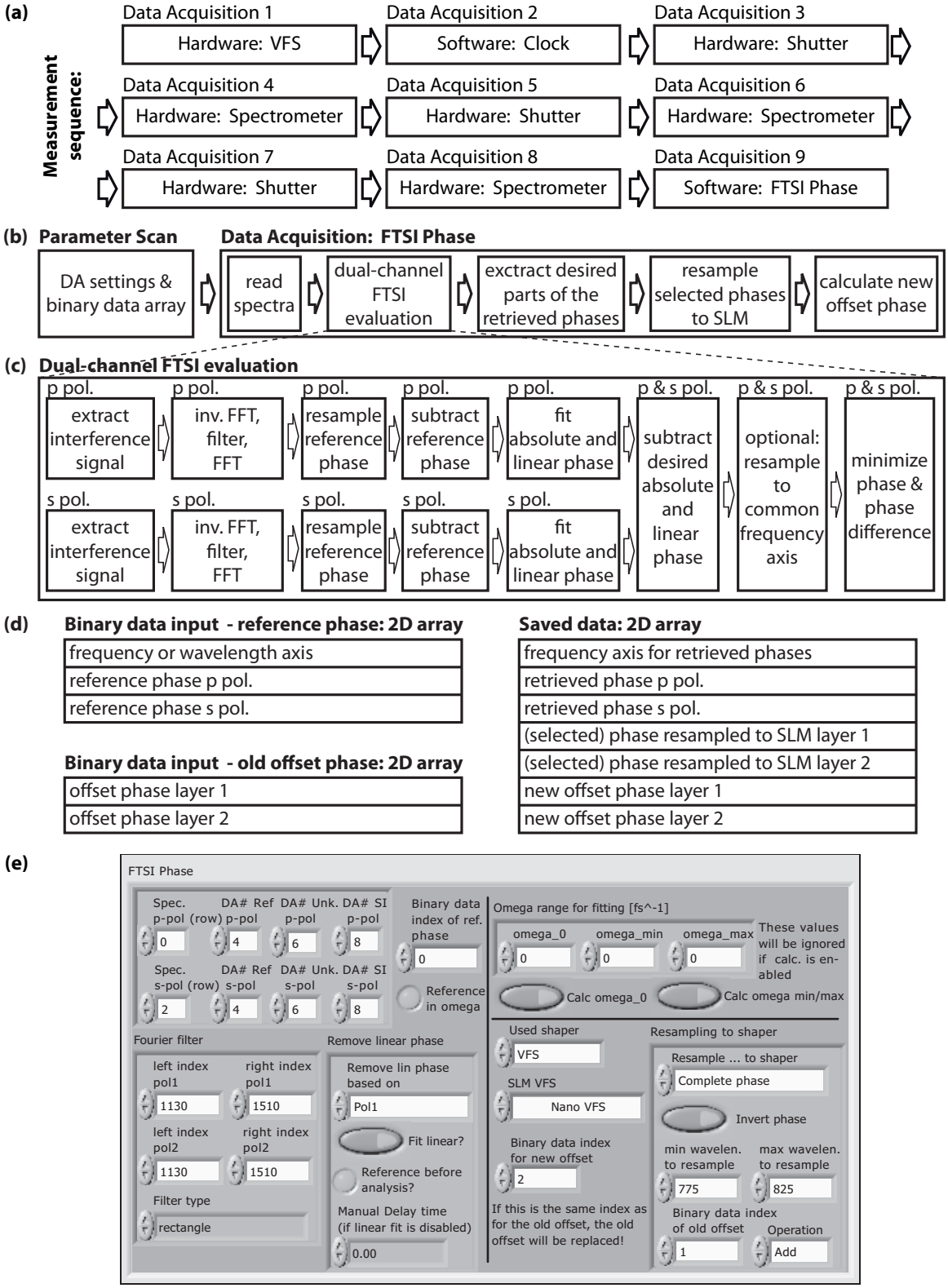

Figure 5.13 | *FTSI Phase* module. (a) Measurement sequence for on-the-fly dual-channel FTSI characterization. (b) Simplified flowchart of the module. (c) Simplified flowchart of the "dual-channel FTSI evaluation" operation. (d) Required input stored in the "binary data" array and output data. (e) *FTSI Phase* control panel.

FTSI Phase DA is illustrated in Fig. 5.13(b,c). The reference phase must be known for both polarization components and specified in the binary data array of the *Parameter Scan* to extract the phase of the unknown pulse. The entries "old offset phase" and "new offset phase" are also stored in the binary data array [Fig. 5.13(d)]. The spectra are directly read from the corresponding data acquisitions [see GUI of the *FTSI Phase* module Fig. 5.13(e)].

The dual-channel FTSI evaluation [Fig. 5.13(c)] follows basically the description given in Section 2.5.2. The interference signal is extracted by subtracting the linear spectrum of the reference and the unknown pulse from the recorded SI signal. The gained interference signal is Fourier filtered using the specified ranges and filter function[7] [see GUI Fig. 5.13(e)]. The reference phase is then sampled to the frequency axis of the measured spectra and subtracted. If the delay between the reference and the shaped pulse is unknown, it can be determined by fitting a first-order polynomial function. These steps are independently executed for both orthogonal polarization components of the shaped pulse (here called p and s polarization). However, in order to maintain the information about the relative phase between the two polarization components and hence the polarization state, the same absolute and linear phase must be subtracted from the retrieved p and s phases. Whether the fitted values of the p or s polarization, or their mean values, should be subtracted, can be selected in the controls of *FTSI Phase* module. In general, both polarization components can be recorded with different spectrometers and the retrieved phase functions may therefore have different frequency axes. If this is the case, the retrieved phases will be sampled to a common frequency axis. In principle, already the interference signal could be sampled to the same frequency axis, however this will cause larger phase error as sampling the retrieved phases [169]. The last step of the dual-channel FTSI evaluation is the minimization of the phases and the phase difference by subtracting the absolute phase at the center frequency ω_0 of either the p or s polarization, or their mean value, from both components and subtracting $n\pi$, where the integral number n is chosen to minimize the phase difference at ω_0. This operation does not alter the relative phase between the p and the s component.

In the next step of the *FTSI Phase* module, the retrieved phases or a derived quantity, like the phase difference, can be sampled to the pixel axis of the selected pulse shaper to generate an offset phase. Current implemented options to determine which parts of the retrieved phases should be used to generate the offset phase are listed in Tab. 5.1. If the option "invert phase" is enabled, all phases are multiplied with -1. Four options are implemented to generate the new offset phase: i) The resampled phase can be added to the old offset, ii) it can be subtracted from the old offset, iii) it can be used as new offset, or iv) the old offset can be kept.

After the execution of *FTSI Phase* module, the frequency axis, the phase of the two polarization components, the resampled phase, and the new offset phase will be stored in a two-dimensional output array [Fig. 5.13(d)].

This module was initially created to actively stabilize the presented setup by using the retrieved phases as feedback (see Section 6.4). To compensate random phase fluctuations of a pulse, either the inverted complete phase or the inverted phase difference can be

[7] The appropriate filter and ranges must be determined once in a VI used to "manually" execute a dual-channel FTSI evaluation. This software program is not presented in this thesis.

Table 5.1 | Options to generate an offset phase. Depending on the selected options, only parts of the retrieved phases will be sampled to the selected polarization component of the pulse. The entry "fit$\{\phi_{\mathrm{p/s}}(\omega)\}$" corresponds to a polynomial fit with respective order.

Option	Sampled to p pol.	Sampled to s pol.
Complete phase	$\phi_{\mathrm{p}}(\omega)$	$\phi_{\mathrm{s}}(\omega)$
Complete phase difference @ pol1	$\phi_{\mathrm{p}}(\omega) - \phi_{\mathrm{s}}(\omega)$	0
Complete phase difference @ pol2	0	$\phi_{\mathrm{s}}(\omega) - \phi_{\mathrm{p}}(\omega)$
0th-order phase	$\phi_{\mathrm{p}}(\omega_0)$	$\phi_{\mathrm{s}}(\omega_0)$
0th-order difference @ pol1	$\phi_{\mathrm{p}}(\omega_0) - \phi_{\mathrm{s}}(\omega_0)$	0
0th-order difference @ pol2	0	$\phi_{\mathrm{s}}(\omega_0) - \phi_{\mathrm{p}}(\omega_0)$
Mean 0th-order phase	fit$\{\phi_{\mathrm{p}}(\omega)\}$	fit$\{\phi_{\mathrm{s}}(\omega)\}$
Mean 0th-order difference @ pol1	fit$\{\phi_{\mathrm{p}}(\omega)\}$ − fit$\{\phi_{\mathrm{s}}(\omega)\}$	0
Mean 0th-order difference @ pol2	0	fit$\{\phi_{\mathrm{s}}(\omega)\}$ − fit$\{\phi_{\mathrm{p}}(\omega)\}$
0th- & 1th-order phase	fit$\{\phi_{\mathrm{p}}(\omega)\}$	fit$\{\phi_{\mathrm{s}}(\omega)\}$
0th- & 1th-order difference @ pol1	fit$\{\phi_{\mathrm{p}}(\omega)\}$ − fit$\{\phi_{\mathrm{s}}(\omega)\}$	0
0th- & 1th-order difference @ pol2	0	fit$\{\phi_{\mathrm{s}}(\omega)\}$ − fit$\{\phi_{\mathrm{p}}(\omega)\}$

used to generate an offset phase for the next measurement step. The derived zero- and first-order phases can be used if higher-order fluctuations should not be compensated, or a chirped pulse should be directly stabilized. Due to the flexibility of the *FTSI Phase* module, it could potentially be used for other applications and with other pulse shapers, too. The retrieved phase could simply be used for an on-the-fly pulse visualization or an iterative pulse compression. The retrieved phase or a "derived quantity" could also be used as feedback signal for an optimization algorithm. The module could even be used for a new type of on-the-fly pulse shaper calibration, where the voltages at layer 1 and layer 2 are varied and the resulting phase change is directly monitored and evaluated using the spectral interference[8].

5.4 Summary

In order to manipulate the entire vector field of an ultrashort laser pulse with the presented setup, five different parameterizations, i.e., so-called bases, were introduced. These bases convert certain parameters, e.g., elliptical pulse parameters, to the corresponding phase retardation functions applied at layer 1 and layer 2 of the liquid-crystal spatial light modulator (LC SLM).

The first discussed basis was the *Calibration Basis*. It provides a simple control of the voltages applied to both LC SLM layers. The *Pixel Basis* and the *Spectral Basis* allow a more advanced manipulation of the laser pulse, not only the voltages, but also the

[8] Conventionally, the measured transmission is used for the calibration. This requires the use of the arccosine to extract the phase difference between layer 1 and 2, which is prone to errors if the cosine approaches unity.

phase retardation at layer 1 and 2, or the applied spectral phase and transmission can be used as parameters for both polarization components individually. Those two bases are ideally used together with an optimization algorithm. To deterministically produce chirped polarization-shaped pulses, the *Spectral Taylor Basis* was developed. It uses the transmissions and polynomial spectral phases as parameters. The *Polarized Four-Pulse Basis* can generate polarization shaped four-pulse sequences for multidimensional spectroscopy. The used parameters are the relative intensity, the ellipticity, the orientation, the relative time delay, and the relative phase between up to four consecutive subpulses. For future experiments, possible extensions of these bases and a new basis based on the von Neumann formalism were suggested.

The realized bases were integrated in two software programs. The first one – the *VFS Control Center* – was exclusively programmed for the presented setup. It is the basis to operate the vector-field shaper and can be used to apply certain phase/voltage functions at the LC SLM layer manually. For more complex experiments, the VFS hardware control and the presented bases were added to our universal in-house measurement suite *Parameter Scan*. For an active stabilization and automated quasi on-the-fly dual-channel Fourier-transform spectral interferometry evaluation, the *FTSI Phase* module was developed for the *Parameter Scan*.

With these software implementations at hand, the setup is ready-to-use for various types of experiments such as multidimensional spectroscopy or quantum control. New bases could be straightforwardly added to the provided software framework, if an experiment requires a different parameterization.

6 Experimental results

In the previous chapters, the design of the setup and the principle of vector-field control using different parameterizations were discussed in detail. However, to generate polarization-shaped pulse sequences with high fidelity, the design goals and parameters, e.g., the angles required for an optimal frequency distribution across the SLM, must first be experimentally realized and the specifications, e.g., for the TFP, must be fulfilled.

In this chapter (partly published in Ref. [1]), the experimental results are presented. The laser system and the setups used for pulse characterization are briefly introduced (Section 6.1). To validate the alignment of the setup, the frequency distribution across the SLM is investigated (Section 6.2). The unshaped pulse and the compressed pulse are compared to each other and the performance of the TFP is examined (Section 6.3). Based on the relative phase between the two polarization components of the compressed pulse, the long-term stability of the interferometric setup is measured. A stabilization routine to compensate long-term phase fluctuations and temporal drifts is developed (Section 6.4) and verified (Section 6.5). The advanced shaping capabilities of the setup are demonstrated by the generation of various polarization-shaped multipulse sequences with up to four subpulses (Section 6.6).

6.1 Laser system and pulse characterization

For building the setup and for the experiments presented in this chapter, a Ti:Sa oscillator (*Mira Basic, Coherent*) served as light source. The laser emits pulses with a repetition rate of 80 MHz and a theoretical bandwidth-limited duration of 55 fs (FWHM). A typical spectrum of the laser is shown in Fig. 6.1(a). The center wavelength is $\lambda_0 \approx 797$ nm and the bandwidth $\Delta\lambda = 13.8$ nm (FWHM). The width of the spectrum considering $I(\omega)/I_{\max}(\omega) > 1.0$ % is 36 nm from 780 to 816 nm, covering 26 % of the working range between 740 and 880 nm of the presented setup. This design range was chosen such that the VFS may be used also with broadband laser systems in the future.

The commercially available *APE pulseCheck* with *FROG Option* was used for the pulse characterization via FROG (see Section 2.5.3). For the dual-channel FTSI characterization (see Section 2.5.2), the setup illustrated in Fig. 6.1(b) was built. The two polarization components of the incoming pulse are separated with a beam splitter cube and two orthogonal linear polarizers and focused into identical high-resolution spectrometers (*HR4000, Ocean Optics*). The polarization-dependent efficiency of this setup is taken into account by comparing the measured spectra with the separately measured power of both components in front of the spectrometer setup. Using two spectrometers in parallel, rather than performing subsequent measurements for p and s polarization

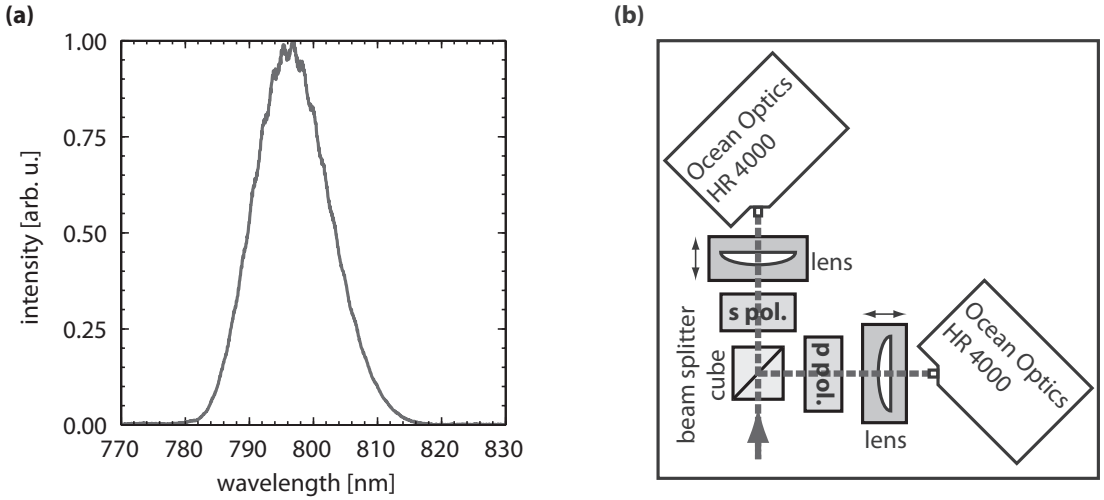

Figure 6.1 | Spectrum of the used laser and setup for the dual-channel FTSI characterization. (a) Typical spectrum of the used laser source with a center wavelength of 797 nm and a spectral width of 13.8 nm (FWHM). (b) Spectrometer setup for dual-channel FTSI characterization. To simultaneously characterize two orthogonal polarization components of the shaped pulse, two identically configured high-resolution spectrometers are employed. The polarization separation is achieved by a beam splitter cube and two linear polarizers. Figure modified and extended from Ref. [1] © (2015) Optical Society of America.

with the same spectrometer, reduces the requirements for interferometric stability between the shaped beam and the reference. If only one spectrometer is used, fluctuations in the time delay τ between the measurements of the p- and s-polarized components might lead to errors in the characterized total polarization state [see Eq. (2.65)].

6.2 Frequency distribution

The goal of the numerical calculations of the $4f$ setup (see Section 4.1) was to optimize the frequency distributions at the SLM. A similar frequency distribution for the two beams of the interferometric VFS, a high number of illuminated pixels, and no spatial overlap of the distributions is desired. In Fig. 6.2, the measured (dark gray circles) wavelength distributions as a function of the SLM pixels are compared with the design goal (solid black line) to prove that these goals are experimentally fulfilled. For the simulation, the calculated parameters δ_{in}, β, and g [see Eq. (4.13)] were used. The frequency distribution was measured by setting the transmission of every fifth pixel to 100 % and assigning these respective pixels to their corresponding frequency. Both beams have a similar frequency distribution in the measured wavelength range of 778–817 nm as beam 1 and beam 2 each cover 83 LC pixels. The simulation predicts 85 pixels for beam 1 and 84 pixels for beam 2 for this wavelength range. Extrapolation of the measured data (light gray circles) shows that the wavelength range of 740–880 nm covers nearly the whole SLM array without spatial overlap of spectral components (beam 1: 295 pixels, beam 2: 293 pixels). In the simulation, the two beams each span 301 pixels for 740–880 nm. The measured and simulated data agree very well,

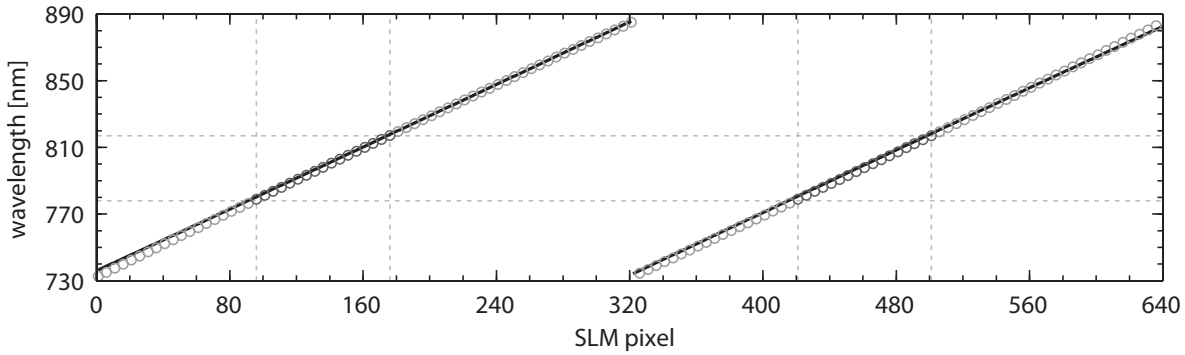

Figure 6.2 | Comparison of the simulated (solid black line) and measured (dark gray circles) wavelength distribution across the LC pixels of the SLM. The calibration was measured (dark gray circles) in the range of 778–817 nm (gray dashed lines) and extrapolated using a second-order polynomial fit (light gray circles). For better visibility, only every fifth data point is plotted. In the measured range, both beams span 83 pixels. For 740–880 nm, they cover 295/293 (beam 1/beam 2) pixels. The simulation for the optimal parameters [Eq. (4.13)] predicts a range of 85/84 (beam 1/beam 2) pixels for 778–817 nm and 301/301 (beam 1/beam 2) pixels for 740–880 nm. Figure modified from Ref. [1] © (2015) Optical Society of America.

demonstrating that the optimal frequency distribution was experimentally achieved for the measured wavelength range and that the setup can be used in the specified wavelength range of 740–880 nm for future experiments. The small discrepancies are either due to simplifications in the simulation, errors in the extrapolation or unavoidable deviations in the alignment of the setup. Nevertheless, for the control software always the actual experimentally determined wavelength calibration is employed.

6.3 Pulse compression

For most applications of the presented setup, it is desired to have a bandwidth-limited linearly polarized pulse as starting point for the pulse shaping. In order to characterize the shaped pulse via dual-channel FTSI (see Section 2.5.2), the complete phase of the reference must be known at the location of the experiment, which is in this case in front of the dual-spectrometer setup. The $\lambda/2$ plate and the linear polarizer in the beam line of the reference (see Section 4.4, Fig. 4.8) are aligned in such a way that the reference pulse is linearly polarized with an orientation of $\theta \approx 45°$ in front of the spectrometer. The orientation of 45° is chosen in order to have equal intensities in both polarization components and to achieve similar modulation depths in the SI signals measured for the FTSI characterization.

The reference phase must be determined via a self-referencing technique, in this case SHG FROG (see Section 2.5.3). However, the information about the relative phase between both polarizations, their relative intensity and thus the ellipticity and orientation of the pulse, cannot be gained by these FROG measurements due to the ambiguity of the SHG FROG technique regarding the absolute phase of laser pulses. Nevertheless, the relative phase between the two polarization components is crucial to characterize

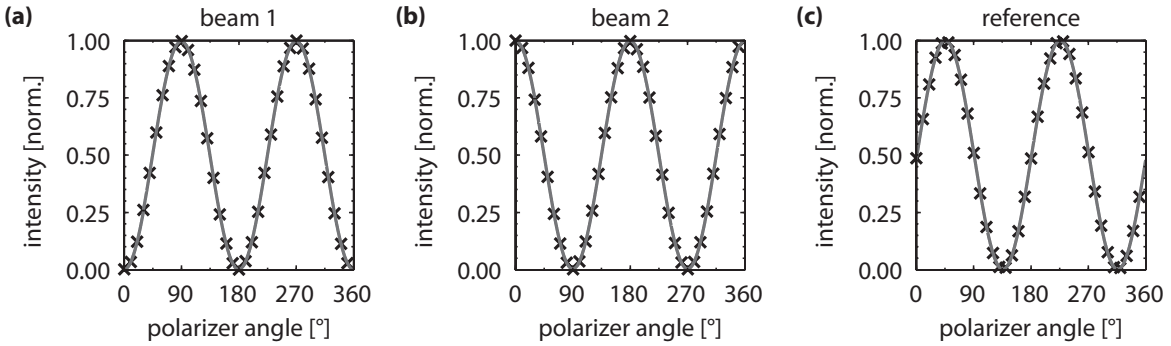

Figure 6.3 | Measured intensity of beam 1, beam 2, and the reference behind a linear polarizer as a function of the polarizer angle. The measured data points are marked by a black cross and the fitted squared sinusoidal is plotted as solid gray line. According to the fit, all three measurements show a vanishing minimal normalized intensity of 0.73×10^{-3}, 3.0×10^{-3}, and 1.3×10^{-3} (beam 1/beam 2/reference), proving that all the pulses are linearly polarized. Their retrieved orientations are 90.013°, −0.014°, and 45.93° (beam 1/beam 2/reference).

a polarization-shaped pulse via dual-channel FTSI based on the FROG phases. For pulses with a simple temporal shape and constant polarization the polarization state can be estimated by measuring the intensity of the pulse behind a linear polarizer as a function of the polarizer angle. This was done for the reference beam and for beam 1 and 2 of the VFS separately. The recorded intensities and a squared sinusoidal fit for all three beams is shown in Fig. 6.3 as a function of the polarizer angle[1]. The data for beam 1 and beam 2 behind the VFS show that both individual pulses are orthogonally and linearly polarized [Fig. 6.3(a,b)], proving the high extinction ratio of the TFP in the used crossed-polarizer arrangement. Based on these polarizer measurements, the ellipticity is $\epsilon = 0.027$ rad for beam 1 and $\epsilon = 0.055$ rad for beam 2. Their orientations are $\theta = 90.013°$ and $\theta = -0.014°$. The small deviations are caused by imprecisions of this measurement method, of the used polarizer and the used power meter. The reference pulse is also linearly polarized ($\epsilon = 0.036$ rad) but with an orientation of 45.93° as desired [Fig. 6.3(c)]. Since the reference pulse is linearly polarized, the relative phase between the p and s component of the reference is $\Delta\phi(\omega) = \phi_{\mathrm{p}}(\omega) - \phi_{\mathrm{s}}(\omega) = 0$ rad. With this information, the FROG phase can be used to characterize the complete vector-field, including the relative phase between the p and s component, of a polarization-shaped pulse via dual-channel FTSI. The phase $\phi_{\mathrm{p/s}}(\omega)$ of the reference could not directly be gained by FROG due to the low intensity of the reference and the resulting insufficient data quality of the FROG measurement. Therefore, the unshaped pulse was characterized via FROG first and the reference phase was measured via FTSI afterwards. The term "unshaped pulse" denotes in this chapter the pulse which is emitted in the crossed-polarizer arrangement if the transmission of each arm is set to 100 % without applying any phase function. To determine the correct sign of the FROG phase, the phase was applied to the SLM and it was checked whether the pulse duration is increased or de-

[1]Beam 1 and beam 2 were already compressed using the VFS in the presented measurements in order to have a simple temporal profile.

creased. For the FTSI characterizations, the reference was delayed by about −1.5 ps with respect to the shaped pulse.

The unshaped pulse, fully characterized by dual-channel FTSI, is plotted in Fig. 6.4(a–d). The spectral/temporal intensity (solid line) and spectral/temporal phase (circles) of the p (blue) and s (red) component is shown in Fig. 6.4(a/b). The s polarization of the unshaped beam is compressed by the alignment of the $4f$ setup as indicated by its almost linear spectral phase (red) while the p polarization exhibits a remaining second-order spectral phase (blue) [Fig. 6.4(a)]. The difference between the p and s component of the spectral phase is caused by a slight asymmetric passing of either the telescope and/or the cylindrical lens due to unavoidable deviations in the alignment of the setup. Due to these alignment errors, the two beams, and thus the polarization components, have a temporal delay of 53.5 fs [Fig. 6.4(b)]. This delay corresponds to a path difference of only 16 µm. Both polarization components differ also in their pulse durations and the p component is chirped as can be seen in the parabolically shaped temporal phase [blue circles in Fig. 6.4(b)]. Therefore, a strongly time-varying polarization profile is observed [Fig. 6.4(c)]. The temporal polarization states are marked by the red dots in the Poincaré plane which are connected via a red dotted line. The temporal intensity is indicated by the lightness of the dots. Lower intensities are represented by lighter colored dots whereas higher intensities are marked by darker dots. A more intuitive representation of the temporal evolution of the pulse in time domain is given by a pseudo 3D plot in Fig. 6.4(d). In this plot, the temporal instantaneous polarization state is depicted by a cylinder with respective orientation and ellipticity. The total size of each cylinder represents the total amplitude. The shadows of the pulse in the p and s plane indicate the amplitude of the p and s component of the pulse. The instantaneous frequency $\omega(t)$ is indicated by the color of each cylinder.

The remaining spectral phases of the unshaped pulse, including the time delay between both beams, are compensated using the VFS by applying the inverted phases of the unshaped pulse to the SLM. This was done iteratively to achieve the best possible compression of the pulse. The obtained compressed pulse is depicted in Fig. 6.4(e–h). Both spectral components feature a flat spectral phase with a relative spectral phase between the p and s polarization of $\Delta\phi(\omega) = \phi_\mathrm{p}(\omega) - \phi_\mathrm{s}(\omega) \approx 0$ rad [Fig. 6.4(e)]. The pulse in time domain has a nearly flat temporal phase and both beams have nearly a perfect temporal overlap. The resulting polarization state, given by the coherent superposition of both components, is therefore linear with an orientation of 44.1° as the average values of the orientation and the ellipticity are $\theta = 0.77$ rad and $\epsilon = -0.27$ mrad for $I(t)/I_\mathrm{max}(t) > 10$ % [Fig. 6.4(g)]. In the 3D representation of the compressed pulse, the perspective is chosen such that the pulse is viewed at an inclination angle of 45°. The resulting image demonstrates the excellent fidelity of the pulse compression as the 3D representation has vanishing "thickness" along the undesired polarization direction [Fig. 6.4(h)].

The temporal duration of the compressed pulse is 74.9 fs based on the FWHM of its total intensity $I_\mathrm{tot}(t)$. The bandwidth-limit is 56.6 fs (FWHM) calculated by Fourier transformation of the measured spectra with constant spectral phase. The total intensity and the total phase of the measured and the simulated bandwidth-limited pulse are compared in Fig. 6.5. The difference of the temporal phases (circles) is small, considering

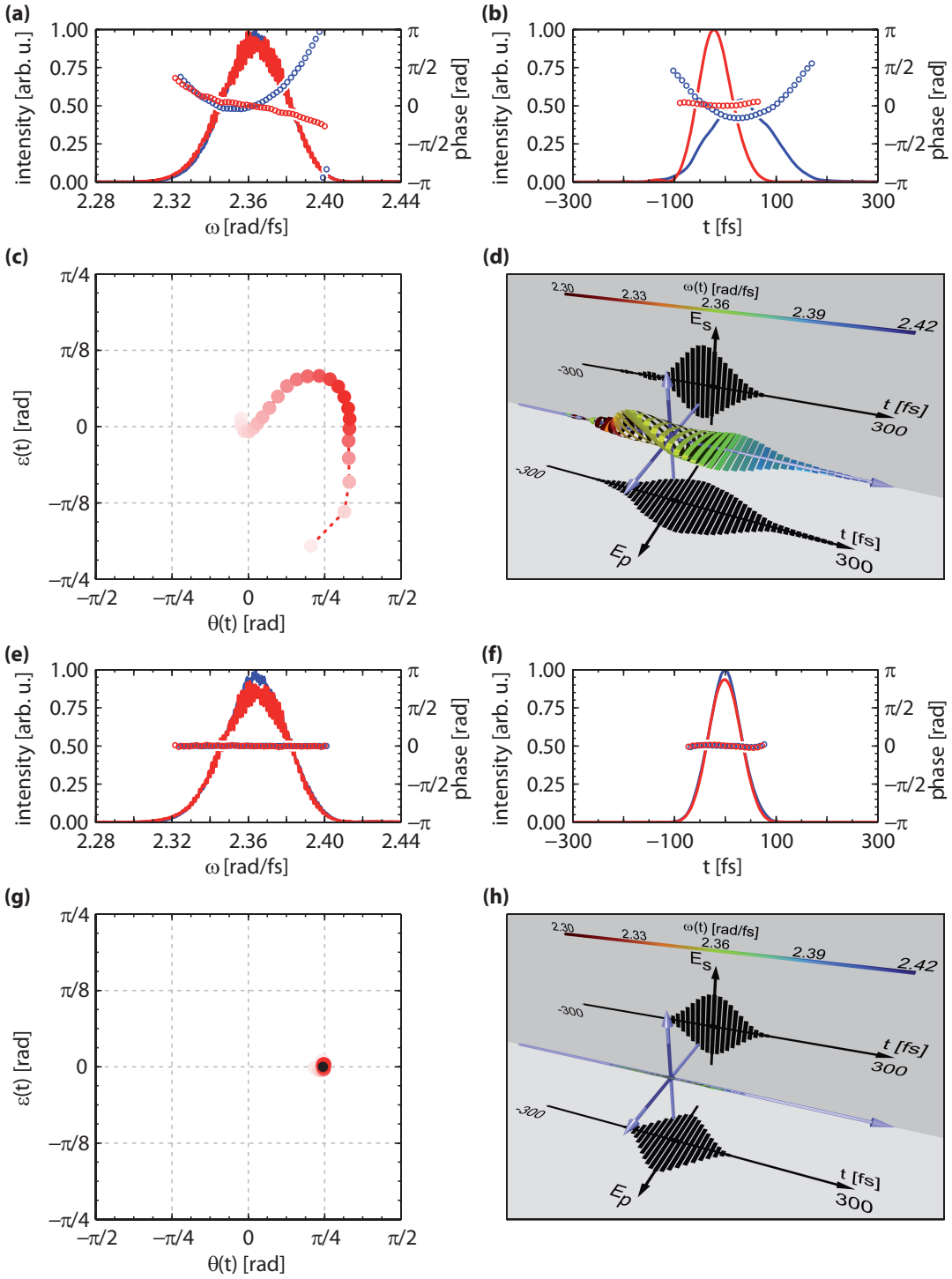

Figure 6.4 | Comparison of the uncompressed [(a–d)] and the compressed pulse [(e–h)]. (a,b) Intensity (solid) and phase (circles) of the p (blue) and the s polarization (red) in frequency [(a)] and time domain [(b)]. (c) Temporal polarization state (red dots) in a Poincaré plot. The temporal intensity is coded in the color lightness. Lighter colors correspond to lower intensities. (d) Pseudo 3D representation in the time domain by cylinders with respective orientations and ellipticities. The instantaneous frequency is color-coded. (e–h) Analogous representations for the compressed pulse. The average orientation θ and ellipticity ϵ of the compressed pulse is marked as black dot in the Poincaré plane [(g)].

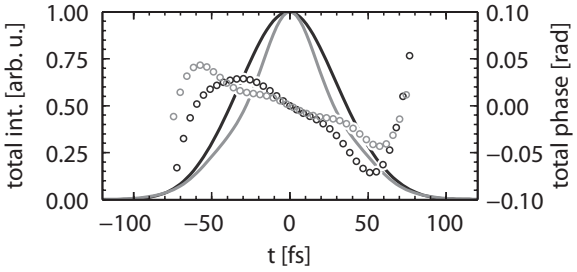

Figure 6.5 | Comparison of the compressed pulse with the simulated bandwidth-limited pulse in time domain. The pulse duration is determined by the FWHM of the total intensity (solid lines). It is 74.9 fs for the compressed pulse (black) and 56.6 fs for the bandwidth-limited pulse (gray). The difference is caused by small deviations in the total phase (circles).

the given range, but a significant elongation of the temporal intensity and thus of the pulse duration of the measured pulse (black solid line) in contrast to the bandwidth-limited pulse (gray solid line) is observed.

The spectra of the uncompressed and the compressed pulse exhibit slight oscillations [Fig. 6.4(a,e)]. These oscillations are lower in amplitude for the p polarization than for the s polarization and arise from multiple reflections inside the TFP (see Section 4.2.2). Fourier transform of the measured spectra and the characterized spectral phases show for the uncompressed and the compressed pulse that the first satellite pulse appears 4.05 ps after the main pulse, almost matching the calculated delay of 3.6 ps (see Section 4.2.2). The intensity ratio between the first satellite pulse and the main pulse is $I_{\mathrm{p}}^{\mathrm{sat.1}}/I_{\mathrm{p}}^{\mathrm{main}} = 0.0079$ % for the p and $I_{\mathrm{s}}^{\mathrm{sat.1}}/I_{\mathrm{s}}^{\mathrm{main}} = 0.20$ % for the s polarization of the uncompressed pulse. For the compressed pulse, $I_{\mathrm{p}}^{\mathrm{sat.1}}/I_{\mathrm{p}}^{\mathrm{main}} = 0.0087$ % and $I_{\mathrm{s}}^{\mathrm{sat.1}}/I_{\mathrm{s}}^{\mathrm{main}} = 0.19$ % are obtained. These values are about a factor of two smaller than expected based on the polarization-dependent transmittances and reflectivities of the TFP given in Section 4.2.2, indicating an even better performance of the TFP. Overall, the influence of these satellite pulses can be neglected for an experiment due to their large temporal delay and vanishing intensity.

6.4 Interferometric stability

The interferometric stability of the setup over almost 24 hours is demonstrated in Fig. 6.6(a). As a benchmark for the stability, the phase difference $\Delta\phi(\omega_0) = \phi_{\mathrm{p}}(\omega_0) - \phi_{\mathrm{s}}(\omega_0)$ between the p and s component of the shaped pulse at the center frequency ω_0 of the compressed pulse was used. Since the p component is generated with beam 2 and the s component with beam 1, this is a direct measure for the relative phase stability between both beams. The pulses were characterized via dual-channel FTSI. The pulse was initially compressed by applying the inverted phase of the uncompressed pulse to the SLM (see Section 6.3). For the black curve [Fig. 6.6(a)], only this initial offset phase was applied to the SLM. The phase difference at $t = 0$ h is larger than zero because the relative phase has already changed with respect to the original pulse compression. The black curve shows a significant long-term drift of the relative phase but also a very high stability along shorter time scales (see inset). The standard deviation of the relative phase is $\sigma = 28.3$ mrad ($\approx \lambda/222$) in this period of 60 minutes. Similar values are reproduced at different temporal sections of this measurement. This high stability

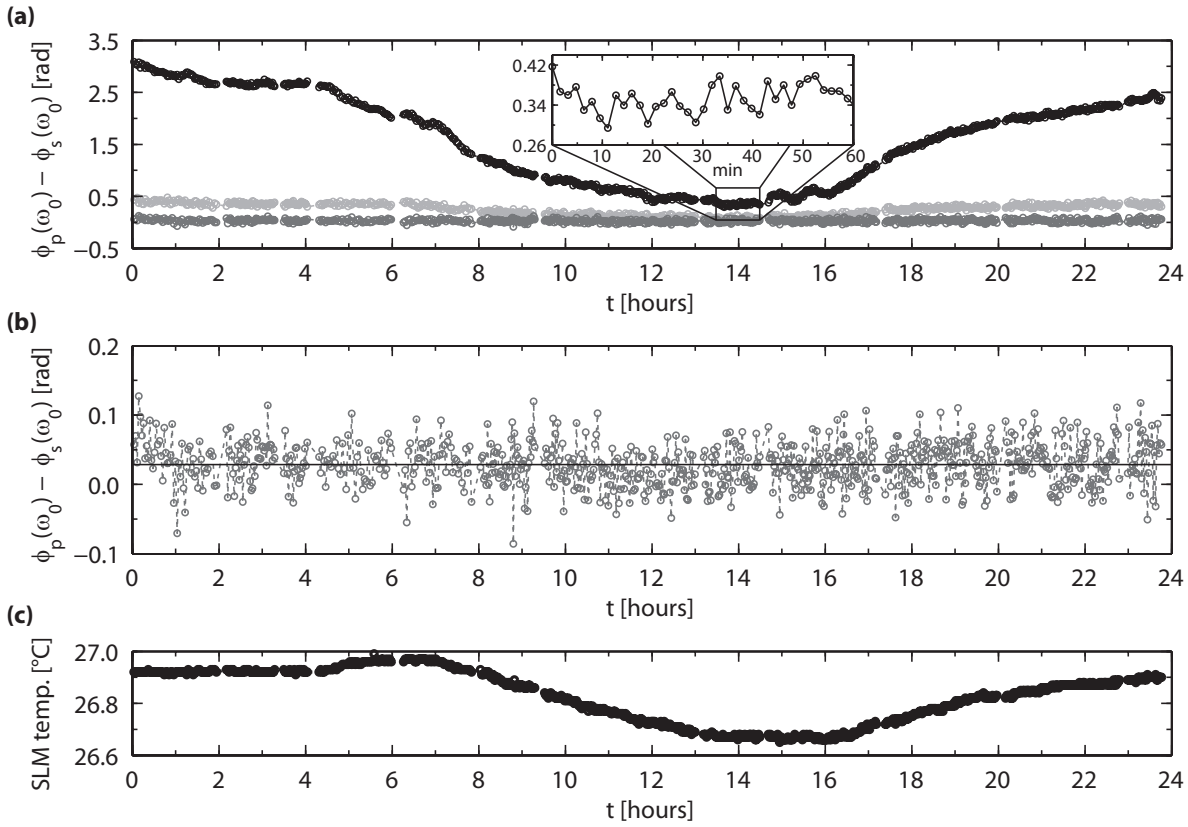

Figure 6.6 | Phase stability of the vector-field shaper setup. (a) Stability over nearly 24 hours. As a quantity for the phase stability, the spectral phase difference at the center frequency between the two orthogonal polarizations is used. In black, the unstabilized phase difference is shown. In light and dark gray, the first and second iteration of an on-the-fly phase reduction and stabilization (OPRAS, see text) using the pulse shaper itself are plotted. The unstabilized curve (black) reveals a significant long-term phase drift but a good short-term stability. The inset shows a period of 60 minutes with a standard deviation of $\sigma = 28.3$ mrad ($\approx \lambda/222$). (b) By employing two iterations of OPRAS, a long-term phase stability of $\sigma = 31.9$ mrad ($\approx \lambda/197$) over nearly 24 hours (iteration 2, dark gray) is achieved. The phase difference is reduced to a mean value of 28.5 mrad (black solid horizontal line). (c) SLM temperature over the course of the measurements. It should be noted that the small gaps in the data set arise from loading times of new measurement parameters. Figure modified from Ref. [1] © (2015) Optical Society of America.

demonstrates the advantage of a common-path setup compared with a non-common path layout. Even for active-stabilized frequency-based non-common setups, lower stability values were reported (see Tab. 3.2), for example $\lambda/10$ over 3 h (Zanni group) and $\lambda/157$ over 1 h (Misawa group). Only with the stabilized time-domain based non-common path setup using two AOPDFs a higher stability of $\lambda/314$ (3 h) was achieved.

Due to the long-term drift an on-the-fly phase reduction and stabilization (OPRAS) procedure utilizing the SLM was implemented. The principle of the routine is that the phase of the pulse is automatically calculated via an FTSI measurement and added

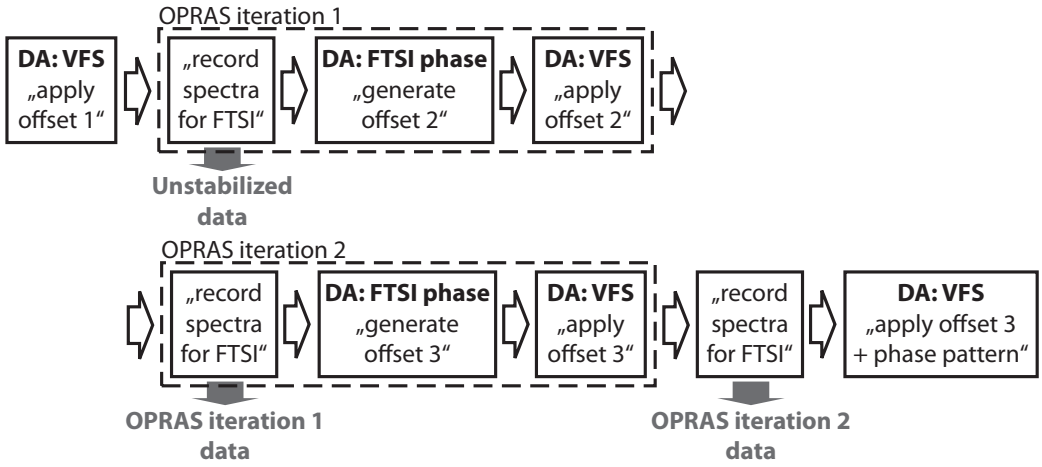

Figure 6.7 | Measurement sequence using two iterations of OPRAS. For each step of the measurement, the constant offset phase (offset 1), gained by the pulse compression as described in Section 6.3, is applied first. In the first iteration of OPRAS, the required spectra for the dual-channel FTSI characterization are recorded, a new offset phase based on the retrieved phases is generated, and applied to the SLM. The new offset phase (offset 2) is the sum of offset 1 and the inverted complete retrieved phase of both polarization components. Offset 3 is analogously generated in a second iteration of OPRAS and used for the consecutive generated pulses in this measurement step. For the next measurement step, the initial manually created offset 1, and not the dynamically generated offset 3, is used as starting point to avoid the accumulation of noise.

to the previous offset phase to compensate for phase fluctuations and temporal drifts between the two arms of the VFS during the experiments. The flowchart of the employed measurement sequence is depicted in Fig. 6.7. First, the offset phase (offset 1) gained by the previous pulse compression (see Section 6.3) was applied. Then, in the first iteration of OPRAS, the pulse generated with offset 1 was characterized via dual-channel FTSI, a new offset phase (offset 2) based on offset 1 and the retrieved phases was generated, and applied to the pulse shaper. In a second iteration of OPRAS, this process was repeated and a third offset phase was generated (offset 3). Afterwards, the pulse generated by offset 3 was characterized, and up to four different pulse shapes were generated and measured (see Section 6.6).

The pulses measured after the first iteration of OPRAS (offset 2) show a much lower phase difference and an improved stability [light gray, Fig. 6.6(a)]. By a second iteration of OPRAS [offset 3; dark gray curve, Fig. 6.6(a)], the relative phase was stabilized to $\sigma = 31.9$ mrad ($\approx \lambda/197$) with a remaining mean value of 28.5 mrad over almost 24 hours [Fig. 6.6(b)]. The time required for one OPRAS iteration is mainly given by the integration time of the spectrometers and not by the data evaluation. By reducing this time and measuring only the essential spectra, one could significantly improve the speed of the stabilization. An improvement of the automatic pulse evaluation could also make the second iteration redundant. Instead of reusing the initially manually-created offset phase (offset 1) as starting point for the OPRAS routine at the beginning of each measurement step, also the last dynamically-generated offset phase (offset 3) of the previous

measurement step could be used. This could make the second iteration of OPRAS obsolete for consecutive measurement steps as the deviation of the phase difference $\Delta\phi(\omega_0)$ between iteration 1 (light gray) and 2 (dark gray) is small if $\Delta\phi(\omega_0)$ obtained with the starting offset phase (black) is already low [see $t = 14$ h in Fig. 6.6(a)]. However, in this case, the accumulation of noise could negatively affect the pulse compression for later measurement steps. Since the setup shows very good short-time stability, it would also be sufficient for time-critical measurements to repeat OPRAS at longer time intervals and not for every data point. The SLM temperature [Fig. 6.6(c)] basically shows the same trend as the curve for the unstabilized phase [black, Fig. 6.6(a)] but slightly delayed. Hence, it can be assumed that the drift in the relative phase is mainly due temporal fluctuations in the laboratory which result in delayed temperature variations of the SLM. The advantages of OPRAS are that no additional stabilization hardware and no moving mechanical parts are required for the stabilization. OPRAS can not only compensate a temporal drift, but in general phase fluctuations of any spectral order, due to the complete characterization of the pulse. Employing dual-channel FTSI, information about the relative phase between both polarization components is directly gained, since the whole vector field is simultaneously characterized. This also eliminates the necessity to characterize or compress the pulse in advance and makes this routine highly suitable to stabilize the output of an interferometric vector-field shaper. By realizing the suggested "dual output", using a special coated glass wedge pair to combine the reference and a small fraction of the shaped pulse in a second outgoing beam line of the VFS (see Section 4.5), OPRAS could be simultaneously utilized while performing any desired experiment with the "main" part of the shaped pulse.

6.5 OPRAS verification

The stabilized pulse generated by OPRAS should not only have a flat spectral phase but also a relative phase of zero between both polarization components. The resulting pulse in the time domain should then be short and linearly polarized (ellipticity $\epsilon = 0$ rad). The actual orientation θ of the polarization ellipse depends on the intensity ratio $I_\mathrm{p}(t)/I_\mathrm{s}(t)$. This ratio was adjusted, using the $\lambda/2$ plate before the TFP (see Section 4.4, Fig. 4.8), to be ≈ 1 and therefore the orientation should be $\theta = 0.25\pi$ rad $= 45°$.

The pulse stabilized via OPRAS was characterized via SHG FROG. The trace for the p polarization [Fig. 6.8(a)] of the stabilized pulse as well as the trace for the s polarization [Fig. 6.8(b)] indicate that the pulse compression was successful. The reconstructed phase (red circles) for the p [Fig. 6.8(c)] and s polarization [Fig. 6.8(d)] agree very well with the phases retrieved by the FTSI characterization (blue circles). Also the reconstructed (red solid line) and measured (blue solid line) spectra match in their overall shape [Fig. 6.8(c,d)]. The measured spectra exhibit again small oscillations due to the satellite pulses generated by the TFP as discussed in Section 6.3.

The information about the relative phase between both polarizations and their relative intensity was extracted by measuring the intensity of the pulse behind a linear polarizer as a function of the polarizer angle and compared with the data gained

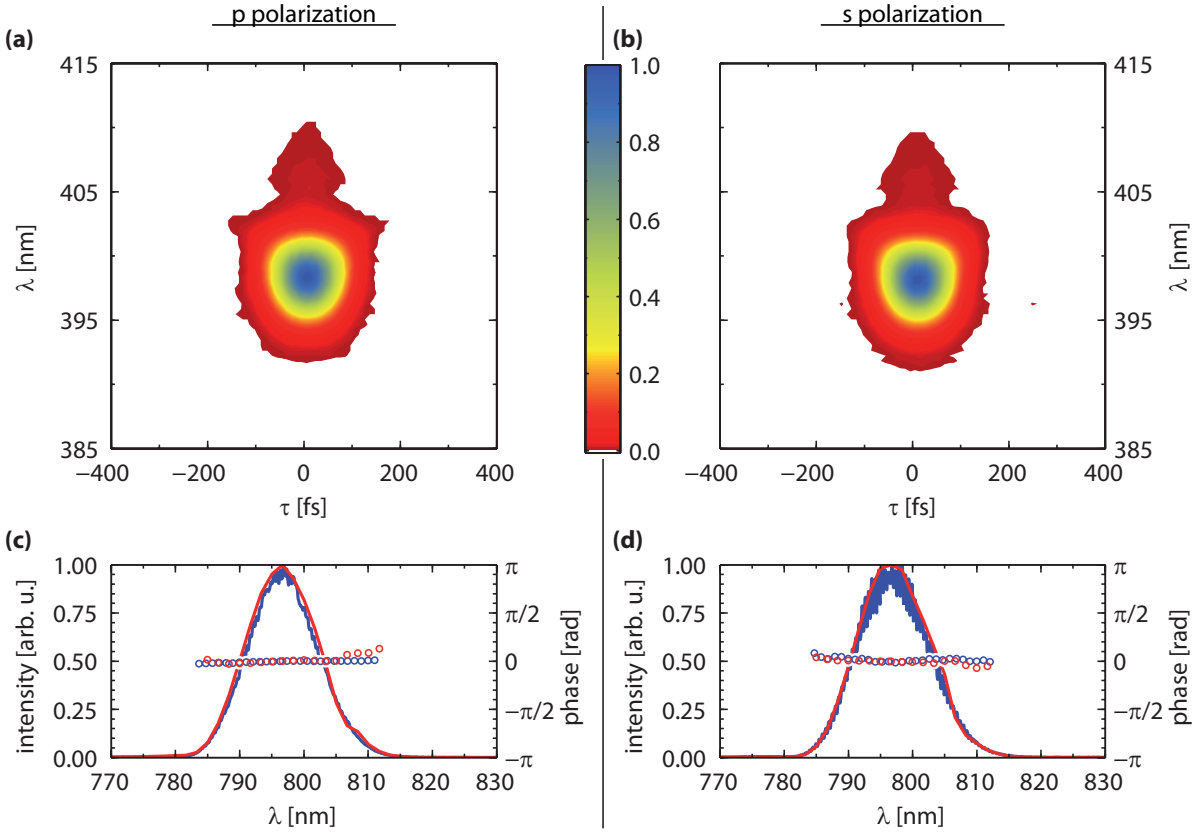

Figure 6.8 | Characterization of the stabilized pulse via SHG FROG. (a) Measured FROG trace of the p and (b) of the s polarization. (c,d) Reconstructed (red) spectrum (solid lines) and phase (circles) compared with the spectrum and phase measured via FTSI (blue) of p [(c)] and s polarization [(d)]. The FROG error is 0.26 %/0.64 % [(a/b)]. Figure adapted from Ref. [1] © (2015) Optical Society of America.

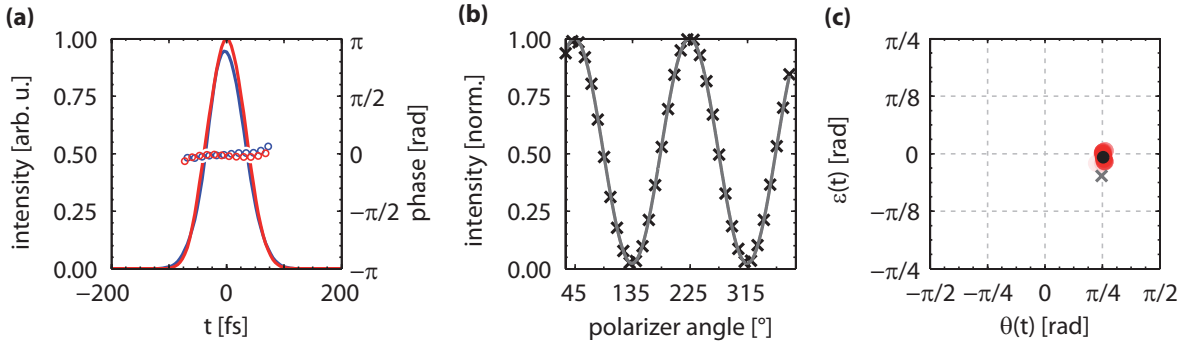

Figure 6.9 | Characterization of the stabilized pulse by rotating a linear polarizer. (a) Intensity (solid line) and phase (circles) of the p- (blue) and s-polarized (red) components in the time domain, gained by FTSI analysis. (b) Measured intensity of the pulse after a linear polarizer as a function of the polarizer angle (black crosses). The orientation of $\theta = 0.77$ rad $= 44.43°$ and the ellipticity of $|\epsilon| = 0.15$ rad are extracted by fitting a squared sinusoidal (gray line). (c) Comparison of the FTSI analysis (red dots), the mean of the FTSI analysis (black dot) and the polarizer measurement (black cross) in a Poincaré plot [152]. Figure modified from Ref. [1] © (2015) Optical Society of America.

via FTSI (Fig. 6.9). The pulse in the time domain [Fig. 6.9(a)] was calculated by Fourier transformation of the spectral data gained via FTSI. Figure 6.9(a) shows the temporal intensities (solid line) as well as the temporal phase (circles) for the p (blue) and s (red) polarization component. The minimum normalized intensity after the linear polarizer is 0.023 for an angle of 134.43° [Fig. 6.9(b)]. This results in $|\epsilon| = 0.152$ rad and $\theta = 0.773$ rad $= 44.43°$. This polarization state is marked by the black cross and the polarization state gained via FTSI by red dots in the Poincaré representation shown in Fig. 6.9(c). The average values of the FTSI data are indicated by the black dot. Both measurements show a pulse which is nearly linearly polarized with $\theta \approx 45°$ but with a difference of $\Delta\epsilon = 0.13$ rad for the ellipticity. This difference of the ellipticity corresponds for this pulse to a change in the relative phase of $\Delta\phi_0 \approx 0.26$ rad [see Eq. (2.25)], which is probably due to a slight temporal phase drift between OPRAS and the polarizer measurement, caused by the imperfect stability of the setup [see Fig. 6.6(a)]. Also the imperfect extinction ratio of the polarizer and the mainly s-polarized subpulses emitted from the TFP contribute to a remaining intensity behind the polarizer and hence to the discrepancy in ϵ. It can be concluded that the OPRAS routine is correct and an efficient tool to characterize, compress, and stabilize polarization-shaped laser pulses. The coherent superposition of the s and p components leads, analogous to the non-automated pulse compression (see Section 6.3), to a single linearly polarized, compressed pulse.

6.6 Generation of polarization-shaped pulses

6.6.1 Single pulses

Based on the pulses stabilized by OPRAS, different pulse sequences with up to four subpulses were generated and characterized to demonstrate the shaping capabilities of the setup. In the first basic example, a single polarization-shaped pulse is shown (Fig. 6.10). The target orientation of $\theta = 0.15\pi$ rad $= 27°$ and ellipticity $\epsilon = 0.09\pi$ rad is not feasible with a conventional 2-layer polarization shaper (see Section 3.2). In order to achieve the desired orientation and ellipticity, it is necessary to adjust the relative intensity and phase between the two orthogonally polarized beams of the interferometric VFS. This can be seen by comparing the spectra and phases of the compressed [Fig. 6.4(e)] and the polarization-shaped pulse [Fig. 6.10(a)]. In this and the following examples, the spectra of the shaped pulse were directly measured with the two spectrometers (see Fig. 6.1) and the spectral phases were retrieved via dual-channel FTSI. As expected, due to OPRAS, the measured pulse in the time domain is still almost bandwidth limited as no additional chirp was introduced by the VFS. The pulse duration is 80.9 fs (FWHM) and comparable to the compressed pulse (see Section 6.3). The measured (red dot) and the target (black cross) polarization state are plotted in Fig. 6.10(c). The red dots accumulate in the target area, indicating an almost temporal-independent polarization state as desired and proving the high accuracy achieved with the pulse shaper. The constant elliptical polarization state and the almost constant instantaneous frequency $\omega(t)$ of the pulse is also clearly visible in the pseudo 3D representation of the measured pulse [Fig. 6.10(d)].

The excellent quality of single polarization-shaped pulses was validated also by other test pulses which are not presented in this thesis. The capacities of the presented setup

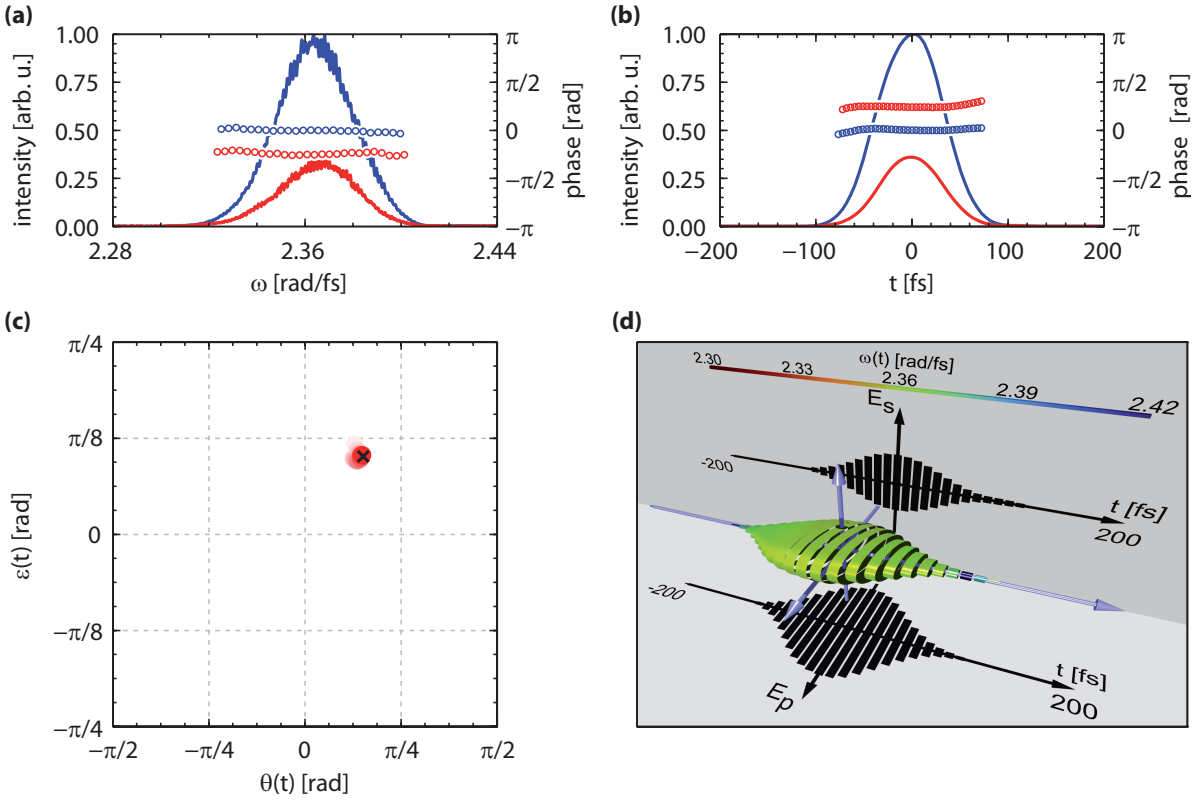

Figure 6.10 | Experimental realization of a single pulse with a constant polarization state. (a) Measured spectrum (solid) and via FTSI retrieved phase (circles) for the p (blue) and s polarization (red). (b) Calculated intensity (solid) and phase (circles) for the p (blue) and s polarization (red) in time domain. (c) Poincaré plot of the measured (red dots) temporal orientation θ and ellipticity ϵ and the target (black cross) polarization state. Lighter dots have a lower temporal intensity as darker ones. (d) Pseudo 3D representation of the measured pulse in time domain. The polarization states are visualized by ellipses with corresponding orientations $\theta(t)$ and ellipticities $\epsilon(t)$. The size of the cylinders is given by the temporal amplitude and the instantaneous frequency is represented by the color of each cylinder (see color bar). The amplitudes of the p and s polarization are indicated by the shadows.

will be rather confirmed in the following by the generation of polarization-shaped multipulse sequences, as those require much more complex frequency-dependent amplitude and phase modulation functions. Multipulse sequences are of particular interest for various spectroscopy methods such as coherent two-dimensional spectroscopy [53, 66, 75, 90, 92] or coherent two-dimensional nanoscopy [110].

6.6.2 Double-pulse sequences

An example of a polarization-shaped double-pulse sequence is shown in Fig. 6.11(a-d). The spectra of the p and s polarization show the typical amplitude modulations required two generate a double pulse [Fig. 6.11(a)]. The frequency-dependent phase and amplitude modulation generates a double-pulse sequence in the time domain with the

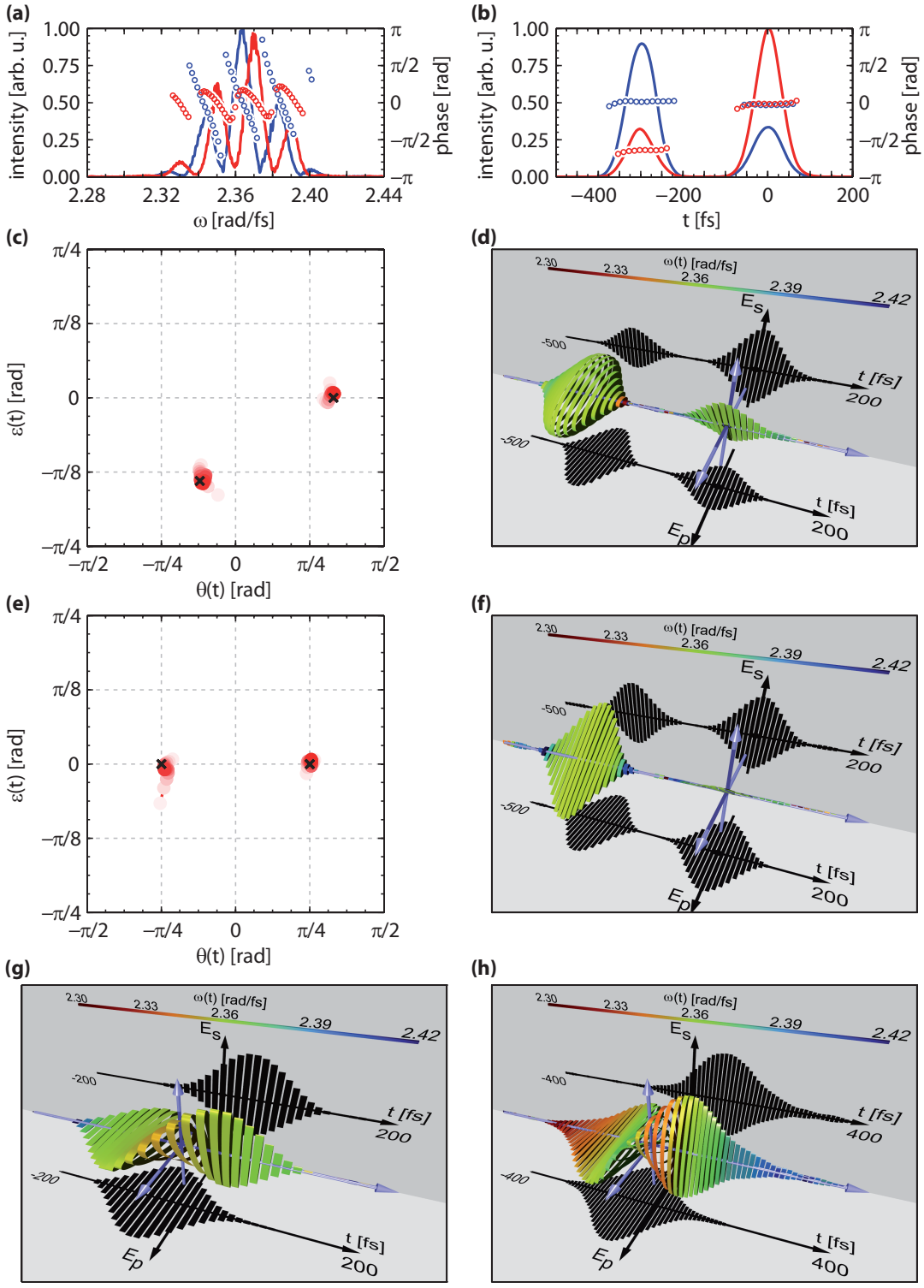

Figure 6.11 | Double-pulse sequences. Color-code and symbols are analogous to Fig. 6.10. (a–d) The first subpulse is elliptically polarized, the second one linearly. (e–f) Both subpulses are linearly polarized with $\theta_1 = -45°$, $\theta_2 = +45°$, (g) The subpulses are linearly polarized ($\theta = 0°/90°$) and have a time delay of 80 fs and a relative phase of $\Delta\phi(\omega_0) = -0.49$ rad. (h) Chirped double pulse ($b_2^{\mathrm{p/s}} = +3000\ \mathrm{fs}^2$) with 150 fs delay and $\Delta\phi(\omega_0) = -0.40$ rad. See text for detailed description. Figure adapted and extended from Ref. [1] © (2015) Optical Society of America.

target delay of 300 fs [Fig. 6.11(b)]. The first subpulse is elliptically polarized ($\theta = -0.12\pi$ rad, $\epsilon = -0.14\pi$ rad) and the second linearly polarized ($\theta = 0.33\pi$ rad, $\epsilon = 0$ rad) [Fig. 6.11(c)]. The temporal phase is still flat and both subpulses remain compressed. The pulse duration of the first subpulse is 79.3 fs and of the second subpulse 74.1 fs. The measured temporal delay based on the maximum of the total intensity of the two subpulses is 300.8 fs. The target polarization states are marked with black crosses in Fig. 6.11(c). The measured polarization states (red dots) agree very well with the desired ones. The fact that the red dots concentrate in the target areas and that they do not extend further out of this area shows that the polarization state is constant throughout each subpulse as desired. The pulse sequence in the time domain is visualized using the pseudo 3D representation depicted in Fig. 6.11(d). The elliptical and the linear polarizations are clearly visible, and the subpulses are well separated in time. Their instantaneous frequency is constant.

This double-pulse sequence, composed of an elliptically and a linearly polarized subpulse, demonstrates nicely the extended shaping capabilities of the vector-field shaper. However, for spectroscopic applications, sequences with linearly polarized multipulse sequences are often preferred. Such a pulse sequence was generated and characterized, as depicted in Fig. 6.11(e,f). The target orientations [black crosses in Fig. 6.11(e)] are $\theta_1 = -45°$ for the first and $\theta_2 = +45°$ for the second subpulse. Both subpulses should be linearly polarized with $\epsilon_1 = \epsilon_2 = 0$ rad. The measured polarization states [red dots in Fig. 6.11(e)] match the target states very well. This is also visible in the pseudo 3D representation [Fig. 6.11(f)]. This representation shows almost straight lines for the first subpulse and vanishing "thickness" in the undesired polarization direction for the second one, due to the viewing angle of 45°. The measured time delay of 299.9 fs between the two subpulses matches the target delay of 300 fs. Both subpulses have an almost constant instantaneous frequency and are compressed with a pulse duration of 77.7 fs and 78.8 fs, respectively. The small deviations between the target values and the measured values are in the same order as in the previous example, demonstrating the high fidelity of the generated double-pulse sequences in terms of the temporal delay and the polarization.

By definition, in the *Polarization Four-Pulse Basis* both subpulses should have the same total intensity in these two examples. However, as a result of the shaping window, the total intensity of the delayed subpulse is reduced with respect to the undelayed subpulse centered at $t = 0$ fs. For a double-pulse sequence, this effect can be taken into account by delaying the two subpulses symmetrically to negative and positive time with respect $t = 0$ fs, or in a more general approach by measuring the delay-dependent intensity reduction caused by the shaping window and by adjusting the total intensity of the undelayed subpulse with the pulse shaper according to the temporal position of the subpulses.

The relative phase between the subpulses can also be controlled using the *Polarization Four-Pulse Basis*. This is illustrated in Fig. 6.11(g) by two orthogonally linearly polarized subpulses with a slight temporal overlap as the first subpulse is delayed by -40 fs and the second by +40 fs with respect to $t = 0$ fs. Their relative phase difference in the frequency domain is $\Delta\phi(\omega_0) = -0.49$ rad. In the range of the temporal overlap the relative phase and the temporal varying intensity ratio between the p and s component

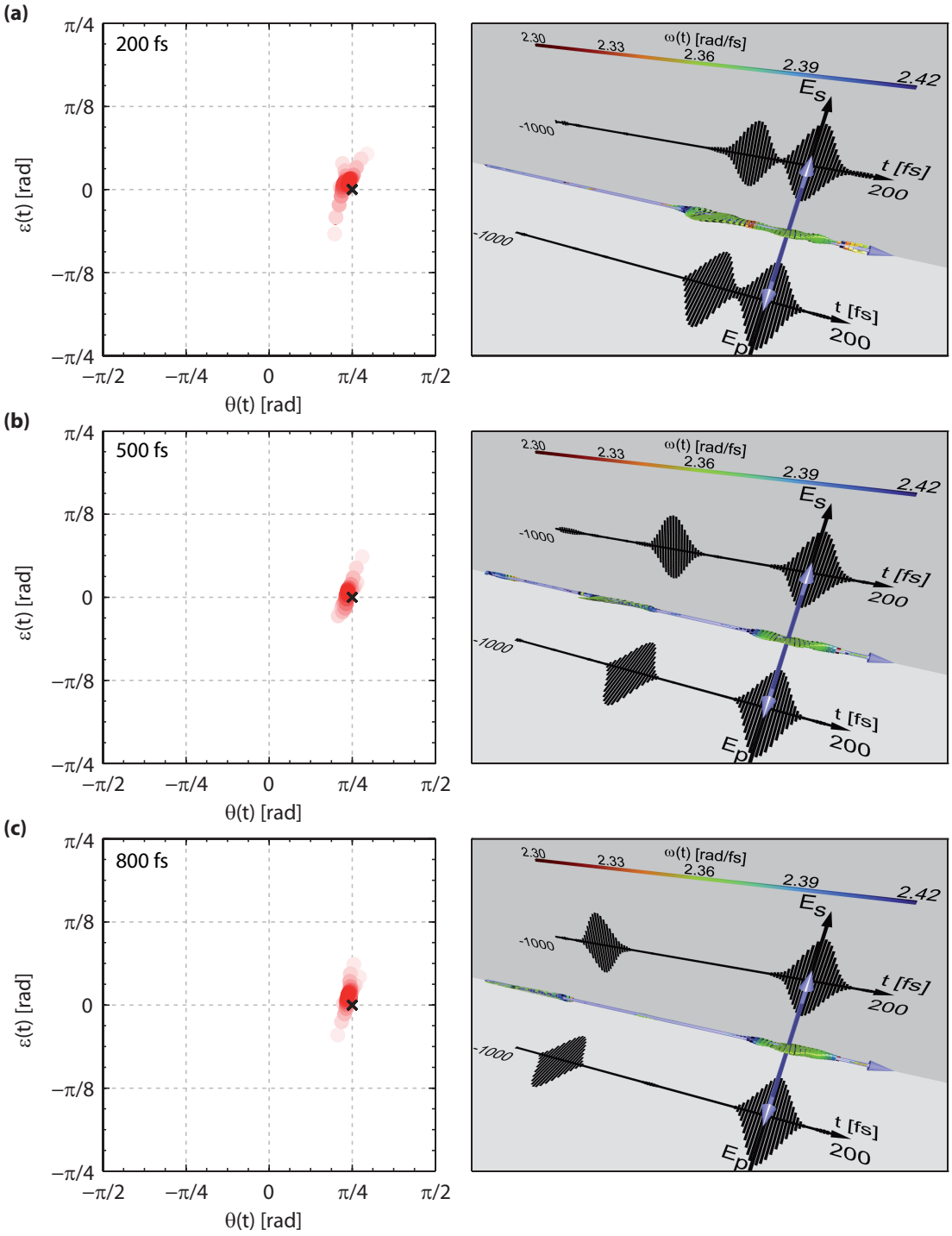

Figure 6.12 | Double-pulse sequence with two linearly polarized subpulses orientated under 45° for various temporal delays. Left side: Poincaré representation with measured (red dots) and target (black cross) polarization state. Right side: Respective pseudo 3D representation in time domain of the measured double-pulse sequence. The depicted delays between the two subpulses are (a) 200 fs, (b) 500 fs, and (c) 800 fs. Figure adapted and extended from Ref. [1] © (2015) Optical Society of America.

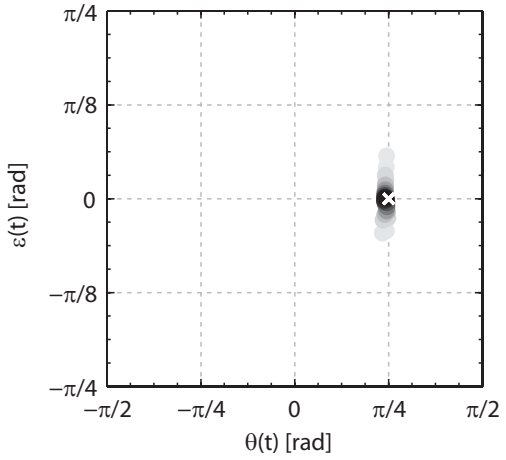

Figure 6.13 | Simulated polarization state of the double-pulse sequence for the delay of 500 fs. The simulation is based on the ideal transfer function and the measured stabilized pulse. The simulated polarization states (black dots) show a similar variation in $\epsilon(t)$ and a systematical deviation in $\theta(t)$ from the target states (white cross) as those of the measured pulses shown in Fig. 6.12(b).

results in a rapidly varying polarization state. The rotation of the orientation is clearly visible in the pseudo 3D representation. In the region of no temporal overlap, their relative phase does not influence their polarization state as it remains linear. Being able to precisely control the relative phase between subpulses is crucial in various spectroscopic applications. Measuring a signal for different relative phases between consecutive subpulses is called phase-cycling and can, for example, be employed to extract certain signal contributions from the measured data in multidimensional spectroscopy [66, 273].

The control of the relative phase, or more precisely, the total phase of each subpulse, can also be employed for strong-field quantum control experiments [227, 279, 280]. While for spectroscopy bandwidth-limited pulse are preferred in order to have the highest possible time resolution, for quantum control also chirped pulses can be utilized to achieve a certain goal [267–271]. A simple example of a double-pulse sequence with two positive chirped subpulses ($b_2^{\mathrm{p}} = b_2^{\mathrm{s}} = 3000$ fs^2) is depicted in Fig. 6.11(h). Due to the chirp, the pulse durations are increased to 129.0 fs and 131.6 fs, and the subpulses overlap temporally despite their large relative temporal delay of 150 fs. The chirp of the two subpulses can be seen in the color-coding of the pseudo 3D representation. Because of to the varying temporal phase and the phase difference of $\Delta\phi(\omega_0) = -0.4$ rad, a rapidly varying polarization profile occurs in the region of the temporal overlap similar to Fig. 6.11(g).

For various spectroscopic methods as well as for quantum control it is important to vary the temporal delay between the subpulses without changing their polarization state. A double-pulse sequence with three different temporal delays [200 fs (a), 500 fs (b), and 800 fs (c)] is depicted in Fig. 6.12. The target polarization state for both subpulses was chosen to be $\theta = 45°$ and $\epsilon = 0$ rad for this demonstration as deviations from this linear polarization state are easily visible in the pseudo 3D representation. It should be noted that even changing only the time delay between the two subpulses is challenging because both beams of the interferometric VFS have to be amplitude modulated, precisely delayed in time, and kept at a fixed relative phase to avoid a change in their polarization state. All three Poincaré representations (left side, Fig. 6.12) show that both subpulses are mainly linearly polarized with an orientation of $\theta \approx 45°$. However, a slight "elongation" in $\epsilon(t)$ direction is visible for low intensities. This is an artifact caused by

the remaining phase due to the imperfect compression of the stabilized pulse used for this measurement. In Fig. 6.13, the simulated polarization states of the double-pulse sequence with a delay of 500 fs [Fig. 6.12(b)] are shown. The simulation was carried out by applying the ideal amplitude and phase transfer function required to generate the target pulse sequence to the measured spectra and phase of the stabilized pulse, which was recorded directly before the characterization of the double-pulse sequence. The simulation shows variation in $\epsilon(t)$ for the parts of the subpulses with low intensity similar to the measurement, verifying that this elongation can be ascribed to the remaining phase of the stabilized pulse. Similar results were obtained for the simulated subpulses with delays of 200 fs and 800 fs (not shown). The measured orientations for the parts with high temporal intensity almost match the orientation obtained by the simulation. The measurements and the simulations show both a slightly lower orientation angle as intended, comparing the darkest dots with the cross. This systematic deviation is probably caused by the fact that the two beams of the interferometric VFS did not have exactly the same intensity for this measurement. Overall, the target polarization states are well matched. The deviations in $\theta(t)$ and $\epsilon(t)$ from the target values which cannot be explained by the remaining phase of the stabilized pulse or the intensity mismatch between the two beams are a result of unavoidable deviations of the realized and the ideal transfer functions. These errors are caused by imperfections of the pulse shaper calibration and inherent shaping artifacts of the LC SLM. All in all, Fig. 6.12 shows the excellent vector-field control provided by the presented setup as only minor differences in the measured polarization states for different delays are visible.

6.6.3 Three- and four-pulse sequences

The previous examples demonstrate precise deterministic control of a double pulse in all degrees of freedom, but many spectroscopic applications require sequences of three or four subpulses with an even more complex SLM transfer function. In Fig. 6.14, three examples of different generated and characterized three- and four-pulse sequences are depicted. The three-pulse sequences were also created using the *Polarization Four-Pulse Basis*, but the time delay between the second and third subpulse was set to 0 fs for these measurements. Analogously to the double-pulse sequences, besides the actual amplitude/phase modulation required to create the target pulse sequence, an offset phase was applied to compensate the phase of the unshaped pulse in order to generate pulse sequences consisting of near bandwidth-limited subpulses. For these examples, the target polarization states are again marked as black crosses in the Poincaré plane and pseudo 3D representations based on the characterized pulse sequences are plotted.

First, a sequence with three elliptically polarized subpulses is shown [Fig. 6.14(a)]. The temporal delay between each subpulse is 300 fs to avoid a temporal overlap and a mixing of the specified polarization states to a complex polarization profile. The measured polarization state of the subpulse at $t = 0$ fs agrees very well with the target state [Fig. 6.14(a)]. Only the two small subpulses at $t = -300$ fs and $t = +300$ fs show small deviations from the desired states. These discrepancies are a result of the remaining phase of the stabilized pulse and unavoidable pulse-shaping artifacts which are common for complex modulation functions. All three subpulses are still compressed as

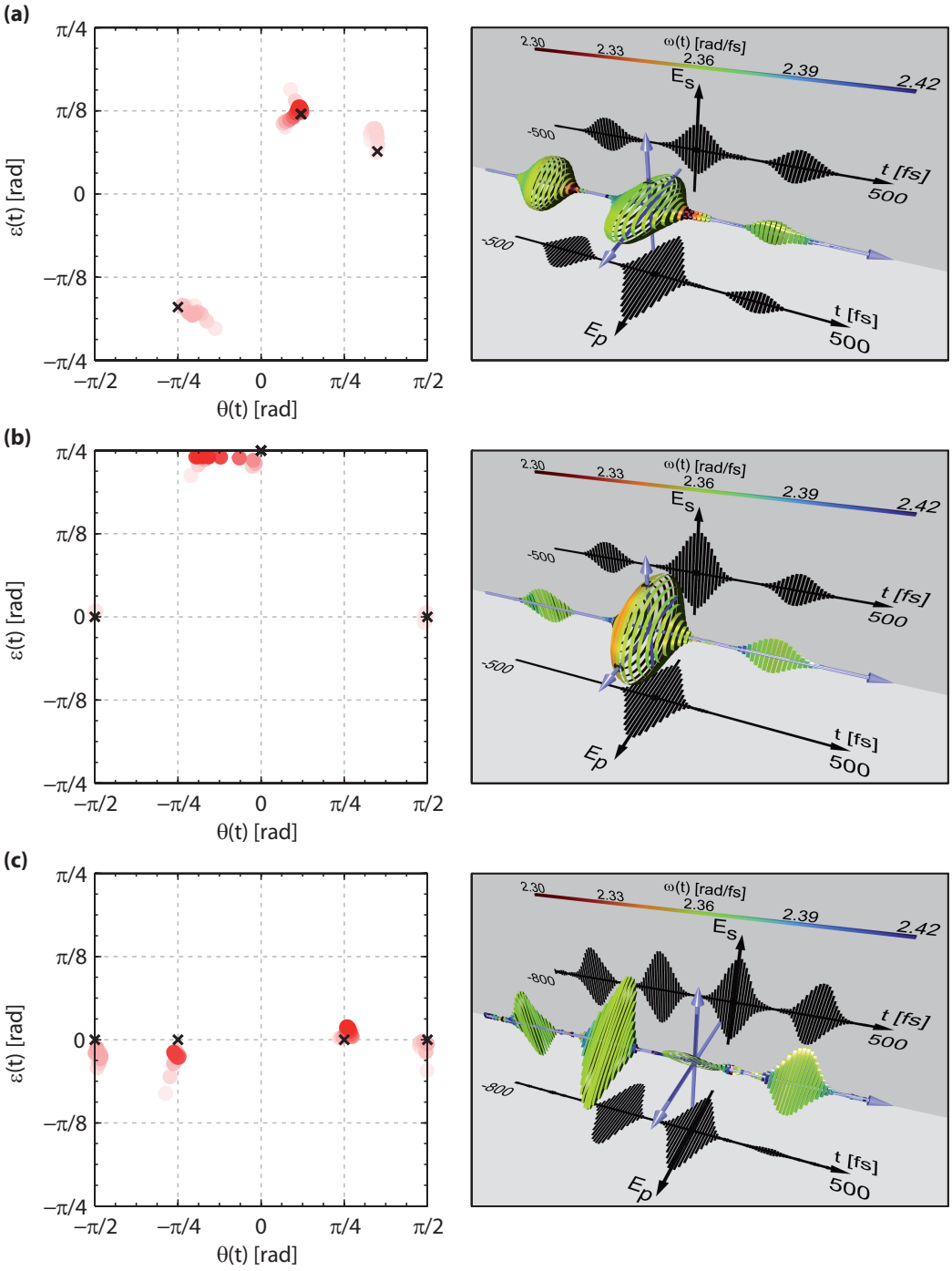

Figure 6.14 | Three- and four-pulse sequences. The delay between each subpulse is 300 fs. (a) Three-pulse sequence with elliptically polarized subpulses $\epsilon = -0.17\pi$, 0.12π, 0.064π rad and $\theta = -0.27\pi$, 0.12π, 0.35π rad. (b) Four-pulse sequence with two linearly s polarized subpulses (1 and 4) and two overlapping subpulses forming a single intense left-handed circularly polarized subpulse. (c) A four-pulse sequence with linearly s-polarized subpulses 1 and 4 while the target orientation angle of subpulses 2 and 3 is $-45°$ and $+45°$. The measured polarization states (left, red dots) agree very well with their target states (left, black crosses). In all three cases, a clean polarization-shaped multipulse sequence is obtained (right). Figure adapted and extended from Ref. [1] © (2015) Optical Society of America.

shown by the almost constant instantaneous frequency in the pseudo 3D representation.

In the second example [Fig. 6.14(b)], a pulse sequence with two linearly ($\theta = \pm 90°$) polarized subpulses at $t = \pm 300$ fs and two temporally overlapping left-handed circularly polarized subpulses at $t = 0$ fs was created. The measured polarization states match the target ones very well. The elongation in the $\theta(t)$ direction of the almost circularly polarized subpulse does not indicate a significant error in the generated polarization state but a result of the insignificance of the orientation θ of a circularly polarized pulse (see Section 2.2).

The generation of the circularly polarized subpulse at $t = 0$ fs is equivalent to generating two orthogonally linearly polarized subpulses with the same amplitudes and a relative phase of $\pi/2$. In the third sequence [Fig. 6.14(c)], all four subpulses are temporally separated by 300 fs and specified to be linearly polarized with orientations of $\theta = -90°, -45°, 45°, 90°$. Such a sequence could, for example, be used for collinear multidimensional spectroscopy. Only minor difference between the target and measured polarization state are observed. The pseudo 3D representation shows clean and distinct subpulses with the desired polarization states and an almost constant instantaneous frequency. The measured pulse durations are 70.9 fs, 79.9 fs, 77.7 fs, and 78.8 fs. The measured delays of 300.45 fs, 301.19 fs, and 297.32 fs between the subpulses show a good agreement with the target delays.

In total, all three measured pulse sequences agree very well with the defined polarization profiles and temporal delays, proving that multipulse sequences with different and deterministically generated polarization states are realizable with the presented polarization pulse-shaper design. So far, temporally constant polarization states have been created, but complex time-dependent polarization states can be created using the *Polarization Four-Pulse Basis*, as well. This can be done by defining subpulses with certain polarization states and only small temporal delays. In Fig. 6.15(a–d), every subpulse exhibits a different polarization state. The temporal delay between subpulse 1 and 2 and subpulse 3 and 4 is 200 fs, while the temporal delay between subpulses 2 and 3 is only 80 fs. The representation in the frequency domain [Fig. 6.15(a)] shows the complex phase and amplitude modulation required to generate such a four-pulse sequence. In time-domain representation [Fig. 6.15(b)], it can be seen that subpulse 1 and 4 are clearly temporally separated. Therefore, they have clean polarization states which correspond to the specified orientations and ellipticities [Fig. 6.15(c)]. The small deviations due to unavoidable shaping artifacts are in the same order as in the previously shown three- and four-pulse sequences. Subpulse 2 and 3 exhibit a temporal overlap [Fig. 6.15(b)] and form a complex polarization profile that varies in time [Fig. 6.15(c,d)].

An even more complex polarization profile can be generated by specifying four different polarized subpulses with a delay of only 80 fs between each subpulse [Fig. 6.15(e,f)]. The superposition of the subpulses leads to a single pulse [Fig. 6.15(f)] with a pulse duration of 252.1 fs. Its polarization state is strongly time dependent and the defined polarization states of subpulse 1 and 4 are only reached at the temporal edges of the pulse. In contrast, the specified polarization states of subpulse 2 and 3 are not reached in the measured pulse [Fig. 6.15(e)]. This is not a result of a shaping artifact but simply caused by the temporal overlap of all four subpulses. A special characteristic of this pulse is that despite the complex temporal polarization profile and an increased pulse

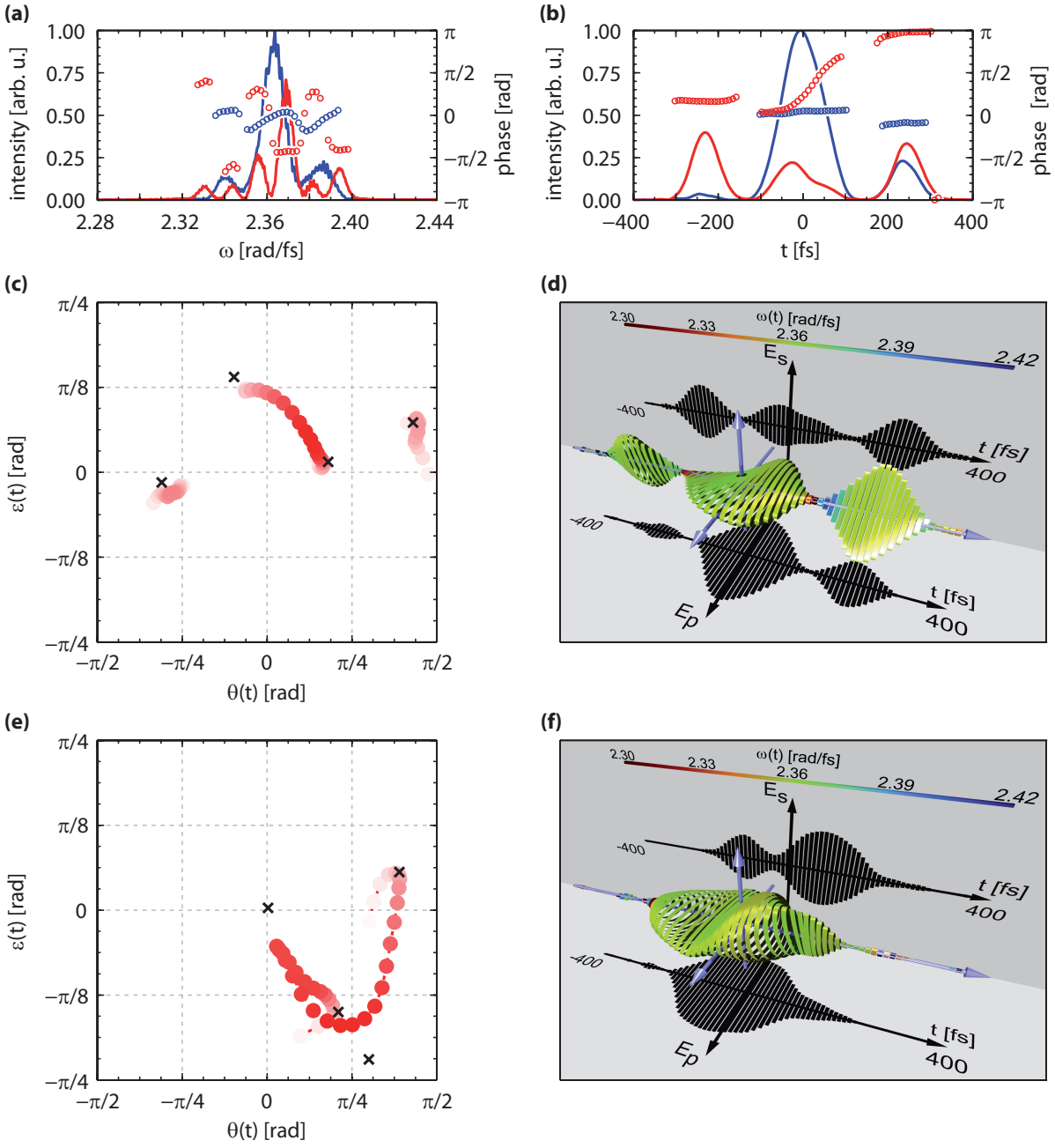

Figure 6.15 | Four-pulse sequences with temporally overlapping subpulses. The color-code and symbols are analogous to Fig. 6.10. (a–d) A four-pulse sequence is generated with relative time delays of 200 fs, 80 fs, and 200 fs. The overlap between subpulse 2 and 3 leads to a varying ellipticity $\epsilon(t)$ and orientation $\theta(t)$. (e–f) Due to the short delay between the four subpulses of only 80 fs, a single pulse with a highly complex polarization state is formed. The specified polarization states for all four single subpulses are marked by black crosses in the Poincaré plot [(c,e)]. Figure adapted and extended from Ref. [1] © (2015) Optical Society of America.

duration compared to the compressed pulse (see Section 6.3, Fig. 6.4), the instantaneous frequency remains almost constant over the entire pulse duration. Such a polarization-

shaped pulse could not be generated using a conventional dual-layer polarization shaper.

Using a different parameterization, also bandwidth-limited pulses with varying polarization profiles and multipulse sequences where each subpulse has a time-dependent polarization state or chirp are viable. As the presented multipulse sequences already require a high complex transfer function it is expected that beforementioned pulses can be generated with comparable fidelity using the presented setup.

6.7 Summary

In this chapter, the first experimental results obtained with the developed vector-field shaper were presented. The measured frequency distribution showed that the two dispersed beams cover the same amount of pixels of the spatial light modulator in the used wavelength range of 778–817 nm, restricted by the laser bandwidth, as desired. Extrapolation of the measured data predicted that both beams have similar frequency distributions covering nearly the entire pixel array without spatial overlap for the specified wavelength range of 740–880 nm, as intended by the design of the setup.

The excellent performance of the thin-film polarizer (TFP) was proven by demonstrating that both individual beams of the interferometric vector-field shaper are linearly and orthogonally polarized and that the intensity of the first satellite pulse emitted from the TFP due to multiple reflections is only in the order of 0.10 %/0.20 % (p/s polarization) of the main pulse. Furthermore, the first satellite pulse is temporally separated by 4.05 ps with respect to the main pulse and will therefore have no significant influence in an experiment.

By the alignment of the setup, the unshaped pulse is mostly temporally compressed and both polarization components have a temporal delay of only 53.5 fs. This delay and the remaining non-linear phase of both polarization components were compensated by characterizing the unshaped pulse and by applying the inverted phases iteratively with the vector-field shaper. The pulse was compressed to 74.9 fs and both beams were centered around $t = 0$ fs. The superposition of both polarization components resulted in a linearly polarized pulse with an orientation of 45°.

The interferometric stability of the setup was measured by characterization of the pulse over almost 24 hours. The presented common-path setup has a very high stability of $\sigma = 28.3$ mrad ($\approx \lambda/222$) over 60 minutes. However, due to unavoidable temperature changes in the laboratory over the course of 24 h, a long-term phase drift was observed. To compensate the latter, an on-the-fly phase reduction and stabilization (OPRAS) routine, utilizing the pulse shaper itself, was developed. With this method, a phase stability of $\sigma = 31.9$ mrad ($\approx \lambda/197$) over nearly 24 hours was achieved. It was further demonstrated that this method leads to a compressed pulse with a minimized phase difference between the two polarization components.

Precise control over the whole vector field of an ultrashort laser pulse, utilizing the presented setup, was verified by the generation and characterization of various multipulse sequences with up to four subpulses. It was shown that the polarization state, the phase, the chirp, and the temporal position of each subpulse can be controlled, independently. In all cases, very high agreement between the target parameters and the experimental

data was achieved. The presented pulse sequences are not feasible with conventional dual-layer polarization pulse shapers, emphasizing the extended shaping capabilities of the vector-field shaper. Employing two spectrometers simultaneously for dual-channel Fourier-transform spectral interferometry, vector-shaped pulses can be analyzed reliably without stringent stability requirements for the delay between the shaped pulse and the reference.

7 Summary and outlook

The controlled shaping of ultrashort laser pulses is a powerful technology and applied in many laser laboratories today. Most of the used pulse shapers are only able to produce linearly polarized pulses shaped in amplitude and phase. Some devices are also capable of producing limited time-varying polarization profiles, but they are not able to control the amplitude. However, for some state-of-the-art non-linear time-resolved methods, such as polarization-enhanced two-dimensional spectroscopy, the possibility of controlling the amplitude and the polarization simultaneously is desirable.

Over the last years, different concepts have been developed to overcome these restrictions and to manipulate the complete vector-field of an ultrashort laser pulse with independent control over all four degrees of freedom – phase, amplitude, orientation, and ellipticity. The aim of this work was to build such a vector-field shaper. While the basic concept used for our setup is based on previous designs reported in the literature, the goal was to develop an optimized optical design that minimizes artifacts, allowing for the generation of predefined polarization pulse sequences with the highest achievable accuracy.

In Chapter 3, different approaches reported in the literature for extended and unrestricted vector-field control were examined and compared in detail. Based on this analysis, we decided to follow the approach of modulating the spectral phase and amplitude of two perpendicularly polarized pulses independently from each other in two arms of an interferometer and recombining them to a single laser pulse to gain control over the complete vector field.

As described in Chapter 4, the setup consists of three functional groups: i) an optical component to generate and recombine the two polarized beams, ii) a $4f$ setup, and iii) a refracting telescope to direct the two beams under two different angles of incidence onto the grating of the $4f$ setup in a common-path geometry. This geometry was chosen to overcome potential phase instabilities of an interferometric vector-field shaper. Manipulating the two perpendicularly polarized pulses simultaneously within one $4f$ setup and using adjacent pixel groups of the same liquid-crystal spatial light modulator (LC SLM) for the two polarizations has the advantages that only a single dual-layer LC SLM is required and that a robust and compact setup was achieved. The shaping capabilities of the presented design were optimized by finding the best parameters for the setup through numerical calculations to adjust the frequency distributions for a broad spectrum of 740–880 nm. Instead of using a Wollaston prism as in previous designs, a thin-film polarizer (TFP) is utilized to generate and recombine the two orthogonally polarized beams. Artifacts such as angular dispersion and phase distortions along the beam profile which arise when a Wollaston prism is used were discussed. Furthermore, it was shown by ray-tracing simulations that in combination with a telescope and the $4f$ setup, a significant deformation of the beam profile

would be present when using a Wollaston prism since a separation of the incoming and outgoing beam in height is needed. The ray-tracing simulations also showed that most optical aberrations of the setup are canceled out when the incoming and outgoing beams propagate in the exact same plane by inverting the beam paths. This was realized by employing a TFP in the so-called crossed-polarizer arrangement which has also the advantage that the polarization-dependent efficiencies of the TFP and the other optics are automatically compensated and that a high extinction ratio in the order of 15000:1 is reached. Chromatic aberrations are, however, not compensated by the crossed-polarizer arrangement. The ray-tracing simulations confirmed that these chromatic aberrations are mainly caused by the telescope and not by the cylindrical lens of the $4f$ setup. Nevertheless, in the experimentally used wavelength range of 780–816 nm, only minor distortions of the beam profile were observed, which were thus considered to be negligible in the presented setup.

The software implementation of the pulse shaper was reviewed in Chapter 5 of this thesis. In order to perform various experiments, five different parameterizations, accounting for the extended shaping capabilities of a vector-field shaper, were developed. The *Pixel Basis*, the *Spectral Basis*, and the *Spectral Taylor Basis* can generally be used in combination with an optimization algorithm and are therefore well suited for quantum control experiments. For multidimensional spectroscopy, the *Polarized Four-Pulse Basis* was established. With this parameterization pulse sequences with up to four subpulses can be created. The polarization state of each subpulse can be specified and the relative intensity, phase, and temporal delay between consecutive subpulses can be controlled. In addition, different software programs were introduced in Chapter 5 which are required to perform the experiments conducted in this work.

The experimental results were presented in Chapter 6. The frequency distribution across the LC SLM was measured proving that the optimal frequency distribution was realized experimentally. Furthermore, the excellent performance of the TFP was verified. In general, satellite pulses are emitted from the TFP due to multiple internal reflections. Various measurements demonstrated that these pulses are temporally separated by at least 4.05 ps from the main pulse and that they have vanishing intensity. The phase stability between the two arms of the presented common-path setup is $\sigma = 28.3$ mrad ($\approx \lambda/222$) over 60 minutes. To further improve this stability over very long measurement times, an on-the-fly phase reduction and stabilization (OPRAS) routine utilizing the pulse shaper itself was developed. This routine automatically produces a compressed pulse with a minimized relative phase between the two polarization components. A phase stability of $\sigma = 31.9$ mrad ($\approx \lambda/197$) over nearly 24 hours was measured by employing OPRAS. Various pulse sequences exceeding the capabilities of conventional pulse shapers were generated and characterized. The experimental results proved that shaped pulses with arbitrary phase, amplitude, and polarization states can be created. In all cases very high agreement between the target parameters and the experimental data was achieved.

For the future use of the setup also possible modifications were suggested. These are not strictly required, but all of them could further improve the performance and flexibility of the setup. Firstly, it was illustrated how a “dual-output” of the setup can be realized. With this modification it would be possible to use the main inten-

sity of the shaped pulse for an experiment while using a small fraction to characterize the pulse or to perform OPRAS simultaneously. Secondly, the basic idea of replacing the telescope by focusing mirrors in order to eliminate the chromatic aberrations was presented. Regarding the different parameterizations for vector-field shaping, some modifications increasing the flexibility of the implemented bases and the realization of a *von Neumann Basis* for the presented setup were proposed. In future experiments, the vector-field shaper will be used in conjunction with a photoemission electron microscope (PEEM). This approach combines the temporal resolution provided by ultrashort laser pulses with the high spatial resolution gained by electron microscopy in order to perform two-dimensional spectroscopy and coherent control on nanostructures with polarization-shaped femtosecond laser pulses. In combination with other chiral-sensitive experimental setups implemented earlier in our group [281–285], the vector-field shaper opens up new perspectives for chiral femtochemistry and chiral control.

The designed vector-field shaper meets all requirements to generate high-precision polarization-shaped multipulse sequences. These can be used to perform numerous polarization-sensitive experiments. Employing the OPRAS routine, a quasi-infinitely long phase stability is achieved and complex and elaborated long-term measurements can be carried out. The fact that OPRAS demands no additional hardware and that only a single dual-layer LC SLM and inexpensive optics are required allows the building of a vector-field shaper at comparatively low costs. We hope that with the detailed insights into the optical design process as well as into the software implementation given in this thesis, vector-field shaping will become a standard technique just as conventional pulse shaping in the upcoming years.

Zusammenfassung und Ausblick

Die gezielte Formung ultrakurzer Laserpulse ist eine leistungsstarke Technik, die heutzutage in vielen Laserlaboren eingesetzt wird. Die meisten Pulsformer können jedoch nur linear polarisierte, in Phase und Amplitude geformte Laserpulse erzeugen. Einige Pulsformer können auch sich zeitlich verändernde Polarisationszustände generieren. Die möglichen Polarisationszustände sind allerdings beschränkt und eine gleichzeitige Formung der Amplitude ist dann nicht mehr möglich. Für einige moderne, nicht-lineare, zeitaufgelöste, spektroskopische Methoden, wie z.B. die polarisationsunterstützte zweidimensionale Spektroskopie, ist aber die gleichzeitige Kontrolle über die Polarisation und die Amplitude erstrebenswert.

In den letzten Jahren wurden verschiedene Konzepte entwickelt, um diese Beschränkungen zu überwinden und eine vollständige Kontrolle des Vektorfeldes über die vier Freiheitsgrade Phase, Amplitude, Orientierung und Elliptizität eines ultrakurzen Laserpulses zu erlangen. Ziel dieser Arbeit war es, einen solchen Vektorfeldformer zu konstruieren. Die Grundidee für das Design unseres Aufbaus basiert auf verschiedenen literaturbekannten Konzepten. Unser Ziel war es jedoch, ein optimiertes Design zu entwickeln, bei dem Formungsartefakte minimal sind und definierte polarisationsgeformte Mehrfachpulse mit der höchstmöglichen Genauigkeit erzeugt werden können.

In Kapitel 3 wurden verschiedene vorherige Ansätze für die erweiterte und vollständige Vektorfeldkontrolle detailliert geprüft und verglichen. Basierend auf dieser Analyse haben wir uns dazu entschlossen, das Konzept eines interferometrischen Vektorfeldformers zu verwenden. Bei diesem werden die spektrale Phase und Amplitude zweier orthogonal polarisierter Pulse unabhängig voneinander in den zwei Armen eines Interferometers manipuliert und durch Überlagerung dieser zwei Pulse die vollständige Kontrolle über das Vektorfeld erlangt.

Wie in Kapitel 4 beschrieben, besteht der Aufbau aus drei funktionellen Gruppen: i) einer optischen Komponente, um die zwei polarisierten Strahlen zu erzeugen und zu rekombinieren, ii) einem sog. $4f$-Aufbau und iii) einem Linsenteleskop, um die zwei Strahlen unter unterschiedlichen Winkeln auf das Gitter des $4f$-Aufbaus zu lenken, so dass beide Strahlen über dieselben Optiken propagieren. Diese Art der Strahlführung wurde gewählt, um die interferometrische Stabilität des Aufbaus zu verbessern. Beide Strahlen werden mit demselben $4f$-Aufbau geformt, indem unterschiedliche benachbarte Pixelbereiche des Flüssigkristall-Lichtmodulators (LC SLM, engl. liquid-crystal spatial light modulator) für die zwei Polarisationskomponenten genutzt werden. Das hat den Vorteil, dass nur ein einzelnes zweilagiges LC SLM benötigt wird und so ein kompakter und robuster Aufbau realisiert werden konnte. Um die Frequenzverteilung für einen breiten Spektralbereich von 740–880 nm anzupassen, wurden die besten Parameter für den Aufbau anhand numerischer Berechnungen bestimmt, und somit die Formungsmöglichkeiten unseres Vektorfeldformers optimiert. Im Gegensatz zu anderen

Designs wird ein Dünnschicht-Polarisator (TFP, engl. thin-film polarizer) anstelle eine Wollaston-Prismas verwendet, um die zwei senkrecht zueinander polarisierten Strahlen zu erzeugen und zu rekombinieren, da ein Wollaston-Prisma Artefakte wie Winkelchirp und eine über das Strahlprofiel variierende Phase verursacht. Bei Verwendung eines Wollaston-Prismas muss zudem der rekombinierte Strahl gegenüber des einfallenden Strahls in der Höhe verkippt werden, um beide räumlich trennen zu können. Raytracing-Simulationen haben gezeigt, dass dies in Kombination mit einem Teleskop und dem $4f$-Aufbau zu einer erheblichen Deformierung des Strahlprofiles führt. Diese Simulationen haben auch gezeigt, dass die Abbildungsfehler des Aufbaus weitestgehend aufgehoben werden, wenn der eingehende und ausgehende Strahl in derselben Ebene propagieren und somit die Strahlwege genau invertiert werden. Dies konnte mit Hilfe des TFPs in einer Konfiguration, die gekreuzten Polarisatoren entspricht, realisiert werden. Diese Konfiguration hat zudem den Vorteil, dass dadurch die polarisationsabhängige Effizienz des TFPs und der anderen Optiken automatisch kompensiert wird und ein hohes Auslöschungsverhältnis in der Größenordnung 15000:1 erzielt wird. Die chromatische Aberration wird allerdings durch diese Polarisator-Konfiguration nicht aufgehoben. Durch Raytracing wurde bestätigt, dass diese primär durch das Teleskop verursacht wird und nicht durch die Zylinderlinse des $4f$-Aufbaus. Allerdings wurden im experimentell genutzten Wellenlängenbereich von 780–816 nm nur geringe Störungen des Strahlprofiles beobachtet, die daher als vernachlässigbar angesehen wurden.

Die softwareseitige Umsetzung der Vektorfeldkontrolle wurde in Kapitel 5 beschrieben. Um verschiedene Experimente durchführen zu können, wurden fünf Parametrisierungen entwickelt, bei denen die erweiterten Formungsmöglichkeiten eines Vektorfeldformers berücksichtigt wurden. Die *Pixel Basis*, die *Spectral Basis* und die *Spectral Taylor Basis* können zusammen mit einem Optimierungsalgorithmus verwendet werden und sind damit bestens für Experimente der Quantenkontrolle geeignet. Für die multidimensionale Spektroskopie wurde die *Polarized Four-Pulse Basis* eingeführt. Mit dieser Parametrisierung können Mehrfach-Pulssequenzen mit bis zu vier Pulsen erzeugt werden. Dabei kann der Polarisationszustand jedes Pulses vorgegeben und die relative Intensität, Phase und der zeitliche Abstand aufeinanderfolgender Pulse festgelegt werden. Zusätzlich wurden in Kapitel 5 verschieden Softwareprogramme vorgestellt, die für die in dieser Arbeit durchgeführten Experimente notwendig sind.

Die experimentellen Ergebnisse wurden in Kapitel 6 präsentiert. Die Frequenzverteilung am LC SLM wurde gemessen und dabei bewiesen, dass die optimale Frequenzverteilung experimentell realisiert werden konnte. Des Weiteren wurden die exzellenten Eigenschaften des TFPs bestätigt. Im Allgemeinen emittiert der TFP Satellitenpulse durch interne Mehrfachreflexe. Mehrere Messungen haben jedoch gezeigt, dass diese Satellitenpulse einen zeitlichen Abstand von mindesten 4,05 ps vom Hauptpuls aufweisen und dass deren Intensität verschwindend gering ist. Die Phasenstabilität des Aufbaus beträgt $\sigma = 28{,}3$ mrad ($\approx \lambda/222$) über einen Zeitraum von einer Stunde. Um die Stabilität für sehr lange Messzeiten zu verbessern, wurde eine Routine zur Phasenreduktion und zur Stabilisierung (OPRAS, engl. on-the-fly phase reduction and stabilization) unter Einbeziehung des Pulsformers entwickelt. Diese Routine erzeugt automatisiert einen komprimierten Puls mit minimierter relativer Phase zwischen den zwei Polarisationskomponenten und ermöglicht so eine Phasenstabilität von $\sigma = 31{,}9$ mrad ($\approx \lambda/197$)

über nahezu 24 Stunden. Ferner wurden verschieden Pulssequenzen erzeugt und charakterisiert, die die Möglichkeiten der konventionellen Pulsformung übertreffen. Die experimentellen Ergebnisse zeigen, dass geformte Pulse mit beliebigen Phasen, Amplituden und Polarisationszuständen generiert werden können. In allen Fällen wurde eine sehr hohe Übereinstimmung zwischen den Zielparametern und den experimentellen Daten erreicht.

Für den zukünftigen Einsatz des Aufbaus wurden mögliche Erweiterungen vorgeschlagen. Diese sind nicht zwingend erforderlich, könnten aber die Leistung und die Einsatzmöglichkeiten des Vektorfeldformers weiter verbessern. Erstens wurde aufgezeigt, wie zwei Ausgangsstrahlen erzeugt werden könnten. Mit dieser Veränderung wäre es möglich, den größten Teil der Intensität des geformten Strahls für ein Experiment zu nutzen und gleichzeitig einen geringen Anteil für die Pulscharakterisierung oder für die Phasenstabilisierung mit der entwickelten Routine zu verwenden. Um chromatische Aberration zu vermeiden, wurde zweitens die prinzipielle Idee, das Linsenteleskop durch fokussierende Spiegel zu ersetzen, diskutiert. Für die verschiedenen erarbeiteten Parametrisierungen zur Vektorfeldkontrolle wurden einige Erweiterungen vorgeschlagen, um deren Einsatzmöglichkeiten noch weiter zu erhöhen. Außerdem wurde noch die Möglichkeit einer *von Neumann Basis* für den präsentierten Aufbau aufgezeigt. In zukünftigen Experimenten wird unser Aufbau mit einem Photoemissionselektronenmikroskop (PEEM) kombiniert. Dadurch kann die zeitliche Auflösung ultrakurzer Laserpulse mit der hohen räumlichen Auflösung der Elektronenmikroskopie vereint werden, was die zweidimensionale Spektroskopie und Quantenkontrolle von Nanostrukturen mit Hilfe polarisationsgeformter Femtosekunden-Laserpulse ermöglicht. Der Vektorfeldformer eröffnet in Verbindung mit anderen zuvor in unserer Gruppe implementierten chiral sensitiven Versuchsaufbauten [281–285] neue Perspektiven für die chirale Femtochemie und Kontrolle.

Der erarbeitete Vektorfeldformer erfüllt alle Anforderungen, um polarisationsgeformte Mehrfachpulssequenzen mit hoher Präzision zu erzeugen. Diese können verwendet werden, um zahlreiche polarisationssensitive Experimente durchzuführen. Durch die Stabilisierungsroutine OPRAS wird eine quasi unendlich lange Phasenstabilität des Aufbaus gewährleistet und komplexe und aufwendige Langzeitmessungen können ausgeführt werden. Die Tatsache, dass OPRAS keine weitere Hardware benötigt und der Aufbau nur einen einzigen zweilagigen Flüssigkristall-Lichtmodulator sowie ansonsten verhältnismäßig günstige Optiken erfordert, ermöglicht den Bau eines Vektorfeldformers zu vergleichsweise niedrigen Kosten. Wir hoffen, dass andere Forschergruppen von den detailreichen Einblicken in den Designprozess und die Software-Implementierung profitieren und dass die vollständige Vektorfeldformung in den nächsten Jahren genauso wie die konventionelle Pulsformung zu einer Standard-Technologie wird.

List of abbreviations

2D	Two dimensional
2D LC SLM	Two-dimensional liquid-crystal spatial light modulator
3D	Three dimensional
AOM	Acousto-optic modulator
AOPDF	Acousto-optic programmable dispersive filter
BBO	Beta Barium Borat
CEP	Carrier-envelope phase
CPA	Chirped-pulse amplifier
DA	Data acquisition
DLL	Dynamic-link library
FROG	Frequency-resolved optical gating
FTSI	Fourier-transform spectral interferometry
FWHM	Full-width at half-maximum
GUI	Graphical user interface
IR	Infrared
LC	Liquid crystal
LC SLM	Liquid-crystal spatial light modulator
ND	Neutral density
NIR	Near infrared
OPA	Optical parametric amplifier
OPRAS	On-the-fly phase reduction and stabilization
PEEM	Photoemission electron microscopy
POLLIWOG	Polarized light interference versus wavelength of only a glint
PS	Pulse shaper
SHG	Second-harmonic generation
SI	Spectral interference
SLM	Spatial light modulator
SVEA	Slowly varying envelope approximation
TEM	Transverse electromagnetic mode
TFP	Thin-film polarizer
TURTLE	Tomographic ultrafast retrieval of transverse light E-fields
VFS	Vector-field shaper
VI	Virtual instrument [software program written in LabVIEW]
VIS	Visible spectrum
UV	Ultraviolet

Bibliography

[1] C. Schwarz, O. Hüter, and T. Brixner, *Full vector-field control of ultrashort laser pulses utilizing a single dual-layer spatial light modulator in a common-path setup*, J. Opt. Soc. Am. B **32**, 933–945 (2015).

[2] U. Selig, F. Langhojer, F. Dimler, T. Löhrig, C. Schwarz, B. Gieseking, and T. Brixner, *Inherently Phase-Stable Coherent Two-Dimensional Spectroscopy Using only Conventional Optics*, Opt. Lett. **33**, 2851–2853 (2008).

[3] S. Rützel, *Pulse-Sequence Approaches for Multidimensional Electronic Spectroscopy of Ultrafast Photochemistry*, Dissertation, Universität Würzburg (2014).

[4] D. E. Spence, P. N. Kean, and W. Sibbett, *60-fsec pulse generation from a self-mode-locked Ti:sapphire laser*, Opt. Lett. **16**, 42–44 (1991).

[5] M. T. Asaki, C.-P. Huang, D. Garvey, J. Zhou, H. C. Kapteyn, and M. M. Murnane, *Generation of 11-fs pulses from a self-mode-locked Ti:sapphire laser*, Opt. Lett. **18**, 977–979 (1993).

[6] J. Zhou, G. Taft, C.-P. Huang, M. M. Murnane, H. C. Kapteyn, and I. P. Christov, *Pulse evolution in a broad-bandwidth Ti:sapphire laser*, Opt. Lett. **19**, 1149–1151 (1994).

[7] A. Stingl, M. Lenzner, C. Spielmann, F. Krausz, and R. Szipocs, *Sub-10-fs mirror-dispersion-controlled Ti:sapphire laser*, Opt. Lett. **20**, 602–604 (1995).

[8] I. D. Jung, F. X. Kärtner, N. Matuschek, D. H. Sutter, F. Morier-Genoud, G. Zhang, U. Keller, V. Scheuer, M. Tilsch, and T. Tschudi, *Self-starting 6.5-fs pulses from a Ti:sapphire laser*, Opt. Lett. **22**, 1009–1011 (1997).

[9] U. Morgner, F. X. Kärtner, S. H. Cho, Y. Chen, H. A. Haus, J. G. Fujimoto, E. P. Ippen, V. Scheuer, G. Angelow, and T. Tschudi, *Sub-two-cycle pulses from a Kerr-lens mode-locked Ti:sapphire laser*, Opt. Lett. **24**, 411–413 (1999).

[10] D. H. Sutter, G. Steinmeyer, L. Gallmann, N. Matuschek, F. Morier-Genoud, U. Keller, V. Scheuer, G. Angelow, and T. Tschudi, *Semiconductor saturable-absorber mirror assisted Kerr-lens mode-locked Ti:sapphire laser producing pulses in the two-cycle regime*, Opt. Lett. **24**, 631–633 (1999).

[11] A. M. Weiner, J. P. Heritage, and E. M. Kirschner, *High-resolution femtosecond pulse shaping*, J. Opt. Soc. Am. B **5**, 1563–1572 (1988).

[12] A. M. Weiner, *Femtosecond optical pulse shaping and processing*, Prog. Quantum Electron. **19**, 161–237 (1995).

[13] A. M. Weiner, *Femtosecond Pulse Shaping Using Spatial Light Modulators*, Rev. Sci. Instrum. **71**, 1929–1960 (2000).

[14] A. M. Weiner, *Ultrafast optical pulse shaping: A tutorial review*, Opt. Commun. **284**, 3669–3692 (2011).

[15] H. Kawashima, M. M. Wefers, and K. A. Nelson, *Femtosecond Pulse Shaping, Multiple-Pulse Spectroscopy, and Optical Control*, Annu. Rev. Phys. Chem. **46**, 627–656 (1995).

[16] F. G. Omenetto, A. J. Taylor, M. D. Moores, and D. H. Reitze, *Adaptive control of femtosecond pulse propagation in optical fibers*, Opt. Lett. **26**, 938–940 (2001).

[17] N. Dudovich, D. Oron, and Y. Silberberg, *Single-pulse coherently controlled nonlinear Raman spectroscopy and microscopy*, Nature **418**, 512–514 (2002).

[18] J. L. Herek, W. Wohlleben, R. J. Cogdell, D. Zeidler, and M. Motzkus, *Quantum control of energy flow in light harvesting*, Nature **417**, 533–535 (2002).

[19] D. Oron, N. Dudovich, and Y. Silberberg, *Femtosecond Phase-and-Polarization Control for Background-Free Coherent Anti-Stokes Raman Spectroscopy*, Phys. Rev. Lett. **90**, 213902 (2003).

[20] N. Dudovich, D. Oron, and Y. Silberberg, *Single-pulse coherent anti-Stokes Raman spectroscopy in the fingerprint spectral region*, J. Chem. Phys. **118**, 9208–9215 (2003).

[21] I. Pastirk, J. Dela Cruz, K. Walowicz, V. Lozovoy, and M. Dantus, *Selective two-photon microscopy with shaped femtosecond pulses*, Opt. Express **11**, 1695–1701 (2003).

[22] B. von Vacano and M. Motzkus, *Time-resolved two color single-beam CARS employing supercontinuum and femtosecond pulse shaping*, Opt. Commun. **264**, 488–493 (2006).

[23] P. Brumer and M. Shapiro, *Laser Control of Molecular Processes*, Annu. Rev. Phys. Chem. **43**, 257–282 (1992).

[24] R. J. Gordon and S. A. Rice, *Active control of the dynamics of atoms and molecules*, Annu. Rev. Phys. Chem. **48**, 601–641 (1997).

[25] A. Assion, T. Baumert, M. Bergt, T. Brixner, B. Kiefer, V. Seyfried, M. Strehle, and G. Gerber, *Control of chemical reactions by feedback-optimized phase-shaped femtosecond laser pulses*, Science **282**, 919–922 (1998).

[26] H. Rabitz, R. de Vivie-Riedle, M. Motzkus, and K. Kompa, *Whither the Future of Controlling Quantum Phenomena?* Science **288**, 824–828 (2000).

[27] S. A. Rice and M. Zhao, *Optical Control of Molecular Dynamics* (Wiley-Interscience, New York, 2000).

[28] T. Brixner, N. H. Damrauer, P. Niklaus, and G. Gerber, *Photoselective adaptive femtosecond quantum control in the liquid phase*, Nature **414**, 57–60 (2001).

[29] T. Brixner and G. Gerber, *Quantum Control of Gas-Phase and Liquid-Phase Femtochemistry*, ChemPhysChem **4**, 418–438 (2003).

[30] M. Dantus and V. V. Lozovoy, *Experimental coherent laser control of physicochemical processes*, Chem. Rev. **104**, 1813–1859 (2004).

[31] P. Nuernberger, G. Vogt, T. Brixner, and G. Gerber, *Femtosecond quantum control of molecular dynamics in the condensed phase*, Phys. Chem. Chem. Phys. **9**, 2470–2497 (2007).

[32] C. Brif, R. Chakrabarti, and H. Rabitz, *Control of quantum phenomena: past, present and future*, New J. Phys. **12**, 075008 (2010).

[33] M. Shapiro and P. Brumer, *Quantum Control of Molecular Processes* (Wiley-VCH, Weinheim, 2012), 2nd ed.

[34] C.-C. Chang, H. P. Sardesai, and A. M. Weiner, *Dispersion-free fiber transmission for femtosecond pulses by use of a dispersion-compensating fiber and a programmable pulse shaper*, Opt. Lett. **23**, 283–285 (1998).

[35] S. Shen and A. Weiner, *Complete dispersion compensation for 400-fs pulse transmission over 10-km fiber link using dispersion compensating fiber and spectral phase equalizer*, IEEE Photonics Technol. Lett. **11**, 827–829 (1999).

[36] Z. Jiang, S.-D. Yang, D. E. Leaird, and A. M. Weiner, *Fully dispersion-compensated ˜500 fs pulse transmission over 50 km single-mode fiber*, Opt. Lett. **30**, 1449–1451 (2005).

[37] A. Mermillod-Blondin, C. Mauclair, A. Rosenfeld, J. Bonse, I. V. Hertel, E. Audouard, and R. Stoian, *Size correction in ultrafast laser processing of fused silica by temporal pulse shaping*, Appl. Phys. Lett. **93**, 021921 (2008).

[38] A. Weiner, D. Leaird, J. Patel, and J. Wullert, *Programmable shaping of femtosecond optical pulses by use of 128-element liquid-crystal phase modulator*, IEEE J. Quantum Electron. **28**, 908–920 (1992).

[39] M. M. Wefers and K. A. Nelson, *Generation of high-fidelity programmable ultrafast optical waveforms*, Opt. Lett. **20**, 1047–1049 (1995).

[40] F. Verluise, V. Laude, Z. Cheng, C. Spielmann, and P. Tournois, *Amplitude and Phase Control of Ultrashort Pulses by Use of an Acousto-Optic Programmable Dispersive Filter: Pulse Compression and Shaping*, Opt. Lett. **25**, 575–577 (2000).

[41] J. C. Vaughan, T. Hornung, T. Feurer, and K. A. Nelson, *Diffraction-based femtosecond pulse shaping with a two-dimensionalspatial light modulator*, Opt. Lett. **30**, 323–325 (2005).

[42] T. Brixner and G. Gerber, *Femtosecond polarization pulse shaping*, Opt. Lett. **26**, 557–559 (2001).

[43] N. Dudovich, D. Oron, and Y. Silberberg, *Quantum Control of the Angular Momentum Distribution in Multiphoton Absorption Processes*, Phys. Rev. Lett. **92**, 103003 (2004).

[44] T. Brixner, G. Krampert, T. Pfeifer, R. Selle, G. Gerber, M. Wollenhaupt, O. Graefe, C. Horn, D. Liese, and T. Baumert, *Quantum Control by Ultrafast Polarization Shaping*, Phys. Rev. Lett. **92**, 208301 (2004).

[45] T. Suzuki, S. Minemoto, T. Kanai, and H. Sakai, *Optimal Control of Multiphoton Ionization Processes in Aligned I_2 Molecules with Time-Dependent Polarization Pulses*, Phys. Rev. Lett. **92**, 133005 (2004).

[46] M. Wollenhaupt, V. Engel, and T. Baumert, *Femtosecond laser photoelectron spectroscopy on atoms and small molecules: prototype studies in quantum control*, Annu. Rev. Phys. Chem. **56**, 25–56 (2005).

[47] M. Aeschlimann, M. Bauer, D. Bayer, T. Brixner, F. J. García de Abajo, W. Pfeiffer, M. Rohmer, C. Spindler, and F. Steeb, *Adaptive subwavelength control of nano-optical fields*, Nature **446**, 301–304 (2007).

[48] M. Wollenhaupt, M. Krug, J. Köhler, T. Bayer, C. Sarpe-Tudoran, and T. Baumert, *Photoelectron angular distributions from strong-field coherent electronic excitation*, Appl. Phys. B **95**, 245–259 (2009).

[49] M. Aeschlimann, M. Bauer, D. Bayer, T. Brixner, S. Cunovic, F. Dimler, A. Fischer, W. Pfeiffer, M. Rohmer, C. Schneider, F. Steeb, C. Strüber, and D. V. Voronine, *Spatiotemporal control of nanooptical excitations*, Proc. Natl. Acad. Sci. U.S.A. **107**, 5329–5333 (2010).

[50] M. Aeschlimann, T. Brixner, S. Cunovic, A. Fischer, P. Melchior, W. Pfeiffer, M. Rohmer, C. Schneider, C. Strüber, P. Tuchscherer, and D. Voronine, *Nano-optical control of hot-spot field superenhancement on a corrugated silver surface*, IEEE J. Sel. Top. Quantum Electron. **18**, 275–282 (2012).

[51] M. Aeschlimann, M. Bauer, D. Bayer, T. Brixner, S. Cunovic, A. Fischer, P. Melchior, W. Pfeiffer, M. Rohmer, C. Schneider, C. Strüber, P. Tuchscherer, and D. V. Voronine, *Optimal open-loop near-field control of plasmonic nanostructures*, New J. Phys. **14**, 033030 (2012).

[52] M. Wollenhaupt, C. Lux, M. Krug, and T. Baumert, *Tomographic Reconstruction of Designer Free-Electron Wave Packets*, ChemPhysChem **14**, 1341–1349 (2013).

[53] S. Mukamel, *Principles of Nonlinear Optical Spectroscopy* (Oxford University Press, New York, 1999).

[54] S. Mukamel, *Multidimensional femtosecond correlation spectroscopies of electronic and vibrational excitations*, Annu. Rev. Phys. Chem. **51**, 691–729 (2000).

[55] D. M. Jonas, *Two-dimensional femtosecond spectroscopy*, Annu. Rev. Phys. Chem. **54**, 425–463 (2003).

[56] R. M. Hochstrasser, *Two-dimensional spectroscopy at infrared and optical frequencies*, Proc. Natl. Acad. Sci. U.S.A. **104**, 14190–14196 (2007).

[57] M. Cho, *Coherent two-dimensional optical spectroscopy*, Chem. Rev. **108**, 1331–1418 (2008).

[58] J. P. Ogilvie and K. J. Kubarych, *Multidimensional Electronic and Vibrational Spectroscopy: An Ultrafast Probe of Molecular Relaxation and Reaction Dynamics (Chapter 5)*, Adv. At. Mol. Opt. Phys. **57**, 249–321 (2009).

[59] M. Cho, *Two-Dimensional Optical Spectroscopy* (CRC Press, Boca Raton, FL, 2009).

[60] P. Hamm and M. Zanni, *Concepts and Methods of 2D Infrared Spectroscopy* (Cambridge University Press, New York, 2011), 1st ed.

[61] S. T. Cundiff and S. Mukamel, *Optical multidimensional coherent spectroscopy*, Physics Today **66**, 44–49 (2013).

[62] A. Mokhtari, P. Cong, J. L. Herek, and A. H. Zewail, *Direct femtosecond mapping of trajectories in a chemical reaction*, Nature **348**, 225–227 (1990).

[63] A. H. Zewail, *Femtochemistry: Recent progess in studies of dynamics and control of reactions and their transition states*, J. Phys. Chem. **100**, 12701–12724 (1996).

[64] A. H. Zewail, *Femtochemistry: atomic-scale dynamics of the chemical bond*, J. Phys. Chem. A **104**, 5660–5694 (2000).

[65] A. H. Zewail, *Femtochemistry. Past, present, and future*, Pure Appl. Chem. **72**, 2219–2231 (2000).

[66] P. Tian, D. Keusters, Y. Suzaki, and W. S. Warren, *Femtosecond phase-coherent two-dimensional spectroscopy*, Science **300**, 1553–1555 (2003).

[67] J. C. Vaughan, T. Hornung, K. W. Stone, and K. A. Nelson, *Coherently Controlled Ultrafast Four-Wave Mixing Spectroscopy*, J. Phys. Chem. A **111**, 4873–4883 (2007).

[68] P. F. Tekavec, G. A. Lott, and A. H. Marcus, *Fluorescence-detected two-dimensional electronic coherence spectroscopy by acousto-optic phase modulation*, J. Chem. Phys. **127**, 214307 (2007).

[69] X. Dai, A. D. Bristow, D. Karaiskaj, and S. T. Cundiff, *Two-dimensional Fourier-transform spectroscopy of potassium vapor*, Phys. Rev. A **82**, 052503 (2010).

[70] X. Dai, M. Richter, H. Li, A. D. Bristow, C. Falvo, S. Mukamel, and S. T. Cundiff, *Two-Dimensional Double-Quantum Spectra Reveal Collective Resonances in an Atomic Vapor*, Phys. Rev. Lett. **108**, 193201 (2012).

[71] M. C. Asplund, M. T. Zanni, and R. M. Hochstrasser, *Two-dimensional infrared spectroscopy of peptides by phase-controlled femtosecond vibrational photon echoes*, Proc. Natl. Acad. Sci. U.S.A. **97**, 8219–8224 (2000).

[72] J. D. Hybl, A. Albrecht Ferro, and D. M. Jonas, *Two-dimensional Fourier transform electronic spectroscopy*, J. Chem. Phys. **115**, 6606 (2001).

[73] O. Golonzka, M. Khalil, N. Demirdöven, and A. Tokmakoff, *Vibrational Anharmonicities Revealed by Coherent Two-Dimensional Infrared Spectroscopy*, Phys. Rev. Lett. **86**, 2154–2157 (2001).

[74] M. Khalil, N. Demirdöven, and A. Tokmakoff, *Obtaining Absorptive Line Shapes in Two-Dimensional Infrared Vibrational Correlation Spectra*, Phys. Rev. Lett. **90**, 047401 (2003).

[75] T. Brixner, J. Stenger, H. M. Vaswani, M. Cho, R. E. Blankenship, and G. R. Fleming, *Two-dimensional spectroscopy of electronic couplings in photosynthesis*, Nature **434**, 625–628 (2005).

[76] J. Zheng, K. Kwak, J. Asbury, X. Chen, I. R. Piletic, and M. D. Fayer, *Ultrafast Dynamics of Solute-Solvent Complexation Observed at Thermal Equilibrium in Real Time*, Science **309**, 1338–1343 (2005).

[77] N. S. Ginsberg, Y.-C. Cheng, and G. R. Fleming, *Two-Dimensional Electronic Spectroscopy of Molecular Aggregates*, Acc. Chem. Res. **42**, 1352–1363 (2009).

[78] T. Elsaesser, *Two-Dimensional Infrared Spectroscopy of Intermolecular Hydrogen Bonds in the Condensed Phase*, Acc. Chem. Res. **42**, 1220–1228 (2009).

[79] M. D. Fayer, D. E. Moilanen, D. Wong, D. E. Rosenfeld, E. E. Fenn, and S. Park, *Water Dynamics in Salt Solutions Studied with Ultrafast Two-Dimensional Infrared (2D IR) Vibrational Echo Spectroscopy*, Acc. Chem. Res. **42**, 1210–1219 (2009).

[80] S. Ruetzel, M. Kullmann, J. Buback, P. Nuernberger, and T. Brixner, *Tracing the steps of photoinduced chemical reactions in organic molecules by coherent two-dimensional electronic spectroscopy using triggered exchange*, Phys. Rev. Lett. **110**, 148305 (2013).

[81] S. Ruetzel, M. Diekmann, P. Nuernberger, C. Walter, B. Engels, and T. Brixner, *Multidimensional spectroscopy of photoreactivity*, Proc. Natl. Acad. Sci. U.S.A. **111**, 4764–4769 (2014).

[82] T. Zhang, I. Kuznetsova, T. Meier, X. Li, R. P. Mirin, P. Thomas, and S. T. Cundiff, *Polarization-dependent optical 2D Fourier transform spectroscopy of semiconductors*, Proc. Natl. Acad. Sci. U.S.A. **104**, 14227–14232 (2007).

[83] S. T. Cundiff, T. Zhang, A. D. Bristow, D. Karaiskaj, and X. Dai, *Optical Two-Dimensional Fourier Transform Spectroscopy of Semiconductor Quantum Wells*, Acc. Chem. Res. **42**, 1423–1432 (2009).

[84] K. Stone, K. Gundogdu, D. Turner, X. Li, S. Cundiff, and K. Nelson, *Two-Quantum 2D FT Electronic Spectroscopy of Biexcitons in GaAs Quantum Wells*, Science **324**, 1169–1173 (2009).

[85] J. Kasprzak, B. Patton, V. Savona, and W. Langbein, *Coherent coupling between distant excitons revealed by two-dimensional nonlinear hyperspectral imaging*, Nat. Photonics **5**, 57–63 (2011).

[86] T. Brixner, I. V. Stiopkin, and G. R. Fleming, *Tunable two-dimensional femtosecond spectroscopy*, Opt. Lett. **29**, 884–886 (2004).

[87] T. Brixner, T. Mančal, I. V. Stiopkin, and G. R. Fleming, *Phase-stabilized two-dimensional electronic spectroscopy*, J. Chem. Phys. **121**, 4221–4236 (2004).

[88] T. Zhang, C. Borca, X. Li, and S. Cundiff, *Optical two-dimensional Fourier transform spectroscopy with active interferometric stabilization*, Opt. Express **13**, 7432–7441 (2005).

[89] V. Volkov, R. Schanz, and P. Hamm, *Active phase stabilization in Fourier-transform two-dimensional infrared spectroscopy*, Opt. Lett. **30**, 2010–2012 (2005).

[90] T. Hornung, J. C. Vaughan, T. Feurer, and K. A. Nelson, *Degenerate four-wave mixing spectroscopy based on two-dimensional femtosecondpulse shaping*, Opt. Lett. **29**, 2052–2054 (2004).

[91] E. M. Grumstrup, S.-H. Shim, M. A. Montgomery, N. H. Damrauer, and M. T. Zanni, *Facile collection of two-dimensional electronic spectra using femtosecond pulse-shaping technology*, Opt. Express **15**, 16681–16689 (2007).

[92] S.-H. Shim and M. T. Zanni, *How to Turn Your Pump–Probe Instrument into a Multidimensional Spectrometer: 2D IR and VIS Spectroscopies via Pulse Shaping*, Phys. Chem. Chem. Phys. **11**, 748–761 (2009).

[93] P. Hamm, M. Lim, W. F. DeGrado, and R. M. Hochstrasser, *The two-dimensional IR nonlinear spectroscopy of a cyclic penta-peptide in relation to its three-dimensional structure*, Proc. Natl. Acad. Sci. U.S.A. **96**, 2036–2041 (1999).

[94] S. Woutersen and P. Hamm, *Structure determination of trialanine in water using polarization sensitive two-dimensional vibrational spectroscopy*, J. Phys. Chem. B **104**, 11316–11320 (2000).

[95] M. T. Zanni and R. M. Hochstrasser, *Two-dimensional infrared spectroscopy: a promising new method for the time resolution of structures*, Curr. Opin. Struct. Biol. **11**, 516–522 (2001).

[96] E. C. Fulmer, P. Mukherjee, A. T. Krummel, and M. T. Zanni, *A pulse sequence for directly measuring the anharmonicities of coupled vibrations: Two-quantum two-dimensional infrared spectroscopy*, J. Chem. Phys. **120**, 8067 (2004).

[97] E. L. Read, G. S. Engel, T. R. Calhoun, T. Mancal, T. K. Ahn, R. E. Blankenship, and G. R. Fleming, *Multidimensional Ultrafast Spectroscopy Special Feature: Cross-peak-specific two-dimensional electronic spectroscopy*, Proc. Natl. Acad. Sci. U.S.A. **104**, 14203–14208 (2007).

[98] J. Réhault and J. Helbing, *Angle determination and scattering suppression in polarization-enhanced two-dimensional infrared spectroscopy in the pump-probe geometry*, Opt. Express **20**, 21665–21677 (2012).

[99] M. T. Zanni, N.-H. Ge, Y. S. Kim, and R. M. Hochstrasser, *Two-dimensional IR spectroscopy can be designed to eliminate the diagonal peaks and expose only the crosspeaks needed for structure determination*, Proc. Natl. Acad. Sci. U.S.A. **98**, 11265–11270 (2001).

[100] M. T. Zanni, S. Gnanakaran, J. Stenger, and R. M. Hochstrasser, *Heterodyned Two-Dimensional Infrared Spectroscopy of Solvent-Dependent Conformations of Acetylproline-NH2†*, J. Phys. Chem. B **105**, 6520–6535 (2001).

[101] K.-K. Lee, K.-H. Park, S. Park, S.-J. Jeon, and M. Cho, *Polarization-Angle-Scanning 2DIR Spectroscopy of Coupled Anharmonic Oscillators: A Polarization Null Angle Method*, J. Phys. Chem. B **115**, 5456–5464 (2011).

[102] M. Cho, *Two-dimensional circularly polarized pump–probe spectroscopy*, J. Chem. Phys. **119**, 7003–7016 (2003).

[103] J.-H. Choi and M. Cho, *Quadrupole contribution to the third-order optical activity spectroscopy*, J. Chem. Phys. **127**, 024507 (2007).

[104] J.-H. Choi, S. Cheon, H. Lee, and M. Cho, *Two-dimensional nonlinear optical activity spectroscopy of coupled multi-chromophore system*, Phys. Chem. Chem. Phys. **10**, 3839–3856 (2008).

[105] A. F. Fidler, V. P. Singh, P. D. Long, P. D. Dahlberg, and G. S. Engel, *Dynamic localization of electronic excitation in photosynthetic complexes revealed with chiral two-dimensional spectroscopy*, Nat. Commun. **5** (2014).

[106] M. Shapiro and P. Brumer, *Controlled photon induced symmetry breaking: Chiral molecular products from achiral precursors*, J. Chem. Phys. **95**, 8658–8661 (1991).

[107] J. Shao and P. Hänggi, *Control of molecular chirality*, J. Chem. Phys. **107**, 9935–9941 (1997).

[108] M. Shapiro, E. Frishman, and P. Brumer, *Coherently Controlled Asymmetric Synthesis with Achiral Light*, Phys. Rev. Lett. **84**, 1669 (2000).

[109] S. Günther, B. Kaulich, L. Gregoratti, and M. Kiskinova, *Photoelectron microscopy and applications in surface and materials science*, Prog. Surf. Sci. **70**, 187–260 (2002).

[110] M. Aeschlimann, T. Brixner, A. Fischer, C. Kramer, P. Melchior, W. Pfeiffer, C. Schneider, C. Strüber, P. Tuchscherer, and D. V. Voronine, *Coherent two-dimensional nanoscopy*, Science **333**, 1723–1726 (2011).

[111] P. Vasa, C. Ropers, R. Pomraenke, and C. Lienau, *Ultra-fast nano-optics*, Laser Photonics Rev. **3**, 483–507 (2009).

[112] L. Novotny and B. Hecht, *Principles of Nano-Optics* (Cambridge University Press, Cambridge, 2012), 2nd ed.

[113] M. Ohtsu, ed., *Handbook of Nano-Optics and Nanophotonics* (Springer, New York, 2013).

[114] W. L. Barnes, A. Dereux, and T. W. Ebbesen, *Surface plasmon subwavelength optics*, Nature **424**, 824–830 (2003).

[115] S. A. Maier, *Plasmonics: Fundamentals and Applications* (Springer, New York, 2007).

[116] B. Lee, I.-M. Lee, S. Kim, D.-H. Oh, and L. Hesselink, *Review on subwavelength confinement of light with plasmonics*, J. Mod. Opt. **57**, 1479 (2010).

[117] M. Pelton and G. W. Bryant, *Introduction to Metal-Nanoparticle Plasmonics* (John Wiley & Sons, Hoboken, New Jersey, 2013), 1st ed.

[118] T. V. Shahbazyan and M. I. Stockman, *Plasmonics: Theory and Applications* (Springer, New York, 2014).

[119] T. Brixner, W. Pfeiffer, and F. García de Abajo, *Femtosecond shaping of transverse and longitudinallight polarization*, Opt. Lett. **29**, 2187–2189 (2004).

[120] T. Brixner, F. J. García de Abajo, J. Schneider, and W. Pfeiffer, *Nanoscopic ultrafast space-time-resolved spectroscopy*, Phys. Rev. Lett. **95**, 093901 (2005).

[121] T. Brixner, F. J. García de Abajo, J. Schneider, C. Spindler, and W. Pfeiffer, *Ultrafast adaptive optical near-field control*, Phys. Rev. B **73**, 125437 (2006).

[122] T. Brixner, F. García de Abajo, C. Spindler, and W. Pfeiffer, *Adaptive ultrafast nano-optics in a tight focus*, Appl. Phys. B **84**, 89–95 (2006).

[123] M. Sukharev and T. Seideman, *Phase and Polarization Control as a Route to Plasmonic Nanodevices*, Nano Lett. **6**, 715–719 (2006).

[124] M. Sukharev and T. Seideman, *Coherent control of light propagation via nanoparticle arrays*, J. Phys. B: At. Mol. Opt. Phys. **40**, 283–298 (2007).

[125] M. Durach, A. Rusina, M. I. Stockman, and K. Nelson, *Toward Full Spatiotemporal Control on the Nanoscale*, Nano Lett. **7**, 3145–3149 (2007).

[126] M. I. Stockman, *Ultrafast nanoplasmonics under coherent control*, New J. Phys. **10**, 025031 (2008).

[127] X. Li and M. I. Stockman, *Highly efficient spatiotemporal coherent control in nanoplasmonics on a nanometer-femtosecond scale by time reversal*, Phys. Rev. B **77**, 195109 (2008).

[128] P. Tuchscherer, C. Rewitz, D. V. Voronine, F. J. García de Abajo, W. Pfeiffer, and T. Brixner, *Analytic coherent control of plasmon propagation in nanostructures*, Opt. Express **17**, 14235–14259 (2009).

[129] P. Geisler, G. Razinskas, E. Krauss, X.-F. Wu, C. Rewitz, P. Tuchscherer, S. Goetz, C.-B. Huang, T. Brixner, and B. Hecht, *Multimode plasmon excitation and in situ analysis in top-down fabricated nanocircuits*, Phys. Rev. Lett. **111**, 183901 (2013).

[130] C. Rewitz, G. Razinskas, P. Geisler, E. Krauss, S. Goetz, M. Pawłowska, B. Hecht, and T. Brixner, *Coherent control of plasmon propagation in a nanocircuit*, Phys. Rev. Applied **1**, 014007 (2014).

[131] T. Brixner, M. Aeschlimann, and W. Pfeiffer, *Ultraschnelle Nanooptik*, Phys. J. **13**, 35 (2014).

[132] L. Polachek, D. Oron, and Y. Silberberg, *Full control of the spectral polarization of ultrashort pulses*, Opt. Lett. **31**, 631–633 (2006).

[133] M. Plewicki, S. Weber, F. Weise, and A. Lindinger, *Independent control over the amplitude, phase, and polarization of femtosecond pulses*, Appl. Phys. B **86**, 259–263 (2006).

[134] M. Plewicki, F. Weise, S. M. Weber, and A. Lindinger, *Phase, amplitude, and polarization shaping with a pulse shaper in a Mach-Zehnder interferometer*, Appl. Opt. **45**, 8354–8359 (2006).

[135] M. Ninck, A. Galler, T. Feurer, and T. Brixner, *Programmable common-path vector field synthesizer for femtosecond pulses*, Opt. Lett. **32**, 3379–3381 (2007).

[136] F. Weise and A. Lindinger, *Full control over the electric field using four liquid crystal arrays*, Opt. Lett. **34**, 1258–1260 (2009).

[137] F. Weise, S. M. Weber, M. Plewicki, and A. Lindinger, *Application of phase, amplitude, and polarization shaped pulses for optimal control on molecules*, Chem. Phys. **332**, 313–317 (2007).

[138] D. B. Strasfeld, C. T. Middleton, and M. T. Zanni, *Mode selectivity with polarization shaping in the mid-IR*, New J. Phys. **11**, 105046 (2009).

[139] C. T. Middleton, D. B. Strasfeld, and M. T. Zanni, *Polarization shaping in the mid-IR and*

polarization-based balanced heterodyne detection with application to 2D IR spectroscopy, Opt. Express **17**, 14526–14533 (2009).

[140] P. Schön, M. Behrndt, D. Aït-Belkacem, H. Rigneault, and S. Brasselet, *Polarization and phase pulse shaping applied to structural contrast in nonlinear microscopy imaging*, Phys. Rev. A **81**, 013809 (2010).

[141] F. Weise, G. Achazi, and A. Lindinger, *Parametrically polarization-shaped pulses via a hollow-core photonic crystal fiber*, Phys. Rev. A **82**, 053827 (2010).

[142] F. Weise, M. Pawłowska, G. Achazi, and A. Lindinger, *Full control of polarization and temporal shape of ultrashort laser pulses transmitted through an optical fibre*, J. Opt. **13**, 075301 (2011).

[143] J.-C. Diels and W. Rudolph, *Ultrashort Laser Pulse Phenomena: Fundamentals, Techniques, and Applications on a Femtosecond Time Scale* (Academic Press, Massachusetts, 2006), 2nd ed.

[144] E. Hecht, *Optics* (Addison Wesley, Reading, Mass, 2002), 4th ed.

[145] D. Meschede, *Optics, light and lasers*, Physics textbook (Wiley-VCH, Weinheim, 2007), 2nd ed.

[146] F. Träger, *Springer Handbook of Lasers and Optics*, Springer handbooks (Springer, Dordrecht, New York, 2012), 2nd ed.

[147] P. Tuchscherer, *A Route to Optical Spectroscopy on the Nanoscale*, Dissertation, Universität Würzburg (2012).

[148] C. Rewitz, *Far-Field Characterization and Control of Propagating Ultrashort Optical Near Fields*, Dissertation, Universität Würzburg (2014).

[149] W. J. Walecki, D. N. Fittinghoff, A. L. Smirl, and R. Trebino, *Characterization of the polarization state of weak ultrashort coherent signals by dual-channel spectral interferometry*, Opt. Lett. **22**, 81–83 (1997).

[150] M. Renard, R. Chaux, B. Lavorel, and O. Faucher, *Pulse trains produced by phase-modulation of ultrashort optical pulses: tailoring and characterization*, Opt. Express **12**, 473–482 (2004).

[151] T. Brixner, G. Krampert, P. Niklaus, and G. Gerber, *Generation and characterization of polarization-shaped femtosecond laser pulses*, Appl. Phys. B **74**, 133–144 (2002).

[152] T. Brixner, *Poincaré representation of polarization-shaped femtosecond laser pulses*, Appl. Phys. B **76**, 531–540 (2003).

[153] M. A. Porras, *Propagation-induced changes in the instantaneous polarization state, phase, and carrier–envelope phase of few-cycle pulsed beams*, J. Opt. Soc. Am. B **30**, 1652–1659 (2013).

[154] S. Rützel, A. Krischke, and T. Brixner, *The von Neumann representation as a joint time–frequency parameterization for polarization-shaped femtosecond laser pulses*, Appl. Phys. B **107**, 1–9 (2012).

[155] H. Poincaré, *Théorie mathématique de la lumière II. Nouvelles études sur la diffraction.–Théorie de la dispersion de Helmholtz.*, vol. 2 (Georges Carré, Paris, 1892).

[156] D. H. Goldstein, *Polarized light*, Optical engineering; 83 (Dekker, New York, 2003), 2nd ed.

[157] R. C. Jones, *A New Calculus for the Treatment of Optical Systems*, J. Opt. Soc. Am. **31**, 488–493 (1941).

[158] A. L. Fymat, *Jones's Matrix Representation of Optical Instruments. 2: Fourier Interferometers (Spectrometers and Spectropolarimeters)*, Appl. Opt. **10**, 2711–2716 (1971).

[159] A. L. Fymat, *Jones's Matrix Representation of Optical Instruments.I: Beam Splitters*, Appl. Opt. **10**, 2499–2505 (1971).

[160] A. Gerrard and J. M. Burch, *Introduction to Matrix Methods in Optics* (Dover Publications, New York, 1994).

[161] J. Magnes, D. Odera, J. Hartke, M. Fountain, L. Florence, and V. Davis, *Quantitative and Qualitative Study of Gaussian Beam Visualization Techniques*, arXiv:physics/0605102 (2006).

[162] M. Rosete, *Position sensing of a Gaussian beam with a power meter and a knife edge*, Rev. Mex. Fis. **39**, 484–492 (1993).

[163] J. M. Khosrofian and B. A. Garetz, *Measurement of a Gaussian laser beam diameter through the direct inversion of knife-edge data*, Appl. Opt. **22**, 3406 (1983).

[164] G. Veshapidze, M. L. Trachy, M. H. Shah, and B. D. DePaola, *Reducing the uncertainty in laser beam size measurement with a scanning edge method*, Appl. Opt. **45**, 8197–8199 (2006).

[165] M. A. de Araújo, R. Silva, E. de Lima, D. P. Pereira, and P. C. de Oliveira, *Measurement of Gaussian laser beam radius using the knife-edge technique: improvement on data analysis*, Appl. Opt. **48**, 393 (2009).

[166] M. González-Cardel, P. Arguijo, and R. Díaz-Uribe, *Gaussian beam radius measurement with a knife-edge: a polynomial approximation to the inverse error function*, Appl. Opt. **52**, 3849–3855 (2013).

[167] L. Lepetit, G. Chériaux, and M. Joffre, *Linear Techniques of Phase Measurement by Femtosecond Spectral Interferometry for Applications in Spectroscopy*, J. Opt. Soc. Am. B **12**, 2467–2474 (1995).

[168] D. N. Fittinghoff, J. L. Bowie, J. N. Sweetser, R. T. Jennings, M. A. Krumbügel, K. W. DeLong, R. Trebino, and I. A. Walmsley, *Measurement of the intensity and phase of ultraweak, ultrashort laser pulses*, Opt. Lett. **21**, 884–886 (1996).

[169] C. Dorrer, N. Belabas, J.-P. Likforman, and M. Joffre, *Experimental implementation of Fourier-transform spectral interferometry and its application to the study of spectrometers*, Appl. Phys. B **70**, 99–107 (2000).

[170] D. Kane and R. Trebino, *Characterization of arbitrary femtosecond pulses using frequency-resolved optical gating*, IEEE J. Quantum Electron. **29**, 571–579 (1993).

[171] R. Trebino, K. W. DeLong, D. N. Fittinghoff, J. N. Sweetser, M. A. Krumbügel, B. A. Richman, and D. J. Kane, *Measuring Ultrashort Laser Pulses in the Time-Frequency Domain Using Frequency-Resolved Optical Gating*, Rev. Sci. Instrum. **68**, 3277–3295 (1997).

[172] R. Trebino, *Frequency-Resolved Optical Gating: The Measurement of Ultrashort Laser Pulses* (Springer, New York, 2002).

[173] K. W. DeLong, R. Trebino, J. Hunter, and W. E. White, *Frequency-resolved optical gating with the use of second-harmonic generation*, J. Opt. Soc. Am. B **11**, 2206–2215 (1994).

[174] P. A. Franken, A. E. Hill, C. W. Peters, and G. Weinreich, *Generation of Optical Harmonics*, Phys. Rev. Lett. **7**, 118 (1961).

[175] Y. R. Shen, *Principles of Nonlinear Optics* (Wiley & Sons, New York, NY, 2002), 1st ed.

[176] R. W. Boyd, *Nonlinear Optics* (Academic Press, Burlington, 2008), 3rd ed.

[177] L. Gallmann, G. Steinmeyer, D. H. Sutter, N. Matuschek, and U. Keller, *Collinear type II second-harmonic-generation frequency-resolved optical gating for the characterization of sub-10-fs optical pulses*, Opt. Lett. **25**, 269–271 (2000).

[178] I. Amat-Roldán, I. Cormack, P. Loza-Alvarez, E. Gualda, and D. Artigas, *Ultrashort Pulse Characterisation with SHG Collinear-FROG*, Opt. Express **12**, 1169–1178 (2004).

[179] G. Stibenz and G. Steinmeyer, *Interferometric frequency-resolved optical gating*, Opt. Express **13**, 2617–2626 (2005).

[180] G. Stibenz and G. Steinmeyer, *Structures of interferometric frequency-resolved optical gating*, IEEE J. Sel. Top. Quantum Electron. **12**, 286–296 (2006).

[181] J. R. Fienup, *Phase retrieval algorithms: a comparison*, Appl. Opt. **21**, 2758–2769 (1982).

[182] R. Trebino and D. J. Kane, *Using phase retrieval to measure the intensity and phase of ultrashort pulses: frequency-resolved optical gating*, J. Opt. Soc. Am. A **10**, 1101–1111 (1993).

[183] K. W. DeLong, D. N. Fittinghoff, R. Trebino, B. Kohler, and K. Wilson, *Pulse retrieval in frequency-resolved optical gating based on the method of generalized projections*, Opt. Lett. **19**, 2152–2154 (1994).

[184] P. Schlup, O. Masihzadeh, L. Xu, R. Trebino, and R. A. Bartels, *Tomographic retrieval of the polarization state of an ultrafast laser pulse*, Opt. Lett. **33**, 267–269 (2008).

[185] A. Monmayrant, S. Weber, and B. Chatel, *A newcomer's guide to ultrashort pulse shaping and characterization*, J. Phys. B: At. Mol. Opt. Phys. **43**, 103001 (2010).

[186] P. Tournois, *Acousto-optic programmable dispersive filter for adaptive compensation of group delay time dispersion in laser systems*, Opt. Commun. **140**, 245–249 (1997).

[187] F. Verluise, V. Laude, J.-P. Huignard, P. Tournois, and A. Migus, *Arbitrary Dispersion Control of Ultrashort Optical Pulses with Acoustic Waves*, J. Opt. Soc. Am. B **17**, 138–145 (2000).

[188] O. E. Martinez, *Grating and prism compressors in the case of finite beam size*, J. Opt. Soc. Am. B **3**, 929–934 (1986).

[189] O. Martinez, *Matrix formalism for pulse compressors*, IEEE J. Quantum Electron. **24**, 2530–2536 (1988).

[190] M. Bass, *Handbook of Optics, Vol. 2: Devices, Measurements, and Properties* (McGraw-Hill Professional, New York, 1994), 2nd ed.

[191] J. Li, C.-H. Wen, S. Gauza, R. Lu, and S.-T. Wu, *Refractive Indices of Liquid Crystals for Display Applications*, J. Display Technol. **1**, 51 (2005).

[192] Jenoptik, *SLM-S640d / SLM-S320d*, Technical Documentation (2012).

[193] M. M. Wefers and K. A. Nelson, *Analysis of programmable ultrashort waveform generation using liquid-crystal spatial light modulators*, J. Opt. Soc. Am. B **12**, 1343–1362 (1995).

[194] A. M. Weiner, D. E. Leaird, J. S. Patel, and J. R. Wullert, *Programmable femtosecond pulse shaping by use of a multielement liquid-crystal phase modulator*, Opt. Lett. **15**, 326–328 (1990).

[195] J. Vaughan, T. Feurer, K. Stone, and K. Nelson, *Analysis of replica pulses in femtosecond pulse shaping with pixelated devices*, Opt. Express **14**, 1314–1328 (2006).

[196] J. Paye and A. Migus, *Space-time Wigner functions and their application to the analysis of a pulse shaper*, J. Opt. Soc. Am. B **12**, 1480–1490 (1995).

[197] M. Wefers and K. Nelson, *Space-time profiles of shaped ultrafast optical waveforms*, IEEE J. Quantum Electron. **32**, 161–172 (1996).

[198] C. Dorrer and F. Salin, *Phase amplitude coupling in spectral phase modulation*, IEEE J. Sel. Top. Quantum Electron. **4**, 342–345 (1998).

[199] T. Tanabe, H. Tanabe, Y. Teramura, and F. Kannari, *Spatiotemporal measurements based on spatial spectral interferometry for ultrashort optical pulses shaped by a Fourier pulse shaper*, J. Opt. Soc. Am. B **19**, 2795–2802 (2002).

[200] T. Tanab, F. Kannari, F. Korte, J. Koch, and B. Chichkov, *Influence of spatiotemporal coupling induced by an ultrashort laser pulse shaper on a focused beam profile*, Appl. Opt. **44**, 1092–1098 (2005).

[201] B. J. Sussman, R. Lausten, and A. Stolow, *Focusing of light following a 4-f pulse shaper: Considerations for quantum control*, Phys. Rev. A **77**, 043416 (2008).

[202] F. Frei, A. Galler, and T. Feurer, *Space-time coupling in femtosecond pulse shaping and its effects on coherent control*, J. Chem. Phys. **130**, 034302 (2009).

[203] M. M. Wefers and K. A. Nelson, *Programmable phase and amplitude femtosecond pulse shaping*, Opt. Lett. **18**, 2032–2034 (1993).

[204] T. Brixner, N. H. Damrauer, G. Krampert, P. Niklaus, and G. Gerber, *Adaptive shaping of femtosecond polarization profiles*, J. Opt. Soc. Am. B **20**, 878–881 (2003).

[205] A. Efimov, C. Schaffer, and D. H. Reitze, *Programmable shaping of ultrabroad-bandwidth pulses from a Ti:sapphire laser*, J. Opt. Soc. Am. B **12**, 1968–1980 (1995).

[206] T. Baumert, T. Brixner, V. Seyfried, M. Strehle, and G. Gerber, *Femtosecond pulse shaping by an evolutionary algorithm with feedback*, Appl. Phys. B **65**, 779–782 (1997).

[207] D. Strickland and G. Mourou, *Compression of amplified chirped optical pulses*, Opt. Commun. **56**, 219–221 (1985).

[208] A. Efimov, M. D. Moores, N. M. Beach, J. L. Krause, and D. H. Reitze, *Adaptive control of pulse phase in a chirped-pulse amplifier*, Opt. Lett. **23**, 1915–1917 (1998).

[209] A. Efimov and D. H. Reitze, *Programmable dispersion compensation and pulse shaping in a 26-fs chirped-pulse amplifier*, Opt. Lett. **23**, 1612–1614 (1998).

[210] T. Brixner, M. Strehle, and G. Gerber, *Feedback-controlled optimization of amplified femtosecond laser pulses*, Appl. Phys. B **68**, 281–284 (1999).

[211] D. E. Goldberg, *Genetic Algorithms in Search, Optimization, and Machine Learning* (Addison-Wesley Professional, Reading, Mass, 1989), 1st ed.

[212] B. Amstrup, J. D. Doll, R. A. Sauerbrey, G. Szabó, and A. Lorincz, *Optimal control of quantum systems by chirped pulses*, Phys. Rev. A **48**, 3830–3836 (1993).

[213] B. Amstrup, G. J. Toth, G. Szabo, H. Rabitz, and A. Loerincz, *Genetic Algorithm with Migration on Topology Conserving Maps for Optimal Control of Quantum Systems*, J. Phys. Chem. **99**, 5206–5213 (1995).

[214] H. P. Schwefel, *Evolution and Optimum Seeking* (Wiley VCH, New York, 1995).

[215] D. Yelin, D. Meshulach, and Y. Silberberg, *Adaptive femtosecond pulse compression*, Opt. Lett. **22**, 1793–1795 (1997).

[216] D. Meshulach, D. Yelin, and Y. Silberberg, *Adaptive ultrashort pulse compression and shaping*, Opt. Commun. **138**, 345–348 (1997).

[217] D. Meshulach, D. Yelin, and Y. Silberberg, *Adaptive real-time femtosecond pulse shaping*, J. Opt. Soc. Am. B **15**, 1615–1619 (1998).

[218] W. S. Warren, H. Rabitz, and M. Dahleh, *Coherent Control of Quantum Dynamics: The Dream Is Alive*, Science **259**, 1581–1589 (1993).

[219] R. S. Judson and H. Rabitz, *Teaching lasers to control molecules*, Phys. Rev. Lett. **68**, 1500–1503 (1992).

[220] D. Meshulach and Y. Silberberg, *Coherent quantum control of two-photon transitions by a femtosecond laser pulse*, Nature **396**, 239–242 (1998).

[221] D. Meshulach and Y. Silberberg, *Coherent quantum control of multiphoton transitions by shaped ultrashort optical pulses*, Phys. Rev. A **60**, 1287 (1999).

[222] M. Bergt, T. Brixner, B. Kiefer, M. Strehle, and G. Gerber, *Controlling the Femtochemistry of $Fe(CO)_5$*, J. Phys. Chem. A **103**, 10381–10387 (1999).

[223] N. Dudovich, B. Dayan, S. M. Gallagher Faeder, and Y. Silberberg, *Transform-Limited Pulses Are Not Optimal for Resonant Multiphoton Transitions*, Phys. Rev. Lett. **86**, 47–50 (2001).

[224] N. Dudovich, D. Oron, and Y. Silberberg, *Coherent Transient Enhancement of Optically Induced Resonant Transitions*, Phys. Rev. Lett. **88**, 123004 (2002).

[225] A. F. Bartelt, T. Feurer, and L. Wöste, *Understanding optimal control results by reducing the complexity*, Chem. Phys. **318**, 207–216 (2005).

[226] G. Vogt, P. Nuernberger, R. Selle, F. Dimler, T. Brixner, and G. Gerber, *Analysis of femtosecond quantum control mechanisms with colored double pulses*, Phys. Rev. A **74**, 033413 (2006).

[227] M. Wollenhaupt, A. Präkelt, C. Sarpe-Tudoran, D. Liese, T. Bayer, and T. Baumert, *Femtosecond strong-field quantum control with sinusoidally phase-modulated pulses*, Phys. Rev. A **73**, 063409 (2006).

[228] A. Pe'er, B. Dayan, A. A. Friesem, and Y. Silberberg, *Temporal Shaping of Entangled Photons*, Phys. Rev. Lett. **94**, 073601 (2005).

[229] V. V. Lozovoy, I. Pastirk, and M. Dantus, *Multiphoton intrapulse interference. IV. Ultrashort laserpulse spectral phase characterization and compensation*, Opt. Lett. **29**, 775–777 (2004).

[230] B. Xu, Y. Coello, V. V. Lozovoy, D. A. Harris, and M. Dantus, *Pulse shaping of octave spanning femtosecond laser pulses*, Opt. Express **14**, 10939–10944 (2006).

[231] T.-w. Wu, J. Tang, B. Hajj, and M. Cui, *Phase resolved interferometric spectral modulation (PRISM) for ultrafast pulse measurement and compression*, Opt. Express **19**, 12961–12968 (2011).

[232] Y. Silberberg, *Quantum coherent control for nonlinear spectroscopy and microscopy*, Annu. Rev. Phys. Chem. **60**, 277–292 (2009).

[233] T. Hornung, R. Meier, D. Zeidler, K.-L. Kompa, D. Proch, and M. Motzkus, *Optimal control of one- and two-photon transitions with shaped femtosecond pulses and feedback*, Appl. Phys. B **71**, 277–284 (2000).

[234] R. J. Levis, G. M. Menkir, and H. Rabitz, *Selective Bond Dissociation and Rearrangement with Optimally Tailored, Strong-Field Laser Pulses*, Science **292**, 709–713 (2001).

[235] J. Degert, W. Wohlleben, B. Chatel, M. Motzkus, and B. Girard, *Realization of a Time-Domain Fresnel Lens with Coherent Control*, Phys. Rev. Lett. **89**, 203003 (2002).

[236] A. Monmayrant, B. Chatel, and B. Girard, *Quantum State Measurement Using Coherent Transients*, Phys. Rev. Lett. **96**, 103002 (2006).

[237] K. Ohmori, *Wave-packet and coherent control dynamics*, Annu. Rev. Phys. Chem. **60**, 487–511 (2009).

[238] J. J. Baumberg, A. Armitage, M. S. Skolnick, and J. S. Roberts, *Suppressed Polariton Scattering in Semiconductor Microcavities*, Phys. Rev. Lett. **81**, 661–664 (1998).

[239] A. Galler and T. Feurer, *Pulse Shaper Assisted Short Laser Pulse Characterization*, Appl. Phys. B **90**, 427–430 (2008).

[240] D. Sofikitis, S. Weber, A. Fioretti, R. Horchani, M. Allegrini, B. Chatel, D. Comparat, and P. Pillet, *Molecular vibrational cooling by optical pumping with shaped femtosecond pulses*, New J. Phys. **11**, 055037 (2009).

[241] Y. Esumi, M. D. Kabir, and F. Kannari, *Spatiotemporal vector pulse shaping of femtosecond laser pulses with a multi-pass two-dimensional spatial light modulator*, Opt. Express **17**, 19153–19159 (2009).

[242] E. Frumker and Y. Silberberg, *Phase and amplitude pulse shaping with two-dimensional phase-only spatial light modulators*, J. Opt. Soc. Am. B **24**, 2940–2947 (2007).

[243] S. M. Weber, M. Plewicki, F. Weise, and A. Lindinger, *Parametric polarization pulse shaping demonstrated for optimal control of NaK*, J. Chem. Phys. **128**, 174306 (2008).

[244] G. Achazi, A. Patas, F. Weise, M. Pawłowska, and A. Lindinger, *Reconstruction of polarization-shaped laser pulses after a hollow-core fiber using backreflection*, Appl. Opt. **50**, 915–923 (2011).

[245] F. Weise, M. Pawłowska, G. Achazi, and A. Lindinger, *Parametrically phase-, amplitude-, and polarization-shaped femtosecond laser pulses guided via a step-index fiber*, J. Opt. Soc. Am. B **28**, 406–415 (2011).

[246] F. Weise, G. Achazi, M. Pawłowska, and A. Lindinger, *Systematic variation of parametrically shaped sub-pulse sequences after transmission through a photonic crystal fiber*, Opt. Commun. **284**, 3759–3771 (2011).

[247] S. M. Weber, F. Weise, M. Plewicki, and A. Lindinger, *Interferometric generation of parametrically shaped polarization pulses*, Appl. Opt. **46**, 5987–5990 (2007).

[248] M. Sato, T. Suzuki, and K. Misawa, *Interferometric polarization pulse shaper stabilized by an external laser diode for arbitrary vector field shaping*, Rev. Sci. Instrum. **80**, 123107 (2009).

[249] P. Tyagi, J. I. Saari, B. Walsh, A. Kabir, V. Crozatier, N. Forget, and P. Kambhampati, *Two-Color Two-Dimensional Electronic Spectroscopy Using Dual Acousto-Optic Pulse Shapers for Complete Amplitude, Phase, and Polarization Control of Femtosecond Laser Pulses*, J. Phys. Chem. A **117**, 6264–6269 (2013).

[250] M. T. Seidel, S. Yan, and H.-S. Tan, *Mid-infrared polarization pulse shaping by parametric transfer*, Opt. Lett. **35**, 478–480 (2010).

[251] M. T. Seidel, Z. Zhang, S. Yan, and H.-S. Tan, *Ultraviolet polarization pulse shaping using sum-frequency generation*, J. Opt. Soc. Am. B **28**, 1146–1151 (2011).

[252] G. Cerullo and S. De Silvestri, *Ultrafast Optical Parametric Amplifiers*, Rev. Sci. Instrum. **74**, 1–18 (2003).

[253] C.-C. Chen, I.-C. Hsieh, S.-D. Yang, and C.-B. Huang, *Polarization line-by-line pulse shaping for the implementation of vectorial temporal Talbot effect*, Opt. Express **20**, 27062–27070 (2012).

[254] O. Masihzadeh, P. Schlup, and R. A. Bartels, *Complete polarization state control of ultrafast laser pulses with a single linear spatial light modulator*, Opt. Express **15**, 18025–18032 (2007).

[255] J. W. Wilson, P. Schlup, and R. A. Bartels, *Ultrafast phase and amplitude pulse shaping with a single, one-dimensional, high-resolution phase mask.* Opt. Express **15**, 8979–8987 (2007).

[256] D. Kupka, P. Schlup, and R. A. Bartels, *Simplified ultrafast pulse shaper for tailored polarization states using a birefringent prism*, Rev. Sci. Instrum. **80**, 053110 (2009).

[257] F. Weise and A. Lindinger, *Full parametric pulse shaping in phase, amplitude, and polarization using an effective four-array modulator*, Appl. Phys. B **101**, 79–91 (2010).

[258] H. Miao, A. M. Weiner, L. Mirkin, and P. J. Miller, *Broadband all-order polarization mode dispersion compensation via wavelength-by-wavelength Jones matrix correction*, Opt. Lett. **32**, 2360–2362 (2007).

[259] O. Hüter, *Planung und Realisierung eines Vektorfeld-Pulsformers*, Diplomarbeit, Universität Würzburg (2010).

[260] F. Ebert, *Aufbau und Charakterisierung eines Vektorfeldpulsformers zur vollständigen Kotrolle des elektrischen Feldes ultrakurzer Laserpulse*, Diplomarbeit, Universität Würzburg (2012).

[261] W. H. Wollaston, *On the Methods of Cutting Rock Crystal for Micrometers*, Phil. Trans. R. Soc. Lond. **110**, 126–131 (1820).

[262] J. Hebling, *Derivation of the pulse front tilt caused by angular dispersion*, Opt. Quantum Electron. **28**, 1759–1763 (1996).

[263] E. Oliva, S. Gennari, L. Vanzi, A. Caruso, and M. Ciofini, *Optical materials for near infrared Wollaston prisms*, Astron. Astrophys. Suppl. Ser. **123**, 179–182 (1997).

[264] G. Wong, R. Pilkington, and A. R. Harvey, *Achromatization of Wollaston polarizing beam splitters*, Opt. Lett. **36**, 1332–1334 (2011).

[265] D. Barnhart and A. Williamson, *Optica 3 for Mathematica* (Barnhart Optical Research LLC).

[266] F. Langhojer, D. Cardoza, M. Baertschy, and T. C. Weinacht, *Gaining mechanistic insight from closed loop learning control: The importance of basis in searching the phase space*, J. Chem. Phys. **122**, 014102 (2005).

[267] C. J. Bardeen, Q. Wang, and C. V. Shank, *Selective Excitation of Vibrational Wave Packet Motion Using Chirped Pulses*, Phys. Rev. Lett. **75**, 3410–3413 (1995).

[268] B. Kohler, V. V. Yakovlev, J. Che, J. L. Krause, M. Messina, K. R. Wilson, N. Schwentner, R. M. Whitnell, and Y. Yan, *Quantum Control of Wave Packet Evolution with Tailored Femtosecond Pulses*, Phys. Rev. Lett. **74**, 3360–3363 (1995).

[269] C. J. Bardeen, V. V. Yakovlev, K. R. Wilson, S. D. Carpenter, P. M. Weber, and W. S. Warren, *Feedback quantum control of molecular electronic population transfer*, Chem. Phys. Lett. **280**, 151–158 (1997).

[270] A. Bartelt, A. Lindinger, C. Lupulescu, S. Vajda, and L. Wöste, *One parameter fs-pulse form control on NaK and Na_2K*, Phys. Chem. Chem. Phys. **5**, 3610–3615 (2003).

[271] P. Nuernberger, *Differences and analogies between linearly chirped and colored double pulses in the femtosecond regime*, Opt. Commun. **282**, 227–235 (2009).

[272] National Instruments, *LabVIEW 2012 SP1* (National Instruments Corporation).

[273] H.-S. Tan, *Theory and Phase-Cycling Scheme Selection Principles of Collinear Phase Coherent Multi-Dimensional Optical Spectroscopy*, J. Chem. Phys. **129**, 124501 (2008).

[274] S. Fechner, F. Dimler, T. Brixner, G. Gerber, and D. J. Tannor, *The von Neumann picture: A new representation for ultrashort laser pulses*, Opt. Express **15**, 15387–15401 (2007).

[275] S. Fechner, *Quantenkontrolle im Zeit-Frequenz-Phasenraum*, Dissertation, Universität Würzburg (2008).

[276] A. Rodenberg, S. Fechner, F. Dimler, D. J. Tannor, and T. Brixner, *Experimental implementation of ultrashort laser pulses in the von Neumann picture*, Appl. Phys. B **93**, 763–772 (2008).

[277] F. Dimler, S. Fechner, A. Rodenberg, T. Brixner, and D. J. Tannor, *Accurate and efficient implementation of the von Neumann representation for laser pulses with discrete and finite spectra*, New J. Phys. **11**, 105052 (2009).

[278] F. Langhojer, *New Techniques in Liquid-Phase Ultrafast Spectroscopy*, Dissertation, Universität Würzburg (2009).

[279] N. F. Scherer, R. J. Carlson, A. Matro, M. Du, A. J. Ruggiero, V. Romero-Rochin, J. A. Cina, G. R. Fleming, and S. A. Rice, *Fluorescence-detected wave packet interferometry: Time resolved molecular spectroscopy with sequences of femtosecond phase-locked pulses*, J. Chem. Phys. **95**, 1487–1511 (1991).

[280] T. Bayer, M. Wollenhaupt, and T. Baumert, *Strong-field control landscapes of coherent electronic excitation*, J. Phys. B: At. Mol. Opt. Phys. **41**, 074007 (2008).

[281] F. Langhojer, F. Dimler, G. Jung, and T. Brixner, *Product accumulation for ultrasensitive femtochemistry*, Opt. Lett. **32**, 3346–3348 (2007).

[282] A. Steinbacher, J. Buback, P. Nuernberger, and T. Brixner, *Precise and Rapid Detection of Optical Activity for Accumulative Femtosecond Spectroscopy*, Opt. Express **20**, 11838–11854 (2012).

[283] F. Kanal, S. Keiber, R. Eck, and T. Brixner, *100-kHz shot-to-shot broadband data acquisition for high-repetition-rate pump–probe spectroscopy*, Opt. Express **22**, 16965–16975 (2014).

[284] S. Schott, A. Steinbacher, J. Buback, P. Nuernberger, and T. Brixner, *Generalized magic angle for time-resolved spectroscopy with laser pulses of arbitrary ellipticity*, J. Phys. B: At. Mol. Opt. Phys. **47**, 124014 (2014).

[285] A. Steinbacher, P. Nuernberger, and T. Brixner, *Optical discrimination of racemic from achiral solutions*, Phys. Chem. Chem. Phys. **17**, 6340–6346 (2015).

Acknowledgements

In general, I would like to thank all group members who have provided an encouraging and pleasant atmosphere over the last few years. I am grateful to all the persons who directly or indirectly contributed to this project and thereby helped me to finish my PhD studies. I would like to thank in person:

- my supervisor **Prof. Dr. Tobias Brixner** for the opportunity to work in his group, for his trust in me to successfully realize the presented vector-field shaper despite some experimental setbacks in this project, for fruitful discussions and suggestions, for the annual "Skiseminar", and last but not least for ensuring funding of the project – primarily via the DFG program SPP 1391.

- **Prof. Dr. Thomas Feurer** for inviting us to Bern to demonstrate their vector-field shaper and for helpful suggestions.

- my diploma student **Ole Hüter** for his support during the design phase of the setup.

- my diploma student **Fabian Ebert** for his help while building the first version of the vector-field shaper and for building the servo-motor based shutters.

- **Dr. Stefan Rützel** for the many inspiring discussions which helped me a lot to carry out this project and for his assistance in the laboratory.

- **Dr. Philip Tuchscherer** and **Christian Kramer** for supporting me in the laboratory, whenever I needed a few more hands or eyes.

- **Florian Kanal** for his training on the alignment of the Lab4 laser system and for his constant willingness to help me to fix the laser.

- our technical assistants **Sabine Fuchs** and **Belinda Böhm** and my laboratory colleague **Tom Bolze** for their efforts to keep the Lab4 laser system running and for their help to install the Lab1 *Mira* in Lab4.

- all members of the mechanic and electronic workshop, especially **Ralf Kohrmann**, **Wolfgang Liebler**, **Katharina Schreckling**, and **Reiner Eck** for their uncomplicated, quick, and high quality solutions to various mechanical and electronic problems.

- **Dr. Johannes Buback** for helping me in programming the phase-to-voltage operation in C++.

- **Prof. Dr. Patrick Nürnberger** for arousing my interest in femtosecond pulse shaping during my studies of physics and for his helpfulness regarding various questions.
- **Dr. Johannes Buback** and **Andreas Steinbacher** for managing the VI-Pool and the computers in the laboratories and for their assistance with LabVIEW related problems.
- **Dr. Philipp Rudolf** and **Sebastian Schott** for maintenance of the literature database.
- my office colleagues **Dr. Stefan Rützel**, **Andreas Steinbacher**, and **Christian Kramer** for the very nice and unique atmosphere and for the scientific and non-scientific discussions and activities.
- **Dr. Stefan Rützel**, **Christian Kramer**, **Andreas Steinbacher**, **Bernhard Huber**, **Sabrina Donnert**, and **Miriam Buchberger** for proofreading this thesis.

Finally, I would like to thank my parents and family for their love and support and my friends for enriching my life.